



Habilitation Thesis

## **Molecular scattering and fluorescence in strongly confined optical fields spectroscopy, sensing and signal processing**

**Author(s):**

Agio, Mario

**Publication Date:**

2011

**Permanent Link:**

<https://doi.org/10.3929/ethz-a-007049705> →

**Rights / License:**

[In Copyright - Non-Commercial Use Permitted](#) →

This page was generated automatically upon download from the [ETH Zurich Research Collection](#). For more information please consult the [Terms of use](#).

# **Molecular Scattering and Fluorescence in Strongly Confined Optical Fields**

**Spectroscopy, sensing and signal processing**

## **Habilitationsschrift**

zur Erlangung der *Venia Legendi*  
für das Fach Physikalische Chemie

eingereicht am

Laboratorium für Physikalische Chemie

Eidgenössische Technische Hochschule

Zürich 2011

vorgelegt von

**Dr. Mario Agio**

geboren am 31.07.1975 in Piacenza



**To Sofia, Anna and Marta**





# Abstract

Common treatments of light-matter interaction in free space consider an electromagnetic beam homogeneous over a transverse area  $A$  and use the concept of a cross section  $\sigma$  to arrive at the probability  $\sigma/A$  for coupling light with a quantum emitter, like an atom or a molecule. In conventional spectroscopy experiments this ratio is very small and a single emitter is expected to have a weak effect on the light incident on it. However, recent experiments have shown that extinctions up to 12% can be attained in free space simply by focusing light or using small apertures. A fundamental question is how close these values are to the theoretical limits. We investigate the interaction of a single oscillating dipole with tightly confined optical fields and demonstrate that light can be perfectly reflected under appropriate conditions. In particular, we find that a focused plane wave can be extinguished up to 85%.

We also discuss possibilities for modifying light-matter interaction using concepts from surface-enhanced spectroscopy. Recent progress in nanotechnology has enabled us to fabricate nanoscale systems that could function as antennas for enhancing the excitation and emission of optical energy by atoms and molecules. We discuss the main features of an optical antenna and show how they can improve the coupling and the radiation properties of molecules. In particular, we present realistic designs that increase fluorescence by more than three orders of magnitude in the ultraviolet up to the near-infrared spectral range.

An important point of concern is whether one could transfer the designs found in many electrical engineering textbooks into the optical domain to control light-matter interaction at the nanometer scale. Moreover, since metals exhibit absorption losses at optical frequencies, it is not obvious that antennas are suitable for light management at the single-photon level and that they achieve performances comparable to those of optical resonators. These concerns go beyond the scope of field-enhanced spectroscopy and sensing, and take us to the ultimate limits of information processing.



# Contents

<b>1</b>	<b>Introduction</b>	<b>11</b>
<b>2</b>	<b>Single-molecule spectroscopy</b>	<b>21</b>
2.1	Optical properties of a single molecule . . . . .	21
2.1.1	Energy level diagrams and transition rates . . . . .	22
2.1.2	Single-molecule detection . . . . .	26
2.2	Scattering theory . . . . .	28
2.2.1	General formulation . . . . .	28
2.2.2	Scattering and absorption by a dipolar radiator . . . . .	33
2.3	Coherent spectroscopy . . . . .	34
2.3.1	Two-level system driven by a laser . . . . .	35
2.3.2	Coherent and incoherent scattering . . . . .	36
<b>3</b>	<b>Coherent spectroscopy in strongly confined fields</b>	<b>41</b>
3.1	Optimal concentration of electromagnetic energy . . . . .	42
3.1.1	Focused beams . . . . .	42
3.1.2	Subwavelength apertures . . . . .	48
3.2	Generalized scattering theory . . . . .	51
3.2.1	The optical theorem . . . . .	52
3.2.2	Scattering and absorption by a dipolar radiator . . . . .	54
3.3	A molecule illuminated by a SNOM aperture . . . . .	56
3.3.1	Layout of the problem . . . . .	56
3.3.2	Far-field pattern and detected signals . . . . .	58
3.4	A single molecule in a strongly focused beam . . . . .	65
3.4.1	The scattering ratio . . . . .	65
3.4.2	Reflection and transmission . . . . .	69
3.4.3	Phase-shift . . . . .	73
<b>4</b>	<b>Shaping molecular fluorescence by optical antennas</b>	<b>75</b>
4.1	Enhancement and quenching of fluorescence . . . . .	76
4.1.1	Field enhancement and quantum efficiency . . . . .	76
4.1.2	Surface-enhanced fluorescence and quenching . . . . .	78
4.1.3	Metal nanoparticles as optical antennas . . . . .	81

4.2	Optical antennas . . . . .	84
4.2.1	Design rules . . . . .	85
4.2.2	Shape dependence . . . . .	89
4.2.3	Materials dependence . . . . .	98
4.2.4	Directional optical antennas . . . . .	104
4.3	Interfacing optical antennas with optics and photonics . . . . .	109
4.3.1	Coupling light to a dipolar antenna . . . . .	109
4.3.2	Coupling to a nanofiber . . . . .	116
4.3.3	Coupling to a focused beam . . . . .	121
4.3.4	High-throughput SNOM . . . . .	126
<b>5</b>	<b>Towards nanoscale cavities</b>	<b>131</b>
5.1	From antenna theory to nanoscale resonators . . . . .	132
5.1.1	Cavity quantum electrodynamics . . . . .	132
5.1.2	Field-enhanced spectroscopy . . . . .	134
5.1.3	Antenna theory . . . . .	135
5.2	Electrically small antennas . . . . .	137
5.2.1	Fundamental limitations . . . . .	137
5.2.2	Figures of merit for optical antennas . . . . .	138
5.3	Optical antennas as nanoscale cavities . . . . .	144
<b>6</b>	<b>Conclusions and outlook</b>	<b>153</b>
<b>A</b>	<b>Strongly focused beams</b>	<b>159</b>
A.1	Debye diffraction integrals . . . . .	159
A.1.1	Focused plane wave . . . . .	160
A.1.2	Directional dipole wave $p_x$ . . . . .	162
A.1.3	Combined electric and magnetic dipole waves . . . . .	162
A.1.4	Directional dipole wave $p_z$ . . . . .	163
A.1.5	Incident power . . . . .	163
A.2	Multipole expansion . . . . .	164
A.2.1	Vector spherical harmonics . . . . .	164
A.2.2	Focused plane wave . . . . .	166
A.2.3	Directional dipole wave $p_x$ . . . . .	166
A.2.4	Focused radially polarized beam . . . . .	167
<b>B</b>	<b>Modeling light-matter interactions near metal nanostructures</b>	<b>171</b>
B.1	The FD-TD algorithm . . . . .	171
B.1.1	Governing equations . . . . .	172
B.1.2	Boundary conditions . . . . .	173
B.1.3	Metals at optical frequencies . . . . .	174
B.1.4	Advanced FD-TD approaches . . . . .	175
B.1.5	Body of revolution . . . . .	179

---

B.2	Modeling interactions . . . . .	181
B.2.1	Molecular scattering . . . . .	181
B.2.2	Decay rates . . . . .	182
B.3	Numerical tests . . . . .	183
B.3.1	Perfect mirror . . . . .	184
B.3.2	Metal mirror . . . . .	186
B.3.3	Gold nanosphere . . . . .	187
	<b>Bibliography</b>	<b>191</b>
	<b>Acknowledgments</b>	<b>231</b>



# Chapter 1

## Introduction

In the 18th century Bouguer studied the attenuation of light through a substance and established a relationship between the absorption coefficient and the transmittance (Bouguer, 1729). About 120 years later Beer extended these findings to solutions and related absorption to the concentration of molecules (Beer, 1852). The so-called Beer-Lambert-Bouguer law<sup>1</sup> can be introduced in the form  $T = \exp(-\alpha l)$ .  $T$  represents the transmittance, whereas  $\alpha$  is the absorption coefficient and  $l$  is the distance that light travels through the substance. Moreover, for a diluted sample one can write  $\alpha = \sigma N$ , where  $N$  is the number of molecules per unit volume and  $\sigma$  is the cross section. The latter represents the probability that light gets absorbed or scattered by one molecule and it characterizes the strength of light-matter interaction at the microscopic level (Allen and Eberly, 1975; Atkins and Friedman, 2005).

Interestingly, the law was discovered before Maxwell formulated the dynamical theory of light (Maxwell, 1865). In fact, the expression  $\exp(-\alpha l)$  seems to suggest that  $T$  does not have a particular dependence on the incident beam, except from the fact that its waist determines the illuminated area, hence the number of probed molecules. Indeed, for many years spectroscopists have applied the Beer-Lambert-Bouguer law to investigate the structural and dynamical properties of atoms and molecules without raising concerns on its validity<sup>2</sup> (Hollas, 2004).

The situation changes when one considers a single-photon source (Kimble and Mandel, 1976), like atoms (Kimble et al., 1977), ions (Diedrich and Walther, 1987), molecules (Brunel et al., 1999), quantum dots (Michler et al., 2000), or color centers in diamond (Brouri et al., 2000; Kurtsiefer et al., 2000). In this case the Beer-Lambert-Bouguer law is commonly written as  $T = 1 - \sigma/A$ , where  $A$  is an area perpendicular to the propagation direction representing the beam spot size (Karrai and Warburton, 2003). In conventional spectroscopic experiments  $\sigma/A$  is very

---

<sup>1</sup>The law is misattributed to Lambert, who quoted the work of Bouguer in his publication (Lambert, 1760).

<sup>2</sup>Note that the law holds only if the spectral bandwidth of the probe light is narrow compared to the linewidths in the spectrum.



small because either  $A$  is large for technical reasons or  $\sigma$  is small for various broadening effects. As a result, testing the limits of the Beer-Lambert-Bouguer law is challenged by the difficulty in detecting the absorption signal of a single emitter.

The invention of the laser gave us highly stable and coherent light sources with very narrow linewidths (Maiman, 1960), which opened the doors to high-resolution spectroscopy (Hollas, 1998). Moreover, the laser pushed forward the resolution limits of optical microscopy (Cremer and Cremer, 1978), hence the possibilities of reducing  $A$  by focusing light to a tighter spot (Bassett, 1986). Lastly, it led to stabilization schemes that significantly improved the sensitivity of a spectroscopic experiment (Black, 2001).

These and other developments led to the first observation of the absorption signal of a single ion in a transmission experiment (Wineland et al., 1987). The measurement was possible also because the interaction cross section of a single ion is a million times larger than that of a typical dye molecule in a host matrix at room temperatures. Indeed, the field of single-molecule spectroscopy started with the detection of pentacene in a para-terphenyl crystal at liquid-helium temperatures (Moerner and Kador, 1989), where the suppression of broadening effects enhances  $\sigma$  by orders of magnitudes (Friedrich and Haarer, 1984; Rebane, 1970). The first steps toward the detection of single molecules focused in fact on the narrow spectral features in hole-burning experiments (Kharlamov et al., 1974) and on its statistical fine structure (Carter et al., 1988).

Single-molecule spectroscopy, however, found its way through a detection scheme based on fluorescence excitation spectroscopy (Orrit and Bernard, 1990). In practice, a fraction of the weak fluorescence signal is spectrally separated from the laser and it can be efficiently isolated from the source noise using a long-pass filter. Since the demonstration of single-molecule detection at room temperatures (Betzig and Chichester, 1993) the technique has become very important in physics, chemistry, biology and materials science (Kulzer and Orrit, 2004; Lupton, 2010; Michaelis and Bräuchle, 2010; Moerner, 2002; Patterson et al., 2010; Tamarat et al., 2000; Weiss, 1999, 2000; Xie and Trautman, 1998). At the more fundamental level of light-matter interaction, single-molecule fluorescent excitation spectroscopy enabled the first quantum optical experiments using solid-state emitters (Basché et al., 1995; Brunel et al., 1998, 1999; Fleury et al., 2000; Tamarat et al., 1995).

The advent of quantum information science (Nielsen and Chuang, 2000) and the increasing attention on light as a reliable hardware for quantum communication and computation (Kimble, 2008; Knill et al., 2001; Ladd et al., 2010; Monroe, 2002; O'Brien, 2007) has renewed the interest for detection schemes that preserve coherence in the interaction process (Cirac et al., 1997; Duan and Kimble, 2004; Savage et al., 1990; Turchette et al., 1995; van Loock, 2011; Waks and Vuckovic, 2006; Wilk et al., 2007). However, one should bear in mind that a major challenge persists, namely the weak coupling of light with matter at the level of single emitters. A well-know solution to this problem relies on the use of optical resonators (Benisty

et al., 1999; Vahala, 2003). Indeed, several proposals of quantum networks and repeaters refer to coherent cavity-assisted interactions (Cirac et al., 1997; Duan and Kimble, 2004; Turchette et al., 1995; van Loock et al., 2008). These have been tested in a number of different realizations based on single quantum emitters coupled to optical resonators (Birnbaum et al., 2005; Dayan et al., 2008; Fushman et al., 2008; Schuster et al., 2008; Turchette et al., 1995; Wilk et al., 2007).

Recent experimental efforts have shown that light focused on single ions, molecules, or quantum dots may be attenuated in transmission by a few percent (Gerardot et al., 2007; Gerhardt et al., 2007b; Tey et al., 2008; Vamivakas et al., 2007; Wrigge et al., 2008a). Indeed one expects that a quantum emitter has a strong effect on the incident light when  $\sigma/A$  is close to unity. However, whether these results are near or far from the maximum possible value was not known. From the theoretical side, the interaction of freely propagating photons with the dipolar transition of a two-level system (TLS) has been investigated for a quasi-one-dimensional case with emphasis on the quantum statistics of the incident light (Carmichael, 1993; Kochan and Carmichael, 1994). The model predicts that a single emitter can be made optically thick, but it does not take into account the dynamical properties of light, as for the case of the Beer-Lambert-Bouguer law.

These phenomena are strongly related to scattering theory, which studies the propagation of light in an inhomogeneous medium from the electrodynamic point of view (Sheng, 1995). For a single spherical object illuminated by a plane polarized wave, the exact solution of the scattering problem is often referred to as Mie theory (Mie, 1908). It turns out that the amount of electromagnetic energy removed in the propagation direction of the incident beam, the so-called extinction, corresponds to the sum of the total absorbed and scattered powers, irrespective of the shape of the object. This intriguing result, which expresses the optical theorem (van de Hulst, 1949b), relates a transmission measurement, i.e. the Beer-Lambert-Bouguer law, to the strength of light-matter interaction.

A point-like obstacle exhibits a cross section  $\sigma$  independent from the type of illumination, because it probes the field amplitude only at one location (Jackson, 1999). Therefore, the Beer-Lambert-Bouguer law seems to be applicable to the case of focused illumination without concerns and the use of scattering theory appears unnecessary. Problems arise though from the choice of  $A$ , which for a diffraction limited focus cannot be easily related to a geometrical feature of the beam (Stamnes, 1986), and from the failure of the optical theorem for focused illumination (Lock et al., 1995). In fact, a more careful look at the interaction process reveals that diffraction plays an important role in determining the attenuation of light by a point-like scatterer, as shown in Figure 1.1 (Paul and Fischer, 1983).

Early attempts to generalize scattering theory to inhomogeneous illuminations regarded the problem of collimated laser beams incident on large colloids (Morita et al., 1968; Tsai and Pogorzelski, 1975), hence on objects having dimensions comparable or bigger than the beam waist. The attention on point-like scatterers came

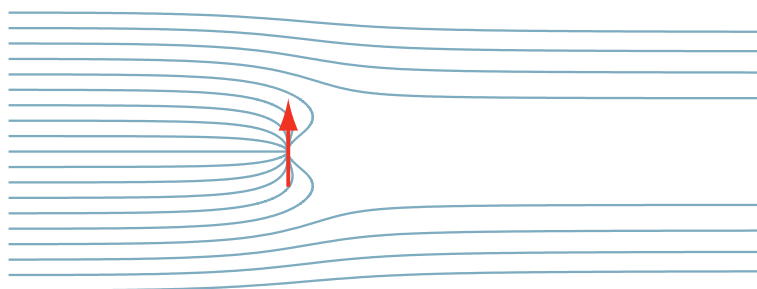


**Figure 1.1:** *The absorption of light by a point-like oscillating dipole (red arrow) illustrated from the electrodynamic point of view (after Paul and Fischer, 1983).*

much later (van Enk, 2004; van Enk and Kimble, 2000, 2001). These latter studies concluded that only the dipolar component of the excitation light can couple to a dipole and that the transmitted power is only weakly attenuated. Interestingly and somewhat in parallel, the literature on the interaction of a TLS with light confined to a waveguide claims that very strong attenuation is possible (Domokos et al., 2002).

The first part of this work investigates light scattering by a TLS in tightly confined fields, obtained either by a subwavelength aperture (Bethe, 1944) of a scanning near field optical microscope (SNOM) or by a strong lens (Richards and Wolf, 1959). The latter case allows us to derive analytical formulae, which take us to the limits of light-matter interaction in free space. On the other hand, the aperture reveals the importance of the coherence between the incident and the scattered fields and how this determines the extinction signal. In particular, we analyze visibility and lineshape and show their complex dependence on the various parameters that define the aperture, the molecule and the detected signal (Gerhardt et al., 2007a,b). For focused beams we theoretically demonstrate that under appropriate conditions the incident light is perfectly reflected and that the transmission can be attenuated by up to 85% for the experimentally important case of a focused plane wave (Zumofen et al., 2009, 2008). These upper bounds reveal the profound relationship between the optimal concentration of electromagnetic energy in free space (Bassett, 1986) and the strength of light-matter interaction for a dipolar oscillator (Jackson, 1999). Moreover, we show that the Beer-Lambert-Bouguer law is still appropriate if  $A$  is the effective area given by the ratio between the total incident power and the field intensity at the focus. Inspired by a number of proposals for quantum information science (Savage et al., 1990; Turchette et al., 1995; van Loock et al., 2006) we calculate the phase shift impressed by a TLS on a focused beam and find that values of a few degrees can be easily achieved (Zumofen et al., 2009). These predictions have been confirmed by recent experiments performed on single trapped atoms (Aljunid et al., 2009) and molecules (Pototschnig et al., 2011).

The resonant cross section of a weakly excited TLS is  $\sigma_o = 3\lambda^2/2\pi$ , where  $\lambda$  is the wavelength associated with the optical transition (Cohen-Tannoudji et al., 2004).

This value is compatible with the diffraction limit, which states that a beam cannot be focused down to an area smaller than  $(\lambda/2NA)^2$ , where NA is the numerical aperture of the optical system (Born and Wolf, 1999). On the other hand, the cross section  $\sigma$  can also be several times smaller than  $\sigma_0$ .

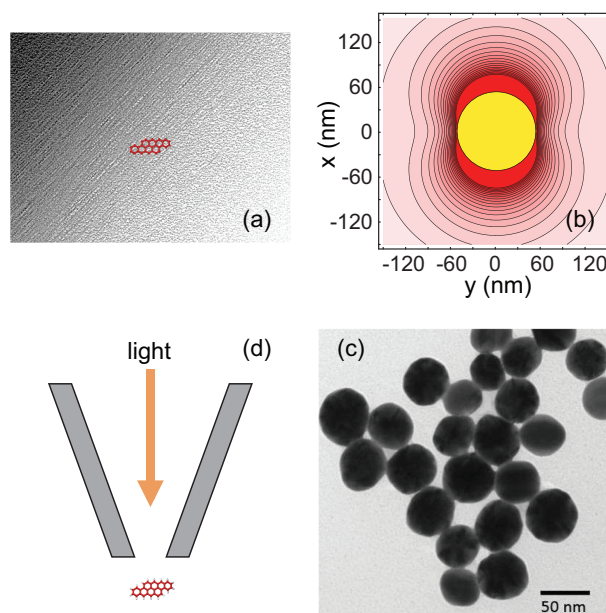


**Figure 1.2:** (a) Molecule (not to scale) adsorbed on a rough metal surface. (b) Field enhancement near a 100 nm gold nanosphere under plane-wave illumination. (c) Chemically synthesized metal nanoparticles. (d) Schematics of an aperture SNOM (molecule not to scale).

A well-known example of a weak interaction is Raman scattering (Raman and Krishnan, 1928), where  $\sigma/A$  can be as small as  $10^{-20}$ ! In the 1970s physical chemists recognized that the enhancement in the Raman signal of molecules adsorbed on rough metal surfaces was due to the strong local electromagnetic fields generated by roughness (Albrecht and Creighton, 1977; Jeanmaire and Duynes, 1977). To explain these phenomena theorists started to develop simplified models based on the electrostatic polarizability of very small metal particles and they soon understood that these could yield better and more controllable enhancements (Aravind et al., 1981; Gersten and Nitzan, 1980; Metiu, 1984; Moskovits, 1985). The first experiments on enhanced Raman scattering by metal nanoparticles took place in the 1980s (Lee and Meisel, 1982), in the same period of time when scanning near-field optical microscopy was being developed (Lewis et al., 1984; Pohl et al., 1984). In the following years, progress in fabrication has initiated a series of activities aimed at replacing nanoparticles and metal-coated fibers with engineered nanostructures to convert localized electromagnetic energy into radiation and vice versa with a higher efficiency (Grober et al., 1997; Pohl, 2000). The dramatic advances of nanotechnology experienced in recent years have boosted the interest in these devices that function as nanoscale antennas (Greffet, 2005; Mühlischlegel et al., 2005).

In fact, the amount of activities on this topic has grown very rapidly in various fields of research, spanning physics, chemistry, electrical engineering, biology, and medicine to cite a few (Anker et al., 2008; Bharadwaj et al., 2009; Novotny and van Hulst, 2011; Schuller et al., 2010).

Our interest focuses on the enhancement of resonant phenomena and in particular on light absorption and emission by a quantum emitter. A series of experiments in the 1960s and in the 1970s discovered that also molecular fluorescence is modified near metal surfaces (Drexhage, 1974, 1966). In subsequent years theoretical works predicted, however, that the signal was quenched due to a drastic reduction in the emission quantum yield caused by absorption in real metals (Chance et al., 1978; Ruppin, 1982). That has led to a longstanding contrast between the huge enhancements discovered in surface-enhanced Raman scattering (Kneipp et al., 1997; Nie and Emory, 1997) and the quenching of fluorescence by metal nanoparticles (Ruppin, 1982; Xu et al., 2004). It turns out that these phenomena are inherent to near-field interactions, which for many years have posed a great challenge to their experimental verification and quantitative understanding (Biteen et al., 2005; Dulkeith et al., 2002; Kulakovich et al., 2002; Kümmerlen et al., 1993; Leitner et al., 1985; Shimizu et al., 2002; Wokaun et al., 1983).

The advent of SNOM (Lewis et al., 1984; Pohl et al., 1984) and single-molecule spectroscopy (Moerner and Kador, 1989; Orrit and Bernard, 1990) provided the experimental tools for controlled investigations of metal enhanced fluorescence and quenching (Anger et al., 2006; Farahani et al., 2005; Frey et al., 2004; Kühn et al., 2006). In particular, it has been shown that a spherical gold nanoparticle acts as an optical antenna that modifies the excitation rate, the spontaneous emission rate, and the radiation pattern of an emitter in its near field (Kühn et al., 2006, 2008). These and previous works have shown that the competition between field enhancement and quenching is distance dependent and that there is a separation where the signal is maximal (Anger et al., 2006; Wokaun et al., 1983).

Several parameters influence the enhancement of fluorescence and the question that arises is to what extent these could be optimized. While a huge literature exists for the design of optical antennas for the field enhancement (Aizpurua et al., 2005), much less attention has been devoted to the improvement of the fluorescence quantum yield (Gersten and Nitzan, 1981; Lakowicz, 2005). In addition, these works had in mind spectroscopy and sensing applications (Anker et al., 2008). Our concern is instead the enhancement of light-matter interaction to a regime where single photons couple with single quantum emitters with a high probability. This may be possible only if large enhancements coexist with high quantum yields. For instance, at room temperature the cross section  $\sigma$  of a typical dye molecule is about five to six orders of magnitude smaller than  $\sigma_0$ . How much could we enhance it using optical antennas? Are these suitable for light management at the single photon level and can they achieve performances comparable to those of optical resonator?

These are the questions that we address in the second part of this work. We an-

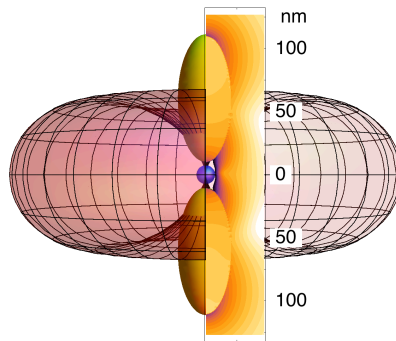


**Figure 1.3:** *An optical antenna made of two spheroidal gold nanoparticles enhances radiation by a quantum emitter placed in the gap. The intense near field and the length scale of the antenna are also shown.*

analyze the various effects that influence the modification of the radiative decay rate and the quantum yield near a metal surface. We then derive a number of empirical rules to design optical antennas that lead to a strong enhancement of the fluorescence signal and, at the same time, to quantum yields close to unity. Next, we take advantage of computational nano-optics (Kaminski et al., 2007) to investigate how these rules perform in reality (Mohammadi et al., 2010, 2008b; Rogobete et al., 2007). Moreover, we propose designs that are fully compatible with state-of-the-art nanofabrication and explore effects related to the antenna composition (Mohammadi et al., 2009b).

An important figure of merit of radio-wave antennas is the so-called directivity (Balanis, 2005). It represents the power radiated in a certain direction with respect to an hypothetical isotropic radiator. For instance, radiating dipoles exhibit a broad pattern in comparison to directive antennas like the Yagi-Uda array (Uda, 1927; Yagi, 1928). Several applications ranging from fluorescence microscopy to quantum information science would very much benefit from “directional” light emitters. Indeed, the past decades have witnessed several attempts to increase the collection efficiency for atoms and molecules using, to cite a few, dielectric planar interfaces (Barnes et al., 2002; Koyama et al., 1999; Lee et al., 2011; Lukosz and Kunz, 1977), optical resonators (Pelton et al., 2002; Strauf et al., 2007), gratings (Kitson et al., 1996; Knoll et al., 1981; Rigneault et al., 1999), surface roughness (Raether, 1988; Yablonovitch, 1982), photonic crystals (Rattier et al., 2002; Ryu et al., 2001; Zelsmann et al., 2003), and more recently nanowires (Babinec et al., 2010; Chang et al., 2007b; Claudon et al., 2010).

Another point of concern is whether one can take an engineering textbook and simply adapt antenna designs to the optical domain. Several authors have shown that this is a workable solution (Hofmann et al., 2007; Li et al., 2007) and their predictions have been experimentally confirmed (Curto et al., 2010). Here we follow a different approach, which considers the different requirements and opportuni-

ties of optics, photonics and antenna theory. More precisely, we require that the antenna radiation pattern corresponds to a well-defined optical mode, i.e. a guided wave or a collimated beam, such that the system operates with a high efficiency also in the excitation channel. Moreover, we design directional antennas that, in addition, exhibit a strong enhancement of the emission rate and a high quantum efficiency. These investigations have led to the proposal of a high-throughput SNOM (Chen et al., 2009, 2010a), a device that may largely improve scanning implementations of fluorescence, Raman, or other nonlinear nanoscopies (Hartschuh, 2008; Hartschuh et al., 2004).

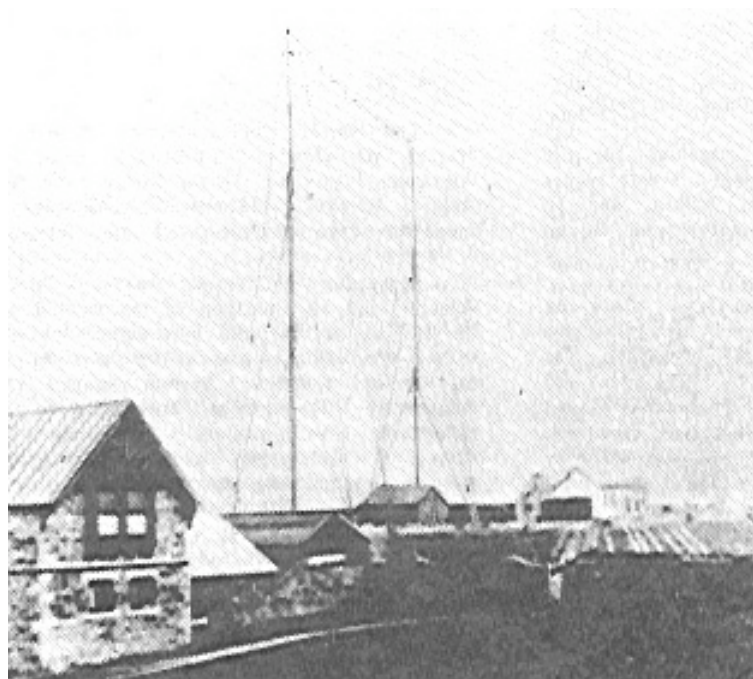


**Figure 1.4:** *Marconi's antenna system at Poldhu, Cornwall (Dec. 1901) (photo by J. Belrose).*

Optical antennas go beyond the issue of spectroscopy or sensing and take us to the ultimate limits of communication and information processing. For more than 100 years electromagnetic waves have been extensively used to exchange signals over long distances, and antennas have been playing a fundamental role since the very beginning. In 1896 Marconi invented wireless telegraphy and in 1901 he managed to send the first wireless signal across the Atlantic with the help of radio-wave antennas (Marconi, 1967). In 1966 Kao and Hockham proposed the use of optical fibers to transmit light over several kilometers (Kao and Hockham, 1966) and today a huge amount of information travels around the globe in thin threads of glass. More recently, optical interconnects are being exploited in high-performance computers. The reason is that electrical wires have energy and bandwidth issues that are rapidly growing in the next integration targets. It is not yet clear how far light will go into a chip, but it is certain that it will be playing an increasing role



---

in information processing and that photonic devices will have to reach nanoscale dimensions (Kirchain and Kimerling, 2007; Miller, 2009).

An optical photon carries energy of the order of  $10^{-19}$  J. The amount of energy required to process a bit of information in a transistor should reach  $10^{-18}$  J in 2016 (ITRS). In a not too distant future we might envision data carried by light pulses made of a few optical photons efficiently interfaced to an electrical transistor that processes information at tiny power levels. Or we could even think of all-optical signal processing where a saturable light absorber like an atom or a molecule is used to achieve strong and controllable interactions between single photons (Hwang et al., 2009). These projections are approaching the even tighter requirements of quantum information science, where bits are replaced by qubits. These are quantum states of light or matter that need to be transmitted, processed and stored with a high fidelity (Monroe, 2002). To this end there is an ongoing incredible amount of work to improve light-matter interaction at a fundamental level, with an explosion of activities in areas where, traditionally, quantum optics and nanophotonics did not play a central role.

We have presented approaches based on optics, field-enhanced spectroscopy and antenna theory to significantly enhance the interaction between light and very small amounts of matter, ideally down to single atoms and molecules. We conclude by discussing their relationship with resonators. To gain further insight on the control of light-matter interaction, we first consider simplified antenna models and discuss basic properties starting from analytical expressions. Since optical antennas have dimensions smaller than the operating wavelength, we base the analysis on the fundamental limitations of electrically small antennas (Hansen, 1981). Next, we select a few popular resonator designs (Vahala, 2003) and compare their figures of merit with those of optical antennas. We show that the enhancement of light-matter interaction is comparable to that achievable with state-of-the-art cavities. Interestingly, the antenna efficiency and the enhancement have opposite trends, but there is a window of opportunity where optical antennas could function as nanoscale resonators with a tiny device footprint and manageable absorption losses. There is another important advantage in optical antennas. Having a low quality factor they are fully compatible with methods and techniques of ultrafast spectroscopy (Dantus and Lozovoy, 2004; Zewail, 2001) and coherent control (Bandrauk et al., 2002; Rabitz et al., 2000). We will return to these aspects in the concluding part.





# Chapter 2

## Single-molecule spectroscopy

Optical spectroscopy studies the properties of atoms, molecules and condensed matter through the absorption and emission of light and under the usual assumption of an incident polarized plane wave (Hollas, 2004). Common treatments of scattering theory consider an incident plane wave too, but here light-matter interaction is expressed in terms of a scattered wave that emerges from the target (Bohren and Huffman, 1983; van de Hulst, 1949a). Before we study in detail molecular scattering in strongly confined optical fields we need to establish a connection between these two pictures. We thus review the semi-classical theory of light-matter interaction at the single-molecule level and formulate scattering theory for a point-like oscillating dipole. We introduce the concept of a cross section to represent the coupling strength and to distinguish between absorption, scattering and extinction. Lastly, we outline the general framework of coherent spectroscopy and specify it for a transmission experiment performed on a single quantum emitter.

### 2.1 Optical properties of a single molecule

Throughout this work we focus our attention on an ideal TLS. Nonetheless it is useful to begin by making a connection with experiments and explain why single molecules are suitable candidates for this type of investigations (Gerhardt, 2006; Kühn, 2006; Wrigge, 2008). In what follows we briefly discuss the optical properties of single molecules and explain how they depend on their microscopic structure (Atkins and Friedman, 2005). In particular, we consider the case of a dopant molecule in a host matrix (Rebane, 1970). Our goal is to point out the differences and the analogies with respect to the response of a TLS. For the sake of completeness, we also include a short historical note on single-molecule detection.

### 2.1.1 Energy level diagrams and transition rates

The energy level structure of a molecule results from a complex hierarchy of interactions between its fundamental constituents. In the Born-Oppenheimer approximation we can distinguish electronic, vibrational and rotational states, which are well separate in the energy scale. This classification has important consequences on the optical properties of molecules, because it determines transition frequencies and rates among the different levels.

#### The Jablonski diagram

The electronic ground state of a molecule is typically a singlet  $S_0$ , because the bonding molecular orbital hosts paired electrons with antiparallel spins. The excited states can be singlets  $S_i$  or triplets  $T_i$ , with the latter tending to have a lower energy due to the first Hund's rule (Atkins and Friedman, 2005). Because of the spin selection rule the strongest optical transitions are singlet-singlet, e.g.  $S_0 \leftrightarrow S_1$ . They typically cover the visible spectrum and have fluorescence lifetimes of the order of 1-10 ns. Triplet-singlet transitions are weakly allowed, hence much less probable. The  $S_1 \rightarrow T_1$  transition is named intersystem crossing, whereas the  $T_1 \rightarrow S_0$  one refers to the so-called phosphorescence, with decay times that are several orders of magnitude longer than fluorescence. These processes, together with the relevant level structure, are illustrated in Figure 2.1a. This schematic representation is called Jablonski diagram, after the Polish physicist Aleksander Jabłoński (1898-1980), a pioneer in the study of the photophysics of molecules.

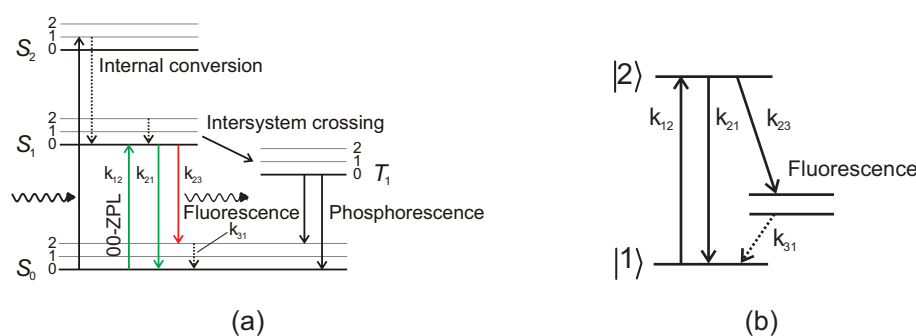


**Figure 2.1:** (a) Jablonski and (b) simplified diagram for the description of the energy level structure and the optical transitions of a single molecule. The transitions relevant for this work are color coded. The green lines refer to resonant excitation and emission using the ground state, whereas the red line labels the red-shifted fluorescence.

Figure 2.1a shows additional sublevels that stem from the vibrational degrees of freedom. These can affect the optical properties of a molecule in two ways. First, an excited state can lose energy through a series of fast nonradiative transitions mediated by the vibrational motion. This internal conversion process can reduce

the quantum yield, i.e. the ratio between the radiative and the total decay rates, and relax the system to the vibrational ground state (Kasha, 1950). Second, optical absorption and emission can involve one or more vibrational transitions. Therefore, the spectra reflect the asymmetry of the energy level structure and present the typical profiles shown in Figure 2.3.

### Strength of the zero phonon line

For dopant molecules hosted in a solid matrix the rotational degrees of freedom can be ignored because the matrix usually prevents this type of motion. However, one has to take into account couplings with the delocalized vibrational excitations of the host lattice, the phonons. In this work we are mainly interested in transitions that approximate the optical properties of a TLS (Allen and Eberly, 1975). These are indicated in Figure 2.1a by green lines. The excitation from the zeroth (0) vibrational level of the  $S_0$  state to the zeroth (0) vibrational level of the  $S_1$  is called the 00-ZPL (Zero Phonon Line). The emission spectrum of dye molecules is typically dominated by this transition and by the red-shifted fluorescence, indicated in Figure 2.1a by a red line.

The strength of the 00-ZPL transition and the direct decay to the ground state vary with the dopant molecule and the host matrix (Friedrich and Haarer, 1984; Rebane, 1970). The ratio between the decay rate  $k_{21}$  to the ground state  $S_0$  and the total decay into the vibrational sublevels  $k_{23}$  is called the branching ratio (see Figure 2.1b). It is associated with the Franck-Condon principle, which states that an electronic transition occurs without changing the interatomic distances in the molecule (Atkins and Friedman, 2005). This is schematically illustrated in Figure 2.2a, where the energy levels are plotted as a function of the normalized nuclear coordinate. It is shown that the excitation of the 00-ZPL is vertical and proportional to the overlap between the ground state vibrational wavefunctions of the  $S_0$  and  $S_1$  electronic states. The mismatch, which depends on the variation  $\Delta q$  of the equilibrium distance of the nuclei, results in the so-called Franck-Condon factor  $\alpha_{FC}$ . For terrylene in hexadecane, a typical system used in single-molecule spectroscopy,  $\alpha_{FC}$  is of the order of 0.4 (Moerner, 1994).

The presence of a host matrix modifies the spectrum of the single molecule by adding a phonon wing to each allowed transition, as shown in Figure 2.2b for the 00-ZPL. This component can be explained by considering a linear electron-phonon coupling that transfers molecular excitations into lattice vibrations. The lineshape of the phonon sideband corresponds to a Poisson distribution, but in many cases it can be approximated by a Gaussian profile (Markham, 1959). The effect can be characterized by the so-called Debye-Waller factor  $\alpha_{DW}$ , which is the intensity of the 00-ZPL normalized with respect to the total intensity (Friedrich and Haarer, 1984; Rebane, 1970). The displacement  $\Delta$  of the phonon wing with respect to the transition frequency  $\nu_0$  of the 00-ZPL is related to the strength of the electron-

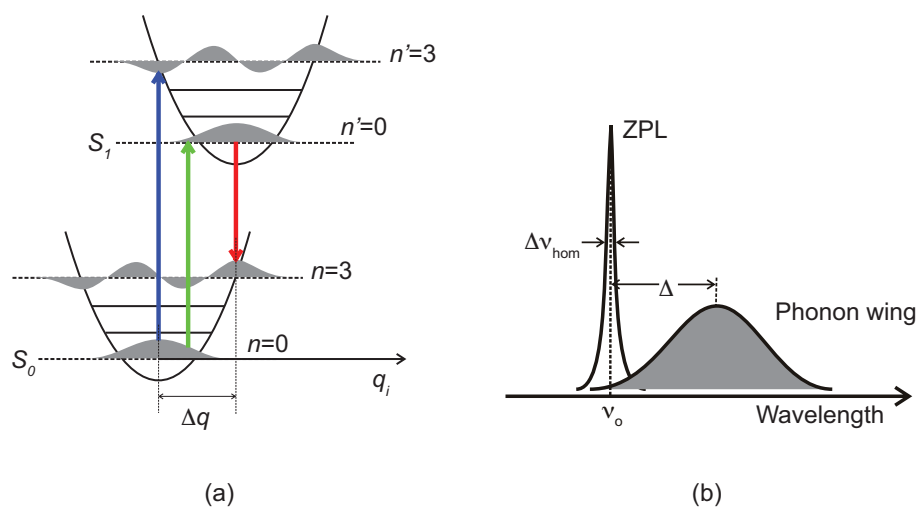


**Figure 2.2:** (a) Energy levels of a single molecule plotted as a function of the normalized nuclear coordinate  $q_i$ . The Franck-Condon principle implies that for any transition from the ground  $S_0$  to the excited  $S_1$  state there is no nuclear momentum transfer. (b) In the presence of linear electron-phonon coupling, momentum conservation implies that the emission spectrum acquires a phonon wing, with a central frequency shifted by  $\Delta$  from the purely electronic transition at  $\nu_0$ . The homogeneous broadening  $\Delta\nu_{\text{hom}}$  is shown for comparison.

phonon coupling (see Figure 2.2b).

In summary, the strength of the 00-ZPL is reduced by the factor  $\alpha = \alpha_{\text{FC}}\alpha_{\text{DW}}$ . Rigid molecules tend to have a larger  $\alpha$ . They thus approach the behavior of a TLS, especially for what concerns the coherent properties of the emitted light. In fact, the inelastic transitions that determine  $\alpha_{\text{FC}}$  and  $\alpha_{\text{DW}}$  give rise to incoherent radiation without phase relationship with the probe laser.

## Molecular spectra

The host matrix has another important effect on the optical properties of molecules. It creates a nanoenvironment that induces spectral shifts that depends on the precise location of each molecule. Therefore, the absorption and emission spectrum of an ensemble is typically very broad, as shown in Figure 2.3. This effect is called inhomogeneous broadening. Even at cryogenic temperatures ( $T \leq 2\text{K}$ ) it ranges from 1 THz in polymers down to less than 1 GHz for unstressed sublimated crystals (Brouwer et al., 1996).

The spectrum of a single molecule is instead characterized by the homogeneous linewidth

$$\Delta\nu_{\text{hom}} = \frac{\Gamma_2}{\pi} = \frac{\Gamma_1}{2\pi} + \frac{\Gamma_2^*}{\pi}, \quad (2.1)$$

where  $\Gamma_1$  and  $\Gamma_2^*$  are the decay rate of the excited state population and the dephasing rate of the polarization, respectively.  $\Gamma_2$  defines instead the total decay rate of

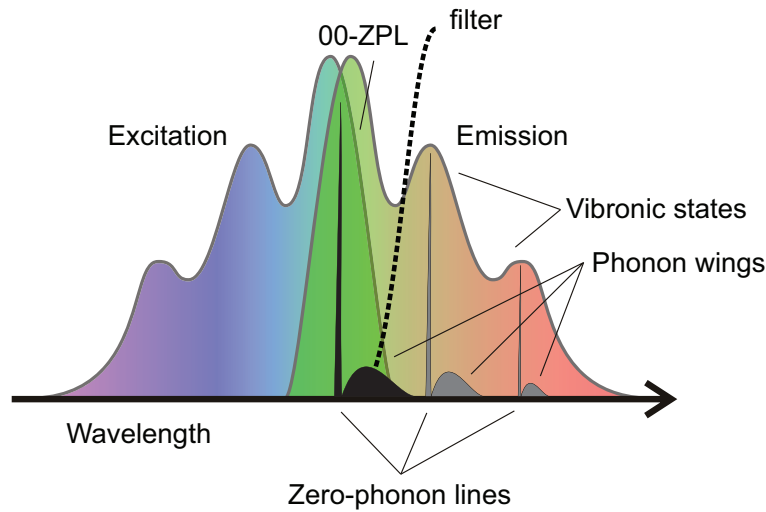


**Figure 2.3:** Typical excitation and emission profiles of dopant molecules in a matrix. At cryogenic temperatures the spectral lines are much narrower. In particular, the direct transitions between electronic levels as well as those that involve a change in the vibrational state are much sharper than the phonon wings. In fluorescence excitation spectroscopy the upper electronic state is populated and the transitions to the vibrational levels of the ground state are probed. Conventional setups use a long-pass filter to block the 00-ZPL emission and its phonon contribution.

the polarization (Allen and Eberly, 1975). In Section 2.3 we will discuss in more detail how light interacts with a TLS and how these quantities affect the coherence properties of the scattered light. The lineshape of the 00-ZPL has a Lorentzian profile with a full-width at half maximum (FWHM) equal to  $\Delta\nu_{\text{hom}}$  (see Figure 2.2b).

Dephasing processes can be largely suppressed by cooling the sample down to cryogenic temperatures and the spectral lines become extremely narrow (Bloess et al., 2001). The lower limit to the linewidth is imposed by the Heisenberg uncertainty principle, which relates the excited state lifetime to the so-called natural or lifetime-limited linewidth  $\Delta\nu$ . For typical dye molecules it is of the order of 10-20 MHz. It is not easy to obtain dopant molecules that exhibit a natural linewidth and the host matrix must be carefully chosen (Boiron et al., 1996; Harms et al., 1999).

### Cross sections

The strength of light-matter interaction is usually expressed in terms of a cross section  $\sigma$ . It has dimensions of a surface so that, to give an intuitive picture, it represents the effective area that a molecule probed by a laser beam exhibits to it. For a TLS under weak resonant excitation one finds (Allen and Eberly, 1975)

$$\sigma = \sigma_0 = \frac{3\lambda^2}{2\pi}. \quad (2.2)$$

For a transition wavelength of 600 nm, the above equation yields an area of about  $1.7 \times 10^{-9} \text{ cm}^2$ , whereas the room temperature cross section of a dye molecule like Rhodamine 6G is only  $4.4 \times 10^{-16} \text{ cm}^2$ . The huge discrepancy can be understood if we take into consideration the various effects that decrease the strength of the 00-ZPL transition. All together they lead to

$$\sigma = \sigma_0 \frac{\Gamma_1}{2\Gamma_2} \alpha_{\text{FC}} \alpha_{\text{DW}} \cos^2 \theta. \quad (2.3)$$

The ratio  $\Gamma_1/2\Gamma_2$  accounts for the presence of dephasing. At room temperatures this factor can be of the order of  $10^{-5}$ , which already makes up most of the size reduction of the cross section. The Franck-Condon and Debye-Waller factors can lead to an additional decrease of more than one order of magnitude, depending on the particular system. The last term is the geometrical factor, which accounts for the orientation of the transition dipole moment with respect to the polarization of the incident electric field. Note that this correction plays an important role in solid samples, where the molecular orientation cannot be changed (Pfab et al., 2004).

According to the Beer-Lambert-Bouguer law the absorption signal is proportional to the ratio  $\sigma/A$ , where  $A$  is the transverse area of the incident laser beam. In order to be able to detect a single molecule, the value of  $\sigma/A$  must be confronted with the various sources of noise.

In the next section we will briefly review the most common experimental approaches for identifying single molecules. Here we bear in mind that under appropriate conditions the cross section can well approximate that of a TLS. Therefore, single molecules in a solid matrix allow us to make proof-of-principle experiments to advance our understanding of light-matter interaction, especially for what concerns coherent phenomena and quantum-optical effects. For instance, a favorable choice for performing this type of studies is the molecule dibenzanthanthrene (DBATT) in a n-hexadecane (Boiron et al., 1996) or in a n-tetradecane (Lettow et al., 2007) Shpol'skii matrix, as well as in a naphthalene crystal (Jelezko et al., 1997). Another system is dibenzoterrylene (DBT) in naphthalene (Jelezko et al., 1996) or in anthracene (Hofmann et al., 2005; Toninelli et al., 2010).

### 2.1.2 Single-molecule detection

At cryogenic temperatures single molecules hosted by an appropriated matrix exhibit very narrow transitions down to linewidths of a few megahertz (Harms et al., 1999). Moreover, the local solid environment induces spectral shifts that lead to distinguishable molecular transitions in the inhomogeneous spectrum of the specific host matrix (Friedrich and Haarer, 1984; Rebane, 1970). Therefore, single molecules can be individually addressed either by optical microscopy of a highly diluted sample or by selective resonant excitation using a narrowband tunable laser. What matters then is the signal-to-noise ratio that is reachable with the selected detection scheme.

### Absorption spectroscopy

The first optical detection of a single molecule was performed on the absorption signal of a para-terphenyl crystal doped with pentacene (Moerner and Kador, 1989). To suppress the laser noise, the resonant frequency of the molecular transition was modulated using the Stark effect and the signal-to-noise ratio was improved using a lock-in amplifier (Kador et al., 1990). Unfortunately, lock-in techniques tend to lose information on the absolute phase of the signal (Wineland et al., 1987) and they are thus not ideal for single-molecule coherent spectroscopy. These types of measurements have not been pursued much farther (Kador et al., 1999) until recently (Chong et al., 2010).

An attempt to perform a phase-sensitive detection of a single-molecule relied on a Sagnac interferometer, where about 20 molecules could be sensed at room temperature (Hwang et al., 2006). Another technique might exploit the interference between the scattered field and the light reflected by a dielectric interface located near the sample (Lindfors et al., 2004). Using ultrasmooth surfaces it was possible to detect the scattering signal of a single colloidal quantum dot (Kukura et al., 2009). Furthermore, these findings have enabled the first absorption measurement of a single molecule at room temperature (Celebrano et al., 2011; Kukura et al., 2010).

In the next chapter we will show that the signal-to-noise ratio of an absorption experiment can be significantly improved using tightly focused light. In particular, we find that at low temperatures the interaction strength becomes so large that a single molecule extinguishes a large fraction of the incident light (Wrigge et al., 2008a; Zumofen et al., 2008) and induces phase shifts of a few degrees (Pototschnig et al., 2011; Zumofen et al., 2009).

### Fluorescence excitation spectroscopy

An alternative strategy to detect single molecules relies on the collection of the red-shifted fluorescence. Here the laser noise is avoided by means of a low-pass filter, which blocks the excitation source in the detection path (see Figure 2.3). The technique is so simple that already in 1976 Hirschfeld demonstrated a sensitivity of less than 100 fluorophores at room temperature (Hirschfeld, 1976). At low temperatures single molecules could be detected by scanning a narrowband laser across a molecular resonance and collecting fluorescence (Orrit and Bernard, 1990). For photostable dye molecules with a high quantum yield the signal-to-noise ratio is only limited by the detector noise. That is why fluorescence excitation spectroscopy rapidly became the standard technique for single molecule detection at cryogenic and room temperatures (Moerner, 2002).

However, not all molecule are efficient light emitters nor are photostable, even at moderate excitation levels. Moreover, since the fluorescence signal is incoherent, any phase information is completely lost. An extinction experiment would not



present these issues and the detection sensitivity could be larger than via fluorescence under certain conditions (Wrigge, 2008; Wrigge et al., 2008b). Because the signal relies on scattering and absorption by a weakly excited molecule, it is useful to formulate the problem starting from scattering theory.

## 2.2 Scattering theory

Having described the optical properties of a single molecule, we now focus on the description of light-matter interaction from the point of view of the electromagnetic field. Here we introduce the fundamental concepts and the basic quantities that we need in the subsequent chapters to investigate the optical response of an emitter probed by strongly confined optical fields.

### 2.2.1 General formulation

For a material body of specified size, shape and composition illuminated by an electromagnetic wave, the goal of scattering theory is to determine the electric and magnetic fields inside and outside the object at any given location. Here we limit ourselves to the situation where the scatterer is embedded in a homogeneous linear non-absorbing medium. Furthermore, we make our considerations for a plane monochromatic wave, keeping in mind that an arbitrary incident field can be expressed as a linear superposition of plane wave components.

It is convenient to treat the problem by introducing the following quantities.  $\mathbf{E}_{\text{inc}}$  is the incident field,  $\mathbf{E}_{\text{sca}}$  the scattered field and  $\mathbf{E}_{\text{int}}$  the field inside the object. Each of them has a corresponding magnetic field  $\mathbf{H}$ . Moreover, the incident field is a linearly polarized plane monochromatic wave propagating along the  $z$ -axis,  $\mathbf{E}_{\text{inc}} = E_0 \exp(ikz - i\omega t)\hat{\mathbf{x}}$ , where we choose the  $x$ -axis as polarization direction. Next we need to impose the boundary conditions at the interface between the object and the surrounding medium. Because there are neither charges nor free currents at the boundary, it is sufficient that the tangential components of the electromagnetic field are continuous across the interface

$$(\mathbf{E}_{\text{inc}} + \mathbf{E}_{\text{sca}}) \times \mathbf{s} = \mathbf{E}_{\text{int}} \times \mathbf{s}, \quad (2.4)$$

where  $\mathbf{s}$  is the unit vector normal to the object surface.

### The amplitude scattering matrix

The scattered field generated when the incident wave impinges on the object propagates in a direction different than  $\mathbf{E}_{\text{inc}}$ . In the direction of observation of  $\mathbf{E}_{\text{sca}}$ , it is convenient to decompose  $\mathbf{E}_{\text{inc}}$  into components parallel and perpendicular to the scattering plane. The latter is uniquely defined by the unit vectors  $\mathbf{n}$ , for the

observation direction, and  $\hat{\mathbf{z}}$ , for the propagation direction.

$$\mathbf{E}_{\text{inc}} = E_{\text{inc},\parallel} \mathbf{e}_{\parallel} + E_{\text{inc},\perp} \mathbf{e}_{\perp}. \quad (2.5)$$

For distances from the object much larger than the wavelength of light, the scattered field is transverse and takes the form of a spherical outgoing wave (Jackson, 1999)

$$\mathbf{E}_{\text{sca}} = -\frac{e^{ikr}}{ikr} \mathbf{A}, \quad (2.6)$$

where  $\mathbf{A} \cdot \mathbf{n} = 0$ . Therefore,  $\mathbf{E}_{\text{sca}}$  can be expressed as the sum of a component parallel and perpendicular to the scattering plane

$$\mathbf{E}_{\text{sca}} = E_{\text{sca},\parallel} \mathbf{e}'_{\parallel} + E_{\text{sca},\perp} \mathbf{e}'_{\perp}. \quad (2.7)$$

Note that  $\mathbf{e}'_{\parallel}$  are basis vectors different from  $\mathbf{e}_{\parallel}$ , because they are respectively orthogonal to  $\mathbf{n}$  and  $\mathbf{z}$ , the latter being the propagation direction of the incident wave.

The linearity in the boundary conditions of Eq. (2.4) and the previous field decompositions establish a relationship between  $\mathbf{E}_{\text{sca}}$  and  $\mathbf{E}_{\text{inc}}$  in matrix form

$$\begin{pmatrix} E_{\text{sca},\parallel} \\ E_{\text{sca},\perp} \end{pmatrix} = -\frac{e^{ik(r-z)}}{ikr} \begin{pmatrix} S_2 & S_3 \\ S_1 & S_4 \end{pmatrix} \begin{pmatrix} E_{\text{inc},\parallel} \\ E_{\text{inc},\perp} \end{pmatrix}, \quad (2.8)$$

where  $\mathbf{S} = (S_2; S_3; S_1; S_4)$  is the amplitude scattering matrix, whose elements depend on the scattering and azimuthal angles,  $\theta$  and  $\varphi$ , respectively. These are associated with the observation direction and the scattering plane in the spherical coordinates  $(r, \theta, \varphi)$  (Bohren and Huffman, 1983).

### Extinction, scattering and absorption

Equation (2.8) represents the most general expression for relating the scattered to the incident field. In the following we assume that we have been able to obtain  $\mathbf{E}_{\text{sca}}$  and move our attention on the energy flow. To do so we consider the time-averaged Poynting vector  $\mathbf{S}$  in the medium surrounding the scattering object, which can be written as the sum of three terms

$$\mathbf{S} = \mathbf{S}_{\text{inc}} + \mathbf{S}_{\text{sca}} + \mathbf{S}_{\text{int}}, \quad (2.9)$$

$$\mathbf{S}_{\text{inc}} = \frac{1}{2} \text{Re}\{\mathbf{E}_{\text{inc}} \times \mathbf{H}_{\text{inc}}^*\}, \quad (2.10)$$

$$\mathbf{S}_{\text{sca}} = \frac{1}{2} \text{Re}\{\mathbf{E}_{\text{sca}} \times \mathbf{H}_{\text{sca}}^*\}, \quad (2.11)$$

$$\mathbf{S}_{\text{int}} = \frac{1}{2} \text{Re}\{\mathbf{E}_{\text{inc}} \times \mathbf{H}_{\text{sca}}^* + \mathbf{E}_{\text{sca}} \times \mathbf{H}_{\text{inc}}^*\}. \quad (2.12)$$

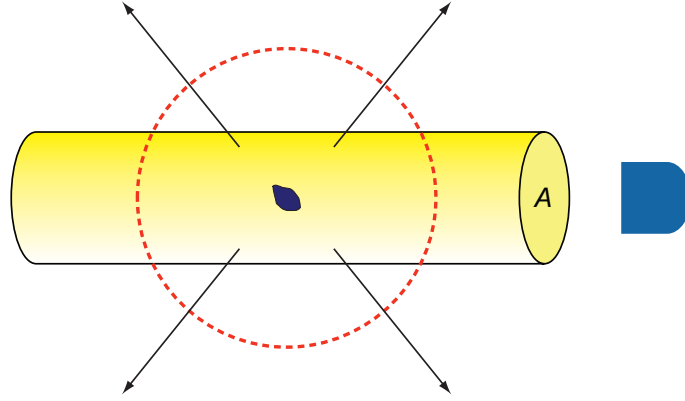


**Figure 2.4:** A material object scatters and absorbs light. The beam has a cross sectional area  $A$  much larger than the region where light propagation is perturbed. The total amount of energy removed by the object can be measured by placing a detector that collects the transmitted power enclosed into an infinitesimal solid angle about the beam axis. The dashed circle indicates the integration path of the Poynting vector.

While  $\mathbf{S}_{\text{inc}}$  and  $\mathbf{S}_{\text{sca}}$  are related to the incident and scattered powers, the term  $\mathbf{S}_{\text{int}}$  results from the interference between the incident and scattered fields.

Figure 2.4 illustrates a typical transmission experiment. A fraction of the incident power  $P_{\text{inc}}$  is either absorbed or scattered by a material object and in both cases it is removed from the beam. This amount of power is called extinction and it can be measured by placing a detector downstream the object along the beam axis. We assume that the beam intensity is constant over a cross section  $A$  much larger than the area where light propagation is perturbed (Bohren, 1983; Paul and Fischer, 1983). According to Poynting theorem (Jackson, 1999), the net power that crosses the surface  $\Sigma$  of a virtual sphere with radius  $r \gg \lambda$  enclosing the object reads

$$P_{\text{abs}} = - \int_{4\pi} \mathbf{S} \cdot \mathbf{n} r^2 d\Omega, \quad (2.13)$$

where  $\mathbf{n}$  is a unit vector normal to  $\Sigma$ .  $P_{\text{abs}}$  represents the power absorbed only by the object, because the surrounding medium is lossless. According to Eq. (2.9)  $P_{\text{abs}}$  can be decomposed into three contributions, namely

$$P_{\text{i}} = - \int_{\Sigma} \mathbf{S}_{\text{inc}} \cdot \mathbf{n} r^2 d\Omega, \quad P_{\text{sca}} = \int_{\Sigma} \mathbf{S}_{\text{sca}} \cdot \mathbf{n} r^2 d\Omega, \quad P_{\text{int}} = - \int_{\Sigma} \mathbf{S}_{\text{int}} \cdot \mathbf{n} r^2 d\Omega. \quad (2.14)$$

$P_{\text{sca}}$  represents the total scattered power and  $P_{\text{i}}$  is always identical to zero for a non-absorbing medium. Hence Eqs. (2.13) and (2.14) lead to

$$P_{\text{int}} = P_{\text{sca}} + P_{\text{abs}}. \quad (2.15)$$

In other words,  $\mathbf{S}_{\text{int}}$  can be used to compute the total amount of power removed from the beam. For this reason it is more often referred to as extinction (Bohren and Huffman, 1983).

### Cross sections

For the case of an incident plane wave, which carries an infinite amount of incident power, it is advantageous introducing the concept of a cross section. It has dimensions of a surface so that, to give an intuitive picture, it represents the effective area that an object placed in an incident beam exhibits to it, as sketched in Figure 2.5. If  $I_{\text{inc}}$  is the intensity of the incident plane wave, we define the scattering, absorption and extinction cross sections as

$$C_{\text{sca}} = \frac{P_{\text{sca}}}{I_{\text{inc}}}, \quad C_{\text{abs}} = \frac{P_{\text{abs}}}{I_{\text{inc}}}, \quad C_{\text{ext}} = \frac{P_{\text{int}}}{I_{\text{inc}}}. \quad (2.16)$$

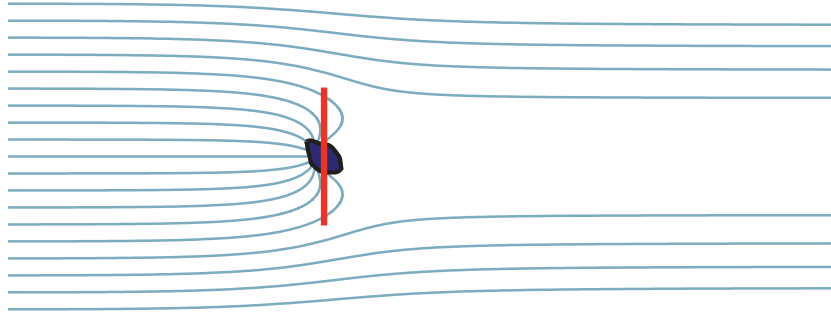


**Figure 2.5:** *An object immersed in a plane wave scatters and absorbs light. This effect is correlated with a perturbation of the energy flow, as nicely described by Paul and Fischer (1983) for a dipole and Bohren (1983) for a nanoparticle. The red line draws the approximate extension of the interaction cross section, which can be larger than the size of the object.*

The amplitude scattering matrix given in Eq. (2.8) contains all the necessary information to yield an expression for these cross sections. For an incident  $x$ -polarized plane wave propagating along the  $z$  axis the scattering problem can be reduced to the calculation of the vector scattering amplitude  $\mathbf{X}$ . This is related to the elements of the scattering matrix as (Bohren and Huffman, 1983)

$$\mathbf{X} = (S_2 \cos \varphi + S_3 \sin \varphi) \mathbf{e}'_{\parallel} + (S_4 \cos \varphi + S_1 \sin \varphi) \mathbf{e}'_{\perp}. \quad (2.17)$$

After some complicated algebraic manipulation we obtain the following expressions

$$C_{\text{ext}} = \frac{4\pi}{k^2} \text{Re}\{(\mathbf{X} \cdot \hat{\mathbf{x}})_{\theta=0}\}, \quad (2.18)$$

$$C_{\text{sca}} = \int_{4\pi} \frac{|\mathbf{X}|^2}{k^2} d\Omega, \quad (2.19)$$

and  $C_{\text{abs}} = C_{\text{ext}} - C_{\text{sca}}$ .  $|\mathbf{X}|^2/k^2$  is often called the differential scattering cross section and it specifies the angular distribution of the scattered light. Note that these

cross sections are purely electromagnetic quantities and as such do not represent the geometrical shadow that an object would produce in the geometrical optics limit (Bohren, 1983; Paul and Fischer, 1983). Indeed, Figure 2.5 indicates that the interaction can lead to cross sections that are larger than the geometrical cross sectional area that an object exhibits to an incident beam. Lastly, we remark that these results assume that the incident beam can be well approximated by a plane wave. This prescription requires some explanation.

### The optical theorem

Equation (2.18) is one particular formulation of the optical theorem, which states that the total amount of power removed from the beam, the so-called extinction, depends only on the vector scattering amplitude  $\mathbf{X}$  in the forward direction  $\theta = 0$ . This theorem is not restricted to electromagnetic waves, but it is valid for all wave scattering phenomena (Feenberg, 1932; Newton, 1976; van de Hulst, 1949b). The fact that the information about the power scattered in all directions and that absorbed in the object is fully contained in a far-field quantity along one specific direction might look puzzling. To show that this is not a surprising result we must consider in more detail what is meant for extinction and how it is measured. We do so by referring to the interpretation of the optical theorem given by van de Hulst (1949a).

Consider the situation depicted in Figure 2.4. The power  $P_{\text{coll}}$  collected by a detector of area  $A_{\text{D}}$  placed after the object in the direction of the incident beam can be written as

$$P_{\text{coll}} = \int_{A_{\text{D}}} \mathbf{S} \cdot \hat{\mathbf{z}} r^2 d\Omega \simeq I_{\text{inc}} \left( A_{\text{D}} + \frac{|\mathbf{X}|^2}{k^2} \Omega_{\text{D}} - C_{\text{ext}} \right), \quad (2.20)$$

where the second equality holds for large  $kz$ , such that the solid angle  $\Omega_{\text{D}} \simeq A_{\text{D}}/z^2$  subtended by the detector is sufficiently small. In such case we can express the received power as

$$P_{\text{coll}} = I_{\text{inc}}(A_{\text{D}} - C_{\text{ext}}). \quad (2.21)$$

Since  $I_{\text{inc}}A_{\text{D}}$  can be obtained by removing the object from the light path,  $C_{\text{ext}}$  is a well defined measurable quantity. If the detector area is increased or if it is moved closer to the object, the scattering term must be taken into account. The same occurs for large targets, where the scattered power tends to be concentrated in the forward direction (Bohren and Huffman, 1983). From Eq. (2.21) we infer that  $C_{\text{ext}}$  is the maximum observable extinction. To arrive at this result we actually made use of the optical theorem in the formulation of Eq. (2.18).

$C_{\text{ext}}$  results at the same time from the integration of  $\mathbf{S}_{\text{int}}$  over a closed surface  $\Sigma$  around the object and from the vector scattering amplitude along the beam propagation direction. The latter explains why  $C_{\text{ext}}$  can be measured by a transmission experiment, but the link between the first and the second expressions remains

undisclosed. The origin of the optical theorem must be sought in the expression of  $\mathbf{S}_{\text{int}}$ . This represents a power flow associated with the interference between the incident and scattered waves. In this particular case  $\mathbf{E}_{\text{inc}}$  is a plane wave propagating along  $\hat{\mathbf{z}}$ . If we now make a plane-wave decomposition of  $\mathbf{E}_{\text{sca}}$ , we find that only the amplitude parallel to  $\mathbf{E}_{\text{inc}}$  contributes to a net power flow. That is why the integration of  $\mathbf{S}_{\text{int}}$  is a projection of the vector scattering amplitude on the propagation direction of  $\mathbf{E}_{\text{inc}}$ , i.e.  $\theta = 0$ .

## 2.2.2 Scattering and absorption by a dipolar radiator

For the scattering and absorption of electromagnetic waves by objects whose dimensions are small compared to the wavelength, it is convenient to think of the incident field as inducing electric and magnetic multipoles that oscillate with a well defined phase with respect to the driving wave and that radiate energy into directions other than the incident one. For nanoscale particles and for single molecules the interaction can be very well described in terms of a single oscillating dipole  $\mathbf{p}$ , which is related to  $\mathbf{E}_{\text{inc}}$  by the polarizability tensor  $\boldsymbol{\alpha}$  through  $\mathbf{p} = \epsilon_0 \boldsymbol{\alpha} \mathbf{E}_{\text{inc}}$ . For our purposes we can greatly simplify the formalism by assuming that the dipole is induced by a scalar polarizability  $\alpha$ .

The induced dipole moment  $\mathbf{p} = \epsilon_0 \alpha E_0 \exp(-i\omega t) \hat{\mathbf{x}}$  is located at  $z = 0$  and oscillates with the frequency of the applied field. Therefore, it radiates an electric field  $\mathbf{E}_{\text{sca}}$  that in the far region ( $kr \gg 1$ ) reads (Jackson, 1999)

$$\mathbf{E}_{\text{sca}} = \frac{k^2}{4\pi\epsilon_0} \frac{e^{ikr}}{r} (\mathbf{n} \times \mathbf{p}) \times \mathbf{n}, \quad (2.22)$$

where  $\mathbf{n}$  is a unit vector in the direction of observation,  $r$  is the distance from the dipole and the time-dependent factor  $\exp(-i\omega t)$  has been omitted. From Eq. (2.22) we can extract the expression for the vector scattering amplitude

$$\mathbf{X} = \frac{ik^3}{4\pi} \alpha \mathbf{n} \times (\mathbf{n} \times \hat{\mathbf{x}}). \quad (2.23)$$

We then use Eqs. (2.18) and (2.19) to arrive at a simple expression for the extinction and scattering cross sections

$$C_{\text{ext}} = k \text{Im}\{\alpha\}, \quad C_{\text{sca}} = \frac{k^4}{6\pi} |\alpha|^2. \quad (2.24)$$

Note that these formulae do not contain any information on the incident field and are thus valid for any type of illumination in free space.

### Classical oscillator

Let us consider a point-like oscillating dipole as a classical model for light-matter interaction and review the Abraham-Lorentz equation in Gaussian (cgs) units (Jack-

son, 1999)

$$\ddot{\mathbf{q}} + \Gamma' \dot{\mathbf{q}} - \tau \ddot{\mathbf{q}} + \omega_0^2 \mathbf{q} = \frac{e}{m} E_0 \hat{\mathbf{x}} e^{-i\omega t}, \quad (2.25)$$

where  $\mathbf{q}$  is the vectorial displacement of a charge  $e$  with mass  $m$ ,  $\omega_0$  is the oscillator resonant frequency and  $\Gamma'$  represents damping by non-radiative channels.  $E_0$  is the electric field amplitude at the place of the oscillator and  $\hat{\mathbf{x}}$  is the unit vector along the direction of the driving field  $\mathbf{E}_{\text{inc}}$ .  $\tau$  is the characteristic time of damping by radiation reaction, whose rate  $\Gamma$  reads (Jackson, 1999)

$$\Gamma = \tau \omega_0^2 = \frac{2e^2 \omega_0^2}{3mc^3}. \quad (2.26)$$

The stationary state solution of  $\mathbf{q}$  is given by

$$\mathbf{q} = \frac{e}{m} \frac{E_0 e^{-i\omega t}}{\omega_0^2 - \omega^2 - i\omega\Gamma_t} \hat{\mathbf{x}}, \quad (2.27)$$

where  $\Gamma_t = \Gamma' + (\omega/\omega_0)^2 \Gamma$  is the total decay constant. For laser frequency detuning  $\Delta = \omega - \omega_0$  such that  $|\Delta| \ll \omega_0$  the previous equation can be approximated by

$$\mathbf{q} \simeq -\frac{e}{m\omega_0} \frac{E_0 e^{-i\omega t}}{2\Delta + i\Gamma_t} \hat{\mathbf{x}}. \quad (2.28)$$

Since  $\mathbf{p} = e\mathbf{q}$ , the polarizability of a classical oscillating dipole reads

$$\alpha_{\text{CL}} = -\frac{e^2}{m\omega_0} \frac{1}{2\Delta + i\Gamma_t} = -\frac{3}{2} \frac{1}{k^3} \frac{\Gamma}{2\Delta + i\Gamma_t} \stackrel{\text{cgs} \rightarrow \text{SI}}{=} -\frac{6\pi}{k^3} \frac{\Gamma}{2\Delta + i\Gamma_t}, \quad (2.29)$$

where  $\text{cgs} \rightarrow \text{SI}$  stands for the conversion to SI units.

### The scattering cross section

From the preceding expression it follows that extinction and scattering cross sections read

$$C_{\text{ext}} = \sigma_0 \frac{\Gamma\Gamma_t}{4\Delta^2 + \Gamma_t^2}, \quad C_{\text{sca}} = \sigma_0 \frac{\Gamma^2}{4\Delta^2 + \Gamma_t^2}, \quad (2.30)$$

where  $\sigma_0 = 3\lambda^2/2\pi$  is the resonant cross section of an ideal radiator (Jackson, 1999). These equations can be conveniently used to compute the extinguished and scattered powers for any incident electric field given at the dipole position.

## 2.3 Coherent spectroscopy

In coherent spectroscopy the response of the system depends not only on the electromagnetic field amplitude, but also on its phase. This statement embraces a number of experimental methods and techniques that find application in a broad research context, ranging from quantum information science to femtochemistry (Kiraz et al., 2004; Zewail, 2001). When dealing with coherent light-matter interaction

and optical transitions it is clear that we cannot describe this process through transition rates, because these have no information on the phase of the field. We thus need to adopt an appropriate formalism that treats the interaction at the Hamiltonian level and not in the framework of perturbation theory. Solving this problem for the complex level structure of a single molecule is a formidable task. Even in the situation of a simplified level diagram the analytical solution of the dynamical equations gets quickly very complicated (Rabitz et al., 2000). Since we are interested in how basic interaction processes are influenced by a complex electromagnetic environment, we limit ourselves to the case of a TLS.

### 2.3.1 Two-level system driven by a laser

We consider a quantum emitter, atom or molecule, as a TLS with a ground  $|1\rangle$  and excited  $|2\rangle$  states, with energies  $E_1$  and  $E_2$ , respectively. We focus on electric dipole transitions and model light-matter interaction in the semi-classical picture. The Hamiltonian that determines the time evolution of the TLS under laser excitation can be written as

$$\hat{H} = \hat{H}_{\text{TLS}} - \hat{\mathbf{d}} \cdot \mathbf{E}(O, t). \quad (2.31)$$

$\hat{H}_{\text{TLS}}$  is the unperturbed Hamiltonian of a TLS and the second term in Eq. (2.31) represents the interaction with the electromagnetic field  $\mathbf{E}(O, t) = E_o \cos(\omega t) \hat{\mathbf{x}}$ , where  $O$  stands for the location of the TLS. Since we only have transitions between  $|1\rangle$  and  $|2\rangle$ , we can work in the two dimensional Hilbert space spanned by these eigenstates. The matrix elements of the operators are thus

$$\hat{H}_{\text{TLS}} = \begin{pmatrix} E_2 & 0 \\ 0 & E_1 \end{pmatrix} = \frac{\hbar\omega_0}{2} \sigma_z, \quad (2.32)$$

where  $\hbar\omega_0 = E_2 - E_1$ ,  $\sigma_z$  is a Pauli matrix (Loudon, 2000) and the constant term  $(E_2 + E_1)/2$  has been omitted because it does not affect the dynamics nor the frequency of the absorbed and emitted light.

$$\hat{\mathbf{d}} \cdot \mathbf{E}(O, t) = \begin{pmatrix} 0 & d_{12}E_o e^{-i\omega t} \\ d_{12}E_o e^{-i\omega t} & 0 \end{pmatrix} = -\hbar\mathcal{V} e^{-i\omega t} \sigma_x, \quad (2.33)$$

where  $d_{12} = \langle 1 | \mathbf{d} \cdot \hat{\mathbf{x}} | 2 \rangle$  is the transition dipole moment, assumed to be real,  $\mathcal{V} = -d_{12}E_o/\hbar$  is the so-called Rabi frequency and  $\sigma_x$  is another Pauli matrix (Loudon, 2000).

The time evolution of the TLS is determined either using the Schrödinger or Heisenberg equations. The expression of  $\hat{H}$  in terms of Pauli matrices makes the second approach more practical. We thus consider the Heisenberg equations of motion in the rotating wave approximation (RWA) (Allen and Eberly, 1975; Cohen-Tannoudji et al., 2004; Loudon, 2000)

$$\begin{aligned} \dot{\tilde{\sigma}}_- &= (i\Delta - \Gamma_2) \tilde{\sigma}_- + \frac{1}{2} i\mathcal{V} \sigma_z, \\ \dot{\tilde{\sigma}}_z &= -\Gamma_1 \sigma_z + i\mathcal{V} (\tilde{\sigma}_- - \tilde{\sigma}_+), \end{aligned} \quad (2.34)$$



where  $\tilde{\sigma}_-, \tilde{\sigma}_+$  and  $\sigma_z$  are operators of a pseudo  $\frac{1}{2}$ -spin. The tilde and the dot indicate the RWA and the derivative with respect to time, respectively. In the Heisenberg equations we have introduced two phenomenological decay constants.  $\Gamma_1$  is the radiative decay rate of the excited state given by the Einstein coefficient,  $\Gamma_1 = d_{12}^2 \omega_0^3 / (3\pi\epsilon_0 \hbar c^3)$ .  $\Gamma_2$  is the damping rate of the polarization,  $\Gamma_2 = \Gamma_1/2 + \Gamma_2^*$  (see Section 2.1.1). In the semi-classical approximation Eqs. (2.34) do not contain the dynamics of the electromagnetic field operators and the expectation values of terms like  $\mathcal{V}\sigma_z$  ignore quantum correlations between the TLS and the electromagnetic field, i.e.  $\langle \mathcal{V}\sigma_z \rangle = \mathcal{V}\langle \sigma_z \rangle$  (Allen and Eberly, 1975). The expectation values at stationary state conditions read

$$\langle \tilde{\sigma}_- \rangle^{\text{ss}} = \frac{\mathcal{V}(\Delta - i\Gamma_2)}{2(\Delta^2 + \Gamma_2^2 + \mathcal{V}^2\Gamma_2/\Gamma_1)}, \quad (2.35)$$

$$\rho_{22}^{\text{ss}} = \frac{1}{2}(1 + \langle \sigma_z \rangle^{\text{ss}}) = \frac{\Gamma_2 \mathcal{V}^2}{2\Gamma_1(\Delta^2 + \Gamma_2^2 + \mathcal{V}^2\Gamma_2/\Gamma_1)}. \quad (2.36)$$

$\rho_{22}^{\text{ss}}$  gives the stationary state population of the upper state  $|2\rangle$ . Equation (2.35) is instead related to the steady state value of the dipole moment induced in the TLS by the driving laser. The polarizability of a TLS  $\alpha_{\text{TLS}}$  can be expressed using  $\langle \tilde{\sigma}_- \rangle^{\text{ss}}$  (Cohen-Tannoudji et al., 2004; Loudon, 2000)

$$\alpha_{\text{TLS}} = -\frac{d_{12}\langle \tilde{\sigma}_- \rangle^{\text{ss}}}{\frac{1}{2}\epsilon_0 E_0}, \quad (2.37)$$

where the factor 1/2 in the denominator comes from the RWA. From Eq. (2.35) we obtain

$$\alpha_{\text{TLS}} = -\frac{d_{12}^2}{\epsilon_0 \hbar} \frac{\Delta - i\Gamma_2}{\Delta^2 + \Gamma_2^2 + \mathcal{V}^2\Gamma_2/\Gamma_1} = -\frac{3\pi}{k^3} \frac{\Gamma_1(\Delta - i\Gamma_2)}{\Delta^2 + \Gamma_2^2 + \mathcal{V}^2\Gamma_2/\Gamma_1}. \quad (2.38)$$

Note that the polarizability  $\alpha_{\text{TLS}}$  depends on the intensity of the driving laser through  $\mathcal{V}^2$ . In other words the coupling strength between a TLS and an external electromagnetic field is parametric and it differs from that of a classical oscillating dipole. Furthermore, this particular expression for  $\alpha_{\text{TLS}}$  does not fulfill the optical theorem (Berman et al., 2006; Loudon and Barnett, 2006). Hence the general expressions for the cross sections derived in Section 2.2.2 must be used with care. We thus take one step backward and discuss light scattering by a TLS starting from Eqs. (2.35) and (2.36).

### 2.3.2 Coherent and incoherent scattering

The light scattered by a TLS, even in the semi-classical picture, can be divided into two parts. One is coherent with respect to the driving field, and the other one is incoherent (Cohen-Tannoudji et al., 2004). Only the coherent part interferes with the incident field and falls into the framework of classical scattering theory.

From Eq. (2.36) the total scattered power  $P_{\text{sca}}$  emitted by a TLS can be determined

$$P_{\text{sca}} = \hbar\omega\Gamma_1\rho_{22}^{\text{ss}} = \frac{\sigma_0}{2} \frac{\Gamma_1\Gamma_2}{(\Delta^2 + \Gamma_2^2 + \gamma^2\Gamma_2/\Gamma_1)} I_{\text{inc}}, \quad (2.39)$$

where  $\sigma_0$  is the cross section of an ideal classical oscillating dipole (Jackson, 1999) and  $I_{\text{inc}}$  denotes the intensity of the incident field.  $\hbar\omega$  in the first equality gives the average energy of the emitted photons and correspondingly the second equality holds for  $|\omega - \omega_0| \ll \omega_0$ . It is interesting to point out that  $P_{\text{sca}}$  is also given by  $k\text{Im}\{\alpha_{\text{TLS}}\}I_{\text{inc}}$ , which is the formula for the sum of the coherently scattered and absorbed powers of a classical oscillator. We thus state that the incoherently scattered light corresponds to a loss channel in classical scattering theory.

For the coherently scattered far field (see Eq. (2.22)), assuming that the dipole moment and  $\mathbf{E}_{\text{inc}}$  are both parallel to the  $x$ -axis, we write

$$\begin{aligned} \mathbf{E}_{\text{sca}}^{\text{coh}} &= \alpha_{\text{TLS}}E_{\text{inc}}(O) \frac{k^2}{4\pi} \frac{e^{ikr}}{r} (\mathbf{n} \times \hat{\mathbf{x}}) \times \mathbf{n} \\ &= -\frac{3\Gamma_1(\Delta - i\Gamma_2)E_{\text{inc}}(O)}{4(\Delta^2 + \Gamma_2^2 + \gamma^2\Gamma_2/\Gamma_1)} \frac{e^{ikr}}{kr} (\mathbf{n} \times \hat{\mathbf{x}}) \times \mathbf{n}, \end{aligned} \quad (2.40)$$

where  $\mathbf{n}$  is a unit vector in the direction of the observation point,  $O$  is the position of the TLS and the time-dependent factor  $\exp(-i\omega t)$  has been omitted. Because Eq. (2.40) has the same expression of the field scattered by a classical oscillating dipole, we can use Eq. (2.24) to write the coherent scattered power  $P_{\text{sca}}^{\text{coh}}$  as

$$P_{\text{sca}}^{\text{coh}} = \frac{\sigma_0}{4} \frac{\Gamma_1^2(\Delta^2 + \Gamma_2^2)}{(\Delta^2 + \Gamma_2^2 + \gamma^2\Gamma_2/\Gamma_1)^2} I_{\text{inc}}. \quad (2.41)$$

### Dependence on the saturation parameter

By defining the saturation parameter  $s = \gamma^2\Gamma_2/[(\Delta^2 + \Gamma_2^2)\Gamma_1]$ , the scattered, coherent and incoherent powers read

$$P_{\text{sca}} = \frac{\hbar\Gamma_1}{2} \frac{s}{s+1}, \quad (2.42)$$

$$P_{\text{sca}}^{\text{coh}} = \frac{\hbar\Gamma_1}{2} \frac{\Gamma_1}{2\Gamma_2} \frac{s}{(s+1)^2}, \quad (2.43)$$

$$P_{\text{sca}}^{\text{incoh}} = \frac{\hbar\Gamma_1}{2} \frac{s}{(s+1)^2} \left( s+1 - \frac{\Gamma_1}{2\Gamma_2} \right). \quad (2.44)$$

Figure 2.6 illustrates their behavior as a function of the saturation parameter  $s$  and for  $\Gamma_2 = \Gamma_1/2$ . The ratio  $P_{\text{sca}}^{\text{coh}}/P_{\text{sca}}^{\text{incoh}}$  is also plotted. For small values of  $s$  the incoherently emitted power is negligible and the TLS can be considered an ideal classical oscillating dipole. When  $\Gamma_2 \gg \Gamma_1$  the incoherent part can be large

even under weak excitation. For instance, this is the typical situation of a dye molecule at room temperature. The ultrafast dephasing processes make this type of spectroscopy very challenging both in terms of signal-to-noise ratio (Celebrano et al., 2011; Kukura et al., 2010) and coherent dynamics (Hildner et al., 2011).

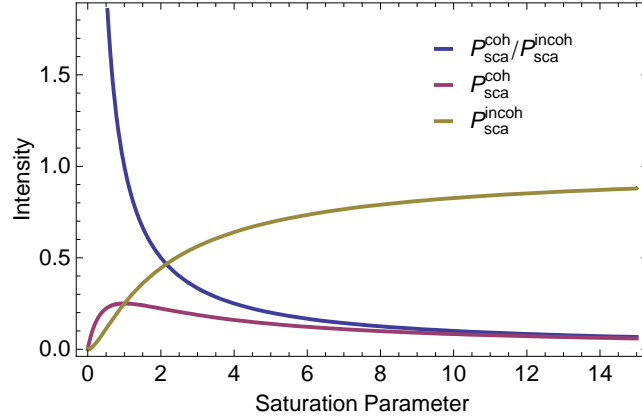


**Figure 2.6:** Coherent and incoherent photons emitted by a TLS as a function of the saturation parameter  $s$  for  $\Gamma_2 = \Gamma_1/2$ .

### Weak excitation and radiative broadening

In the following we limit our analysis to weak excitation, i.e.  $s \ll 1$ , and neglect  $\mathcal{V}$  in the previous equations. In this case the polarizability  $\alpha_{\text{TLS}}$  fulfills the optical theorem and Eqs. (2.24) give the cross sections for the extinguished and the scattered powers. Furthermore, we assume that the TLS does not suffer from dephasing processes other than the radiative decay. The important quantities that we use in the next sections read

$$\sigma = \sigma_0 \frac{\Gamma_1^2}{4\Delta^2 + \Gamma_1^2} \quad (2.45)$$

$$\mathbf{E}_{\text{sca}}^{\text{coh}} = -\frac{3}{2} \frac{\Gamma_1}{(2\Delta + i\Gamma_1)} E_{\text{inc}}(O) \frac{e^{ikr}}{kr} (\mathbf{n} \times \hat{\mathbf{x}}) \times \mathbf{n}, \quad (2.46)$$

### Visibility and lineshapes

When a plane wave weakly excites a TLS, the power collected in the forward direction is always attenuated. Since for a TLS  $C_{\text{ext}} = C_{\text{sca}}$ , according to Eq. (2.20), the extinction dip amounts to  $\sigma/A_D$  for very small collection angles. For a collimated laser beam, the detector area can be replaced with the beam area  $A$  and the transmission takes the form

$$T = 1 - \frac{\sigma}{A}. \quad (2.47)$$

---

This is the commonly-used expression of the Beer-Lambert-Bouguer law for a single emitter (Karrai and Warburton, 2003). Equation (2.47) can be further analyzed by writing  $\sigma/A = VL(\Delta)$ , where  $V$  is the visibility and  $L(\Delta)$  is the lineshape, which depends on detuning. From Eq. (2.45) we find that the visibility of a TLS is equal to  $\sigma_0/A$  and the lineshape is a Lorentzian (Loudon, 2000).



## Chapter 3

# Coherent spectroscopy in strongly confined fields

In the previous chapter we have established a connection between the coherent detection of a single emitter and the ratio  $\sigma/A$ . At the very beginning of single-molecule spectroscopy, efforts for reducing  $A$  by focused illumination and near-field probes mainly concerned the improvement of the signal-to-noise ratio and the achievement of a better spatial resolution. For example, one major goal was to address individual molecules in a dense sample by focusing light below the diffraction limit (Betzig and Trautman, 1992). The first images of single fluorescent molecules at room temperatures were indeed delivered using a SNOM (Betzig and Chichester, 1993). Since then several groups have combined SNOM with spectroscopy of single emitters by detecting the inelastic fluorescence that is red shifted by the excitation light at room and at cryogenic temperatures (Guest et al., 2002; Hess et al., 1994; Matsuda et al., 2003; Moerner et al., 1994; Trautman et al., 1994)

At low temperatures dephasing processes are largely suppressed and the cross section of a single emitter approaches the value given in Eq. (2.45). Based on Eq. (2.47) we therefore expect that a laser beam focused down to the diffraction limit would produce a large dip in the transmittance. However, it turns out that it is not easy to explore this idea experimentally, because systems in the gas phase are not easily compatible with strongly confined laser fields (Wineland et al., 1987).

Recent developments in far-field techniques have been able to explore the interference between the coherent radiation of a single emitter and a part of the excitation beam (Alén et al., 2006; Plakhotnik and Palm, 2001). Soon after, a series of experiments have demonstrated that light focused on single ions, molecules, or quantum dots may be attenuated by a few percent in transmission (Gerardot et al., 2007; Gerhardt et al., 2007a,b; Tey et al., 2008; Vamivakas et al., 2007; Wrigge, 2008; Wrigge et al., 2008a).

The intriguing question that arises is whether the experimentally observed coupling efficiencies are close to or far from the theoretical maximum. In particular, is it possible to make an atom optically thick? Is it possible for an atom to imprint a

large phase shift on a photon that passes by? In order to answer these questions we need to explore the connection between the strength of light-matter interaction and the limits to the optimal concentration of electromagnetic energy in free space.

A laser beam can be focused to a spot of about  $(\lambda/2\text{NA})^2$ , where NA is of the order of one, or even to a subwavelength area using a SNOM aperture. If we consider an ideal TLS for which  $\sigma = \sigma_0 = 3\lambda^2/2\pi$ , the ratio  $\sigma/A$  can be close to unity and we are led to think that a single emitter can fully extinguish the incident light. However, when the beam waist is comparable to the emitter cross section a proper definition of  $A$  becomes important, because a slightly different value for  $A$  can have a large effect on the transmission dip. We thus need to step back to the fundamentals of scattering theory and coherent spectroscopy to derive the correct formulae that describe the extinction of a strongly confined field by a TLS.

### 3.1 Optimal concentration of electromagnetic energy

We begin our analysis by reviewing concepts and methods related to tightly-focused beams and near-field optics. We discuss first high-NA optics and vectorial diffraction theory in free space. Later we move the attention to diffraction in the near field of subwavelength apertures, to the generalization of scattering theory for evanescent waves and to source-probe interactions (Girard and Dereux, 1996),

#### 3.1.1 Focused beams

In laser spectroscopy the incident field can be often described as a beam whose transverse intensity profile is a Gaussian function. The latter originates from the approximate solution of Helmholtz equation in the paraxial form (Born and Wolf, 1999). In this case the amplitude of the electric field  $\mathbf{E}$  reads

$$E(\rho, z) = E_0 \frac{w_0}{w(z)} e^{-\rho^2/w^2(z)} e^{i(kz + k\rho^2/2R(z) - \zeta(z))}. \quad (3.1)$$

$\rho$  is the radial distance,  $k = 2\pi/\lambda$  is the wavevector,  $w_0$  is the beam waist,  $R(z) = z(1 + (z_R/z)^2)$  is the radius of curvature of the wavefront,  $\zeta(z) = \arctan(z/z_R)$  is the Gouy phase shift, and  $w(z) = w_0\sqrt{1 - (z/z_R)^2}$  is for variation of the beam spot size, where  $z_R = \pi w_0^2/\lambda$  is the Rayleigh range. In order the paraxial approximation to be valid, the angle  $\theta$  between the beam radius  $w(z)$  and the beam axis has to be much smaller than one, which implies  $w_0 \gg \lambda$ . We are instead interested in situations where the beam waist is of the order of the wavelength, such that  $A$  becomes comparable to  $\sigma_0$ . Even though descriptions of Gaussian beams beyond the paraxial approximation are possible (Barton and Alexander, 1989; Sheppard and Saghafi, 1999), they are not convenient for describing the complex structure of the electromagnetic field near the focus of a high-NA optical system.

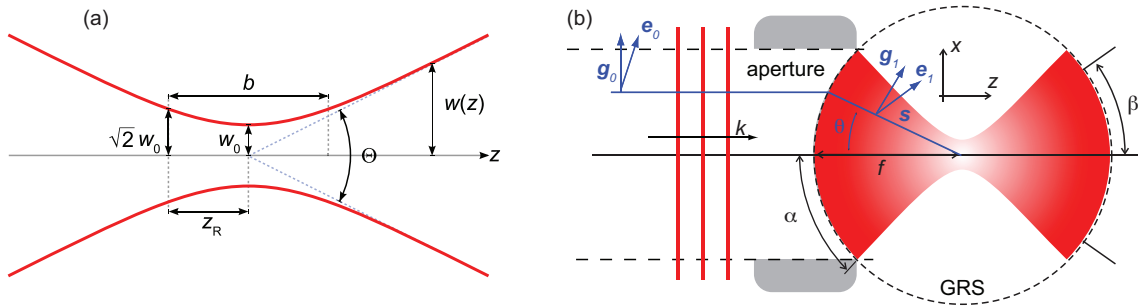


**Figure 3.1:** (a) A Gaussian beam and its main parameters.  $b = 2z_R$  is the confocal parameter and  $\Theta \simeq 2w_0/z_R$  represents the total angular spread of the beam. See text for details on the other labels. (b) A plane wave focused by a high-aperture optical system. The wavevector  $k$  indicates the plane wave propagation direction,  $f$  is the lens focal length.  $\alpha$  is the focusing semi-angle and  $\beta$  the collection semi-angle on the Gaussian reference sphere (GRS). The blue lines and labels refer to the procedure for determining the transformation of the field after the aperture.

Figure 3.1b sketches a tightly-focused beam obtained by a plane wave passing through a high-NA objective, simplified by an aperture that contains some optical elements. These refract the incident field in a way that at the right side of the aperture the wavefront corresponds to a strongly converging wave. A satisfactory description of the focusing process requires vector diffraction theory (Born and Wolf, 1999; Jackson, 1999) because, as we will see later, the vector nature of electromagnetic waves plays an important role in determining the structure of the field in the focal region. Moreover, there exist several kinds of high-aperture optical systems that implement different focusing schemes (Born and Wolf, 1999; Stamnes, 1986). In the following we restrict our analysis to a certain number of focused waves, which we consider as representative examples.

### The diffraction limit

The possibility to concentrate light down to a certain cross sectional area is related to the diffraction limit. This is a quantity that is typically used to express the resolving power of image-forming system, like a microscope or a telescope. Note, however, that a diffraction-limited spot does not imply that light has been confined to the smallest possible area. It just means that the focusing degree corresponds to the instrument theoretical limit (Born and Wolf, 1999). If  $\text{NA} = \sin \alpha$  is the numerical aperture of an optical system in vacuo, the diffraction limit states that it is possible to focus light to a spot of about  $(\lambda/2\text{NA})^2$ .  $\alpha$  is the focusing semi-angle as indicated in Figure 3.1.

The intensity distribution  $I(\rho)$  in the focal plane of an optical system of revolution with a small NA was first determined by Airy using scalar diffraction the-



ory (Airy, 1835), when he derived the celebrated expression

$$I(\rho) = I_{\text{inc}} \left( \frac{2J_1(k\rho \sin \alpha)}{k\rho \sin \alpha} \right)^2, \quad (3.2)$$

where  $\rho$  is the radial direction in the cylindrical coordinates  $(\rho, \phi, z)$ ,  $I_{\text{inc}}$  is the incident intensity and  $J_1(\rho)$  is the cylindrical Bessel function (Abramowitz and Stegun, 1972). Defining the beam spot size in the focal plane by choosing the first zero of the Bessel function yields

$$A = \pi \left( 0.61 \frac{\lambda}{\text{NA}} \right)^2, \quad (3.3)$$

which agrees with the previous statement that  $A$  should be of the order of  $(\lambda/2\text{NA})^2$ . Since this expression has been derived using scalar diffraction theory, we cannot use it for large NA focusing systems.

### Expressing the field in the image space

A wave incident on an aplanatic focusing system is transformed into converging spherical waves with a common center, which defines the so-called Gaussian reference sphere (GRS) (Born and Wolf, 1999). An expression of the electromagnetic field on the GRS can be conveniently obtained starting from a geometric ray picture. In Figure 3.1b consider the ray (blue line) that is bent in the image space to form an angle  $\theta$  with the optical axis. If the incident ray is linearly polarized that is also true for the refracted ray in the image space. An aplanatic system satisfies the sine condition, meaning that the ray meets the GRS at the same height at which the corresponding incident ray enters the system. Next we define the electric fields  $\mathbf{E}_0 = E_0 e^{ikS_0} \mathbf{e}_0$  and  $\mathbf{E}_1 = E_1 e^{ikS_1} \mathbf{e}_1$  associated with the incident and converging rays, respectively.  $S_0$  and  $S_1$  represent the eikonal function of geometrical optics (Born and Wolf, 1999), whereas  $\mathbf{e}_0$  and  $\mathbf{e}_1$  are the polarization vectors of the electric field. Energy conservation implies the relation  $E_1 = \sqrt{\cos \theta} E_0$ , where the term  $\sqrt{\cos \theta}$  is the apodization function  $a(\theta)$  of an optical system (Richards and Wolf, 1959). Next we need to relate  $\mathbf{e}_1$  to  $\mathbf{e}_0$  for every value of  $\theta$  and  $\varphi$ , the angles that define a point on the GRS in the spherical coordinates  $(r, \theta, \varphi)$ . Here we omit the technical details of this procedure and give the result (Richards and Wolf, 1959)

$$\mathbf{e}_1 = (\mathbf{g}_0 \cdot \hat{\mathbf{x}}) \mathbf{g}_1 + (\mathbf{g}_0 \cdot \hat{\mathbf{y}}) (\mathbf{g}_1 \times \mathbf{s}), \quad (3.4)$$

where  $\mathbf{g}_0$  and  $\mathbf{g}_1$  are unit vectors perpendicular to the rays and lie in the meridional plane as shown in Figure 3.1b.  $\hat{\mathbf{x}}$  and  $\hat{\mathbf{y}}$  are unit vectors for the  $x$  and  $y$  axes, respectively, and  $\mathbf{s}$  is a unit vector along the converging ray. In conclusion, the electric field on the GRS reads

$$\mathbf{E}(f, \theta, \varphi) = E_0 \sqrt{\cos \theta} e^{ikf} [(\mathbf{g}_0 \cdot \hat{\mathbf{x}}) \mathbf{g}_1 + (\mathbf{g}_0 \cdot \hat{\mathbf{y}}) (\mathbf{g}_1 \times \mathbf{s})] \Theta(\alpha - \theta), \quad (3.5)$$

where the step function  $\Theta(\alpha - \theta)$  determines the NA of the focusing system. This expression has been derived for a plane wave, but the procedure is identical for any type of incident beam.

Once that we have the electric field on the GRS we need to solve a vectorial diffraction problem, namely the field radiated by an aperture with a boundary condition determined by Eq. (3.5). In the following we make use of two equivalent, yet complementary, approaches, which are described in more detail in Appendix A.1 and A.2.

### Debye diffraction integrals

The first method relies on the Huygens-Fresnel principle, where every point of the wave front in Eq. (3.5) can be seen as a source of a secondary wave that propagates toward the center of the GRC. The field in the focal region is thus given by a coherent superposition of plane waves, which is expressed by so-called diffraction integrals. These depend on the polarization of light and are thus able to account for diffraction phenomena that originate from the vector nature of electromagnetic waves. The approach was initiated by Debye using Greens theorem (Debye, 1909) and was extended by Wolf using the method of stationary phase (Wolf, 1959). For an incident plane wave the formalism was first applied by Richards and Wolf (Richards and Wolf, 1959).

For a focused plane wave (FPW), the electric field in the focal region reads

$$E_x(\rho, \phi, z) = -iA_0(\mathcal{I}_0(\rho, z; \alpha) + \mathcal{I}_2(\rho, z; \alpha) \cos 2\phi), \quad (3.6)$$

$$E_y(\rho, \phi, z) = -iA_0\mathcal{I}_2(\rho, z; \alpha) \sin 2\phi, \quad (3.7)$$

$$E_z(\rho, \phi, z) = -2\mathcal{I}_1(\rho, z; \alpha) \cos \phi, \quad (3.8)$$

where  $\rho$ ,  $\phi$  and  $z$  are cylindrical coordinates with respect to the focal spot and  $A_0 = E_0fk/2$ . Similar expressions hold for the magnetic field  $\mathbf{H}$  in the focal region. The diffraction integrals  $\mathcal{I}_0$ ,  $\mathcal{I}_1$  and  $\mathcal{I}_2$  depend on the focusing semi-angle  $\alpha$  and are given in Appendix A.1.1. Equations (3.6)-(3.8) reveal that all three field components appear in the focal region even if the incident field is a linearly-polarized plane wave. Since the strength of light-matter interaction is proportional to  $\mathbf{d} \cdot \mathbf{E}$ , polarization effects in vectorial diffraction play an important role here.

### Multipole expansion

Diffraction integrals are advantageous for representing a tightly-focused beam in the focal point. There they assume a simpler form that allows one to derive analytical expressions. On the other hand, they offer less insight on the general properties of the focused beam, because every point requires a different diffraction integral.

An alternative approach relies on the multipole expansion of the electromagnetic field in the image space (Sheppard and Török, 1997a). Symmetry arguments select the appropriate multipoles that need to be used in the expansion, whereas the multipole coefficients are found by imposing the boundary condition that the field must match Eq. (3.5) at the GRS. Adopting the notation of (Bohren and Huffman, 1983) we write for the electric field of a FPW

$$\mathbf{E}(\mathbf{r}) = \sum_l A_{e,1,l} (\mathbf{N}_{e,1,l}(\mathbf{r}) - i\mathbf{M}_{o,1,l}(\mathbf{r})). \quad (3.9)$$

$\mathbf{N}_{e,1,l}$  and  $\mathbf{M}_{o,1,l}$  are vector spherical harmonics and the coefficients are provided in Eq. (A.39) of the Appendix.

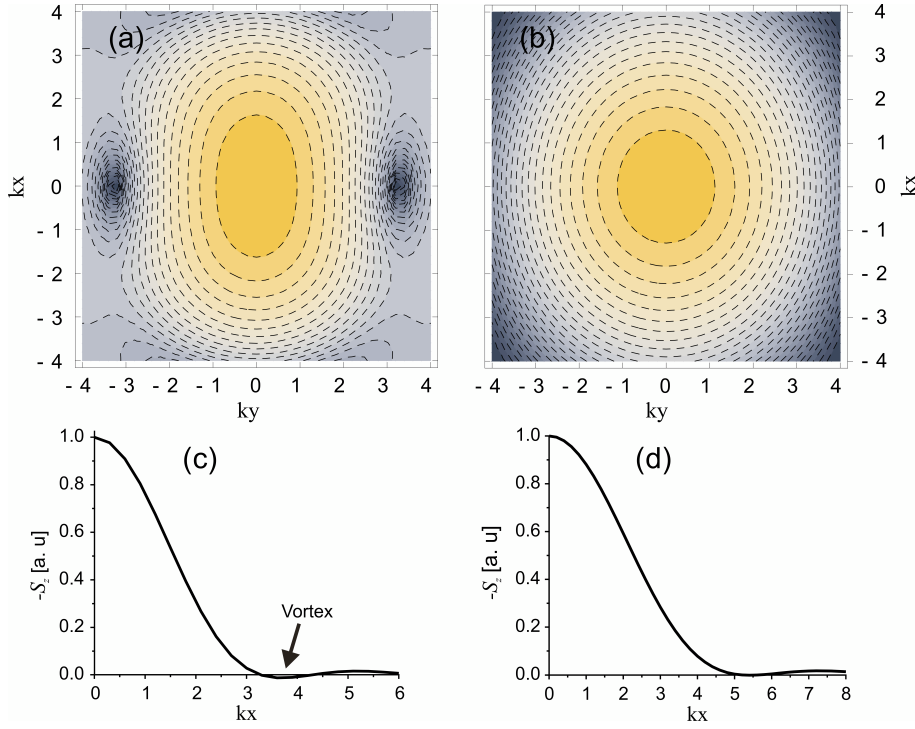
### Structure of the field in the focal region

Figure 3.2a and 3.2b represent the electric energy density of a FPW in the focal plane for  $\alpha = 90^\circ$  and  $\alpha = 45^\circ$ , respectively. The graphs compare a situation under extreme focusing, where vectorial diffraction gives rise to a spot size elongated in the polarization direction of the incident wave, with the case where the intensity distribution is well approximated by Eq. (3.2), which is the result of scalar diffraction theory. Figures 3.2c and 3.2d show instead the z-component of the Poynting vector in the focal plane for  $\alpha = 90^\circ$  and  $\alpha = 45^\circ$ , respectively. In the first case the Poynting vector presents areas with positive and negative values, which are a signature of field vortices (Boivin et al., 1967; Stamnes, 1986).

The structure of the electromagnetic field in the focal region can also be controlled by changing the incident wave. The past two decades have witnessed a large number of contributions aimed at obtaining diffraction-limited spots with engineered focal field distributions, for applications in lithography, storage, microscopy (Sheppard, 2007), particle trapping (Ashkin, 1970) and quantum optics (van Enk, 2004). In particular, purely theoretical studies include annular apertures (Sheppard, 1978), radially polarized beams (Quabis et al., 2000, 2001; van Enk, 2004), and dipole waves (Dhayalan and Stamnes, 1997; Sheppard and Larkin, 1994; Sheppard and Török, 1997b; Stamnes and Dhayalan, 1996). While these focused fields exhibit various confinement and polarization properties (Stamnes, 1986), what interests us is the amount of energy in the focal spot that couples with the TLS.

### The Bassett limit

Several restrictions exist on the degree to which light can be concentrated by passive optical systems, like a lens or an optical resonator (Bassett, 1984, 1986; Bassett and Winston, 1984; Mandel, 1961). They all originate from a geometrical optics principle, the conservation of *étendue*, which is the optical analogue of Liouville's theorem in classical statistical mechanics (Welford and Winston, 1978). For our



**Figure 3.2:** The electric energy density (on  $\log_{10}$  scale) at the focus of a FPW with (a)  $\alpha = 90^\circ$  and (b)  $\alpha = 45^\circ$ . (c) and (d) show the Poynting vector in the z direction for the same conditions as (a) and (b) respectively.

purposes we are interested in the limit for the energy density that can be obtained at a point when light passes only once (Bassett, 1986).

Consider the situation where a beam is focused by an optical system. We would like to derive an upper bound for the ratio  $W/P_{\text{inc}}$ , where  $W$  is the energy density at the focal point and  $P_{\text{inc}}$  is the incident power. It is convenient to describe the focused wave in terms of multipoles, because they yield additive contributions to  $P_{\text{inc}}$  and  $W$ . This follows from the orthogonality properties of multipoles and not from the fact that we deal with incoherent fields. Moreover, we take the origin of the multipole expansion to coincide with the focus, such that we can establish an immediate link between this derivation and the multipole description of a focused wave (Sheppard and Török, 1997a). First, we note that only the dipole waves do not vanish at focus. Second, to find an expression for  $P_{\text{inc}}$  we consider only incoming multipoles (Bohren and Huffman, 1983). The electric energy density  $W_E$  at the origin is  $\epsilon_0 k^2 / 12\pi$  for each of the three electric dipole waves  $\mathbf{N}_{e,-1,1}$ ,  $\mathbf{N}_{e,0,1}$  and  $\mathbf{N}_{e,1,1}$ , where we adopt the notation from Bohren and Huffman (1983). If we assume that  $P_{\text{inc}}$  is carried only by an incident dipole wave  $\mathbf{N}_{e,m,1}$ , we find  $P_{\text{inc}} = 1/4Z$  irrespective of  $m$ , where  $Z$  is the vacuum impedance. Hence we find

$$\frac{W_E}{P_{\text{inc,E}}} = \frac{k^2}{3\pi c'} \quad (3.10)$$

where  $P_{\text{inc,E}}$  stands for the power carried by a dipole wave and  $c$  is the speed of

light.

For an arbitrary superposition of multipole waves we also have the energy density  $W_M$  associated with the magnetic dipoles. It is easy to show that  $W_M = W_E$  independently of  $m$ . The same is true for the power  $P_{\text{inc},M}$  carried by an incident magnetic dipole wave and the result of Eq. (3.10) is also valid for  $W_M/P_{\text{inc},M}$ . If we now consider the additive contributions of the other multipoles to  $P_{\text{inc}}$ , we obtain the upper bound

$$\frac{W}{P_{\text{inc}}} \leq \frac{k^2}{3\pi c'} \quad (3.11)$$

which is the expression derived by Bassett (1986). In summary, the ratio  $W/P_{\text{inc}}$  is far or close to the upper bound given in Eq. (3.10) depending on the multipole content of the incident field.

We will find that there is a profound relationship between this limit and the maximum possible strength of light-matter interaction in free space. Before doing so, we want to discuss the other approach that we have followed for confining light to tighter spots. In near-field microscopy we are not restricted by the diffraction limit and we intuitively expect to achieve stronger interactions. On the other hand, we need to include evanescent waves that considerably complicate the description of the incident field (Girard and Dereux, 1996) and also of the scattering problem (Carney, 1999).

### 3.1.2 Subwavelength apertures

The ability to achieve high spatial resolutions in scanning near field optical microscopy relies on the strongly confined evanescent fields that exist near a subwavelength aperture. Electromagnetic diffraction by apertures of dimensions smaller than the wavelength of light is a theoretical problem that has received considerable attention over many years (Bethe, 1944; Bouwkamp, 1954; García de Abajo, 2007). As shown in Figure 3.3a, a classic configuration is a plane wave incident on a perfectly conducting and infinitely thin metal screen with a circular aperture. An approximate solution was first proposed by Bethe (1944) and a few years later corrected and improved by a number of authors (Bouwkamp, 1950; Meixner and Andrejewski, 1950; Nomura and Katsura, 1955).

Even if these analytical theories qualitatively explain the basic features of a SNOM aperture, the first works that analyzed geometries relevant for near-field microscopy were published after the first experimental demonstrations of subwavelength optical resolution (Lewis et al., 1984; Pohl et al., 1984). For example, Roberts (1987) was the first to consider an aperture in a thick metal screen. Soon after there have been other works focused on aspects relevant for SNOM probes (Leviatan, 1986; Roberts, 1989, 1991). A rigorous electrodynamic analysis of light propagation, diffraction, and image formation for realistic apertures, like the one shown in Figure 3.3b, became possible with the development of more elaborate theories and

with the first applications of computational electrodynamics to nano-optical problems (Berntsen et al., 1993; Kann et al., 1995a,b; Labeke and Barchiesi, 1992, 1993; Martin et al., 1995; Novotny and Pohl, 1995; Novotny et al., 1995). More details on past and recent theoretical developments in near-field optics can be found in two topical review papers (Girard, 2005; Girard and Dereux, 1996).

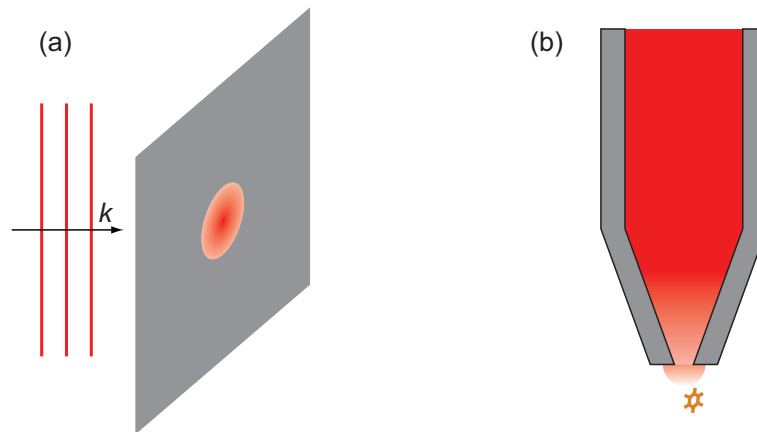


**Figure 3.3:** (a) An incident plane wave is diffracted by a subwavelength aperture in a perfectly conducting screen. (b) A subwavelength aperture is used in SNOM to achieve a spatial resolution below the diffraction limit.

### The near field

The subwavelength aperture of a SNOM probe creates an illumination that is sub-diffraction limited in the near field. In this region the electromagnetic field contains evanescent waves, whose occurrence can be qualitatively explained by invoking the Heisenberg uncertainty principle (Dürig et al., 1986; Vigoureux and Courjon, 1992).

In the following section we exploit computational electrodynamics to obtain the near field of a realistic SNOM probe. Here we are more interested in qualitative features and for this purpose we are satisfied with the approximate analytical theory developed by Bethe and Bouwkamp (Bethe, 1944; Bouwkamp, 1950). An aperture with radius  $a$  in a perfectly conductive and infinitely thin metal screen is illuminated by an  $x$ -polarized plane wave at normal incidence. The  $z$ -axis is chosen for the propagation direction. The diffraction problem leads to a power-series solution in the variable  $ka$  if the aperture dimensions are subwavelength. In Figure 3.4 we plot the electric field components in the first order approximation. The  $x$ -component is the strongest one and it has an antinode at the center. Even if the aperture is perfectly circular the pattern has an elongated shape in the polarization direction. This is a confirmation that the diffraction process strongly depends on the vector nature of the electromagnetic field. Note also that the spot size is of the order of the aperture area, as desired. The  $y$  and  $z$ -components are much weaker and have a node on the aperture axis. Since we assume that the molecule is located

there, we neglect these contributions and consider only the  $x$  polarization. However, in scanning the SNOM tip across the sample one has to take into account all three field components (Gerhardt, 2006).

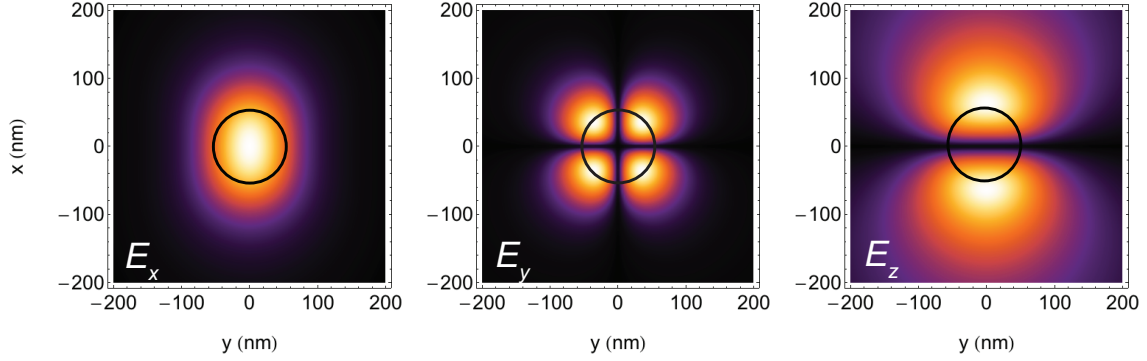


**Figure 3.4:** Electric field in a plane located 50 nm from a 100 nm aperture in a perfect metal screen. The calculation is based on the Bethe-Bouwkamp approximate theory for  $\lambda = 615$  nm (Bethe, 1944; Bouwkamp, 1950).

The tight lateral confinement of the electromagnetic field is possible because its Fourier spectrum contains evanescent components. These, however, are non-propagating waves and hence limit this type of illumination to a few decades of nanometers from the aperture. Figure 3.5 depicts this behavior for each field component. The amplitude drops very rapidly for all polarizations, even though the  $x$ -component extends over a longer distance.

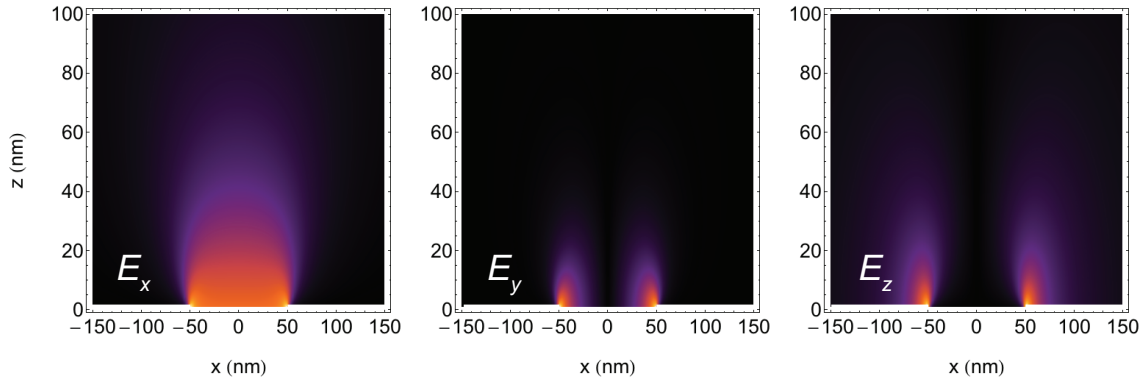


**Figure 3.5:** Electric field in the  $xz$  plane for a 100 nm aperture in a perfect metal screen. The cut corresponds to  $y = 0$  nm. The calculation is based on the Bethe-Bouwkamp approximate theory for  $\lambda = 615$  nm (Bethe, 1944; Bouwkamp, 1950).

## Throughput

Since the electric field decays exponentially as one moves away from the aperture, it is important to pay attention to the throughput of the system. According to Bethe theory the transmission of a subwavelength aperture in an infinitely thin

perfect conductor drops as  $(a/\lambda)^4$ . It means that for a 100 nm aperture and a 600 nm wavelength the throughput is of the order of  $5 \times 10^{-5}$ . Adding the fact that most of the diffracted field contains evanescent components that decay with  $z$ , the amount of incident electromagnetic energy that reaches the molecule is very small. Furthermore, in a real SNOM probe a lot of light is reflected and absorbed even before getting to the aperture. From the practical point of view one has to find a compromise between aperture size, working distance and signal-to-noise ratio in the photon flux (Gerhardt, 2006). Note that for subwavelength apertures in a flat metal screen it is possible to achieve extraordinary transmission by engineering surface plasmon-polariton resonances (García de Abajo, 2007; Genet and Ebbesen, 2007). In the next chapter we will discuss how these electromagnetic modes can be exploited to obtain a high throughput SNOM (Chen et al., 2009, 2010a).

### The far field

In coherent spectroscopy we are interested in the interference between the incident and the scattered fields in the far field. In Section 3.3 we will compute them by means of a near-to-far field transformation of the near-field data. To gain insight on the field diffracted by the aperture in the detector region, we once more consider a hole in a perfectly conducting plane screen. The radiation can be viewed as originating from effective sources located in the aperture (Jackson, 1999). For a subwavelength radius the contribution of high-order multipoles is negligible and the far field is due to an effective electric  $\mathbf{p}$  and magnetic  $\mathbf{m}$  dipole. These are expressed in terms of integrals of the tangential electric field in the aperture

$$\mathbf{p} = \epsilon_0 \mathbf{n} \int_A \mathbf{n} \cdot \mathbf{E}_{\text{tan}} dA, \quad \mathbf{m} = \frac{2}{i\omega\mu_0} \int_A \mathbf{n} \times \mathbf{E}_{\text{tan}} dA, \quad (3.12)$$

where  $\mathbf{E}_{\text{tan}}$  is the exact tangential electric field in the aperture,  $\mathbf{n}$  is the normal to the screen and  $A$  is the aperture area. These considerations indicate that the radiation pattern of the aperture resembles that of a tightly focused wave made by the combination of electric and magnetic dipoles (Dhayalan and Stamnes, 1997; Sheppard and Larkin, 1994). We thus expect that the far field analysis of the scattering process be similar to that for a tightly focused beam.

## 3.2 Generalized scattering theory

In Section 2.2 we introduced scattering theory as the appropriate framework for coherent spectroscopy. We have considered the most standard formulation of the theory, which assumes that the incident field is a linearly polarized plane wave and the scatterer is embedded in an infinite homogeneous and non-absorbing medium. When one considers the scattering problem in the context of focused or evanescent illumination, there are some important aspects that need to be addressed.



Morita et al. (1968) as well as Tsai and Pogorzelski (1975) were the first to extend the theory to the case of an incident focused Gaussian beam. Their work must be associated with the invention of the laser, which made available narrow-band collimated beams that can have cross sections smaller than the target. For particle scattering these developments have led to the so-called generalized Mie theory (Gouesbet and Grehan, 1982). It is found that there are significant deviations from the case of plane-wave illumination if the size of the scatterer is larger than the beam waist. Till recently, much less attention has been devoted to the case of subwavelength targets (Mojarad and Agio, 2009; Mojarad et al., 2008, 2009). Scattering theory has also been extended to the context of evanescent illumination (Quinten et al., 1999) and SNOM. In the latter case much emphasis has been given to the near-field distribution (Girard et al., 1993) and the tip-sample interaction (Girard et al., 1994).

While the accurate electromagnetic description of the incident field can be circumscribed to the solution of a technical problem, the analysis of the scattering signal and, in particular, the applicability of the optical theorem requires some discussion.

### 3.2.1 The optical theorem

The optical theorem establishes a relationship between the total power removed from a beam, i.e. the sum of the absorbed and scattered powers, and the vector scattering amplitude in the forward direction (Feenberg, 1932; Newton, 1976). Because this property is profoundly linked to the interference between the scattered and incident fields, we expect deviations from the original result of plane-wave scattering (van de Hulst, 1949b).

#### Failure of the optical theorem

The interpretation of extinction in generalized scattering theory and the extension of the optical theorem has been thoroughly investigated (Carney, 1999; Lock, 1995; Lock et al., 1995). Here we present a demonstration of its failure for the case of a spherical particle illuminated by a focused plane wave. The scattering problem is solved using a multipole description of the incident field (Mojarad et al., 2008). An expression for  $\mathbf{E}_{\text{inc}}$  is provided in Eq. (3.9) and the scattered field  $\mathbf{E}_{\text{sca}}$  reads

$$\mathbf{E}_{\text{sca}} = - \sum_l A_{e,1,l} (a_l \mathbf{N}_{e,1,l}(\mathbf{r}) - ib_l \mathbf{M}_{o,1,l}(\mathbf{r})), \quad (3.13)$$

where  $A_{e,1,l}$  are the same multipole coefficients of  $\mathbf{E}_{\text{inc}}$ , and  $a_l$  and  $b_l$  are the scattering coefficients for a sphere (Bohren and Huffman, 1983). From the far-field expressions of Eqs. (3.9) and (3.13) we can find an analytical formula for the total

scattered and extinguished power (Mojarad et al., 2008)

$$P_{\text{sca}} = \frac{\pi}{2Zk^2} \sum_l |A_l|^2 \frac{2l^2(l+1)^2}{2l+1} (|a_l|^2 + |b_l|^2), \quad (3.14)$$

$$P_{\text{ext}} = \frac{\pi}{2Zk^2} \sum_l |A_l|^2 \frac{2l^2(l+1)^2}{2l+1} (a_l + b_l). \quad (3.15)$$

Next we write  $\mathbf{E}_{\text{sca}}$  using the vector scattering amplitude

$$\mathbf{x} = i \frac{\cos \varphi}{E(O)} \sum_l (-i)^l A_l (a_l \tau_l - b_l \pi_l) \mathbf{e}_\theta - i \frac{\sin \varphi}{E(O)} \sum_l (-i)^l A_l (a_l \pi_l - b_l \tau_l) \mathbf{e}_\varphi, \quad (3.16)$$

where  $\pi_l(\theta)$  and  $\tau_l(\theta)$  are the angular dependent function introduced in Section A.2.2 and  $E(O)$  is the field amplitude at the position of the scatterer. The polarization versors  $\mathbf{e}_\theta$  and  $\mathbf{e}_\varphi$  are related to  $\mathbf{e}'_{\parallel}$  and  $\mathbf{e}'_{\perp}$  of Eq. (2.17), respectively. Using the expression for  $\pi_l$  and  $\tau_l$  for  $\theta = \pi$  and  $\varphi = 0$ , the propagation direction of the incident plane wave<sup>1</sup>, we obtain the relevant element of the amplitude scattering matrix

$$S_2 = i \frac{1}{2E(O)} \sum_l i^l A_l l(l+1) (a_l + b_l). \quad (3.17)$$

According to the optical theorem the expression  $4\pi I_{\text{inc}} \text{Re}\{S_2\}/k^2$ , where  $I_{\text{inc}} = |E(O)|^2/2Z$  is the incident intensity, must be equal to Eq.(3.15). This condition requires that the multipole coefficients read

$$A_l = -iE(O)(-i)^l \frac{2l+1}{l(l+1)}, \quad (3.18)$$

which indeed corresponds to the expansion of an  $x$  polarized plane wave of amplitude  $E(O)$  that propagates towards  $-\hat{\mathbf{z}}$  (Bohren and Huffman, 1983). Therefore we conclude that a multipolar scatterer fulfills the optical theorem in its standard formulation *only if it is illuminated by a plane wave*.

### Focused waves

A generalization of the optical theorem to focused illumination has been proposed by Lock et al. (1995). They interpret the forward scattering amplitude  $S_2$  as the first moment of the partial waves that form the incident beam. The extinguished power is thus given by an infinite series that contains the weighting factors of the partial waves and higher order moments of the forward scattering amplitude. Even though their formulation leads to an expression that relates the forward scattering amplitude to the extinction cross section it turns out to be not relevant for practical applications.

<sup>1</sup>This particular multipole expansion has been done assuming that the propagation direction is along  $-\hat{\mathbf{z}}$ .

Another intuitive way to explain the failure of the optical theorem considers the power flow associated with the Poynting vectors introduced in Eqs. (2.9)-(2.12) and their integration over the virtual surface depicted in Figure 2.4. The Poynting vector  $\mathbf{S}_{\text{int}}$ , which is associated with the interference between the incident and scattered fields, has a net power flow in the forward direction with an angular spread determined by  $\mathbf{E}_{\text{inc}}$ . This can be understood if one decomposes these fields into plane waves. For each component of  $\mathbf{E}_{\text{sca}}$  there must be one component of  $\mathbf{E}_{\text{inc}}$  with the same wavevector in order to contribute to  $P_{\text{int}}$ . Therefore, in a transmission experiment the maximum extinction does not correspond to the dip measured by an infinitesimal on-axis detector. To measure  $P_{\text{int}}$  one has to integrate the received power over the solid angle subtended by the incident wave. However, by doing so, Eq. (2.20) shows that we are also collecting a portion of  $P_{\text{sca}}$ . Therefore, associating the transmission dip with  $P_{\text{ext}}$  alone is not possible.

### Evanescent waves

When the incident field contains evanescent waves the scattering problem exhibits one more difficulty. If we now enclose the scatterer in a virtual sphere and apply Poynting theorem, we find that it is not possible to follow the same steps that hold for propagating fields. The reason is that an evanescent field must be generated at finite distances from the scatterer and the surface of integration cannot be taken as large as we like. Therefore, all asymptotic methods used for the calculation of extinction are not applicable in this case (Bohren and Huffman, 1983). To overcome these issues Carney introduced a model for the generation of evanescent waves based on total internal reflection at a dielectric interface between two semi-infinite half spaces. He derived a generalized expression for the optical theorem to relate the scattering amplitude to the total power removed from the incident wave. In particular, he found that for each evanescent plane wave in the incident field, the optical theorem has the same expression for a propagating plane wave, but with the scattering amplitude being an analytical function of the complex wavevector (Carney, 1999). Since the generation of evanescent fields depends on the chosen geometry, we will not pursue this formalism. We will instead base our analysis on an analytical model whose parameters have to be found via numerical solution of the scattering problem.

### 3.2.2 Scattering and absorption by a dipolar radiator

We now discuss generalized scattering theory for a point-like scatterer and extend the results presented in Section 2.2.2.

### Focused waves

When the target is a point-like oscillating dipole, the scattered field is the dipolar wave defined in Eq. (2.22). For the case of focused illumination it is convenient to express  $\mathbf{E}_{\text{sca}}$  in terms of the vector spherical harmonic  $\mathbf{N}_{e,1,1}^{(3)}$ . The superscript (3) indicates that we have chosen the Hankel function of the first kind (Abramowitz and Stegun, 1972). This corresponds to an outgoing wave. The subscripts explain that we consider a wave generated by an electric dipole oriented towards the  $x$ -axis. Moreover, we include the multipole coefficient  $A_1$  from the electric dipole wave component  $\mathbf{N}_{e,1,1}^{(1)}$  of the incident field, where the superscript (1) refers to the spherical Bessel function of the first kind (Abramowitz and Stegun, 1972), as explained in Appendix A.2.1. We thus write

$$\mathbf{E}_{\text{sca}} = -cA_1\mathbf{N}_{e,1,1}^{(3)}, \quad (3.19)$$

where  $c$  is a complex number. When we calculate the scattered and extinguished powers for any incident field that contains  $\mathbf{N}_{e,1,1}^{(1)}$  in the expansion, the orthogonality of vector spherical harmonics yields (see also Eqs. (3.14) and (3.15))

$$P_{\text{sca}} = \frac{\pi}{2Zk^2} \frac{8}{3} |A_1|^2 |c|^2, \quad P_{\text{ext}} = \frac{\pi}{2Zk^2} \frac{8}{3} |A_1|^2 \text{Re}\{c\}. \quad (3.20)$$

Since only the electric dipole wave  $\mathbf{N}_{e,1,1}^{(1)}$  contributes to electric field intensity at the origin, we find  $E(O) = 2A_1/3$ . This result has two important consequences. The first one is that the cross sections, obtained by dividing the quantities in Eq. (3.20) by  $I_{\text{inc}} = |E(O)|^2/2Z$ , read

$$C_{\text{sca}} = \sigma_0 |c|^2, \quad C_{\text{ext}} = \sigma_0 \text{Re}\{c\}. \quad (3.21)$$

These expressions correspond to Eq. (2.30) if

$$c = i \frac{\Gamma}{2\Delta + i\Gamma_t}. \quad (3.22)$$

In fact the intrinsic dipole cross sections do not depend on the shape of the incident field. We can thus write  $P_{\text{sca}} = C_{\text{sca}} I_{\text{inc}}$  and  $P_{\text{ext}} = C_{\text{ext}} I_{\text{inc}}$ . By equating these expressions with those of Eq. (3.20) we indeed find that  $c$  is given by Eq. (3.22). Note that for an ideal oscillating dipole  $\Gamma_t = \Gamma$ , which yields  $|c|^2 = \text{Re}\{c\}$  and  $P_{\text{sca}} = P_{\text{ext}}$ . In summary, a weakly excited TLS responds to illumination with a scattered field proportional to the dipole coefficient of the incident wave. The second important consequence of  $E(O) = 2A_1/3$  and Eq. (3.20) is that a dipolar scatterer fulfills the optical theorem in its standard form irrespective of the incident field, because the condition given in Eq. (3.18) holds only for  $A_1$  and reads, indeed,  $A_1 = 3E(O)/2$ .

### Evanescent waves

For a point-like dipolar scatterer the optical theorem is valid also for evanescent waves, because an infinitesimal scatterer cannot discriminate between waves of different types. The only amendment that need to be done is the analytical continuation of the vector scattering amplitude in the complex plane, to include the fact that the wavevectors of evanescent waves are complex (Carney, 1999).

## 3.3 A molecule illuminated by a SNOM aperture

An early analysis of coherent spectroscopy under near-field illumination has been given by Plakhotnik (1995). He considered the source field diffracted by a sub-wavelength aperture in the Bethe-Bouwkamp approximation. Even if he predicted modification of the visibility and lineshape in the transmitted signal, he was unable to conclude on the question of maximum extinction that can be achieved, even for the idealized model of an aperture in a perfectly conducting and infinitely thin metal screen.

Here we present a study where we consider a realistic SNOM aperture and parameters that are relevant for experiments (Gerhardt et al., 2007a,b). We show that the detected far field traces the complex behavior of the near field and of the coherent tip-sample interaction produced by the currents induced on the tip surface by the molecule. To gain insight on these processes we have developed a numerical model based on the Finite-Difference Time-Domain method (FD-TD) (Taflove and Hagness, 2005) and generalized scattering theory.

### 3.3.1 Layout of the problem

We first specify the general layout of the problem, namely the SNOM tip, the near and far-field detection schemes. We furthermore discuss some aspects of the FD-TD implementation, leaving the details in the Appendix B.

#### Illumination and detection

Figure 3.6 sketches the arrangement of the scattering configuration. The illumination is provided by a SNOM aperture, which is modeled as a truncated aluminum-coated conical waveguide with a glass core. The aperture radius is 50 nm and the cladding thickness 200 nm. The tip head has thus a diameter of 500 nm. These are dimensions that are compatible with fabricated probes (Gerhardt, 2006). To avoid spurious effects due to the truncation of the SNOM probe, which is only 600 nm, we terminate the structure in perfectly matched layers (Roden and Gedney, 2000). These can absorb any incident wave without reflections such that the tip behaves like if it were a semi-infinite scatterer. We excite the field inside the tip

using an  $x$ -polarized Gaussian profile, which approximates the linearly-polarized guided mode of a metal-coated fiber. Moreover the time profile of the source is Gaussian and it enables us to obtain spectral information in one single simulation. The FD-TD algorithm gives immediate information on the near field, which is used to excite the molecule. The latter is located along the tip axis, at distances between 40 and 600 nm. In order to obtain far-field quantities that can be compared with experiments (Gerhardt et al., 2007a,b), we perform a near-to-far field transformation using the fields recorded at the near-field detector indicated by dashed lines in Figure 3.6. The transformation yields the field in the radiation zone as a function of the angles  $\theta$  and  $\varphi$ . The detected power contains the incident and scattered fields and it can be recorded taking a small solid angle along a certain direction or in full collection.

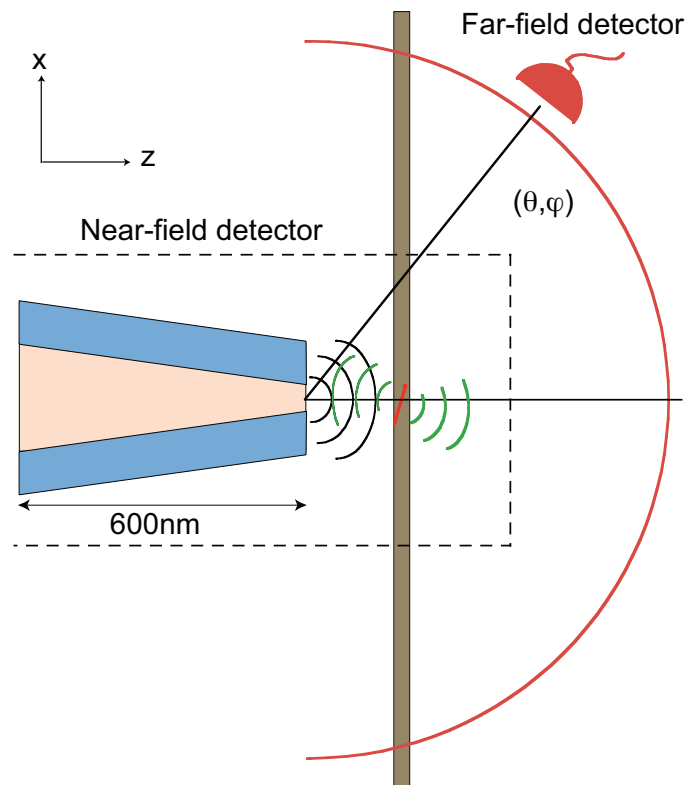


**Figure 3.6:** Layout of the scattering problem. Tip parameters: core ( $\text{SiO}_2$ ), cladding (Al), cladding thickness 200 nm, aperture radius 50 nm. Molecule parameters: dipole oriented along  $x$ , resonant at  $\lambda = 615$  nm. In the experiments the molecule is embedded in a thin crystalline matrix. Here we assume that the molecule is in vacuo and approximate it with a TLS.

### Modeling molecular scattering

While FD-TD modeling of nano-optical problems has concerned the resolution in the near field (Kann et al., 1995a,b) or the analysis of the incoherent fluorescent

emission (Bian et al., 1995), much less attention has been dedicated to coherent interactions.

Since we are working in the weak-excitation limit, we can replace the molecule with a classical oscillating dipole. In the FD-TD scheme the dipole is represented by cubic cell of material with a polarizability  $\alpha$  given by a Lorentz dispersion model. We take into account the molecular orientation by assigning this polarizability only to the  $x$ -component of the field, while the rest is equal to the surrounding medium. The electric field  $\mathbf{E}_{\text{tip}}$  near the tip induces a coherent dipole moment

$$\mathbf{p} = \epsilon_0 \alpha (\mathbf{E}_{\text{tip}} \cdot \mathbf{x}) \mathbf{x}, \quad (3.23)$$

where

$$\alpha = -\frac{A}{2} (\Delta - i\gamma) L(\omega), \quad L(\omega) = \frac{1}{\pi} \frac{\gamma}{\Delta^2 + \gamma^2}. \quad (3.24)$$

An expression for  $A$  is derived in the Appendix B.2.1.  $\Delta$  is the detuning from resonance,  $2\gamma$  is the radiative linewidth and  $L(\omega)$  a Lorentzian. The molecular dipole driven by the incident field oscillates and radiates energy into the far field. Figure 3.7 presents two snapshots of the  $y$ -component of the magnetic field for two molecule-tip distances. Note that in both cases the scattered field reaches the tip and it is reflected<sup>2</sup>. Later we will find that this phenomenon leaves an important footprint in the scattering spectra.

### Electromagnetic field near the aperture

Before moving to the far field and the detected signals it is useful to compare the near field of a realistic SNOM aperture with that of Bethe-Bouwkamp theory. Figure 3.8 plots the result of an FD-TD calculation with steady excitation at  $\lambda = 615$  nm. The symmetry of the field components corresponds to that of Figure 3.4. Furthermore,  $E_x$  is elongated in the polarization direction of the excitation field in agreement with Bethe-Bouwkamp theory. The largest deviation occurs for  $E_y$ , which shows here the termination of the cladding layer on top of the aperture. In the following we consider only the  $E_x$  component, since the molecule is located on-axis and it has its dipole moment oriented along  $x$ .

### 3.3.2 Far-field pattern and detected signals

We now focus our attention on the far field and on the interpretation of the detected visibilities and lineshapes. The far field of a subwavelength aperture in an infinite perfect metal screen can be represented by a combination of electric and magnetic dipoles (Jackson, 1999). In place of computing these effective sources, we obtain the

<sup>2</sup>In the FD-TD calculations we can easily separate the incident from the scattered fields, because the latter is emitted by a dipolar oscillator with a high quality factor. Hence, the scattered field persists in the near-field region much longer than the incident pulse

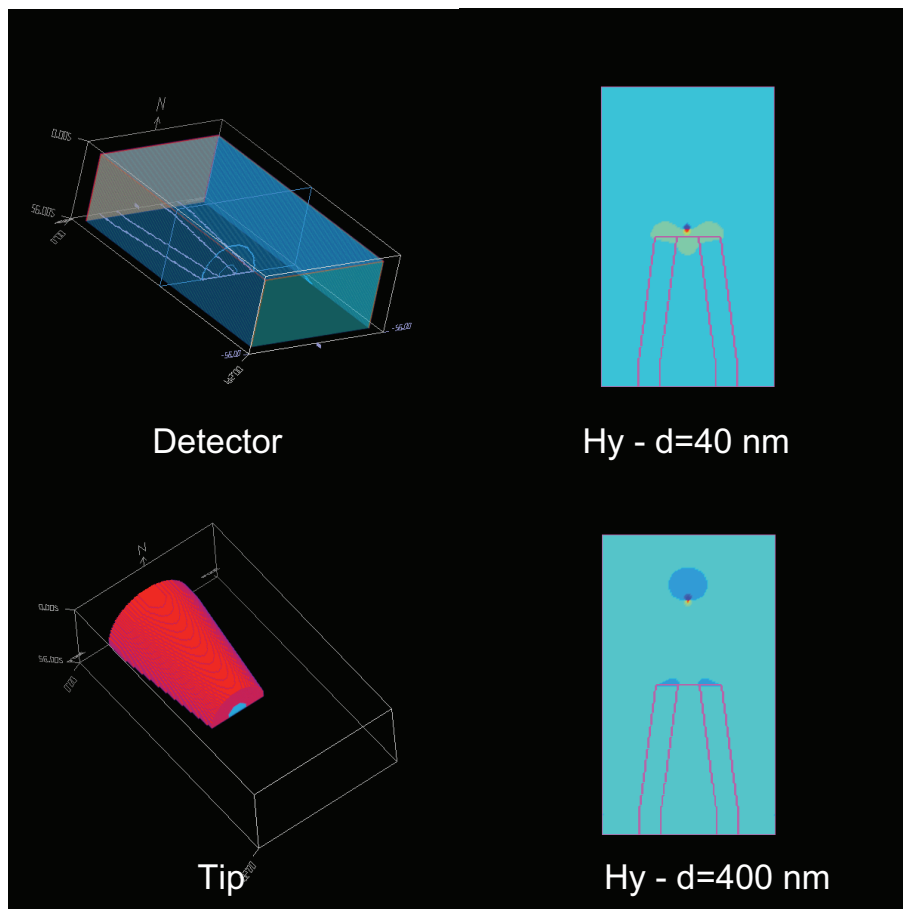


**Figure 3.7:** (top left panel) Layout of the near-field detector used for the near-to-far field transformation. (bottom left panel) FD-TD implementation of a SNOM tip. Only the last section of the tip is modeled. To avoid spurious finite size effects the tip is terminated inside the absorbing boundary conditions (see Appendix B.1.2 for details). (right panels) Magnetic field component  $H_y$  for two different distances  $d$  of the molecule from the tip. Tip parameters: core ( $\text{SiO}_2$ ), cladding (Al) cladding thickness 200 nm, aperture radius 50 nm. Molecule parameters: oriented along  $x$ , resonant at  $\lambda = 615$  nm.

field by means of a near-to-far field transformation of the FD-TD data. Figure 3.9 shows the power distribution as a function of  $\theta$  along two azimuthal directions, namely  $\varphi = 0^\circ$  and  $\varphi = 90^\circ$ . The spread is indeed close to that of a dipolar source, even if here some power propagates in the backward directions. The tip is not an aperture in an infinite metal screen and diffraction effects can direct optical energy even in the opposite direction with respect to the excitation wave in the aperture.

The signal detected in the far field contains two contributions, the field radiated by the SNOM tip and the field coherently scattered by the molecule excited near the aperture. In the received power we also have to take into account the interference between these two fields (Plakhotnik and Palm, 2001). To simplify the analysis and work with scalar quantities, it is convenient to parametrize the incident field with



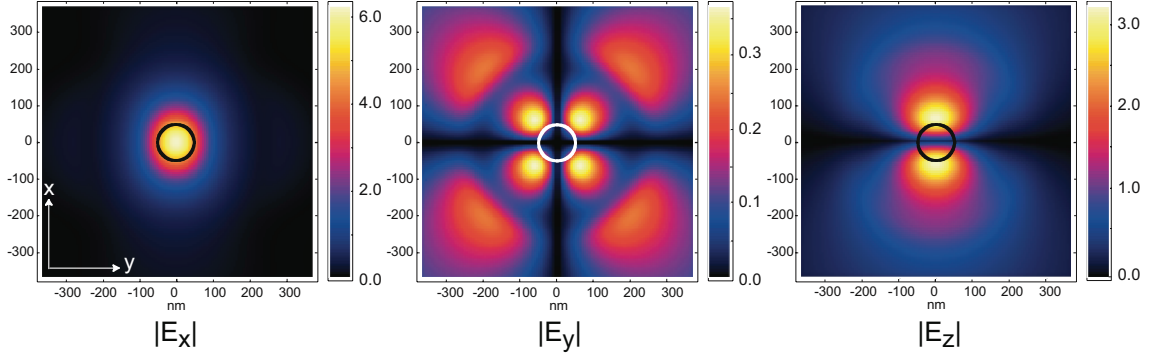


**Figure 3.8:** Electric near field near the SNOM probe as described in the caption of Figure 3.6. The calculation is based on the FD-TD method with steady state excitation at  $\lambda = 615$  nm.

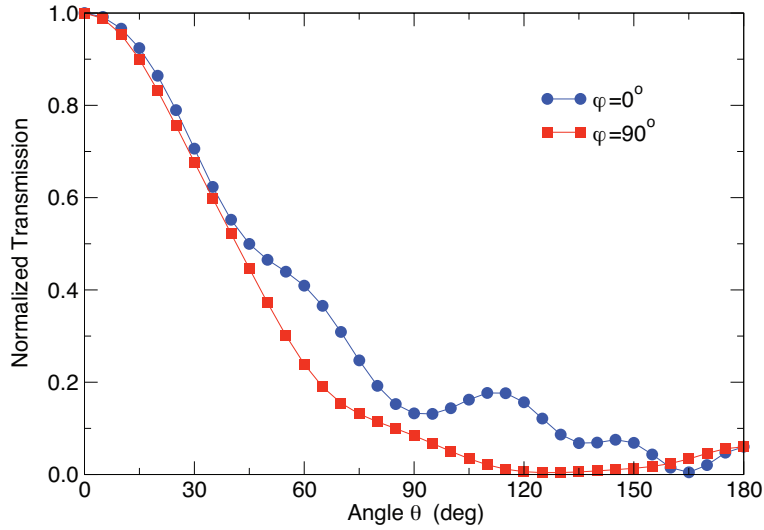


**Figure 3.9:** Far-field radiation pattern of the SNOM tip calculated using a near-to-far-field transformation.

respect to its value at the molecule position  $\mathbf{r}_m$ .

$$\mathbf{E}_{\text{tip}}(\mathbf{r} \rightarrow \infty) = (\mathbf{E}_{\text{tip}}(\mathbf{r}_m) \cdot \mathbf{u}_m)g\mathbf{u}_d = Bg\mathbf{u}_d. \quad (3.25)$$

$\mathbf{u}_m$  stands for the orientation of the molecular dipole and it corresponds to  $\mathbf{x}$  in our model.  $\mathbf{u}_d$  is instead the field orientation that is detected in the far field and  $g$  is a complex number that accounts for the propagation from the near to the far region. Likewise the scattered field  $\mathbf{E}_{\text{sca}}$  is proportional to the molecular dipole moment, hence to the near field through the polarizability  $\alpha$ . In the far field it reads

$$\mathbf{E}_{\text{sca}}(\mathbf{r} \rightarrow \infty) = -\frac{A}{2}(\Delta - i\gamma)L(\omega)Bf\mathbf{u}_d. \quad (3.26)$$

Note that the complex number  $f$  includes contributions of scattered light reflected by the SNOM tip, which is illustrated in Figure 3.7. At the detector the signal  $S$  is

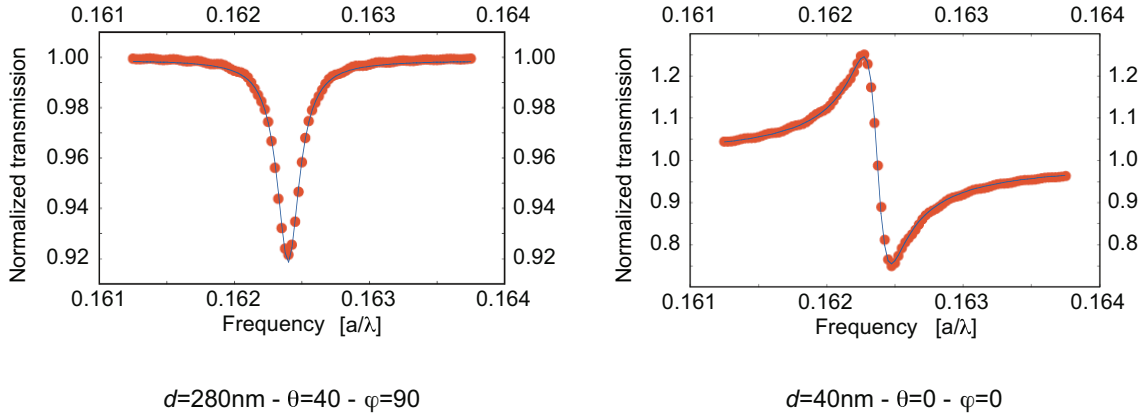
thus determined by the total electric field

$$\mathbf{E}_{\text{tot}} = \mathbf{E}_{\text{tip}} + \mathbf{E}_{\text{sca}} = B \left[ g - f \frac{A}{2} (\Delta - i\gamma) L(\omega) \right] \mathbf{u}_d. \quad (3.27)$$

Normalizing with respect to the radiated power in absence of the molecule leads to

$$S = \frac{|\mathbf{E}_{\text{tot}}|^2}{|\mathbf{E}_{\text{tip}}|^2} = 1 + \frac{\gamma}{4\pi} V^2 L(\omega) - VL(\omega) (\Delta \cos \psi + \gamma \sin \psi) \quad (3.28)$$

where the visibility  $V(\theta, \varphi) = A|f/g|$  and phase shift  $\psi(\theta, \varphi) = \psi_f - \psi_g$  refer to the amplitude ratio and phase difference of  $f$  and  $g$ , respectively.  $S$  depends on the detector position  $(\theta, \varphi)$ , polarization  $\mathbf{u}_d$  and also on the molecule distance  $d$  with respect to the SNOM tip.



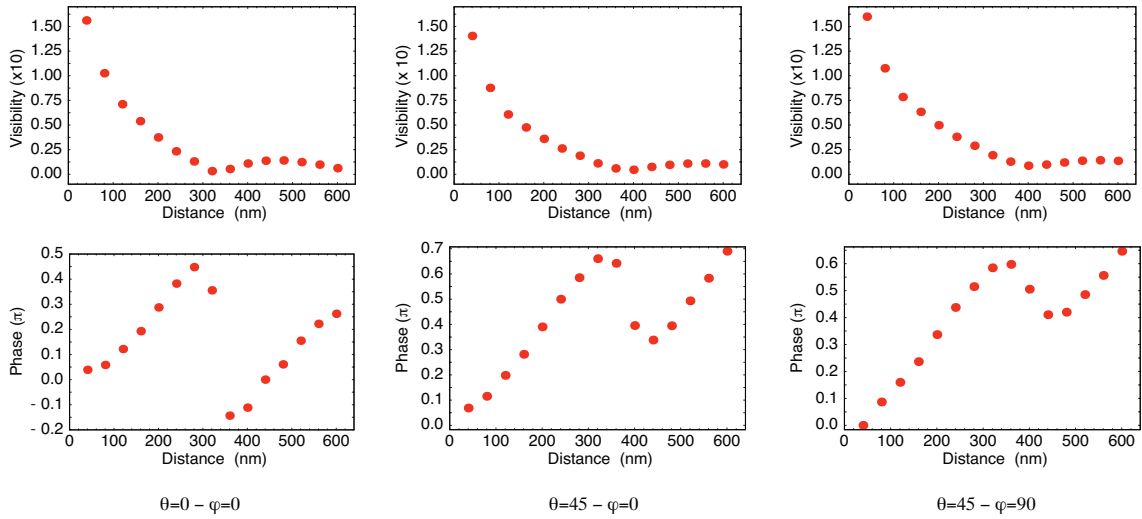
**Figure 3.10:** FD-TD results (red dots) and fit of the detected signal  $S$  (thin solid line) based on Eq. (3.28) for two different set of parameters.  $a = 100 \text{ nm}$  is the length scale used in the FD-TD simulations.

Figure 3.10 illustrates these considerations for two situations. The numerical results given by the FD-TD model are fitted using Eq. (3.28). The agreement between FD-TD and analytical fit is remarkable. Interestingly the lineshape can change from absorptive to dispersive depending on the value of  $\psi$  (Karrai and Warburton, 2003; Plakhotnik and Palm, 2001). To gain further insight we have performed several FD-TD calculations changing  $d$ ,  $\theta$  and  $\varphi$  and fitted the spectra to extract  $V$  and  $\psi$ .

### Distance dependence

We first consider the behavior of  $V$  and  $\psi$  as the molecule moves away from the SNOM tip. In the first 300 nm the visibility drops because its denominator  $g$  is inversely proportional to the near field (see Eq. (3.25)). When the distance crosses a value of the order of  $\lambda/2$ , there is a minimum in the visibility curve. The effect is explained by considering that a fraction of  $\mathbf{E}_{\text{sca}}$  is reflected by the SNOM tip, which acts as a mirror. Its strength in the visibility curves depends on several

parameters, such as the tip geometry, tip optical constants, molecule orientation, and collection angles. In practice, the situation is similar to that of a molecule in front of a mirror. The reflected field acts as a coherent feedback that modulates the molecular polarizability as a function of distance. This model has been used to explain the modification of the spontaneous emission rate (Chance et al., 1978), but it is also applicable to the coherent part of the emitted field. In conclusion,  $V$  depends on the strength of the near field and also on the coherent interaction between molecule and SNOM tip.



**Figure 3.11:** Visibility  $V$  and phase shift  $\psi$  as a function of distance  $d$  from the SNOM tip and for various detection angles. Each circles corresponds to the fit of an FD-TD simulation.

These features can also be recognized in the distance dependence of the phase shift  $\psi$ . In correspondence with a visibility minimum there is a variation of  $\psi$  over distances that are much smaller than the wavelength and that could not be explained by the tip near field alone.

### Angle dependence

The change of  $V$  and  $\psi$  with the angle  $\theta$  is less pronounced than the case of the distance dependence. The reason is that the tip far field can be approximated by the field produced by the sum of two crossed electric and magnetic dipoles, whose angular spread is quite similar to that of the molecule.

### Tip dependence

Lastly we discuss the dependence of  $V$  and  $\psi$  on two relevant tip parameters: the aperture diameter and the extent of the tip end facet. As expected, a smaller aperture yields a larger visibility, which however has the drawback of a significantly

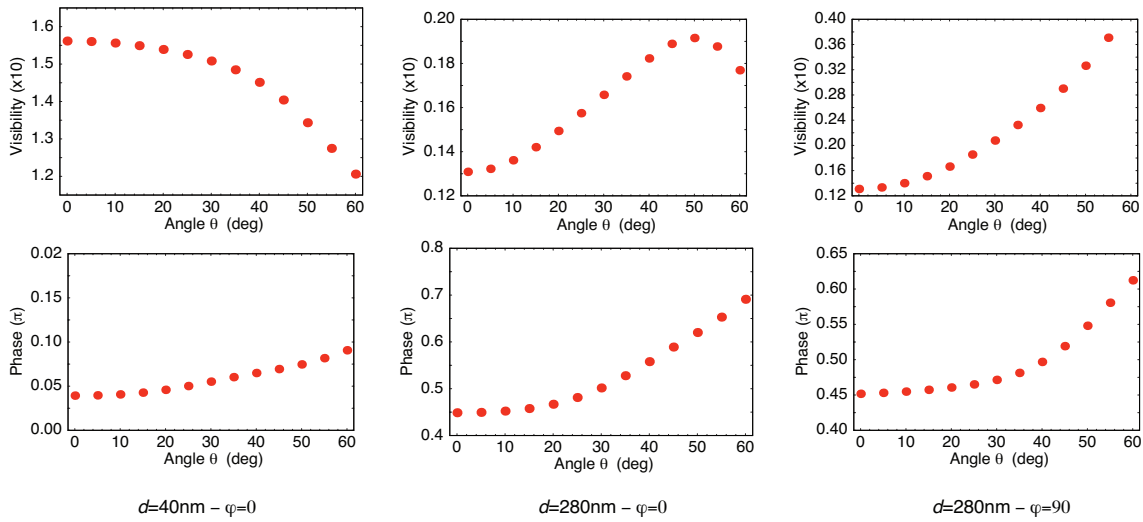


**Figure 3.12:** Visibility  $V$  and phase shift  $\psi$  as a function of the angle  $\theta$  and for various molecule-tip distances. Each circles corresponds to the fit of an FD-TD simulation.

reduced throughput. The effects of the tip parameters in the coherent feedback are instead more apparent in the phase shift. A smaller aperture in a large tip facet makes a better mirror than a larger aperture or a smaller tip and it gives rise to a sharper phase variation in correspondence of the visibility minimum.

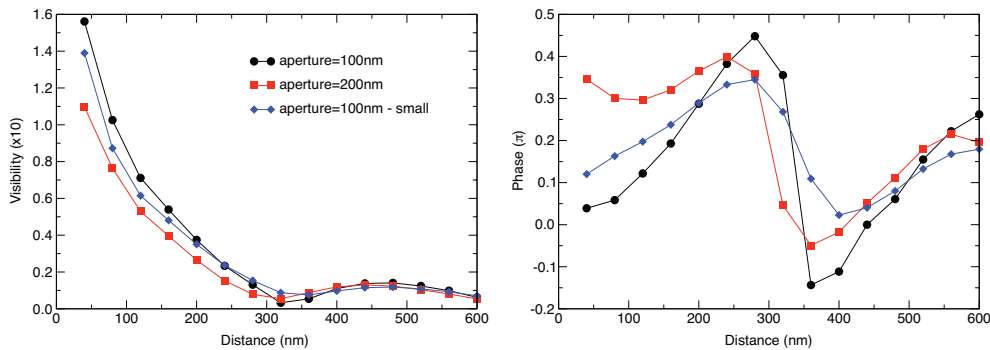


**Figure 3.13:** Visibility  $V$  and phase shift  $\psi$  as a function of two relevant tip parameters: aperture and tip diameters. Each mark corresponds to the fit of an FD-TD simulation.

## Fluorescence

A point of concern in the previous analysis is the fact that we have neglected the quantum electrodynamics (QED) effects that take place when a molecule is near a metal interface. These can modify its spectroscopic properties by changing the transition frequency and the spontaneous emission rate (Chance et al., 1978; Drexhage, 1974). A detailed study of these effects for the case of a molecule near SNOM tips indicates that the changes are appreciable only at very short distances (Ambrose

et al., 1994; Bian et al., 1995). We verify that indeed we can ignore QED phenomena by computing the modification of the spontaneous emission rate as a function of distance for two orientations of the dipole moment. Figure 3.14 confirms that for a molecule oriented parallel to the tip surface the deviations from free space are small, especially when the distance is larger than 50 nm.

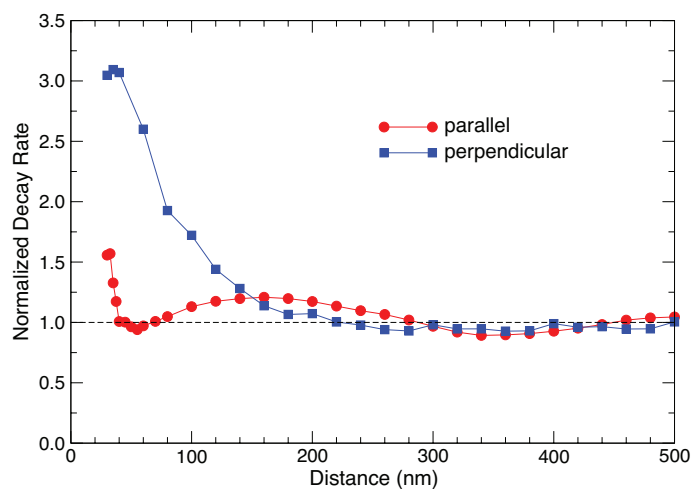


**Figure 3.14:** *Modification of the spontaneous emission rate for a molecule near a SNOM tip. The legend indicates the orientation of the dipole moment with respect to the tip facet.*

The FD-TD model predicts strong extinction of a dipolar emitter placed in front of a subwavelength aperture. The visibility and the phase depend in a non-trivial manner on several parameters: the detection angle, the position of the molecule in the near field of the tip, the orientation of the molecule with respect to the incident field (not shown), and the tip geometry. Our model captures the phenomena observed in recent experiments (Gerhardt, 2006), with which it is in good quantitative agreement (Gerhardt et al., 2007a).

We remark that the dispersive shapes (see Figure 3.10) disappear if the received power is integrated over a solid angle comparable to the angular spread shown in Figure 3.9, in agreement with the generalized optical theorem discussed in Section 3.2.1. Nonetheless, the complex diffraction phenomena involved in the solution of this scattering problem and the need for brute force numerical analysis hinder the derivation of upper bounds for light-matter interaction and extinction. Diffraction-limited focused waves are unable to confine light as much as a sub-wavelength aperture, but allow an analytical solution of the scattering problem and do not include the cumbersome treatment of evanescent fields and multipole scattering.

## 3.4 A single molecule in a strongly focused beam

The interaction between focused light and a single quantum emitter has been first addressed by Carmichael (1993). He reduced the problem to a one-dimensional system, where the ratio between the focusing angle and the angular spread of spontaneous emission determines the coupling efficiency. He predicted that light is perfectly reflected when this ratio is equal to one. A few years later van Enk and Kimble (2000) gave the correct dimensionality to the scattering problem by considering a focused Gaussian beam incident on an atom. They introduced the scattering ratio, defined as the ratio between the scattered and incident powers, to express a measure of the coupling strength. Their analysis concluded that "...by strongly focusing light on a single atom in free space, one may create an appreciable light-atom interaction, which, however, is not as strong as might be naively expected. On the one hand, this implies that a coherent-state field employed for classical addressing of a single atom in implementations of quantum computing and communication carries little information about that atom, so that entanglement of the atom with other atoms in a quantum register can be preserved. On the other hand, there are serious obstacles associated with using a single atom to process quantum information encoded in single photons in free space." Subsequent work based on a more elaborate analysis of the focused field did not change the above statement (van Enk, 2004; van Enk and Kimble, 2001).

In the following we reconsider this fundamental problem with the help of generalized scattering theory and derive, for the first time, an upper bound for the level of interaction achievable in free space (Zumofen et al., 2009, 2008). The previous sections explain how we describe a tightly focused beam and the basic scattering properties of a dipolar emitter. Here we establish a relationship between the optimal concentration of electromagnetic energy and the strength of light-matter interaction.

### 3.4.1 The scattering ratio

The strength of the interaction between a light beam and an oscillating dipole can be expressed by  $\mathcal{K}_{\text{sca}}$ , the ratio of the scattered to the incident powers.  $\mathcal{K}_{\text{sca}}$  can also be given as the ratio of two independent quantities, the scattering cross-section  $\sigma$  defined in Eq. (2.45) and the inverse of an effective focal area  $A$  (van Enk, 2004; Zumofen et al., 2008)

$$\mathcal{K}_{\text{sca}} = \frac{P_{\text{sca}}}{P_{\text{inc}}} = \frac{\sigma}{A}. \quad (3.29)$$

For a point-like oscillator the scattered power depends solely on the field strength at the position of the oscillator. Accounting for the electric nature of the interaction, the effective focal area can be given as the ratio of the incident power

and the electric energy density at the focal spot

$$A = \frac{P_{\text{inc}}}{2cW_{\text{el}}(O)} = \frac{P_{\text{inc}}}{S_z(O)}, \quad (3.30)$$

where  $S_z(O)$  denotes the  $z$ -component of the Poynting vector and  $W_{\text{el}}(O)$  the electric energy density at the focal spot  $O$ . The second equality holds for circular symmetry of the incident field strength with respect of the  $z$ -axis; a condition which, for instance, is obeyed by a focused plane wave (FPW) but not by a directional dipole wave ( $p_x$ ).  $A$  is closely related to the normalized energy density  $W_{\text{el}}/P_{\text{inc}}$  that has been studied for various focal systems using vectorial diffraction theory (Sheppard, 2007; Sheppard and Larkin, 1994; Sheppard and Török, 1997b). The peculiarities of the incident field enter  $\mathcal{K}_{\text{sca}}$  via  $A$ . Consequently, as we will show below, the problem of maximum extinction is shifted to that of a minimal  $A$ , and a strong photon oscillator interaction is reachable for  $\mathcal{K}_{\text{sca}} > 1$  (Domokos et al., 2002).

We first consider an incident  $x$ -polarized plane wave of amplitude  $E_0$ . The calculation of the power incident over the aperture is straightforward and yields  $P_{\text{inc}} = c\epsilon_0 E_0^2 \pi a^2 / 2$ , where  $a$  is the radius of the entrance aperture shown in Figure 3.1b. We also have  $W_{\text{el}}(O) = \epsilon_0 (\pi f E_0 \mathcal{I}_0(O) / 2\lambda)^2$ , where  $f$  is the focal length of the focusing system and  $\mathcal{I}_0(O)$  is the diffraction integral given in Eq. (A.8) of the Appendix. The resulting value of  $A$  then yields

$$\mathcal{K}_{\text{sca}} = \frac{128}{75} \frac{1}{\sin^2 \alpha} \left( 1 - \frac{1}{8} (5 + 3 \cos \alpha) \cos^{3/2} \alpha \right)^2, \quad (3.31)$$

where  $\alpha$  specifies the focusing semi-angle. For  $\alpha = \pi/2$ ,  $\mathcal{K}_{\text{sca}}$  reaches the maximum value of  $128/75 \simeq 1.7$ . Assuming full collection in a backward and forward half space and accounting for the fact that half of the power is scattered in each direction, it follows that up to 85% of the incident light is reflected into the backward half space. For this configuration, the reflectance and transmittance are thus limited to  $R \leq 0.85$  and  $T = 1 - R \geq 0.15$ , respectively.

An alternative way of calculating  $P_{\text{inc}}$  is to consider the energy flow in the focal plane (FP). Because the intensity has cylindrical symmetry about the optical axis, the electric and the magnetic energy densities are equal at the focal spot (Richards and Wolf, 1959) so that  $2cW_{\text{el}}(O) = S_z(O)$ . The calculation of  $A$  then becomes

$$A = \frac{\int_{\text{FP}} S_z d^2r}{S_z(O)} = \frac{\int_{\text{FP}} (|\mathcal{I}_0|^2 - |\mathcal{I}_2|^2) d^2r}{|\mathcal{I}_0(O)|^2}, \quad (3.32)$$

where  $\mathcal{I}_2$  is again a diffraction integral given in Eq. (A.10). The integration in the numerator turns out to be straightforward when an orthogonality relationship for Bessel functions is considered (Abramowitz and Stegun, 1972). We note that the fields in a strongly focused beam show vortices in the FP (Stamnes, 1986) so that  $S_z$  takes on positive and negative values as shown in Figure 3.2. Thus, in general,  $S_z$  cannot be substituted by  $2cW_{\text{el}}$ , which is a positive quantity. We remark in passing

that van Enk and Kimble (2000) predict a much lower value than 1.7 for a quantity equivalent to our parameter  $\mathcal{K}_{\text{sca}}$ . We believe one of the origins of this discrepancy is that they took the integrand in the definition of  $A$  to be  $2cW_{\text{el}}$ .

In order to derive an upper limit of  $\mathcal{K}_{\text{sca}}$  for the general class of transverse axially symmetric systems, we consider the field produced by the combination of an electric and a magnetic dipole which has been suggested for optimal focusing (Dhayalan and Stamnes, 1997; Sheppard and Larkin, 1994). To emulate such a field, one considers the emission field patterns at the GRS of virtual electric and magnetic dipoles orthogonal to each other and placed at  $O$  and then reverses the field propagation. Using Eq. (3.32) for the calculation of  $A$ , we obtain

$$\mathcal{K}_{\text{sca}} = \frac{1}{4}(7 - 3 \cos \alpha - 3 \cos^2 \alpha - \cos^3 \alpha). \quad (3.33)$$

At  $\alpha = \pi/2$ ,  $\mathcal{K}_{\text{sca}} = 7/4$  establishes the maximum value for transverse axially symmetric systems. This is only slightly larger than  $128/75$  obtained for the plane wave.

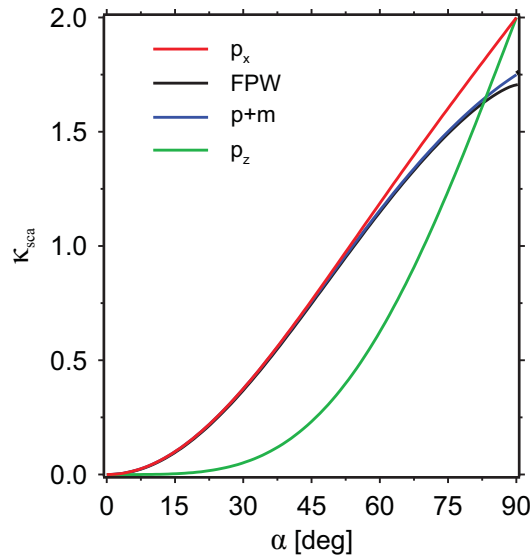


**Figure 3.15:** Scattering ratio  $\mathcal{K}_{\text{sca}}$  as a function of  $\alpha$  for several focused waves.  $p_z$  denotes the dipole wave with the electric dipole along the  $z$ -axis, FPW a focused plane wave,  $p+m$  stands for a combined electric and magnetic dipole wave, and  $p_x$  a wave that corresponds to an electric dipole oriented along the  $x$ -axis.

We next abandon the restriction of axial symmetry and search for an upper limit of  $\mathcal{K}_{\text{sca}}$  in general. Guided by a mode matching argument (Sondermann et al., 2007; van Enk and Kimble, 2000), we consider a directional dipolar incident wave. In this case the incident field stems from the emission pattern at the GRS of a virtual dipole parallel to the  $x$ -axis and placed at the origin (Stamnes and Dhayalan, 1996). Following Eq. (3.30), we obtain

$$\mathcal{K}_{\text{sca}} = \frac{1}{2}(4 - 3 \cos \alpha - \cos^3 \alpha). \quad (3.34)$$



At  $\alpha = \pi/2$ ,  $A$  reaches its minimum value of  $\sigma_0/2$  and  $\mathcal{K}_{\text{sca}}$  its ultimate maximum value of 2, respectively. This is consistent with the limit  $W(O)/P_{\text{inc}} \leq k^2/(3\pi c)$  given by Bassett for the sum  $W(O)$  of the time-averaged electric and magnetic energy densities at the focal spot, as discussed in Section 3.1.1.

As a last case study, we consider the interaction of an oscillating dipole oriented along the  $z$ -axis with a radially polarized dipolar incident field obtained from the radiation of a virtual dipole oriented along the  $z$ -axis and located at  $O$  (Sheppard and Larkin, 1994). In this case

$$\mathcal{K}_{\text{sca}} = (2 + \cos \alpha)(1 - \cos \alpha)^2. \quad (3.35)$$

Here, too, we find that  $\mathcal{K}_{\text{sca}}$  reaches the maximum value of 2 at  $\alpha = \pi/2$ .

Figure 3.15 displays  $\mathcal{K}_{\text{sca}}$  as a function of  $\alpha$  for various illuminations considered above. In all cases,  $\mathcal{K}_{\text{sca}} \geq 1$  is met for realistic numerical apertures. We are, thus, facing the paradoxical seeming situation that the power emitted by the oscillator may be larger than the incident power. However, this finding does not violate the law of power conservation because there is destructive interference in the forward direction. We now analyze this interference by determining the incident and scattered fields at the GRS for  $z > 0$ .

### The dipole wave content

A particularly insightful approach is to expand an arbitrary excitation field in terms of vectorial multipoles, as described in details in the Appendix A.2. All multipoles become zero at the origin except the electric dipole mode, which for a transverse system reads (Bohren and Huffman, 1983)

$$\mathbf{N}_{e,1,1} = \begin{cases} \frac{2}{3} & \mathbf{r} = 0 \\ (\cos \theta \cos \varphi \hat{\mathbf{e}}_\theta - \sin \varphi \hat{\mathbf{e}}_\varphi) \frac{e^{i(kr - \pi/2)}}{kr}, & kr \gg 1. \end{cases} \quad (3.36)$$

We note that the field for  $kr \gg 1$  is given only for the outgoing wave. The advancing phase shift of  $-\pi/2$  is interpreted as a Gouy phase accumulated when propagating from the focal spot  $O$  to the GRS for  $z > 0$  (Collett and Wolf, 1980; Wolf, 1980). According to Eq. (3.9), the electric dipole-wave component of the excitation field can be written as

$$\mathbf{E}_{\text{inc}}^{(d)}(\mathbf{r}) = A_1 \mathbf{N}_{e,1,1}(\mathbf{r}). \quad (3.37)$$

The field scattered by the oscillator also forms a dipole wave, whose expression derived from Eqs. (2.46) and (3.19) reads

$$\mathbf{E}_{\text{sca}}(r) = -\frac{i\Gamma}{2\Delta + \Gamma} A_1 \mathbf{N}_{e,1,1}(\mathbf{r}). \quad (3.38)$$

Therefore, at resonance the dipole-wave component of the excitation field is completely reflected just as in the reflection of a collimated beam from a perfect metal.

The total field assumes the general expression

$$\mathbf{E}_{\text{tot}} = \mathbf{E}_{\text{inc}} - \frac{i\Gamma}{2\Delta + \Gamma} A_1 \mathbf{N}_{e,1,1}. \quad (3.39)$$

In summary, there is a profound relationship between the optimal concentration of electromagnetic energy, the dipole-wave content of a focused beam and the strength of light-matter interaction.

### 3.4.2 Reflection and transmission

This approach allows for an easy calculation of the transmittance  $T$  as a function of the angles  $\alpha$  and  $\beta$ . In particular, for  $\beta = \pi/2$  one finds

$$T = 1 - R = 1 - \frac{1}{2} \frac{\sigma}{A'}, \quad (3.40)$$

where  $R$  is the reflectance. The factor  $1/2$  in the second equality accounts for the fact that an equal amount of scattering takes place in the forward and backward directions. For an oscillating dipole with non-radiative damping the transmission formula reads

$$T = 1 - \mathcal{K}_{\text{abs}} - \mathcal{K}_{\text{sca}}/2, \quad (3.41)$$

where  $\mathcal{K}_{\text{abs}}$  is the ratio between the absorbed and incident powers (Mojarad et al., 2009).

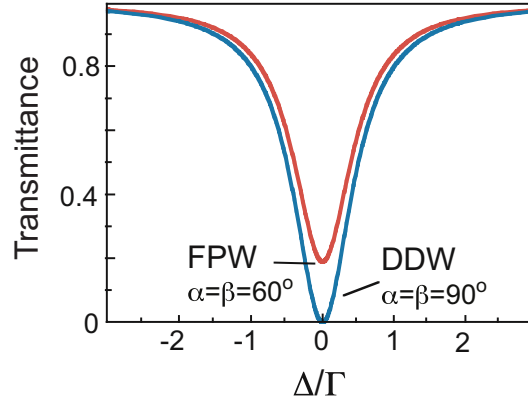


**Figure 3.16:** Transmittance as a function of laser detuning displayed for a focused plane wave (FPW) with  $\alpha = \beta = \pi/3$  and for a directional dipole wave ( $p_x$ ) with  $\alpha = \beta = \pi/2$ .

#### Focused plane wave

For the calculation of the transmittance in the general case of  $\beta \leq \pi/2$  we assume resonance and consider a solid angle  $\Omega_\beta$  forming a cone of semi-opening  $\beta$  in the

forward direction, as indicated in Figure 3.1b. Moreover, we consider a focused plane wave and give first the ratio of the power  $P_{\text{out}}$  of the outgoing incident wave collected in  $\Omega_\beta$  to the incident power

$$\frac{P_{\text{out}}(\beta)}{P_{\text{inc}}} = \begin{cases} \frac{\sin^2 \beta}{\sin^2 \alpha} & , \beta \leq \alpha \\ 1 & , \beta > \alpha . \end{cases} \quad (3.42)$$

For the ratio of the scattered to incident power we write

$$\frac{P_{\text{sca}}(\beta)}{P_{\text{inc}}} = \frac{3}{2 \sin^2 \alpha} [\mathcal{I}_0(\alpha)]^2 X(\beta) , \quad (3.43)$$

irrespective of whether  $\beta$  is larger or smaller than  $\alpha$ . Here  $\mathcal{I}_0(\alpha)$  denotes the diffraction integral of Eq. (A.8) at  $O$  and  $\alpha$  is the only argument retained in the following expressions.  $X(\beta)$  gives the ratio of power radiated into the solid angles  $\Omega_\beta$  and  $4\pi$

$$X(\beta) = \frac{\pi \int_0^\beta (1 + \cos^2 \theta) \sin \theta d\theta}{\pi \int_0^\pi (1 + \cos^2 \theta) \sin \theta d\theta} = \frac{1}{8} (4 - 3 \cos \beta - \cos \beta^3) . \quad (3.44)$$

The time-averaged interference is given by

$$P_{\text{int}}(\beta) = 2 \frac{c}{8\pi} \int_{\Omega_\beta} r^2 \text{Re} \{ \mathbf{E}_{\text{out}} \cdot \mathbf{E}_{\text{sca}}^* \} d\Omega , \quad kr \gg 1, \quad z > 0 . \quad (3.45)$$

Taking the incident electric field  $\mathbf{E}_{\text{out}}$  from Eq. (A.3) and the scattered field  $\mathbf{E}_{\text{sca}}$  from Eq. (3.38), the  $\beta$ -dependence of the interference turns out to be proportional to the scattering integral  $\mathcal{I}_0(\beta)$  (see Eq. (A.8) and replace  $\alpha$  by  $\beta$ ). This proportionality can also be seen from a reciprocity type of argument: only the dipole-wave component of the incident field gives rise to an electric field at the origin, the field strength being proportional to  $\mathcal{I}_0(O)$ . Reciprocally, the interference induced by the radiation of a dipole located at the focal spot is also expected to be proportional to  $\mathcal{I}_0(O)$ . We therefore write for the ratio of the interference power collected in the solid angles  $\Omega_\beta$  and  $\Omega_\alpha$

$$\frac{P_{\text{int}}(\beta)}{P_{\text{int}}(\alpha)} = \begin{cases} \frac{\mathcal{I}_0(\beta)}{\mathcal{I}_0(\alpha)} & , \beta \leq \alpha \\ 1 & , \beta > \alpha . \end{cases} \quad (3.46)$$

We further make use of the fact that the power radiated into a solid angle of  $4\pi$  has to be balanced by the total interference,  $P_{\text{sca}}(4\pi) + P_{\text{int}}(\alpha) = 0$ . With this condition and with Eqs. (3.42) - (3.46) we find for the transmittance in closed form

$$\begin{aligned} T(\alpha, \beta) &= \frac{P_{\text{out}}(\beta) + P_{\text{sca}}(\beta) + P_{\text{int}}(\beta)}{P_{\text{out}}(\beta)} \\ &= 1 + \frac{3\mathcal{I}_0(\alpha)}{2 \sin^2(\min\{\alpha, \beta\})} [\mathcal{I}_0(\alpha)X(\beta) - \mathcal{I}_0(\min\{\alpha, \beta\})] . \end{aligned}$$

This expression is used for the calculation of the transmission at resonance in Figure 3.17, while the shape of the dip is Lorentzian according to Eq. (2.45). For  $\beta \geq \alpha$  the preceding expression simplifies to

$$T(\alpha, \beta) = 1 - \frac{3[\mathcal{I}_0(\alpha)]^2}{2 \sin^2 \alpha} [1 - X(\beta)] , \quad (3.47)$$

where the rightmost term in rectangular brackets denotes, according to Eq. (3.44), the relative power radiated into the solid angle  $4\pi - \Omega_\beta$ , complementary to the collection solid angle  $\Omega_\beta$ . Correspondingly, the transmittance is given by the incident power reduced by the power scattered into the solid angle  $4\pi - \Omega_\beta$  for  $\beta \geq \alpha$  and the calculation of the interference is not required for this case.

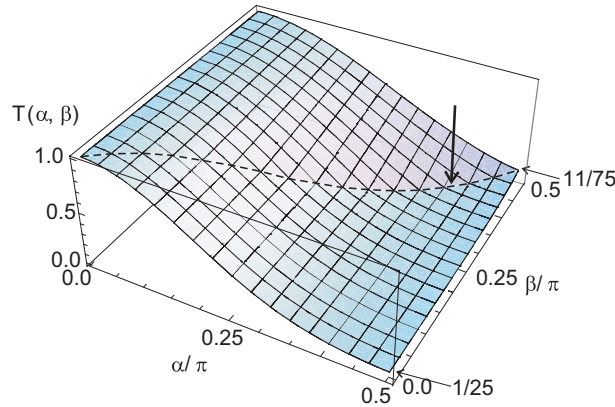


**Figure 3.17:** Transmittance for an incident FPW as a function of the angles  $\alpha$  and  $\beta$  as defined in Figure 3.1b. The dashed curve indicates the edge along the geometrical shadow boundary  $\alpha = \beta$ . The vertical arrow indicates the location  $\alpha = \beta \simeq 0.43\pi$  of the minimum, which is approximately equal to 10%.  $T$  values for the cases  $\alpha = \pi/2$ ,  $\beta \rightarrow 0$ , and  $\alpha = \beta = \pi/2$  are also marked.

The numerical data in Figure 3.17 display a rapid decrease of  $T$  with increasing  $\alpha$ , while the dependence on  $\beta$  is less pronounced. Of particular experimental relevance is the geometrical shadow boundary where  $\alpha = \beta$ ; i.e., all of the incident light is collected. Along this line, the transmittance experiences a minimum of  $T \simeq 0.1$  at  $\alpha \simeq 0.43\pi$ .  $T$  as a function of the detuning is presented in Figure 3.16 for  $\alpha = \beta = \pi/3$ . We point out that more complicated expressions are expected if the dipole is displaced from the focal spot. Particularly, the phase fronts of the scattered and excitation fields no longer match at the GRS (Celebrano et al., 2010).

### Directional dipole wave

Based on the same procedure as for a focused plane wave we have also determined the transmittance as a function of  $\alpha$  and  $\beta$  for a directional dipole wave  $p_x$ .

$$T(\alpha, \beta) = 1 - \frac{1}{16} (4 - 3 \cos \alpha - \cos^3 \alpha) \times \left( 4 + 3 \cos(\max\{\alpha, \beta\}) + \cos^3(\max\{\alpha, \beta\}) \right), \quad (3.48)$$

where the dipole is assumed to be on resonance. An example as a function of detuning is presented in Figure 3.16. Figure 3.18 displays a rapid decrease of  $T$  with increasing  $\alpha$  and an edge along the geometrical shadow boundary  $\alpha = \beta$ , as for the focused plane wave. As shown in Eq. (3.48),  $T$  is invariant with respect to  $\beta$  for  $\beta < \alpha$ , while for  $\beta > \alpha$ ,  $T$  increases with  $\beta$ . Contrary to the previous case of a focused plane wave,  $T$  decreases monotonously with increasing  $\alpha$  and reaches the value of zero at  $\alpha = \pi/2$ .<sup>3</sup>

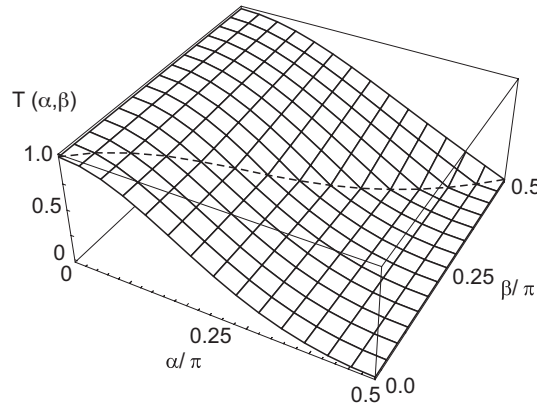


**Figure 3.18:** Transmittance for an incident  $p_x$  wave as a function of the angles  $\alpha$  and  $\beta$  as defined in Figure 3.1b. The dashed curve indicates the edge along the geometrical shadow boundary  $\alpha = \beta$ .

### Transmission and energy flow

In the previous sections we have analyzed the behavior of  $\mathcal{K}_{\text{sca}}$  as a function of  $\alpha$  for several types of focused beams, finding that a directional dipole wave yields  $\mathcal{K}_{\text{sca}} = 2$  for  $\alpha = 90^\circ$ . To gain more insight we consider the dependence of the Poynting vectors on the angle  $\theta$ . Figure 3.19 displays  $\mathbf{S}_{\text{inc}}$ ,  $\mathbf{S}_{\text{sca}}$  and  $\mathbf{S}_{\text{int}}$  for a  $p_x$  wave at  $\alpha = 90^\circ$ . The fact that in the forward direction  $\mathbf{S}_{\text{inc}}$  and  $\mathbf{S}_{\text{sca}}$  coincide explain

<sup>3</sup>We remark that perfect reflection does not imply perfect excitation of a TLS. The latter requires a full dipole wave and time reversal of the spontaneously emitted single-photon pulse (Stobińska et al., 2009). These differences with respect to our work can also be understood by considering the TLS as an optical resonator (Heugel et al., 2010).

why  $\mathcal{K}_{\text{sca}}$  must be equal to 2 since  $P_{\text{sca}}$  is symmetrically distributed with respect to the focal plane. Furthermore,  $\mathbf{S}_{\text{int}}$  is not zero only in the forward direction and it shares the same angular dependence of  $\mathbf{S}_{\text{inc}}$  and  $\mathbf{S}_{\text{sca}}$ . A more careful look at Figure 3.19 shows that  $\mathbf{S}_{\text{int}} = (\mathbf{S}_{\text{sca}} + \mathbf{S}_{\text{inc}})$ . Thus, in the forward direction the collected power is always zero irrespective of the collection angle  $\beta$ , which is also noticeable in Figure 3.18. The small differences between  $\mathbf{S}_{\text{inc}}$  and  $\mathbf{S}_{\text{sca}}$  must be attributed to the finite number of multipoles (typically 15) used in Eq. (A.40). For comparison we add in Figure 3.19 the Poynting vectors for a FPW.  $\mathbf{S}_{\text{sca}}$  has the same angular profile as for a  $p_x$  wave. The different amplitudes are due to a normalization proportional to  $P_{\text{inc}}$ , which is different for a FPW and a  $p_x$  wave. However,  $\mathbf{S}_{\text{inc}}$  and  $\mathbf{S}_{\text{sca}}$  do not overlap anymore and  $\mathbf{S}_{\text{int}}$  has a different behavior. Therefore,  $\mathcal{K}_{\text{sca}} < 2$  and the FPW is not perfectly reflected. In conclusion, a  $p_x$  wave maximizes  $\mathcal{K}_{\text{sca}}$  because it matches the radiation pattern of a dipolar scatterer.

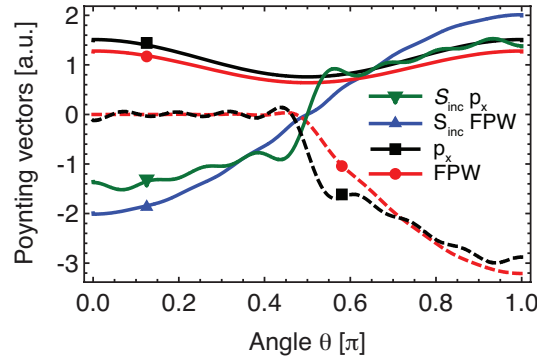


**Figure 3.19:** Poynting vectors  $\mathbf{S}_{\text{sca}}$ ,  $\mathbf{S}_{\text{inc}}$  (solid curves) and  $\mathbf{S}_{\text{int}}$  (dashed curves) as a function of the angle  $\theta$  for the case of a dipole under a FPW and a  $p_x$  wave for  $\alpha = 90^\circ$ . These quantities have been integrated over the azimuthal angle  $\varphi$ .

### 3.4.3 Phase-shift

The strong interaction demonstrated in the previous section may have important implications for a number of proposals in quantum information science. For instance, quantum logic operations could be implemented by exploiting the phase shift created by a quantum emitter on an incident light field (Savage et al., 1990; Turchette et al., 1995; van Loock et al., 2006). To this end previous experiments have measured phase shifts of up to  $30^\circ$  for atoms or quantum dots coupled to optical resonators (Fushman et al., 2008; Turchette et al., 1995).

With our formalism it is also easy to calculate the phase shift  $\phi$  imposed on the beam by a single oscillator at the focal spot. The phase shift  $\phi$  is defined by

$$\phi = \arg(\mathbf{E}_{\text{tot}} \cdot \mathbf{E}_{\text{inc}}^*), \quad (3.49)$$

where  $\mathbf{E}_{\text{inc}}$  is introduced as a reference field for the detection of the phase shift. Making use of Eq. (3.39) and assuming that a detector is positioned on the  $z$ -axis,

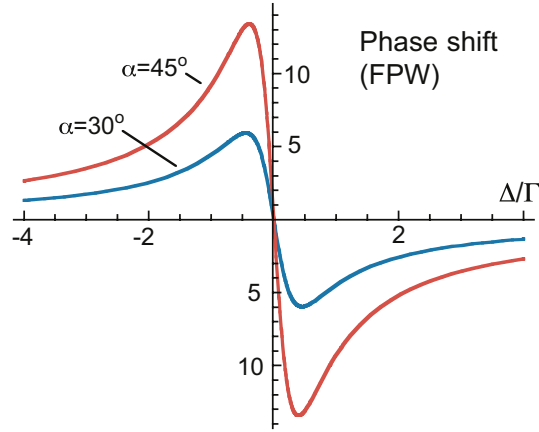


**Figure 3.20:** Phase shift  $\phi$  of Eq. (3.50) in units of degrees as a function of laser detuning. The results are plotted for a FPW and for two different semi-aperture angles  $\alpha$ , as indicated.

we find

$$\phi = \arg \left( 1 - i \frac{\Gamma}{2\Delta + i\Gamma} \frac{\mathcal{K}_{\text{sca}}}{2} \right). \quad (3.50)$$

An extra negative sign is introduced to account for the Gouy phase shift of  $\pi$  imposed on the incident field (Collett and Wolf, 1980; Wolf, 1980). Figure 3.20 shows a typical dispersive behavior. It amounts to  $5^\circ$ - $15^\circ$  at the extremal points for semi-aperture angles accessible in experiments and it approaches the value of  $90^\circ$  when  $\mathcal{K}_{\text{sca}}$  tends to 2. The extremal points are located at approximately  $\Delta/\Gamma=1/2$  and  $\phi$  decays only slowly with increasing detuning. We expect that integration over a collection solid angle would not change substantially the picture gained from Eq. (3.50) because of the coinciding phase fronts of the incident and scattered field (Aljunid et al., 2009).

Considering a quantized field, we are led to conclude that a few or even single photon pulses can be fully reflected or phase shifted by a single TLS if the coherence time of the photon is sufficiently long compared to the excited state lifetime (Domokos et al., 2002). The modal formalism developed in this section can be extended in the context of QED to analyze such phenomena and should be the subject of a future study.

# Chapter 4

## Shaping molecular fluorescence by optical antennas

In the previous chapter we investigated light-matter interaction in free space and showed that the coupling efficiency becomes very strong if light is focused onto a TLS by a high NA objective. We now move to situations where the interaction process exhibits cross sections that are much smaller than  $3\lambda^2/(2\pi)$ . Unfortunately it is not easy to make  $A$  accordingly smaller to keep the ratio  $\sigma/A$  large. This difficulty is related to the diffraction limit and to the fact that it is not trivial to find ways to miniaturize the wavelength of light at will. One may argue that a solution could be SNOM. However, a subwavelength electromagnetic spot does not necessarily imply a significant reduction of  $A$ . In fact, since  $A = P_{\text{inc}}/(2cW_{\text{el}})$ , what matters is the electric energy density obtained for a given amount of incident photons. Therefore both field confinement and throughput are important for achieving a large  $\mathcal{K}_{\text{sca}}$ .

Optical antennas are metal nanostructures that convert strongly localized energy into radiation and vice versa with a high throughput (Grober et al., 1997; Pohl, 2000). They could be exploited to enhance the cross section of a quantum emitter by improving its radiative properties, and to focus light below the diffraction limit. In this chapter we investigate these phenomena in detail. In particular, we analyze the conflict between strong field enhancement and quenching of molecular fluorescence (Ruppin, 1982). We derive design rules for optimizing the antenna performances, taking into account material properties as well as constraints imposed by nanofabrication. Next, assisted by computational nano-optics we propose geometries that lead to huge enhancements of the radiative decay rate without compromising the quantum yield of the emitter (Mohammadi et al., 2010, 2008b, 2009b; Rogobete et al., 2007). We find that these performances occur for molecule-antenna separations that are fully accessible using state-of-the-art experimental techniques. Moreover, these distances are such that microscopic effects (Ford and Weber, 1984; Leung, 1990; Persson, 1978) can be safely neglected and the design strategies are only based on electrodynamics considerations like for radio-wave antennas (Bal-



anis, 2005). Lastly, we investigate the possibility of channeling molecular fluorescence into a well defined optical mode by means of monolithic directional antennas that are fully compatible with scanning-probe technology (Chen et al., 2009, 2010a).

## 4.1 Enhancement and quenching of fluorescence

Before focusing on the antenna designs we review the basic phenomena that take place when a quantum emitter interacts with a metal nanostructure. Like in the previous chapter, we limit our analysis to the weak excitation limit, where the semi-classical theory of light-matter interaction is greatly simplified. Furthermore, we describe the emission process in the perturbative regime and compute the modification of decay rates.

### 4.1.1 Field enhancement and quantum efficiency

In the weak-excitation limit, the relevant quantities that need to be considered when a molecule is coupled to an optical antenna are the fluorescence signal, the field enhancement, the spontaneous emission rate, the quantum yield and the collection efficiency. These are discussed in the following subsections except for the last topic, which will be explained at a later stage, when the connection with radio-wave antenna theory is more evident.

#### Fluorescence signal

Under weak resonant excitation Eq. (2.39), which gives the power emitted by a TLS, can be approximated by the formula

$$S_o = \zeta_o \eta_o |\mathbf{E}_o \cdot \mathbf{d}|^2. \quad (4.1)$$

The parameter  $\zeta_o$  represents the collection efficiency,  $\mathbf{d}$  is the transition electric dipole moment, and  $\mathbf{E}_o$  is the electric field at the emitter position.  $\eta_o = \Gamma_r^o / \Gamma_t^o$  is the quantum yield and it corresponds to the ratio between the radiative and total decay rates.<sup>1</sup> The latter takes into account the fact that the excited state can lose energy also via non-radiative channels, i.e.  $\Gamma_t^o = \Gamma_r^o + \Gamma_{nr}^o$ . The label  $o$  indicates that these quantities refer to an isolated emitter.

#### Field enhancement

Away from saturation the fluorescence signal can be increased either by giving more power to the incident beam or by placing the molecule near a nanostructure that enhances the field locally (Metiu, 1984; Moskovits, 1985). The field enhancement is often accompanied by changes in polarization and phase, because

<sup>1</sup> $\Gamma_r^o$  and  $\Gamma_t^o$  respectively correspond to  $\Gamma_1$  and  $\Gamma_2$  used in the previous chapters.

the nanostructure imposes additional boundary conditions. Since the fluorescence signal depends only on the square of the field  $\mathbf{E}$ , we can ignore phase shifts and concentrate our attention on amplitude and polarization.<sup>2</sup> Because the excitation rate is proportional to  $|\mathbf{E} \cdot \mathbf{d}|$  (Allen and Eberly, 1975), polarization and amplitude play a similar role. We thus write that the fluorescence signal is enhanced by a factor  $K = |\mathbf{E} \cdot \mathbf{d}|^2 / |\mathbf{E} \cdot \mathbf{d}|^2$ . Later we show that the polarization of the local field is important for shaping the radiation pattern as well as for the modification of the decay rates.

### Spontaneous emission

It is well known that the spontaneous emission rate is not an intrinsic property of an atom or molecule, but it also depends on the local electromagnetic environment (Purcell, 1946). Indeed the spontaneous emission rate  $\Gamma_t$  of a molecule near a material structure is different than its free space value  $\Gamma_t^o$ . Depending on the particular configuration,  $\Gamma_t$  can be larger or smaller than  $\Gamma_t^o$ . Here we are primarily interested in situations where  $\Gamma_t \gg \Gamma_t^o$  and neglect the other case. Note that a larger emission rate permits a higher degree of light extraction as it postpones saturation to higher excitation power levels.

The modification of the radiative decay rate can be obtained by computing the power emitted by a classical dipole placed in proximity of the optical antenna. The correspondence between quantum and classical theory is valid if the normalized quantities are used (Chance et al., 1978; Wylie and Sipe, 1984; Xu et al., 2000), i.e.

$$\frac{\Gamma_r}{\Gamma_r^o} = \frac{P_r}{P_o}, \quad (4.2)$$

where  $\Gamma_r^o$  and  $P_o$  are respectively the fluorescence decay rate and the radiated power of a classical dipole in free space.  $P_r$  is instead the power radiated to the far field when the optical antenna is present.

Because part of the emitted power is absorbed by Ohmic losses, a full characterization of the system requires the calculation of both radiative and non-radiative decay rates (Chance et al., 1978). The latter can be obtained from  $\Gamma_t$  by subtracting  $\Gamma_r$ . The corresponding classical quantities are easily derived from the Poynting theorem (Jackson, 1999). The total decay rate  $\Gamma_t$  is expressed by

$$\frac{\Gamma_t}{\Gamma_r^o} = \frac{P_t}{P_o}, \quad (4.3)$$

where  $P_t$  is the total power dissipated by the dipole. Further details on the calculation of these quantities are provided in Appendix B.2.2.

<sup>2</sup>The phase shift is important in coherent spectroscopy, as discussed in Section 3.3

## Quantum efficiency

The enhancement of the radiative decay rate is expected to improve the quantum yield of a light emitter. Unfortunately optical antennas suffer from absorption losses due to real metals and the previous statement requires some attention. In the next sections we will discuss the consequences of that in more detail. Here we follow an approach borrowed from antenna theory (Balanis, 2005). The antenna efficiency  $\eta_a$  is defined as the ratio between the radiated power  $P_r$  and the total power  $P_t$  transferred from the load to the antenna. Based on the equivalence between the modification of transition rates in classical and quantum electrodynamics (Xu et al., 2000), we define an antenna efficiency also for the case of a *quantum* load, i.e. an atom or a molecule. This reads  $\eta_a = \Gamma_r / (\Gamma_t - \Gamma_{nr}^o)$  and the quantum yield  $\eta$  takes the expression

$$\eta = \frac{\eta_o}{(1 - \eta_o)\Gamma_r^o / \Gamma_r + \eta_o / \eta_a}. \quad (4.4)$$

We assume that the intrinsic non-radiative decay rate  $\Gamma_{nr}^o$  is not affected by the presence of electromagnetic boundaries.<sup>3</sup>

For  $\eta_o = 1$  the quantum yield  $\eta$  is solely determined by  $\eta_a$ , whereas when  $\eta_o \ll 1$  the enhancement of the radiative decay rate  $F = \Gamma_r / \Gamma_r^o$  becomes relevant. For  $F \gg 1$  it turns out that  $\eta = \eta_a$ . Hence the antenna efficiency is important as much as the modification of the spontaneous emission rate and plays a fundamental role in the enhancement and quenching of fluorescence.

### 4.1.2 Surface-enhanced fluorescence and quenching

Before discussing optical antennas in detail we review the case of a molecule near a flat metal surface. We do so not just for historical reasons, but because it represents an ideal system to gain insight on the modification of spontaneous emission and fluorescence quenching.

The pioneering experimental works date back to late '60s in which the fluorescence lifetime of an excited ion was measured near gold, silver and copper surfaces (Drexhage, 1974, 1966; Drexhage et al., 1966, 1968). The decrease in the lifetime when the distance becomes small, compared to the wavelength, was unclear until the analogy between these experiments and the problem of radio-wave propagation near the surface of the earth became apparent (Chance et al., 1974). In the classical viewpoint, the emitting molecule acts as an oscillating dipole (antenna) near a partially absorbing and partially reflecting surface (earth). Sommerfeld (1909) provided the first theoretical treatment of the radio problem and pointed out the possibility of a surface wave being present for the antenna close to the earth.

---

<sup>3</sup>We keep the emitter at a distance where the nanostructure does not affect its electronic structure and where the interaction can be fully described using macroscopic Maxwell's equations.

### Polarization effects

Even for a flat metal surface the analytical calculation of the modification of the decay rates is not a simple task, as it involves the near and far-field interaction of the emitter with the interface. Nevertheless, if the metal is approximated by a perfect mirror one obtains the exact analytical solution with the help of image theory (Jackson, 1999). The dipole moment is made of two closely-spaced opposite charges and each of them has an image charge of opposite sign located inside the perfect metal at the position  $-d$ , where  $d$  is the distance from the mirror as illustrated in Figure 4.1. The image charges build up a dipole that, if  $d$  is much smaller than the wavelength, radiates in phase or in opposite phase with respect to the other one. In the first case the emitted power is twice the free-space value, whereas in the second case it is zero. This result indicates that the modification of spontaneous emission depends on the orientation of the dipole moment with respect to the metal surface and that for enhancing fluorescence the dipole moment needs to be perpendicular to the metal surface.

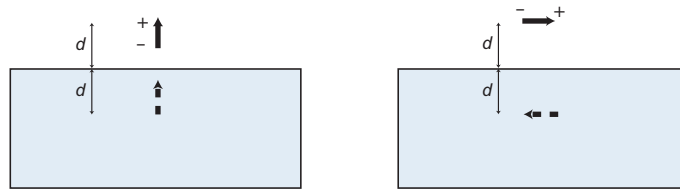


**Figure 4.1:** *Dipoles near a perfect mirror with orientation perpendicular and parallel to the interface. The dashed arrows represent the image dipoles.*

### Near-field energy transfer

Like Sommerfeld did for radio waves it has been shown that the *surface-plasmon polariton* (SPP) modes at a metal dielectric interface (Raether, 1988) are those that couple to the near field of the emitting molecule (Amos and Barnes, 1997; Morawitz and Philpott, 1974). The consequences can be seen in Figure 4.2, which shows that when the emitter is less than about  $\lambda/4$  from the surface a strong distance dependent quenching sets in.

The non-radiative decay processes involve the transfer of energy from the excited dipole to the substrate (Vaubel et al., 1971). For the small separation under consideration the dipole field can be treated in the electrostatic approximation. Again, we can make use of image theory for boundary value problems with dielectrics (Jackson, 1999) to find a simplified formula for the normalized non-radiative decay rate

$$\frac{\Gamma_{\text{nr}}}{\Gamma_{\text{r}}^0} = \frac{s\eta_0}{4d^3} \text{Im} \left\{ \frac{\epsilon_{\text{m}} - \epsilon_{\text{b}}}{\epsilon_{\text{m}} + \epsilon_{\text{b}}} \right\}, \quad (4.5)$$

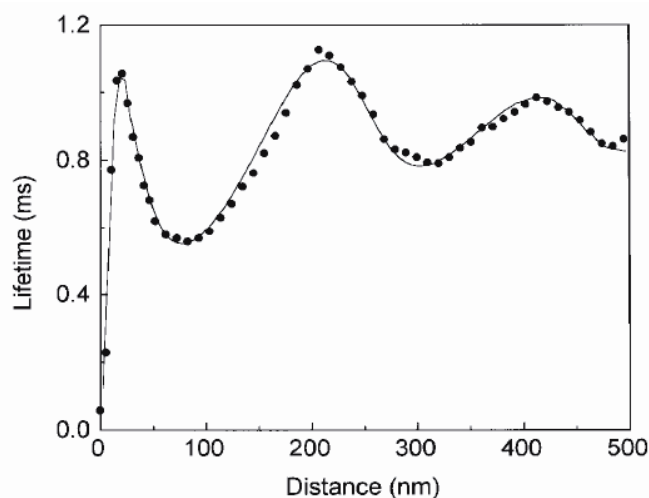


**Figure 4.2:** Lifetime of  $\text{Eu}^{3+}$  ions in front of a Ag mirror as a function of separation between the ions and the mirror. The solid curve is a theoretical fit (adapted from Amos and Barnes, 1997). The ions emit at a wavelength  $\lambda \simeq 614$  nm.

where the orientation parameter  $s$  is equal to  $3/2$  ( $3/4$ ) for the perpendicular (parallel) dipole configurations (Chance et al., 1978).  $\epsilon_b$  and  $\epsilon_m$  are the dielectric functions of the medium where the emitter is located and the metal, respectively. Note that the rate has an inverse cubic power dependence on the distance  $d$ , in agreement with simple dimensionality considerations. Equation (4.5) shows that, when the angular frequency  $\omega$  of the dipole transition is such that  $\epsilon_m(\omega)$  is close to  $-\epsilon_b$ , the non-radiative decay rate is strongly enhanced. This corresponds to the excitation of a SPP in the region where its dispersion relation is almost flat (Raether, 1988), i.e. where the density of photonic states is larger (Barnes, 1998)<sup>4</sup>. There are other mechanisms that contribute to energy absorption, like Ohmic losses and non-localities in the dielectric function (Ford and Weber, 1984; Leung, 1990). Moreover, if the molecule is very close to the surface (less than 3 nm) the dominant process may become the direct excitation of electron-hole pairs in the metal (Persson, 1978). All together these effects rapidly decrease the excited state lifetime with distance and quench the fluorescence signal.

The energy coupled into SPPs would not be lost if these modes were strongly radiative. For instance, a simple strategy to avoid quenching could rely on metallic gratings (Kitson et al., 1996; Knoll et al., 1981) or on rough metal surfaces (Raether, 1988). These configurations are particularly attractive for applications based on planar fabrication technology, such as light-emitting devices, fluorescence-based assays and solar cells (Feng et al., 2005; Lakowicz, 2005), but they are unable to yield enhancements larger than one order of magnitude. Moreover, their size must be large with respect to the wavelength of light. To overcome these limitations we

<sup>4</sup>In Chapter 5 we will discuss the relationship between the field enhancement and the local density of states.

take advantage of the unique optical properties of metal nanoparticles (Bohren and Huffman, 1983; van de Hulst, 1949a).

### 4.1.3 Metal nanoparticles as optical antennas

The beautiful colors of metal colloids have been used for centuries to make artistic glasses and pottery. When a plane wave illuminates a nanoparticle, the applied electric field drives the motion of the free electrons in the metal. Under appropriate conditions they oscillate in phase to build up collective modes that are similar to the SPP introduced in the previous section. For a spherical shape, they can be classified as dipole, quadrupole, and so on (Mie, 1908). The multipoles have different oscillator strengths with respect to the incoming light and also diverse radiative properties that vary with size, composition and surrounding. For the noble metals these modes lie in the visible spectral range and determine the color of nanoparticles via resonant scattering and absorption.

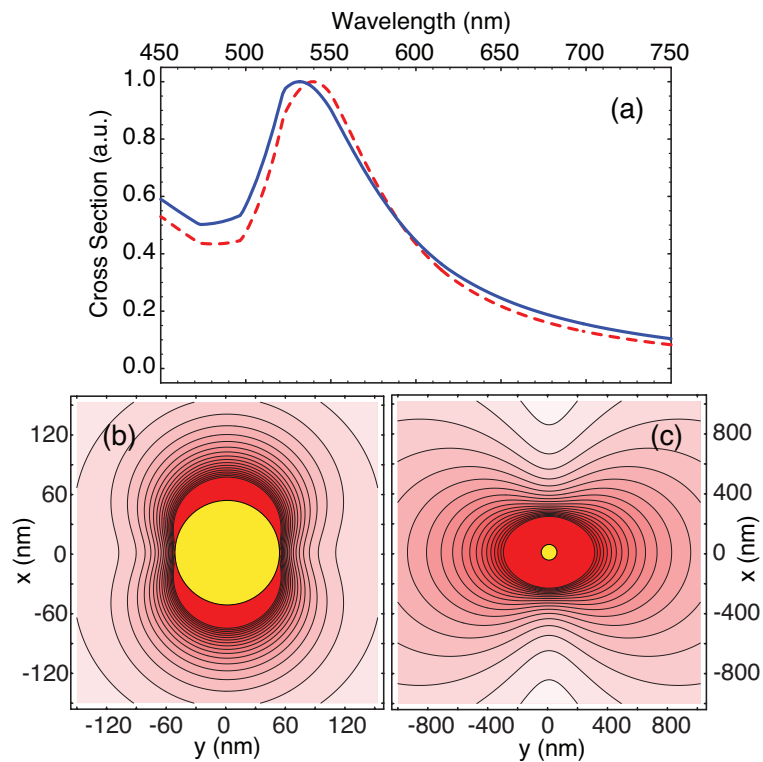


**Figure 4.3:** (a) Scattering spectrum of a 100 nm gold nanoparticle in air ( $\epsilon_b=1$ ) computed using Mie theory (blue line) and the effective polarizability of Eq. (4.7) (red dashed line). (b) and (c) represent the amplitude of the scattered electric field calculated using Mie theory (Bohren and Huffman, 1983). The illumination is a plane wave propagating along  $z$  and polarized along the  $x$  direction. The yellow disks depict the nanoparticle to scale.

The solid curve in Figure 4.3a shows the spectrum of a 100 nm gold nanoparticle

in air computed using Mie theory (Bohren and Huffman, 1983; Mie, 1908). The particle dimensions are such that only the dipole mode can be excited by a plane wave. Moreover, most of the incident light is scattered and the broad spectrum implies that radiative broadening is very strong. What makes metal nanoparticles particularly interesting for our purposes is also the intense and strongly confined near field. Figure 4.3b indicates that it can be very large near the metal surface and thus lead to stronger enhancements than SPPs at flat interfaces (Messinger et al., 1981).

### Polarizability models

The optical response of a metal nanosphere can be modeled with the dipolar polarizability

$$\alpha = \frac{\pi D^3}{2} \frac{\epsilon_m - \epsilon_b}{\epsilon_m + 2\epsilon_b}, \quad (4.6)$$

where  $D$  is the diameter,  $\epsilon_b$  and  $\epsilon_m$  are the dielectric functions of the background medium and of the nanoparticle, respectively (Bohren and Huffman, 1983). For  $\epsilon_m = -2\epsilon_b$  the polarizability exhibits a singularity that corresponds to the SPP resonance condition.

Gold nanospheres of diameter of 50 to about 100 nm are in the regime where the dynamical effects become important and the observed SPP resonance begins to deviate from that predicted by the simple formula in Eq (4.6). Nevertheless, it has been shown that the spectra of such particles can be reproduced very well if one takes into account radiation damping (Wokaun et al., 1982) and dynamic depolarization (Meier and Wokaun, 1983) to arrive at an effective dipolar polarizability given by

$$\alpha_{\text{eff}} = \alpha \frac{1 - \frac{\pi^2 \epsilon_b D^2}{10\lambda^2}}{1 - \alpha \frac{2\pi\epsilon_b}{D\lambda^2} - i\alpha \frac{4\pi^2 \epsilon_b^{3/2}}{3\lambda^3}}. \quad (4.7)$$

Figure 4.3a shows that the far-field scattering cross section calculated according to Mie theory (blue) agrees quite well with that evaluated by using  $\alpha_{\text{eff}}$  (dashed red). The contribution of higher multipoles is negligible in the far field, but it could amount to up to 10% of the dipolar one in the near field. This deviation becomes more important for larger particles or higher values of  $\epsilon_b$ .

These models have been extensively used in the '80s (Metiu, 1984; Moskovits, 1985), when it was difficult to perform an electrodynamic analysis of metal nanoparticles using computational methods. Larger metal nanoparticles can still be described by considering the response of the first electric multipole (Bohren and Huffman, 1983). The corresponding Mie coefficient  $a_1$  leads to a dipole polarizabil-

ity  $\alpha = i6\pi a_1/k^3$  that reads

$$\alpha = \frac{i6\pi}{k^3} \frac{m\psi'(ka)\psi(mka) - \psi'(mka)\psi(ka)}{m\chi'(ka)\psi(mka) - \psi'(mka)\chi(ka)} \quad (4.8)$$

where  $\psi(\rho) = -\cos\rho + (\sin\rho)/\rho$  and  $\chi(\rho) = -(i + \rho)\exp(i\rho)/\rho$  are Riccati-Bessel functions of the first and third kind, respectively (Abramowitz and Stegun, 1972). The prime indicates the first-order derivative,  $m$  is the ratio between the nanosphere and the surrounding medium refractive indices, and  $a$  is the radius. Equation (4.8) is more accurate than the electrostatic approximation, even when the latter includes radiative and dynamic depolarization corrections (Meier and Wokaun, 1983; Wokaun et al., 1982). Dipolar polarizabilities can give satisfactory results for what concerns the calculation of the field enhancement by isolated nanoparticles. On the other hand, when the driving field is highly inhomogeneous, higher order terms need to be taken into account (Aravind et al., 1981; Gersten and Nitzan, 1981).

### Decay rates and quenching

The modification of the spontaneous emission rate corresponds indeed to the situation where a dipolar radiating source is near a metal nanoparticle. The first electrodynamic analysis of this phenomenon is due to Ruppin (1982). He showed that the non-radiative decay rate dominates when the dipole approaches the metal surface. The reason for that must be found in the transfer of energy to higher order multipoles that are primarily damped by absorption. As the distance decreases, the source field becomes more and more inhomogeneous across the nanoparticle volume and the same happens for the induced current distribution, which determines the multipole response (Jackson, 1999).

Figure 4.4 illustrates the behavior of the decay rates as a function of distance and excitation wavelength (Rogobete et al., 2007). The dotted curve in the left panel shows the sphere scattering cross section calculated for plane wave illumination. The solid and dashed curves display the wavelength dependence of  $\Gamma_r$  and  $\Gamma_{nr}$  normalized to the unperturbed decay rate  $\Gamma_r^0$  for an emitter-sphere separation of 3 nm. Both  $\Gamma_r$  and  $\Gamma_{nr}$  are enhanced around the SPP resonance, but  $\Gamma_{nr}$  clearly dominates. The right panel of Figure 4.4 displays  $\Gamma_r$  and  $\Gamma_{nr}$  at the spectral maximum of  $\Gamma_r$  as a function of the emitter-sphere separation, showing the distance-dependent competition between them. This is indeed what has been pointed out in the literature for truncated tips (Thomas et al., 2004) and spherical particles (Carminati et al., 2006). In what follows, we show that this is not a general rule and that it is possible to design antenna architectures that strongly enhance  $\Gamma_r$  and at the same time maintain a large  $\eta$ .



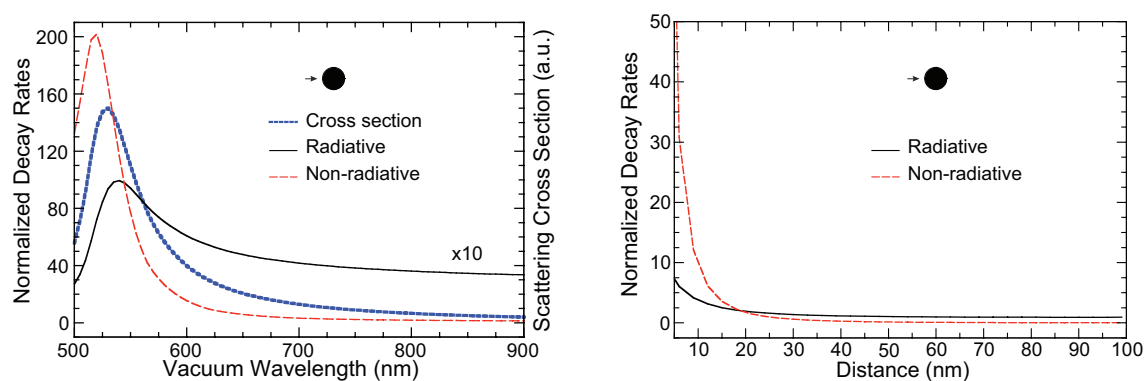


**Figure 4.4:** Normalized decay rates for an emitter coupled to a gold nanosphere with diameter 24.5 nm (2D model (after Rogobete et al., 2007)). (left panel) Wavelength dependence for a particle-emitter distance of 3 nm. The scattering cross section of the nanosphere is also plotted (dotted curves) to show its SPP resonance for comparison. (right panel) Distance dependence of the radiative (solid curves) and non-radiative (dashed curves) decay rates. The emission wavelength is tuned to  $\lambda = 535$  nm. The emitter is oriented as shown in the graph.

## 4.2 Optical antennas

Optical antennas share several concepts of radio-wave antennas, but they also have distinctive features, which are illustrated in Figure 4.5. First, the coupling between the antenna and its load is not via wired electric currents, but via displacement currents proportional to the near field vector  $\mathbf{E}$ , which makes the interaction strongly position and polarization dependent (Rogobete, 2007). Second, the load is typically a quantum system, like an atom or a molecule, and as such it is affected by QED phenomena associated with the modification of the local electromagnetic environment. Third, metals at optical frequencies are not perfect conductors and their optical properties are strongly affected by the existence of SPP resonances. These modes are tightly confined and can be controlled at the nanoscale by shaping metals using state-of-the-art nanofabrication (Barnes et al., 2003). Furthermore, they also depend on intrinsic material properties such as the optical constants and the electron mean free path (Kreibig, 2008). Fourth, in optics we often work with focused beams and guided waves. These should be considered as additional degrees of freedom for interfacing light with optical antennas (Mojarad and Agio, 2009; Mojarad et al., 2008). In summary, optical antennas represent a truly interdisciplinary effort that involves electrical engineering, physical chemistry, quantum optics, materials science as well as optics and photonics. In this respect, there are ongoing efforts to reconcile these differences with standard antenna theory (Alù and Engheta, 2008; Greffet et al., 2010; Novotny, 2007).

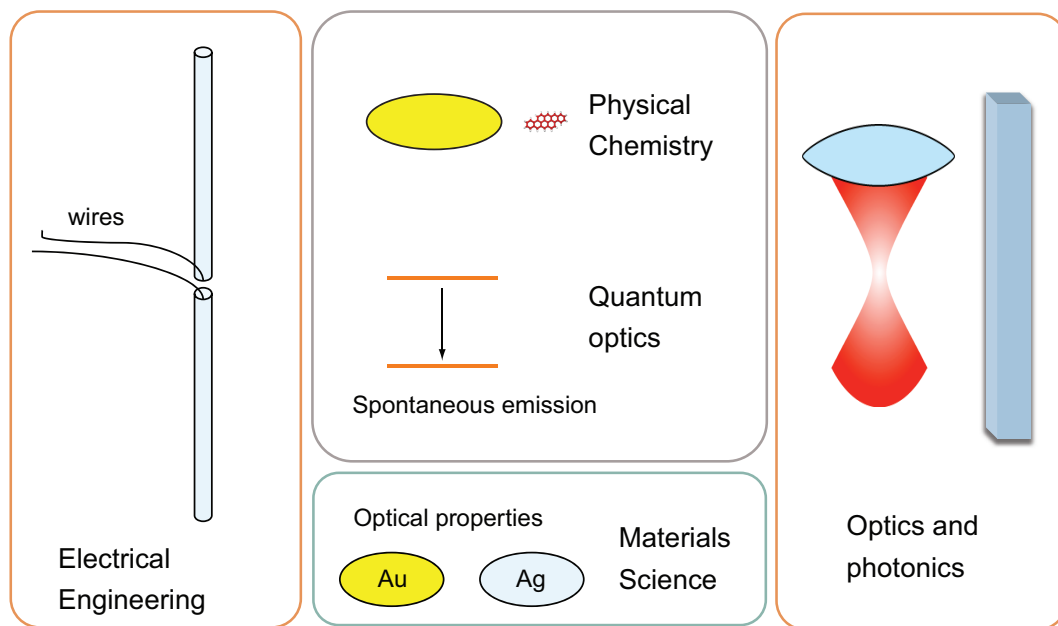


**Figure 4.5:** *Optical antennas: a truly interdisciplinary research field that involves diverse areas like electrical engineering, physical chemistry, quantum optics, materials science, as well as optics and photonics.*

### 4.2.1 Design rules

The differences between optical and radio-wave antennas have consequences on the design rules (Balanis, 2005). Here we summarize the most important features for the optical domain and give some general guidelines. In the next section we will instead focus on the modification of the spontaneous emission rate and investigate its dependence on the relevant antenna parameters.

#### Field enhancement

Engineering textbooks do not discuss the field enhancement because it is not an important design parameter for radio-wave antennas (Balanis, 2005). In optics the phenomenon has been thoroughly investigated in the context of surface-enhanced Raman spectroscopy. Pioneering works based on polarizability models indicated the SPP resonance and the lightning rod effect as the two most important electromagnetic enhancement mechanisms (Moskovits, 1985). The latter can be intuitively explained by considering the increase in the surface charge density  $\sigma$  with the curvature of a metal surface (Jackson, 1999). Since the near field is directly proportional to  $\sigma$ , nanoparticles with sharp edges tend to exhibit larger enhancements than nanospheres. Other strategies to improve the strength of the near field include the exploitation of nanoscale gaps between two nanoparticles (Aravind et al., 1981), the suppression of radiative broadening (Wokaun et al., 1982) and the choice of different metals (Cline et al., 1986; Zeman and Schatz, 1987). These basic de-

sign concepts have been applied in a more aggressive manner in the subsequent years, when computational methods for nano-optics became available (Girard and Dereux, 1996).

### Radiative decay rate

Following the analogy between classical and quantum electrodynamics (Xu et al., 2000), we take advantage of the reciprocity argument (Balanis, 2005) to state that a strong field enhancement is also associated with a strong modification of the radiative decay rate. Indeed, it can be shown that for an antenna that does not modify the radiation pattern of the emitter, these two quantities are exactly equal (Taminiau et al., 2008b). Therefore, one could simply refer to the design strategies discussed in the previous subsection to obtain a large modification of spontaneous emission.

### Antenna efficiency

In the past years much less attention has been dedicated to the antenna efficiency, a parameter that is instead very important to assess the performances of radio-wave antennas (Balanis, 2005). Once more we make the analogy between the modification of the radiative decay rate by a quantum emitter and that of radiation by a classical oscillating dipole to arrive at the efficiency

$$\eta_a = \frac{\Gamma_r}{\Gamma_t} = \frac{\Gamma_r}{\Gamma_r + \Gamma_{nr}}, \quad (4.9)$$

where we assume that the quantum emitter does not have an intrinsic non-radiative decay channel. For single-molecule spectroscopy and quantum optical applications it is very important that  $\eta_a$  be close to unity.

Equation (4.9) shows that  $\eta_a$  is large if  $\Gamma_r \gg \Gamma_{nr}$ . In the previous sections we have explained that  $\Gamma_{nr}$  is related to the non-radiative energy transfer to the metal. In particular, it is mainly associated with the excitation of higher-order SPP modes that are strongly damped by absorption. Therefore, the polarizability models based on the electric dipole approximation are not suitable for describing this process. That is why the design rules for the field enhancement are not sufficient for guiding the optimization of the antenna efficiency. Gersten and Nitzan (1981) used higher-order electrostatic polarizabilities to investigate this effect, but their model has been shown to yield efficiencies larger than one (Mertens et al., 2007; Mertens and Polman, 2009). Moreover, there is a contrast between the field enhancement and the antenna efficiency. For example, while radiative effects reduce the near-field strength (Wokaun et al., 1982), they tend to increase  $\eta_a$ . Obtaining a large modification of the spontaneous emission rate without compromising the quantum efficiency is thus not trivial.

A central idea in our work is to minimize the dissipation of energy into the antenna. Here we exploit the property that the SPP resonance of a gold nanorod

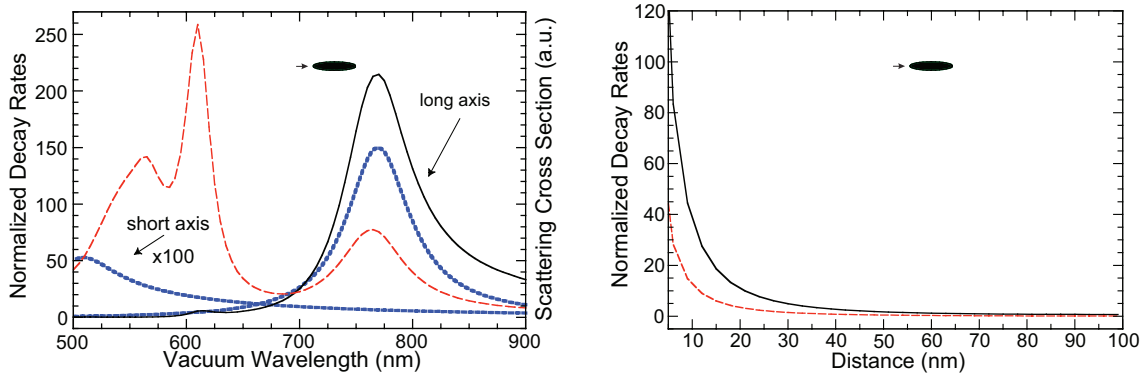


**Figure 4.6:** Normalized decay rates for an emitter coupled to a gold ellipse (long axis = 60 nm, short axis = 10 nm, corresponding to the same area of the nanosphere of Fig. 4.4) (2D model (after Rogobete et al., 2007)). (left panel) Wavelength dependence for a particle-emitter distance of 3 nm. The scattering cross section of the ellipse is also plotted (dotted curves) to show its SPP resonances for comparison. (right panel) Distance dependence for the radiative (solid curves) and non-radiative (dashed curves) decay rates. The emission wavelength is tuned to  $\lambda = 770$  nm. The emitter is oriented as shown in the graph.

can be sharper than that of a gold nanosphere of the same volume (Sönnichsen et al., 2002) because the resonance corresponding to the longer axis of the particle shifts to the near-infrared region, where the imaginary part of the dielectric function is smaller (Lide, 2006). Inspired by this phenomenon and by the fact that the enhancement of the excitation field is expected to be strong at the apex of an elongated particle, we have considered the emission of a dipole close to an elliptical particle. As shown in the left panel of Figure 4.6, we see that, although both  $\Gamma_r$  and  $\Gamma_{nr}$  experience a substantial enhancement,  $\Gamma_r$  overshadows the non-radiative losses at the SPP resonance of the long axis. The right panel of Figure 4.6 plots the distance dependence of  $\Gamma_r$  and  $\Gamma_{nr}$  at the long-axis SPP resonance, illustrating that in this case  $\Gamma_r$  dominates for all separations larger than 3 nm. We note that in this work we do not discuss the strong quenching observed at shorter wavelengths, which we attribute to the excitation of higher multipoles.

The key design principles for achieving a strong modification of the spontaneous emission rate with minimal suffering from non-radiative losses can be summarized as follows. First, tailor the geometry such that the SPP resonance of the antenna lies in a favorable spectral region for minimizing dissipation in the metal. Second, choose elongated objects to benefit from strong near fields at sharp corners. Third, choose antennas with dipolar resonances and adjust the emitter orientation such that its electric dipole moment is aligned with that of the antenna. Fourth, ensure that in the antenna higher order SPP modes are spectrally separated from the dipolar one. An exhaustive exploration of parameters such as the material, size, and shape of the antenna, as well as the transition wavelength of the emitter,

is provided in the following sections.

### Antenna bandwidth

The antenna bandwidth is one of the most crucial parameters for radio-wave antennas (Balanis, 2005). At optical frequencies the bandwidth is not a major concern, because the spectrum is typically quite broad, e.g. of the order of 20 to 50 nm. Nonetheless, a finite bandwidth is responsible for the modification of the emission spectrum (Kühn et al., 2008; Ringler et al., 2008). Moreover, there are applications where a broader response is desired. For instance, in Raman spectroscopy to enhance the signal across several Stokes-shifted lines or in photovoltaics to fully absorb the solar spectrum (Aubry et al., 2010).

### Radiation pattern and polarization

Radiation pattern and polarization are two other features that have received a great deal of attention in the radio frequency domain (Balanis, 2005), whereas the problem of directing molecular emission with metal nanoparticles did not find substantial consideration in field-enhanced spectroscopy (Metiu, 1984; Moskovits, 1985). In the past few years, much interest has been devoted to this topic in the context of optical antennas. The modification of the radiation pattern has been theoretically studied for various systems (Blanco and García de Abajo, 2004; Bonod et al., 2010; Chen et al., 2010a; Li et al., 2007; Novotny, 1996; Rogobete, 2007) and recently demonstrated in a number of experimental arrangements (Curto et al., 2010; Kühn, 2006; Kühn et al., 2008; Taminiau et al., 2008a).

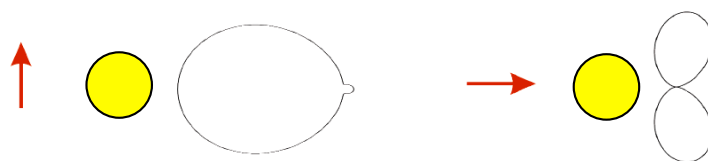


**Figure 4.7:** *Far-field emission pattern (solid curves) for a molecule coupled to a gold nanosphere for two different dipole orientations.*

We will discuss the phenomenon in more detail in Section 4.2.4. Here we provide a simple and intuitive explanation through the concept of energy transfer and polarization. For simplicity we consider two limiting cases. In the first situation the molecule is strongly coupled to the optical antenna. Its energy is efficiently transferred to the SPP modes and these radiate to the far field. Therefore, the emission pattern is completely determined by the antenna (Taminiau et al., 2008a). The other setting considers one or more nanoparticles polarized by a nearby molecule (Li et al., 2007). The arrangement is similar to a phased array, where the interference between dipolar radiators gives rise to a tailored emission pattern (Balanis, 2005).

Figure 4.7 illustrates this situation for the case of a gold nanosphere (Rogobete, 2007). Note that in this case the redistribution of radiation strongly depends on the orientation of the molecular dipole moment. The intermediate cases are more difficult to interpret and their analysis requires a numerical approach.

### Computational nano-optics

In the previous subsections we have introduced the main features of optical antennas and given design rules for directing and enhancing molecular emission. Progress in nanotechnology has enabled us to fabricate systems with controlled dimensions at the nanometer scale. An immediate concern is whether one could transfer the designs found in many electrical engineering textbooks into the optical domain. While simple systems like flat interfaces and spheres can be analytically solved (Chance et al., 1978; Ruppin, 1982), the investigation of more complex structures requires numerical solution of Maxwell's equations.

Computational electrodynamics plays a fundamental role as a tool to optimize the performances of conventional antennas. The development and application of numerical methods for the electrodynamic analysis of optical nanostructures dates back to the onset of near-field optical microscopy (Girard and Dereux, 1996) and it is still a subject of active research (Girard, 2005; Hafner et al., 2010). Among the existing approaches (Chari and Salon, 2000; Jin, 2002) we chose the three-dimensional (3D) Finite-Difference Time-Domain (FD-TD) method (Taflove and Hagness, 2005), which has been extensively tested and applied to the calculation of decay rates in dielectric environments (Hermann and Hess, 2002; Xu et al., 2000). Moreover, the following calculations are performed using the body-of-revolution (BOR) algorithm, which increases the accuracy while reducing the computational cost. Details on this approach can be found in Appendix B.1.5 as well as in Mohammadi et al. (2008b) and references therein. We choose emitter-antenna distances larger than 5 nm to ignore effects due to nonlocality in the optical constants of the metal interface (Ford and Weber, 1984; Leung, 1990), other microscopic effects (Persson, 1978), and convergence issues in the FD-TD method (Kaminski et al., 2007).

#### 4.2.2 Shape dependence

In Figure 4.6 we have shown that changing the shape of the optical antenna can have a huge impact on its performances. In this section we analyze this in more detail, with emphasis on the modification of the spontaneous emission rate and the antenna efficiency. In particular, we pay attention to systems and parameters that are within the reach of standard nanofabrication methods and of the common experimental techniques used in nano-optics.

### Adding a second nanoparticle

It is well known that the field enhancement produced by two metal nanoparticles is larger than for a single one (Aravind et al., 1981). Here we wish to investigate if the same trend occurs for the quantum efficiency. The decay rates of one emitter coupled to two gold nanospheres have already been studied in the literature (Blanco and García de Abajo, 2004), but without focusing on  $\eta_a$  and on situations accessible to experiments. Moreover, instead of placing the emitter right in the middle of the gap, a better comparison with the single nanoparticle case can be seen if the molecule is at a fixed distance from one of the two nano-objects, while the other one is approached from far away (Agio et al., 2007).

The inset of Figure 4.8 schematically shows how the coupling between emitter and nano-antenna is modified by changing the distance  $d$ . The molecule is oriented towards the nanoparticle and, for the case of two, one is fixed at a distance of 10 nm from the emitter. The gold nanoparticles have a radius of 50 nm and the background medium is air. The calculations are performed analytically for the single nanoparticle (Klimov et al., 1996; Ruppin, 1982), whereas the FD-TD method is employed for the case of two. The excitation wavelength chosen for computing the field enhancement is  $\lambda_{\text{ex}}=532$  nm, while the emission wavelength for the decay rates and the quantum efficiency is  $\lambda_{\text{em}}=580$  nm, which correspond to terrylene molecules in para-terphenyl (Kühn et al., 2006; Pfab et al., 2004).

Figure 4.8a shows the normalized total decay rate as a function of  $d$  and for  $\eta_o=1$ . For distances of the order of 100 nm, the total decay rate for the emitter coupled to two nanoparticles is almost equal to the one coupled to a single nanoparticle when the distance is 10 nm. Indeed, the curve corresponding to a single nanoparticle shows that the modification of the decay rate begins when  $d$  is smaller than 30 nm. When both nanoparticles are close to the emitter, the decay rate is clearly larger than for a single nanoparticle.

Figure 4.8b shows the antenna efficiency  $\eta_a$  for one and two nanoparticles. For one nanoparticle the quantum yield rapidly drops to zero when the distance becomes smaller than 20 nm (Kühn et al., 2006; Ruppin, 1982; Wokaun et al., 1983), whereas for two nanoparticles the quantum efficiency slightly increases up to  $d \simeq 15$  nm and then starts decreasing until quenching (not shown), but at shorter distances than for the previous case. When the second nanoparticle is far away  $\eta$  corresponds to the case of a single nanoparticle at 10 nm from the emitter. Figure 4.8c displays the excitation enhancement as a function of the nanoparticle distance. As expected, the near field is stronger when the two nanoparticles are close. The data from Figures 4.8b and c highlight the competition between intensity enhancement and antenna efficiency. It is evident that the balance between them is different for one and two nanoparticles. That is even more apparent in Figure 4.8d, where the fluorescence enhancement is plotted assuming that the emitter has  $\eta_o$  equal to one. While the enhancement achievable with a single nanoparticle

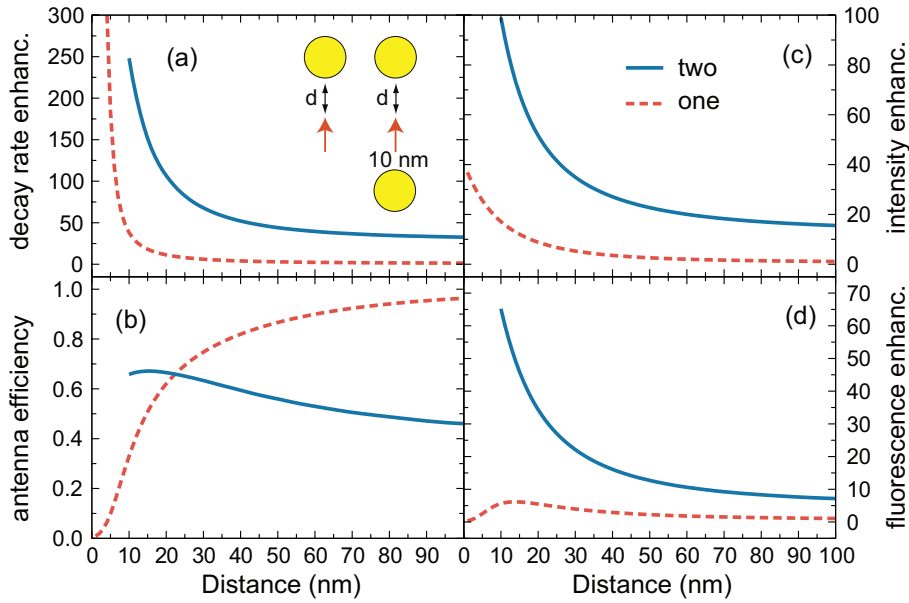


**Figure 4.8:** (a) Enhancement of the total decay rate  $\Gamma_t/\Gamma_t^0$ ; (b) antenna efficiency  $\eta_a$ ; (c) intensity enhancement  $|E/E_0|^2$ ; (d) fluorescence enhancement  $S/S_0$  for a single molecule coupled to one or two gold nanospheres. The inset describes the coupling scheme: molecule position and dipole orientation, nanosphere position, and distance  $d$  from the molecule. For the two-nanospheres case, the one at the bottom is kept at 10 nm from the molecule. Parameters: background medium air, nanosphere radius 50 nm, excitation wavelength  $\lambda_{\text{ex}} = 532$  nm, emission wavelength  $\lambda_{\text{em}} = 580$  nm.

is maximal at a distance of approximately 14 nm, with a nano-antenna made of two nanoparticles the enhancement is still increasing when the emitter is 10 nm from both nanoparticles. Therefore, in a well controlled experiment one should be able to see an order of magnitude improvement with respect to the single nanoparticle studied in previous works (Anger et al., 2006; Kühn et al., 2006). One has to keep in mind that the coupling of the two nanoparticles shifts the SPP resonance towards longer wavelengths (Aravind et al., 1981; Rechberger et al., 2003; Sundaramurthy et al., 2005). This dynamical detuning makes the overall enhancement more difficult to control.

### Changing the nanoparticle shape

We now explore the possibility of even further enhancing  $\Gamma_r$  by combining the design of the antenna shape with the addition of a second nanoparticle (Rogobete et al., 2007). The solid and dashed curves in Figure 4.9 with the upward-pointing triangles depict the wavelength dependence of  $\Gamma_r$  and  $\eta_a$  for an emitter placed in the middle of two identical ellipses with a gap of 6 nm. The curves with the diamonds replot the data of a single ellipse from Figure 4.6 for comparison. We find that  $\Gamma_r$  has been enhanced by about 1000 times. Furthermore, although more



metal surrounds the emitter, in the double-ellipse antenna  $\eta_a$  reaches the value of 0.9. Note that the SPP resonance of the new structure has shifted to longer wavelengths and has become broader because of the near-field coupling of the two ellipses (Aravind et al., 1981; Rechberger et al., 2003). We emphasize that this broadening stems from a larger polarizability and therefore a stronger scattering cross section; it should not be confused with a dissipative broadening.

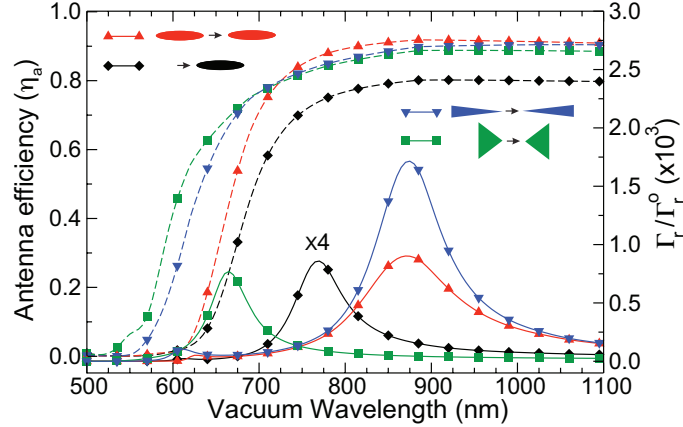


**Figure 4.9:** Normalized radiative decay rates (solid curves) and antenna efficiencies (dashed curves) for different gold nano-antennas (2D model (after Rogobete et al., 2007)). All structures have the same area ( $A = 491 \text{ nm}^2$  per particle) and a gap width of 6 nm. The emitter is placed at the center of the gap and oriented as shown in the graph.

Next, we compare the performance of the double-ellipse antenna with the bow-tie antenna, which has been studied recently (Schuck et al., 2005). To isolate the role of the antenna shape in its performance, we keep the overall structure area the same and maintain a constant separation between the emitter and its nearest metallic surface. As seen from the curves with squares in Figure 4.9,  $\Gamma_r$  and  $\eta_a$  are both less favorable than for the double-ellipse geometry at the respective SPP resonances. However, the situation changes when we elongate the triangles to have a tip radius of curvature of the order of 1 nm. The curves with the downward-pointing triangles reveal an enhancement of  $\Gamma_r$  in excess of 1700 while keeping  $\eta_a = 0.9$ . This substantial improvement is unfortunately not within reach of the current technology because of the difficulty in fabricating sharp corners and in avoiding problems such as tip snipping (Hao and Schatz, 2004). Moreover, very sharp corners also pose a serious challenge in theoretical studies<sup>5</sup>. As a result, in what follows we identify the double-ellipse structure as the ideal compromise for obtaining very large emission enhancement.

<sup>5</sup>Purely electromagnetic calculations are known to become inaccurate at very small distances due to local field effects so that we do not consider closer emitter-metal separations.

### Nanorods and nanospheroids

Here we present a more detailed study of nanospheroids (Calander and Willander, 2002; Gersten and Nitzan, 1981; Klimov et al., 2002; Liu et al., 2007) and compare them with gold nanorods (Aizpurua et al., 2005; Liu et al., 2007; Mühlischlegel et al., 2005; Sönnichsen et al., 2002). We focus on the wavelength range between 600 nm and 1100 nm, which covers the emission frequency of several molecules (Anger et al., 2006; Bakker et al., 2008; Kühn et al., 2006; Zhang et al., 2007) and nanocrystals (Biteen et al., 2005; Farahani et al., 2005; Schietinger et al., 2009). Because the enhancement is maximum when the emitter is placed at and oriented along the longitudinal symmetry axis of the nanoparticle, we consider only this situation and keep in mind that other configurations yield worse results. Furthermore, to treat a more realistic and experimentally feasible situation, we set the distance between emitter and nanoparticle to 10 nm, while the nanoparticle aspect ratio and volume change (see inset of Figure 4.10c). For the case of an optical antenna made of two nanoparticles, the gap between them is fixed to 20 nm. The antenna dimensions are chosen such that the SPP resonance is placed in the visible and near-infrared spectral range.

Figure 4.10a-c shows that the SPP resonance peak red shifts when the nanorod long axis  $a$  increases or the nanorod short axis  $b$  decreases. Therefore, by tuning the aspect ratio  $b/a$  one can easily place the SPP resonance at the desired spectral location (Aizpurua et al., 2005; Liu et al., 2007). The increase of the radiative decay rate is close to 3000 for wavelengths around 1100 nm. However, when the resonance shifts towards the visible spectrum, the enhancement drops very rapidly. Moreover, because the interaction between the two nanorods red shifts the SPP resonance, obtaining a strong enhancement at wavelengths below 750 nm is quite difficult.

Another important quantity that enters Eq. (4.4) is the antenna efficiency  $\eta_a$ . As shown in Figure 4.10a-c,  $\eta_a$  increases with the volume of the nanorod, i.e. as  $b$  becomes larger. Unfortunately, the largest enhancements correspond to the lowest efficiencies because a higher aspect ratio implies a reduced volume. Interestingly, for this system the antenna  $\eta_a$  is not smaller at the SPP resonance as predicted for a nanosphere (Thomas et al., 2004) and a SNOM tip (Carminati et al., 2006). Instead, by comparison of Figure 4.10a with Figure 4.10c one sees that  $\eta_a$  gets larger when the resonance moves towards shorter wavelengths. This happens despite the fact that material losses in the nanoparticle increase in going to higher frequencies (Lide, 2006), showing that the SPP resonance plays a fundamental role in keeping the antenna efficiency high.

The steep decrease of the enhancement upon reduction of the aspect ratio comes from the fact that the nanorods ends are flat. We thus replace the nanorods with nanospheroids. In comparing Figure 4.10a-c with Figure 4.10d-f we identify three important aspects. First, for high aspect ratios the nanospheroids exhibit smaller enhancements, while  $\eta_a$  remains almost the same. Second, for low aspect ratios

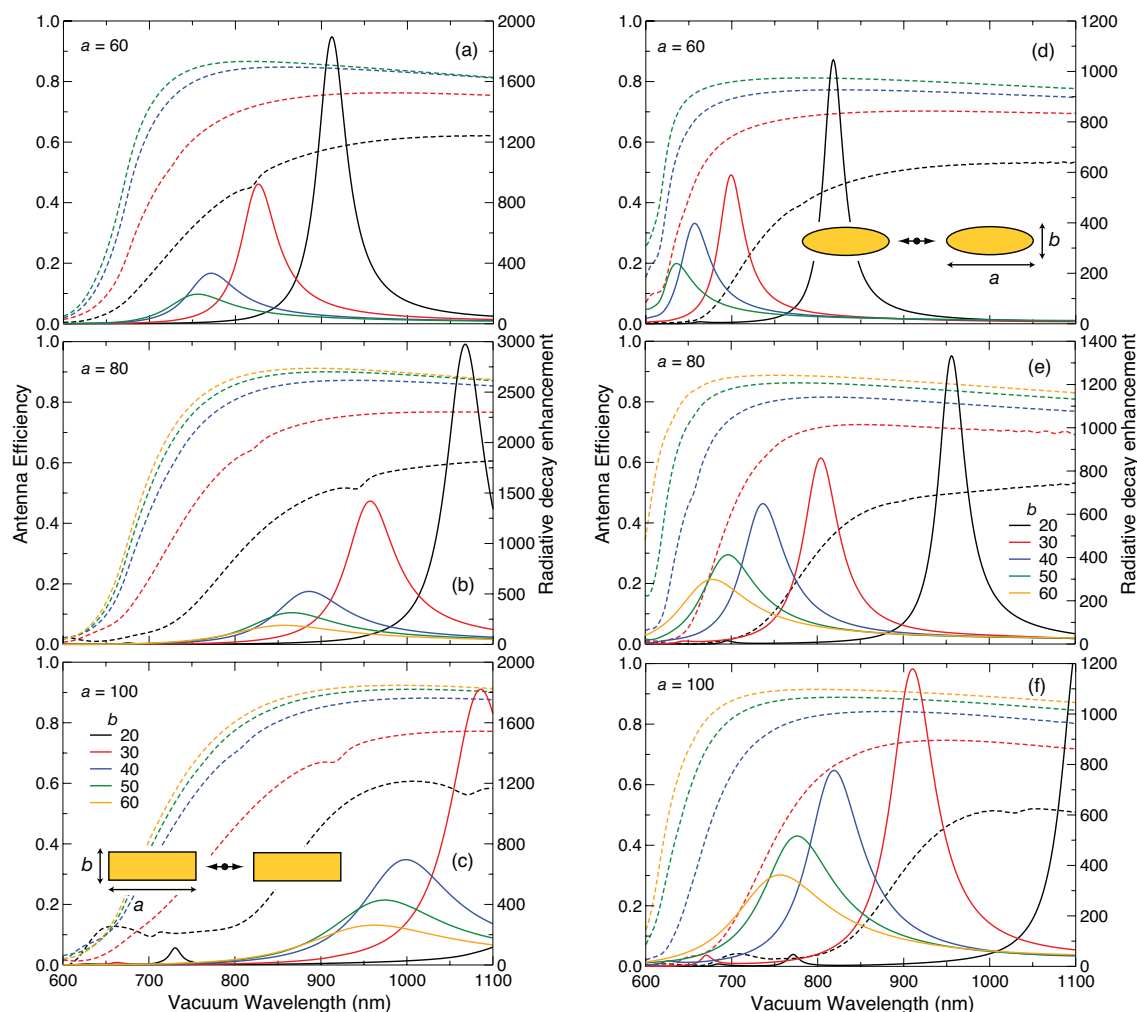


**Figure 4.10:** (a)-(f) Antenna efficiency  $\eta_a$  (dashed curves) and radiative decay enhancement (solid curves) for an emitter coupled to two gold nanorods for various aspect ratios and volumes. The insets in (c) and (d) show the position and orientation of the emitter with respect to the nanoparticles, whose dimensions  $a$  and  $b$  are given in nanometres. The emitter is centered at a fixed distance  $d = 10$  nm from both nanoparticles. The surrounding medium is glass (refractive index 1.5).

the enhancement decreases more slowly and the SPP resonance is less red-shifted. Consequently, finding a structure that has a strong enhancement at shorter wavelengths is easier. Third, the antenna efficiency reaches its plateau already at wavelengths close to 650 nm if the aspect ratio is less than 2. Compared to nanorods the enhancement is larger at shorter wavelengths because the reduced aspect ratio is partially compensated by a sharper rounding of the nanoparticle ends. For the parameters considered here nanospheroids exhibit larger enhancements near the visible range, whereas nanorods with high aspect ratios work better in the near infrared (Aizpurua et al., 2005).

In the spectral range between 600 and 1100 nm we have found that

nanospheroids exhibit a better performance than nanorods in term of radiative decay enhancement and antenna efficiency  $\eta_a$ . A more detailed comparison of the two antenna systems can be found in Mohammadi et al. (2008b). These results highlight the fact that experiments require a great control over the emitter position and particle shape, especially if large enhancements are desired.

### Nanocones

One of the issues that we identify is that the antenna efficiency  $\eta_a$  and the enhancement of spontaneous emission are maximal for different antenna parameters. In particular, for gold nanorods and nanospheroids increasing  $\eta_a$  involves a rapid decrease of the enhancement in the visible and near-infrared range. The question now is if one can improve the antenna design to increase the enhancement without decreasing  $\eta_a$  and loosing control on the spectral position of the resonance. A simple solution is to use a nanocone, where one end can be sharp to increase the field enhancement and the spontaneous emission rate, whereas the other end can be larger for increasing the volume, which favors a high antenna efficiency. The nanocone antenna is similar to the (bi-) conical antenna, which is the canonical example of a broadband antenna for applications in the VHF and UHF frequency bands. However, for practical reasons such as the antenna weight, it is often realized in the form of a bow-tie (Balanis, 2005). The latter design has received significant attention also in the optical domain (Crozier et al., 2003; Farahani et al., 2005; Schuck et al., 2005).

Finite and semi-infinite metal nanocones are not a new concept in optics, especially in scanning near-field optical microscopy (Betzig et al., 1991; Hartschuh et al., 2003a,b; Ichimura et al., 2004; Sánchez et al., 1999) For example, conical SNOM probes could be exploited to focus SPPs down to a spot size limited only by the tip curvature (Babadjanyan et al., 2000; Keilmann, 1999; Stockman, 2004; Vogel and Gramotnev, 2007). Moreover, the field enhancement for semi-infinite (Goncharenko et al., 2006b) and finite (Goncharenko et al., 2007, 2006a) silver nanocones has been studied as a function of the cone angle. In both situations, like for the bow-tie (Crozier et al., 2003), there exists an optimal angle that maximizes the enhancement. Moreover, it was pointed out that finite nanocones give rise to a stronger field than semi-infinite ones because of the SPP resonance effect (Krug II et al., 2002; Martin et al., 2001). Other groups investigated the modification of the fluorescence lifetime and the emission pattern by semi-infinite metal tips (Chang et al., 2006; Issa and Guckenberger, 2007a; Kramer et al., 2002), where coupling to SPPs leads to quenching. Previous investigations have also concluded that quenching dominates at the SPP resonance of a metal cone (Thomas et al., 2004).

Here we concentrate our attention on finite gold nanocones to demonstrate that they exhibit very interesting performances in terms of spontaneous emission enhancement and antenna efficiency at the SPP resonance wavelength. In particular,

we discuss the role of  $\eta_a$  in determining the optimal angle for enhancing fluorescence. We investigate single and double gold nanocones as a function of cone angle. Moreover, we explore the effect of adding a supporting substrate and of rounding the tip (Mohammadi et al., 2010).

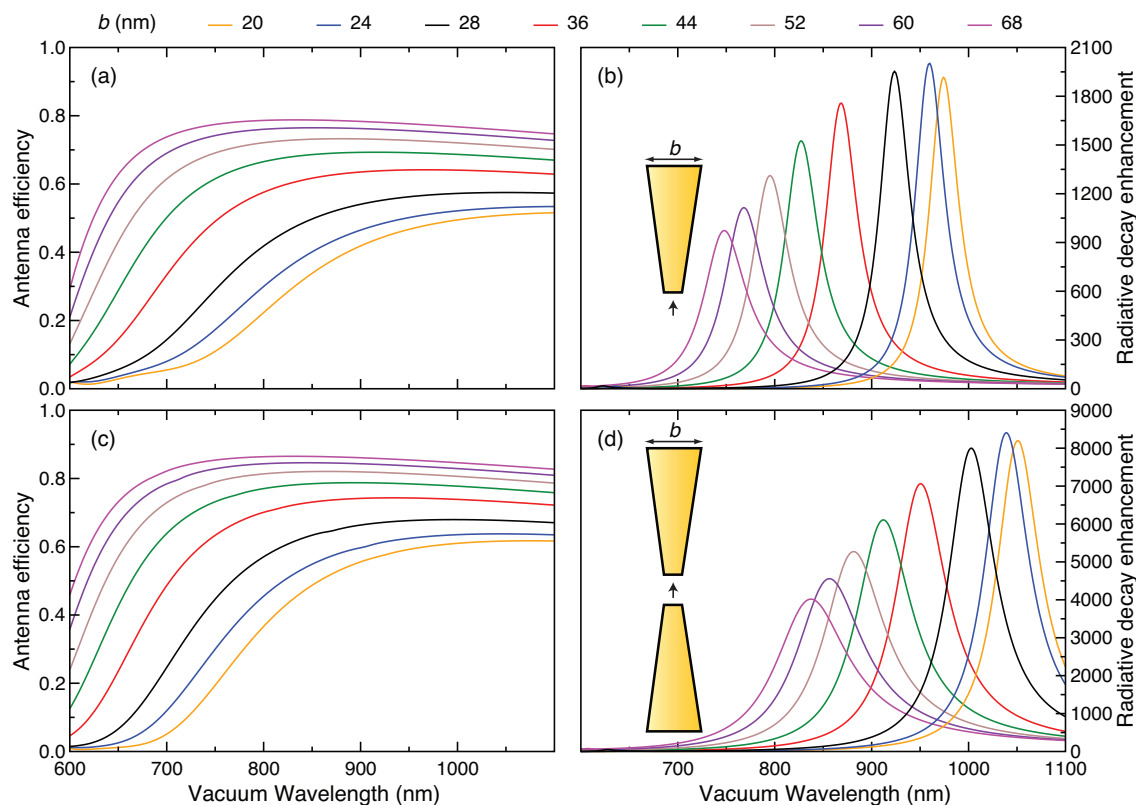


**Figure 4.11:** Single, (a) and (b), and double, (c) and (d), conical optical antenna in air (refractive index  $n_b=1.0$ ). Radiative decay enhancement, (b) and (d), and antenna efficiency  $\eta_a$ , (a) and (c), as a function of the base diameter  $b$ . The nanocone is 140 nm long and it has a fixed tip diameter of 20 nm. The optical antenna gap for the case of two nanocones is 20 nm.

Figure 4.11 displays the radiative decay enhancement and  $\eta_a$  for single and double nanocone antennas in air as a function of the nanocone base  $b$  and the wavelength. The nanocone height is 140 nm and the tip end is flat with a fixed diameter of 20 nm. The black curves correspond to the case of a nanorod (Mohammadi et al., 2008b). Starting from this structure, the enhancement increases slightly and then decreases, confirming that there exists an optimal value for  $b$  (Goncharenko et al., 2007, 2006a). This trend is also seen for an optical antenna made of two nanocones. However,  $\eta_a$  steadily grows with  $b$  because the volume of the optical antenna increases. That occurs because radiation is proportional to the volume squared, while absorption only to the volume (Bohren and Huffman, 1983). If both enhancement and  $\eta_a$  have to be optimized, one sees that  $b$  might be different than the optimal value found when only the enhancement is taken into account. An important ad-

vantage with respect to nanorods and nanospheroids is that here the resonance can be tuned towards the visible spectrum simply by changing the nanocone angle, without a significant loss of enhancement. Note that the enhancement factor is as high as 2000 for a single nanocone and 8000 for a double nanocone antenna. Such large values combined with a very good antenna efficiency and a wide spectral tunability of the SPP resonance make nanocones ideal systems for enhancing the radiative properties of solid-state quantum emitters.

An important aspect for the experimental realization of nano-antennas is the effect of a supporting substrate. The optical antenna is often grown on a dielectric substrate (Fleischer et al., 2009; Fredriksson et al., 2007; Kim et al., 2008; Stade et al., 2007) or is attached to the end of a fiber (De Angelis et al., 2008; Fleischer et al., 2008; Kühn et al., 2006; Zou et al., 2009). Previous works concluded that the presence of a substrate has a negligible effect on the field enhancement and on the spectral position of the SPP resonance for nanocones (Goncharenko et al., 2007, 2006a). In Figure 4.12 we show that adding a glass substrate can shift the resonance by more than 50 nm. Furthermore, the SPP resonance exhibits a stronger radiative broadening, which decreases the the field enhancement (Meier and Wokaun, 1983), but increases the antenna efficiency  $\eta_a$ . Note that the shift is smaller for the nanocone having the largest base diameter.

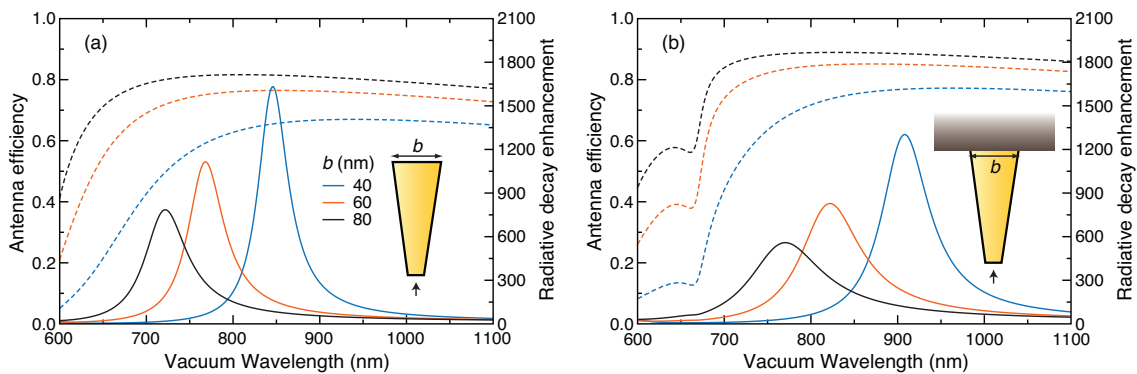


**Figure 4.12:** *Effect of a supporting substrate on nanocone optical antennas in air. Radiative decay enhancement (solid curves) and antenna efficiency  $\eta_a$  (dashed curves) without (a) and with (b) a glass substrate (refractive index  $n_b = 1.5$ ). The nanocone is 140 nm long, it has a base diameter of 40, 60 or 80 nm and a fixed tip diameter of 20 nm.*

The last important aspect that we would like to address is the effect of the tip termination. Previous studies on the field enhancement in triangular nanoparticles have shown that changing the tip termination can affect the results (Hao and Schatz, 2004; Kottmann et al., 2001). Here we compare the case of a flat tip, shown in Figure 4.13a, with the case of a rounded tip of the same diameter, shown in Figure 4.13b. We see that the resonance frequency and the antenna efficiency  $\eta_a$  are almost the same. The only noticeable difference occurs for the enhancement factor,

which is larger for the case of a flat tip. This holds also if the flat and rounded ends have a diameter of 10 nm in place of 20 nm. Nevertheless, the difference between the two situations is not huge. When the emitter is only 6 nm from the metal surface, the 20 nm rounded tip yields a stronger field enhancement in comparison to the flat one. These results stem essentially from the complex behavior of the electric field close to a metal tip (Novotny et al., 1995).

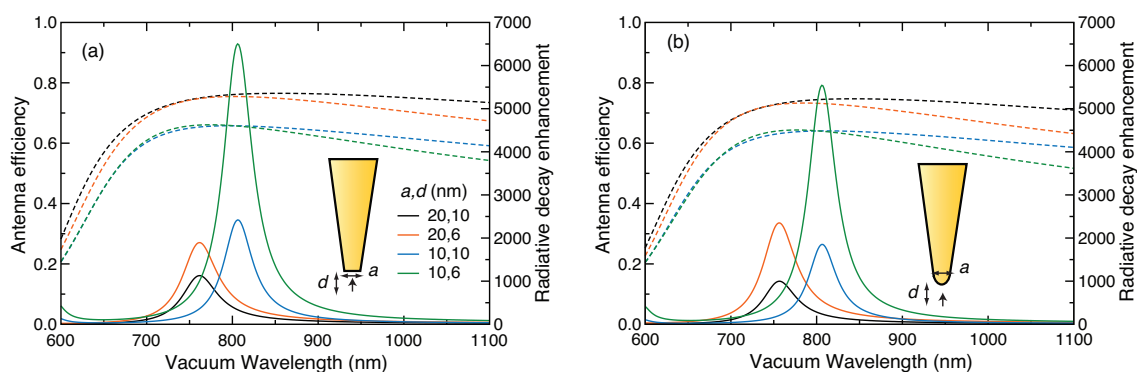


**Figure 4.13:** *Effect of the tip termination on nanocone optical antennas in air. Radiative decay enhancement (solid curves) and antenna efficiency  $\eta_a$  (dashed curves) for a flat (a) and rounded (b) tip. The nanocone is 140 nm long, it has a fixed base diameter of 60 nm and a tip diameter of 10 or 20 nm. The emitter is at a distance of 6 or 10 nm from the end of the tip.*

Another important practical aspect in favor of nanocones is the increased robustness and stability for the vertical orientation because the base is larger than for nanorods (De Angelis et al., 2008; Fleischer et al., 2008, 2009; Fredriksson et al., 2007; Kim et al., 2008; Stade et al., 2007; Zou et al., 2009). For the recent progress in the fabrication of single and double gold nanocone on substrates (Fleischer et al., 2009; Fredriksson et al., 2007; Kim et al., 2008; Stade et al., 2007), cantilevers (Zou et al., 2009), and on the facet of optical fibers (De Angelis et al., 2008; Fleischer et al., 2008), we anticipate an increasing attention on this kind of antenna system. The strong fluorescence and field enhancement as well as the electric field localization at the nanocone tip holds great promise for high-resolution fluorescence, Raman and other nonlinear nanoscopies (Hartschuh et al., 2003a,b; Ichimura et al., 2004; Sánchez et al., 1999).

### 4.2.3 Materials dependence

We have discussed examples where the antenna properties are tuned by changing its shape and size. While these degrees of freedom offer a wide range of performances, there are situations where other parameters need to be adjusted. For example, the efficiency of gold nano-antennas is significantly affected by the onset of strong material absorption in gold when the operating wavelength falls below



600 nm, as shown in Figure 4.10. Therefore molecules that emit in the blue spectral range cannot be strongly enhanced by a gold nano-antenna. Using a metal that exhibits lower losses in the wavelength range of interest could be a solution to this problem. However, since these are often accompanied by different optical constants, the parameters of the antenna need to be redesigned also in terms of shape and size in order to keep resonance wavelength, enhancement, efficiency and other relevant properties under control. There are other reasons for choosing different materials for the antenna. For instance, the surface chemistry could be more easily adapted to a specific application.

While gold and silver have been the materials of choice for nano-antennas, other metals may also exhibit interesting opportunities for applications, especially if technological issues are involved. For instance, recent works have been focusing on the spectroscopy of copper (Tilaki et al., 2007), aluminum (Chan et al., 2008; Chowdhury et al., 2009; Ekinici et al., 2008; Langhammer et al., 2008; Mohammadi et al., 2009b) and palladium (Pakizeh et al., 2009) nanoparticles. While theoretical studies have been carried out for the field enhancement in surface-enhanced Raman scattering (Cline et al., 1986; Moskovits, 1985; Zeman and Schatz, 1987), here we focus on the modification of the spontaneous emission rate and on the antenna efficiency.

We use spheroidal nanoparticles as a model system because they have been extensively studied for field-enhanced spectroscopy (Cline et al., 1986; Zeman and Schatz, 1987) and for fluorescence enhancement (Agio et al., 2007; Gersten and Nitzan, 1981; Mertens et al., 2007; Mertens and Polman, 2009; Mohammadi et al., 2008b; Rogobete et al., 2007). We discuss nano-antenna designs that cover the spectral range from the ultraviolet to the near-infrared. Even if the SPP resonance can be easily tuned by changing the spheroid aspect ratio, one has to consider that the decay rates might not be enhanced as much as desired. Therefore, both geometric effects and material properties have to be taken into account.

### Gold and copper

Figure 4.14a and b show the real and imaginary parts of the dielectric functions of gold and copper in the visible and near infrared spectral range. The real part for the two materials is quite similar, whereas the imaginary part for copper is slightly larger than for gold if the experimental data are taken from Johnson and Christy (1972). On the other hand, if for gold we consider the experimental values from Lide (2006), the imaginary part becomes even smaller than for copper. We choose the optical constants from Lide (2006) for gold and from Johnson and Christy (1972) for copper.

Figure 4.15a clarifies how the enhancement of the radiative decay rate and the antenna efficiency  $\eta_a$  depend on the background index for an emitter coupled to a gold spheroid with semi-axes  $a = 70$  nm and  $b = 25$  nm. Even a small change in the refractive index shifts the SPP resonance by more than hundred nanometers. At the



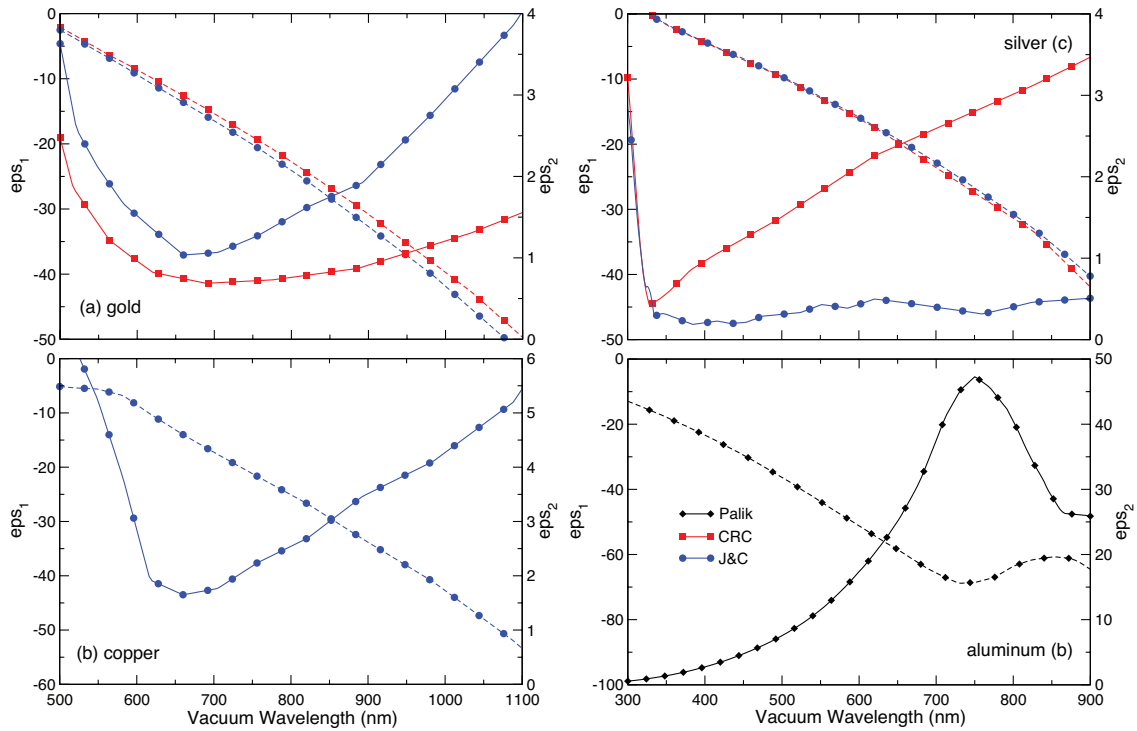


**Figure 4.14:** Real (dashed curves) and imaginary parts (solid curves) of the dielectric functions of (a) gold, (b) copper, (c) silver, and (d) aluminum. The experimental data are compiled from Lide (2006) (CRC), Johnson and Christy (1972) (J&C), and Palik and Ghosh (1998) (Palik). Details on the fitting parameters used in the FD-TD simulations can be found in (Mohammadi et al., 2009a,b)

same time, the resonance gets wider because radiative broadening increases with the refractive index (Wokaun et al., 1982). That also explains the small decrease in the enhancement. As a consequence of material losses,  $\eta_a$  drops to zero below 600 nm. However, the shift of the SPP resonance towards shorter wavelengths improves  $\eta_a$ . For instance, it is larger than 70% around 650 nm if the nano-antenna is embedded in air (refractive index  $n_b = 1$ ).

We now move our attention to copper spheroids. Figure 4.16a shows the radiative decay enhancement and the antenna efficiency  $\eta_a$  for an emitter coupled to a single spheroid in glass (refractive index  $n_b = 1.5$ ), for  $a = 60$  nm and variable  $b$ . Compared to gold antennas the enhancement is smaller and the resonances are broader as expected by the fact that the imaginary part of copper is larger. The antenna efficiency is lower, but it shows the same trend as for gold antennas. Namely, if the SPP resonance shifts to shorter wavelengths the efficiency increases. For an aspect ratio equal to 2, with  $a = 60$  nm and  $b = 30$  nm, the enhancement is about 75 and the quantum efficiency is close to 70%. If we consider a nano-antenna made of two copper spheroids, we can improve both enhancement and  $\eta_a$ , but we also red shift the resonance wavelength, as shown in Figure 4.16b. Note that the antenna efficiency is now more sensitive to the nanoparticle geometry than in the case of

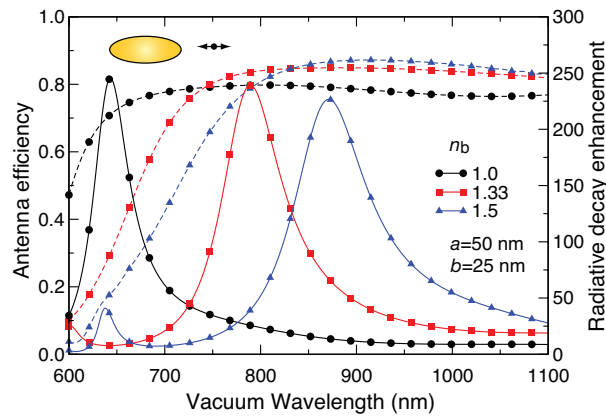


**Figure 4.15:** Radiative decay enhancement (solid curves) and antenna efficiency (dashed curves) for an emitter coupled to a gold spheroid for  $d=10$  nm (see inset). Dependence on the background index  $n_b$  for  $a=50$  nm and  $b=25$  nm.

gold, while the opposite holds for the enhancement. These differences stem from the imaginary part of the dielectric function, which is larger for copper.

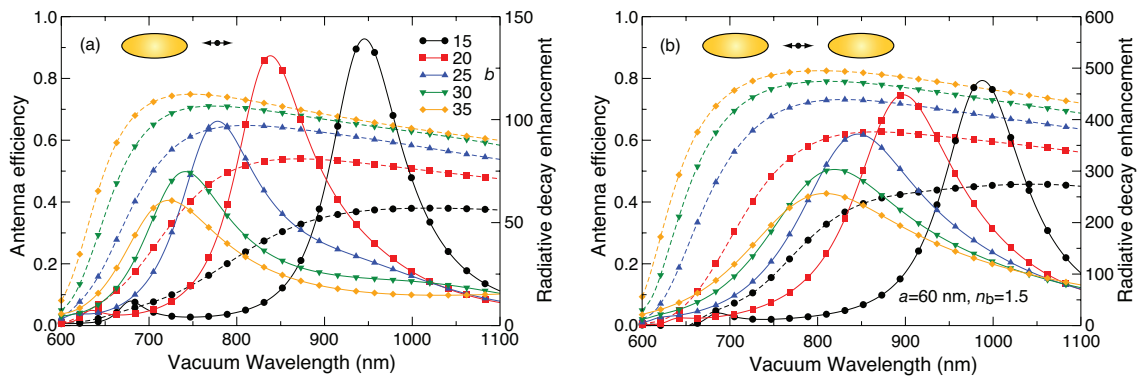


**Figure 4.16:** Radiative decay enhancement (solid curves) and antenna efficiency (dashed curves) for an emitter coupled to a nano-antenna made of (a) one or (b) two copper spheroids in glass (refractive index  $n_b = 1.5$ ). Dependence on the aspect ratio for  $a=60$  nm for  $d=10$  nm (see insets).

### Silver and aluminum

We now consider nano-antennas made of silver or aluminum. As before, we start looking at the real and imaginary parts of the dielectric function, presented in Figure 4.14c. Silver appears to be similar to gold if the experimental data are taken from Lide (2006) and from Johnson and Christy (1972), respectively. The main difference is that silver has a higher plasma frequency so that the curves are shifted towards shorter wavelengths. Therefore, we expect that silver yields results similar to gold, but in a spectral range closer to the ultraviolet. However, if for silver we consider the experimental data of Johnson and Christy (1972), the imaginary part

drops to much lower values. In this case, silver nano-antennas should perform much better than their gold counterparts. Because nanostructured silver exhibits a lower optical quality than the bulk, we choose the experimental dielectric function with the largest imaginary part (Lide, 2006).

Figure 4.14d displays the optical constants of aluminum as given in Palik and Ghosh (1998). Aluminum has a plasma frequency even higher than silver. Even if the imaginary part is significantly larger than in the noble metals, in the region below 600 nm the large and negative real part ensures that the skin depth is sufficiently small to prevent significant Ohmic losses.<sup>6</sup> On the other hand, there is an interband absorption peak located at 800 nm, which creates a dispersive profile in the real part of the dielectric function and, most importantly, a strong increase in the imaginary part. This makes aluminum less attractive for nano-antenna applications in the spectral range around 800 nm.

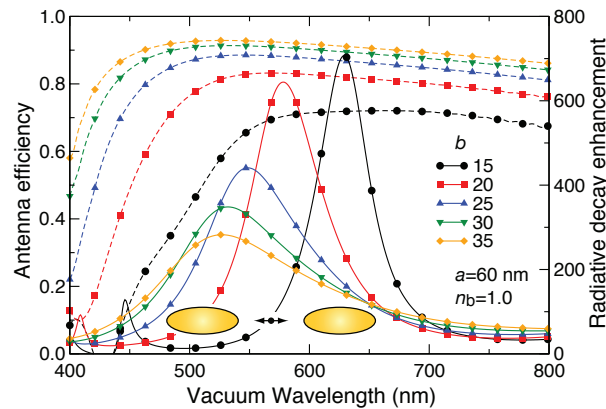


**Figure 4.17:** Radiative decay enhancement (solid curves) and antenna efficiency (dashed curves) for an emitter coupled to a nano-antenna made of two silver spheroids in air (refractive index  $n_b=1.0$ ). Dependence on the aspect ratio for  $a=60$  nm for  $d=10$  nm (see inset).

Figure 4.17 shows the antenna efficiency  $\eta_a$  and the radiative decay enhancement for an emitter coupled to a nano-antenna made of two silver spheroids in air. The general trend agrees with what we have previously discussed for gold and for copper nano-antennas. Because the plasma frequency of silver is higher than that of gold and copper, the resonances are shifted by about 200 nm towards shorter wavelengths. Furthermore,  $\eta_a$  and the enhancement factor are higher. Using the optical constants of Johnson and Christy (1972) would have yielded even better results.

The antenna efficiency  $\eta_a$  and the radiative decay enhancement for an emitter coupled to a nano-antenna made of two aluminum spheroids in air is provided

<sup>6</sup>In chapter 5 we will show that absorption losses depend on the ratio  $\gamma/\omega_p$  for a Drude metal, where  $\omega_p$  and  $\gamma$  are the plasma and damping frequencies, respectively (Ashcroft and Mermin, 1976).

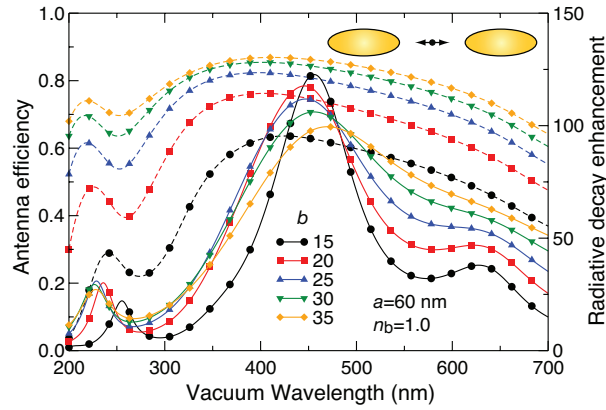


**Figure 4.18:** Radiative decay enhancement (solid curves) and antenna efficiency (dashed curves) for an emitter coupled to a nano-antenna made of two aluminum spheroids in air (refractive index  $n_b=1.0$ ). Dependence on the aspect ratio for  $a=60$  nm for  $d=10$  nm (see inset).

in Figure 4.18. While  $\eta_a$  decreases when the aspect ratio increases, the SPP resonance is not red shifted. The reason for that can be found in the electromagnetic interaction between the two spheroids. For a single aluminum spheroid, the SPP resonance exhibits a small red-shift in agreement with the polarizability theory (Meier and Wokaun, 1983; Zeman and Schatz, 1987). For the case of two aluminum spheroids separated by a gap  $2d = 20$  nm, the interaction between the two SPP modes is weaker for small aspect ratios than for larger ones because sharper particles have larger but more rapidly decaying near fields at their tips. This also explains why the enhancement does not drop much when the aspect ratio decreases: the two spheroids act together more effectively to increase the near field. The enhancements given by the aluminum nano-antennas of Figure 4.18 are not as large as found for the same system made from other materials. Since  $\eta_a$  is large the reason for that should be attributed to radiative broadening rather than to losses (Wokaun et al., 1982). For instance, since the radiative broadening is proportional to  $1/\lambda^3$ , the effect is 8 times stronger at 400 nm than at 800 nm. Indeed optimizations of the field enhancement have shown that the SPP resonance should be located around 200-300 nm and the semi-major axis of the spheroid should not be larger than 40 nm (Zeman and Schatz, 1987). Aluminum nano-antennas are thus more suitable for applications in the ultraviolet spectral region (Chowdhury et al., 2009; Ray et al., 2007).

In summary, we have investigated the performances of nano-antennas for improving light emitters by considering different materials, namely gold, copper, silver and aluminum, aspect ratios and background media. While gold and copper can both operate in the near infrared spectral range, silver is more suitable for the visible and aluminum for the ultraviolet range. Moreover, nano-antennas cannot be simply scaled to operate at different wavelengths and the material properties play

an important role in determining their performances. The choice of the experimentally determined optical constants from the literature is also a point of concern. In particular, these data have been obtained for bulk samples, while nano-antennas are truly nanoscale objects. Even if the volume of a nano-antenna is sufficiently large to ignore quantum-size effects (Bohren and Huffman, 1983) the fabrication methods might influence the actual optical properties.

### Enhancing the quantum yield of emitters

From the application point of view, a stronger enhancement of  $\Gamma_r$  compared with  $\Gamma_{nr}$  allows improvement of the quantum efficiency of poor emitters (Lakowicz, 2005) such as silicon nano-crystals (Biteen et al., 2005), nanotubes (O'Connell et al., 2002) or diamond color centers (Turukhin et al., 1996) and could provide a handle on the photophysics of emitters in general (Mackowski et al., 2008). Furthermore, even for emitters with high quantum efficiency  $\eta_o$  a larger emission rate permits a higher degree of light extraction by postponing saturation to higher intensities. These phenomena could be exploited for a range of light-emitting devices such as displays or pigments based on composite material made of a careful combination of nano-antennas and emitters.

Considering the antenna performances of Figure 4.19, i.e.  $\Gamma_r/\Gamma_r^o = 10^3$  and  $\eta_a \simeq 0.8$ , to an initial quantum yield  $\eta_o = 0.01$  corresponds a 74-fold enhancement and thus an apparent quantum yield  $\eta = 0.74$  (see Eq. (4.4)). To assess the sensitivity of this result we also plot  $\eta$  with respect to the emitter position within the antenna gap. Note that if the antenna performances are sufficiently large, the tolerances for obtaining a significant improvement of fluorescence emission are fully compatible with state-of-the-art experimental techniques. It is also worth to point out the fact that  $\eta$  is larger if the emitter is not at the center of the antenna gap, but closer to one of the two nanoparticles. This trend can be explained by considering the near-field profile along the antenna axis, which has a minimum in the middle of the gap (Aravind et al., 1981).

### 4.2.4 Directional optical antennas

We have designed antennas that increase the spontaneous emission rate of quantum emitters by orders of magnitude with very small absorption losses. These findings and the fact that the optical response of optical antennas is extremely fast envision a highly efficient coherent optical access to single emitters under conditions where dephasing processes occur at very short time scales. However, for achieving controllable few-photon interactions it is also crucial that the antenna directs and receives light with a high throughput in a well-defined optical mode.

Two parameters are commonly used in engineering textbooks to assess the quality of the antenna radiation pattern. These are the maximal directivity and gain,

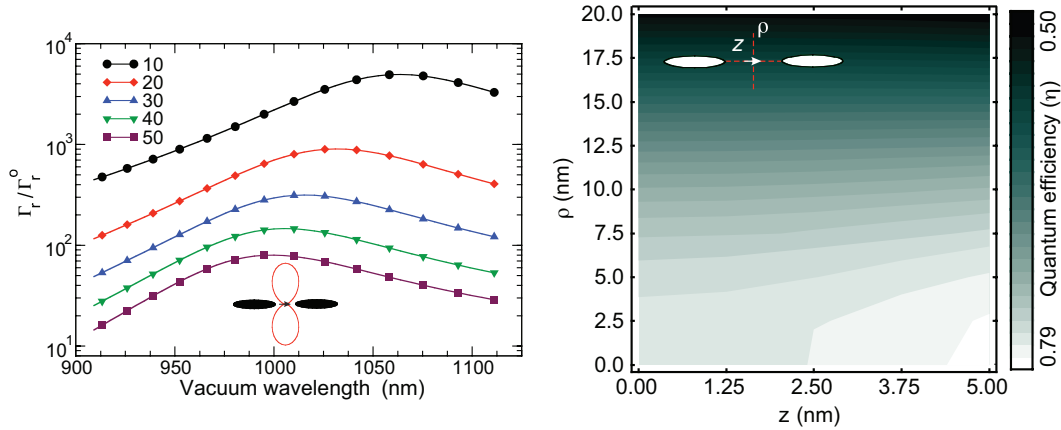


**Figure 4.19:** (left panel) Normalized radiative decay rates for nano-antennas made of two prolate gold spheroids (long axis 120 nm, short axes 38 nm). The legend gives the gap width  $d$  in nm. The emitter is placed at the center of the gap and oriented along the nano-antenna. The inset shows that the emission pattern remains dipolar. (right panel) Quantum efficiency map calculated assuming  $\eta_o = 0.01$  for various emitter positions in the antenna gap.

which read

$$D_{\max} = \frac{4\pi}{P_r} \max\{P_r(\theta, \varphi)\}, \quad G_{\max} = \eta_a D_{\max}, \quad (4.10)$$

where  $\max\{P_r(\theta, \varphi)\}$  is the maximal amount of power radiated in a certain direction and  $P_r$  is the total radiated power. The  $4\pi$  in the numerator is to normalize the angular distribution with respect to an ideal isotropic radiator (Balanis, 2005).  $D_{\max}$  and  $G_{\max}$  quantify how much fraction of the radiated energy is channeled into a certain direction. A high directivity gives rise to improved transmission and operation at lower power levels. These features are extremely desirable also in the optical domain. For example, to establish a link between distant nodes of a quantum network (Kimble, 2008).

To this end there has been an explosion of activities on the design and fabrication of directive optical antennas. The first attempts have tried to adapt solutions that are commonly used in radio-wave applications. In particular, the Yagi-Uda antenna has received much attention because it can be readily transferred into optics using metal nanoparticles as array elements (Hofmann et al., 2007; Li et al., 2007). However, one should bear in mind that a large antenna gain, i.e. a directional emission pattern, might not be sufficient for achieving controlled operations with few-photons. The problem here is to find an antenna that modifies the emission pattern of a quantum emitter in a way that it matches optical modes that can be realized in optics and photonics. In the next section we will present strategies that go in this direction.

### The Yagi-Uda antenna

The Yagi-Uda antenna is an array made of several dipole antenna elements that under appropriate conditions form a directional emission pattern (Uda, 1927; Yagi, 1928). Typically only one element is active, whereas the other function as reflectors or directors to control the angular distribution of radiation. To understand this in more detail we review the underlying theory (Balanis, 2005).

The far field  $\mathbf{E}(\mathbf{r})$  and Poynting vector  $\mathbf{S}(\mathbf{r})$  of an array of induced dipoles  $\mathbf{p}_i$  placed at locations  $\mathbf{d}_i$  reads

$$\mathbf{E}(\mathbf{r}) = \frac{Zck^2}{4\pi} \frac{e^{ikr}}{r} \sum_i e^{-ik\mathbf{n}\cdot\mathbf{d}_i} (\mathbf{n} \times \mathbf{p}_i) \times \mathbf{n}, \quad (4.11)$$

$$\mathbf{S}(\mathbf{r}) = \frac{Zc^2k^4}{32\pi^2r^2} \sum_{i,j} \text{Re} \left\{ e^{-ik\mathbf{n}\cdot(\mathbf{d}_i-\mathbf{d}_j)} \left[ \mathbf{p}_i \cdot \mathbf{p}_j^* - (\mathbf{n} \cdot \mathbf{p}_i)(\mathbf{n} \cdot \mathbf{p}_j^*) \right] \right\} \mathbf{n}, \quad (4.12)$$

where  $\mathbf{n} = \mathbf{r}/r$ ,  $r = |\mathbf{r}|$  and  $k = |\mathbf{k}|$ . The dipoles are coupled by the free-space Green tensor  $\mathbf{G}$

$$\mathbf{G}(\mathbf{r}) = \frac{e^{ikr}}{4\pi\epsilon r} \left[ k^2(\mathbb{I} - \mathbf{nn}) + (3\mathbf{nn} - \mathbb{I}) \right]. \quad (4.13)$$

Depending whether there is a driving dipole  $\mathbf{p}_o$  or a driving external field  $\mathbf{E}_{\text{ext}}$ , one obtains the two following system of equations

$$\mathbf{p}_i = \alpha_i \left[ \sum_{j \neq i} \mathbf{G}(\mathbf{r}_i - \mathbf{r}_j) \cdot \mathbf{p}_j + \mathbf{G}(\mathbf{r}) \cdot \mathbf{p}_o \right], \quad (4.14)$$

$$\mathbf{p}_i = \alpha_i \left[ \sum_{j \neq i} \mathbf{G}(\mathbf{r}_i - \mathbf{r}_j) \cdot \mathbf{p}_j + \mathbf{E}_{\text{ext}}(\mathbf{r}_i) \right], \quad (4.15)$$

where  $\alpha_i$  are dipole polarizabilities. The solution of Eqs. (4.14) or (4.15) yields the amplitude and phase of the dipoles  $\mathbf{p}_i$ . These are plugged into Eq. (4.12) to obtain the radiation pattern. The latter is shaped by tuning various degrees of freedom, such as the polarizabilities  $\alpha_i$  and the positions  $\mathbf{d}_i$ .

For example, Li et al. (2007) designed a Yagi-Uda optical antenna using nanoshells as array elements. Figure 4.20 shows amplitude and phase of the nanoshell polarizability  $\alpha$  as a function of the filling ratio  $b/a$ , and a layout of the proposed optical Yagi-Uda array. The nanoshell dipoles can be retarded (reflector) or advanced (director) with respect to the driving dipole by choosing appropriate values of  $b/a$ , where  $a$  and  $b$  are the outer and inner radii, respectively.

Other designs of an optical Yagi-Uda antenna construct directors and reflectors by changing the aspect ratio of metal nanorods (Hofmann et al., 2007; Taminiau et al., 2008b). Nanorod arrays are more amenable for fabrication than nanoshells, because their properties can be controlled by standard lithography. Indeed there

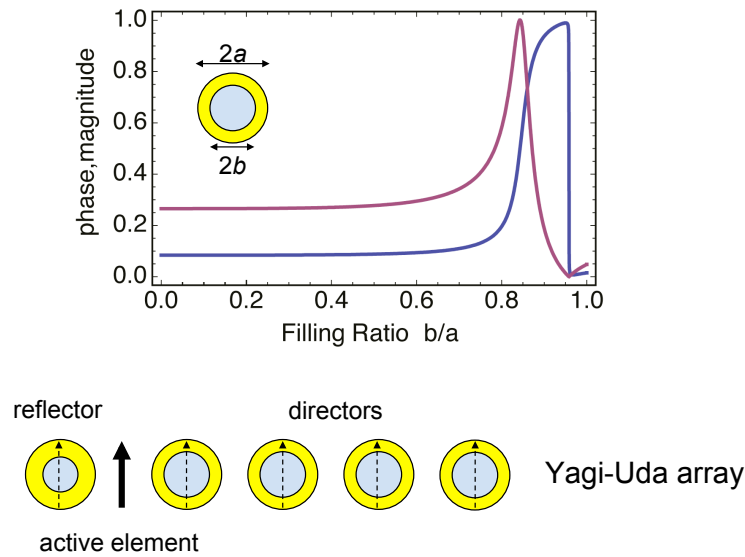


**Figure 4.20:** The nanoshell Yagi-Uda array proposed by Li et al. (2007) The nanoparticle has a silica ( $\epsilon = 2.2$ ) core and a silver ( $\epsilon = -15.33 + i0.451$ ) shell. The outer radius  $a$  is fixed ( $a = 0.1\lambda$ ), and  $b$  is varied. The upper graph shows the polarizability magnitude (red line) and phase (blue lines) in units of  $\pi$  as a function of  $b/a$  for  $\lambda = 620$  nm.

have been two recent experimental demonstrations of directional emission using a nanoparticle (Kosako et al., 2010) and even a single quantum emitter (Curto et al., 2010) as driving elements. Approaches based on one-dimensional arrays of nanospheres have also been proposed (Koenderink, 2009).

### Traveling wave antennas

Since propagating optical modes have the energy flow in a well-defined direction, it may be convenient to use traveling wave antennas (Balanis, 2005) to modify the emission pattern of quantum emitters. In this respect, metal and dielectric nanowires are interesting structures because they offer at the same time directionality and broadband coupling. Moreover, compared to antenna arrays they are much easier to fabricate and handle.

If  $\Gamma_{\text{nw}}$  represents the transfer rate of energy from an emitter to a nearby nanowire, the coupling efficiency is expressed by the  $\beta$  factor, which reads  $\beta = \Gamma_{\text{nw}} / (\Gamma_{\text{nw}} + \Gamma_o)$ , where  $\Gamma_o$  is the spontaneous emission rate without nanowire.  $\beta$  depends on many parameters such as the nanowire radius and composition, operating wavelength, emitter position and orientation. In order to achieve efficient coupling,  $\beta$  has to be as close as possible to 1, meaning that  $\Gamma_{\text{nw}}$  must be much larger than  $\Gamma_o$ . Dielectric nanowires or nanofibers do not exhibit a strong enhancement of the spontaneous emission rate. The strategy to improve their  $\beta$  primarily relies on a careful choice of the dispersion relation of the guided modes, which



leads to  $\Gamma_{\text{nw}}$  a factor of ten larger than  $\Gamma_o$  (Klimov and Ducloy, 2004) and to coupling efficiencies of the order of 90% distributed in two directions, as shown in Figure 4.21. Larger  $\beta$  can be achieved using metal nanowires. Here the enhancement of the spontaneous emission rate relies on the existence of SPP modes that remain tightly confined even for very small nanowire radii. They give rise to enhanced near fields that modify light emission very much like the strong near fields of optical antennas. Unfortunately, metal nanowires suffer from huge propagation losses and great care has to be taken in order to design a high-performance light-emitter interface (Chang et al., 2006, 2007b).

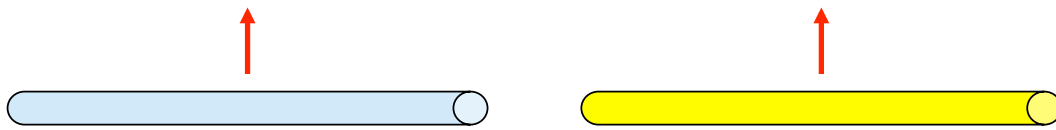


**Figure 4.21:** *Dipole emitter coupled to a nanofiber (left panel) and to a metal nanowire (right panel). The dipole orientation can also be parallel to the nanowire, but that leads to lower coupling efficiencies.*

Similar considerations are valid for emitters coupled to other waveguide designs, such as nanowires with non-cylindrical cross sections (Chen et al., 2010b; Guzatov and Klimov, 2007), photonic crystal waveguides (Lecamp et al., 2007; Lund-Hansen et al., 2008) or slot waveguides (Jun et al., 2009; Quan et al., 2009).

### Dielectric antennas

Dielectric optical antennas, in contrast to dielectric microcavities (Vahala, 2003), are weakly resonant nanostructures that do not exhibit a strong change of the spontaneous emission neither a strong field enhancement. Nonetheless they can control the radiation pattern to largely improve the collection efficiency. In the past years these ideas have mostly relied on thin-film technology assisted by solid immersion lenses and on the modification of the emission pattern near a dielectric interface (Barnes et al., 2002). Recent designs have shown, theoretically and experimentally, that near unity collection efficiencies are possible (Lee et al., 2011).

Dielectric antennas can be semiconductor nanowires that embed a quantum dot as single-photon source (Borgström et al., 2005). These nanowire antennas could have engineered shape, for instance a tapered end (Gregersen et al., 2008), and be assisted by a metal mirror (Friedler et al., 2008) to further improve the fraction of light emitted in a preferential direction (Claudon et al., 2010; Friedler et al., 2009). Similar concepts have been developed to enhance diamond-based single-photon sources (Babinec et al., 2010).

### Other antenna designs

To achieve more compact directional antenna structures, there have been further investigations based on nanoparticle pairs, either nanodisks (Pakizeh and Käll, 2009) or nanospheres (Bonod et al., 2010), or patches (Esteban et al., 2010). Other approaches concerned hybrid systems made of dielectric and metallic antennas (Devilez et al., 2010). To overcome the poor enhancement features of dielectric nanoparticles, it has been shown that geometric resonances in nanoparticle arrays lead to strong modification of spontaneous emission (Pellegrini et al., 2009). These dielectric antenna systems can be tuned in a broad spectral range from the ultraviolet to the near-infrared without suffering from the absorption losses intrinsic to metallic antennas.

## 4.3 Interfacing optical antennas with optics and photonics

In the previous section we have discussed a few examples on how the radiation pattern of a quantum emitter gets modified by an optical antenna. Our aim here is designing mode converters that interface a quantum emitter and light with a high throughput and, at the same time, yield a large enhancement of the radiative decay rate. Matching a well-defined optical mode may improve the overall efficiency of a quantum-optical link and enable few-photon interactions (Schuster et al., 2008; Stobińska et al., 2009; Zumofen et al., 2008). We show that conical antennas fulfill these conditions if their aspect ratio is appropriately chosen. In addition, being fully compatible with scanning probe technology they are promising candidates for realizing a high-throughput SNOM (Chen et al., 2009, 2010a).

We approach this result in a number of steps that emphasize the various aspects that one has to take into account in the design of high-performance directional antennas. First, we revert to the results of the previous chapter and point out the limitations of high NA objectives in coupling single photons to dipolar optical antennas (Agió et al., 2009). Second, we consider the problem of converting light to SPP in metal nanowires using either guided waves or weakly focused beams. Third, we replace nanowires with nanocones and investigate performances like throughput and collection efficiency.

### 4.3.1 Coupling light to a dipolar antenna

The recent years have witnessed increasing attention towards the use of tightly focused beams for improving and controlling the coupling of light with nanoscale objects. These efforts primarily concern the detection and spectroscopy of single emitters (Gerardot et al., 2007; Tey et al., 2008; Vamivakas et al., 2007; Wrigge

et al., 2008a), non-fluorescent nanoparticles (Kalkbrenner et al., 2004; Kukura et al., 2009), and elementary biological entities (Ewers et al., 2007). We have shown that an ideal dipole placed at the focus has a very strong effect on the transmission of light. However, quantum emitters in the solid state behave as ideal dipoles only at cryogenic temperatures (Gerardot et al., 2007; Vamivakas et al., 2007; Wrigge et al., 2008a), whereas single atoms exhibit other difficulties such as trapping and alignment in a tight focus (Tey et al., 2008). On the other hand, a silver nanoparticle at room temperature scatters light as an ideal point-like dipole (Mojarad et al., 2009). This property stems from the SPP resonance, which has a radiative decay of the order of femtoseconds (Bohren and Huffman, 1983). Such an extremely fast relaxation ensures that other dephasing and non-radiative processes at room temperature have a small effect on the nanoparticle optical response. Metal nanoparticles are thus ideal systems for conducting experimental studies on the scattering of focused light by a dipole (Celebrano et al., 2010). Moreover, the strong field enhancement and localization combined with the efficient radiation into the far field make metal nanoparticles promising candidates for building an interface between photons and single quantum emitters in free space (Anger et al., 2006; Greffet, 2005; Kühn et al., 2006; Rogobete, 2007).

The coupling of photons to SPPs confined in metal nanowires has been performed by considering the fraction of power transmitted to a nanofiber, and vice versa, by evanescent (Chang et al., 2006) or butt coupling (Chen et al., 2009). Furthermore, the excitation of SPPs on metal films has been investigated using the quantum theory of light (Tame et al., 2008). Here, we limit our analysis to classical electrodynamics and the coupling strength is defined as the ratio of the total power that has interacted with the metal nanoparticle and the incident power. We point out that, as for a TLS, maximizing scattering or excitation does not lead to the same result. In the first case, perfect reflection of photons is achieved when the incident light is a directional dipole wave and the system is under weak excitation (Zu-mofen et al., 2008). In the second situation, perfect excitation by a single photon is obtained using a dipole wave under time reversal (Stobińska et al., 2009; van Enk, 2004).

We thus study the interaction of focused light with metal nanoparticles and discuss to what extent one can maximize the coupling strength. For this reason, we include the effect of the entrance pupil, which blocks a fraction of the incident power in the beam. Furthermore, because we want to investigate parameters that are meaningful for experimental situations, we choose focused Gaussian beams (FGBs) and focused radially-polarized beams (FRBs) in aplanatic systems. Both of them are easily obtainable in the laboratory and represent two significant cases. FGBs approach a focused plane wave if the beam waist is much larger than the entrance pupil (Richards and Wolf, 1959), whereas FRBs resemble a directional dipole wave (Quabis et al., 2001; van Enk, 2004). To conclude, we consider the reduction in the metal nanoparticle cross section due the presence of absorption and dis-

cuss how the coupling efficiency can be determined by performing transmission experiments.

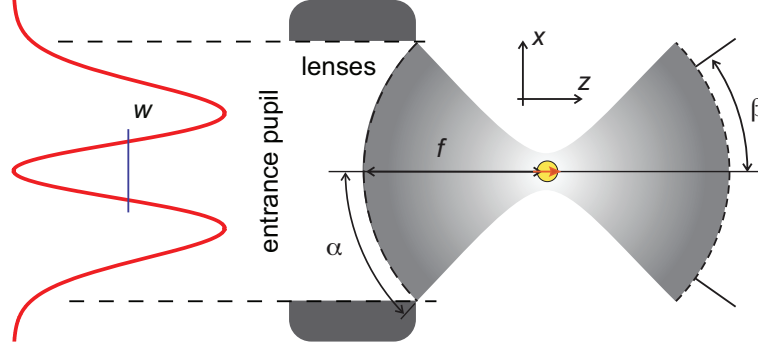


**Figure 4.22:** Sketch of an incident beam focused by an aplanatic system, which is scattered by an ideal electric dipole or a metal nanoparticle placed in the focus. The red curve at the left represents the electric field profile of a radially-polarized beam.  $w$  is the beam waist and  $f$  is the focal length of the lens.  $\alpha$  is the focusing semi-angle and  $\beta$  is the collection semi-angle. The horizontal dashed lines delimit the portion of the beam that intercepts the lens (entrance pupil). Note that for a FRB the dipole in the focus must be oriented along the  $z$ -axis, while for a FGB along the  $x$ -axis.

### Incident beam efficiency

We consider the coupling efficiency step by step, starting from the entrance pupil. It is located at the beam waist  $w$ , where the electric field for a Gaussian and a radially-polarized beams reads, respectively,

$$\mathbf{E}(\rho) = E_o \exp\left(-\frac{\rho^2}{2w^2}\right) \hat{\mathbf{x}}, \quad (\text{FGB}) \quad (4.16)$$

$$\mathbf{E}(\rho) = E_o \frac{\rho}{w} \exp\left(-\frac{\rho^2}{2w^2}\right) \hat{\boldsymbol{\rho}}, \quad (\text{FRB}) \quad (4.17)$$

where  $\rho$  is the distance from the optical axis  $z$ ,  $\hat{\mathbf{x}}$  is the  $x$ -axis versor in the Cartesian coordinates  $(x, y, z)$ , and  $\hat{\boldsymbol{\rho}}$  is the  $\rho$ -axis versor in cylindrical coordinates  $(\rho, \varphi, z)$ . The field profile for a radially-polarized beam is sketched in Figure 4.22. Depending on the beam waist and on the entrance pupil, only a fraction of the incident power gets focused by the lens. We thus define the incident beam efficiency  $\eta_{\text{inc}}$  as the ratio of power that is collected by the entrance pupil with respect to the total power carried by the beam. For an aplanatic system, if  $f$  is the lens focal length and  $\alpha$  the focusing angle, the radius of the pupil is  $f \sin \alpha$ . If we call  $d = f/w$  the

beam parameter, we find that for a FGB and a FRB  $\eta_{\text{inc}}$  reads, respectively,

$$\eta_{\text{inc}}(\alpha, d) = 1 - \exp\left(-d^2 \sin^2 \alpha\right), \quad (\text{FGB}) \quad (4.18)$$

$$\eta_{\text{inc}}(\alpha, d) = 1 - \left(1 + d^2 \sin^2 \alpha\right) \exp\left(-d^2 \sin^2 \alpha\right). \quad (\text{FRB}) \quad (4.19)$$

Note that the quantity only depends on the focusing angle  $\alpha$  and the beam parameter  $d$ . In other words, increasing  $f$  or decreasing  $w$  by the same amount leads to the same result. Figure 4.23a and b respectively display  $\eta_{\text{inc}}$  for a FGB and a FRB for different focusing angles and values of  $d$ . In both situations,  $\eta_{\text{inc}}$  increases when  $d$  increases, because either the radius of the entrance pupil gets larger, or the beam waist gets smaller. For focusing angles obtainable using commercial high-NA lenses,  $\eta_{\text{inc}}$  is above 0.8 if  $d$  is close to or larger than 2.

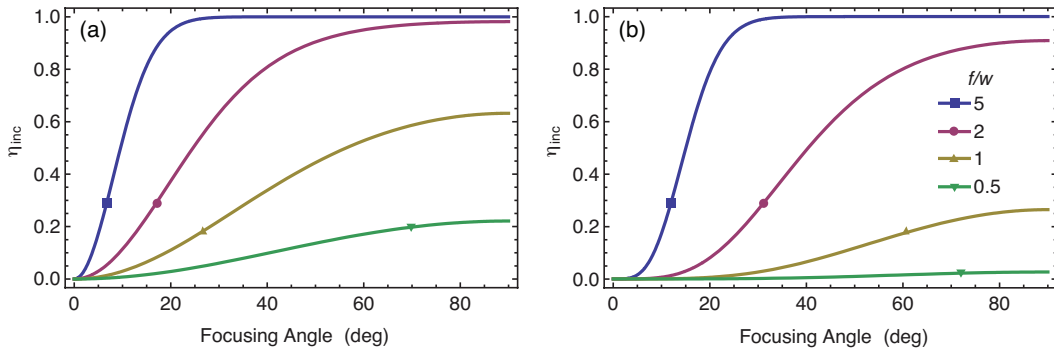


**Figure 4.23:** Incident beam efficiency  $\eta_{\text{inc}}$  as a function of the focusing angle  $\alpha$  and the beam parameter  $d = f/w$  for a FGB (a) and a FRB (b).

### Scattering ratio and focusing efficiency

The fraction of power collected by the entrance pupil is then focused by the lens. To quantify the strength of the interaction between an ideal dipolar scatterer placed at the focus and the beam, we have introduced the scattering ratio  $\mathcal{K}_{\text{dp}}$ .<sup>7</sup> Here we define the focusing efficiency  $\eta_{\text{foc}}$  as  $\mathcal{K}_{\text{dp}}/2$ . The total scattered power is proportional to the squared amplitude of the electric field times the cross section, which for an ideal oscillating dipole on resonance reads  $\sigma_o = 3\lambda^2/(2\pi)$  (Jackson, 1999). The incident power is more easily computed using the field at the entrance pupil right before the lens, which is given in the Appendix by Eqs. (A.29) and (A.30).

<sup>7</sup> $\mathcal{K}_{\text{dp}}$  stands for  $\mathcal{K}_{\text{sca}}$  defined in Chapter 2.

These quantities lead to

$$\eta_{\text{foc}}(\alpha, d) = \frac{3d^2 \mathcal{I}_0^2(\alpha, d)}{4 [1 - \exp(-d^2 \sin^2 \alpha)]}, \quad (\text{FGB}) \quad (4.20)$$

$$\eta_{\text{foc}}(\alpha, d) = \frac{6d^4 \mathcal{I}_1^2(\alpha, d)}{1 - (1 + d^2 \sin^2 \alpha) \exp(-d^2 \sin^2 \alpha)}, \quad (\text{FRB}) \quad (4.21)$$

where  $\mathcal{I}_0(\alpha, d)$  and  $\mathcal{I}_1(\alpha, d)$  are diffraction integrals given in the Appendix by Eqs. (A.12) and (A.27), respectively. Note that for a FRB the dipole is oriented along  $\hat{\mathbf{z}}$ , whereas for a FGB it is oriented along  $\hat{\mathbf{x}}$ .

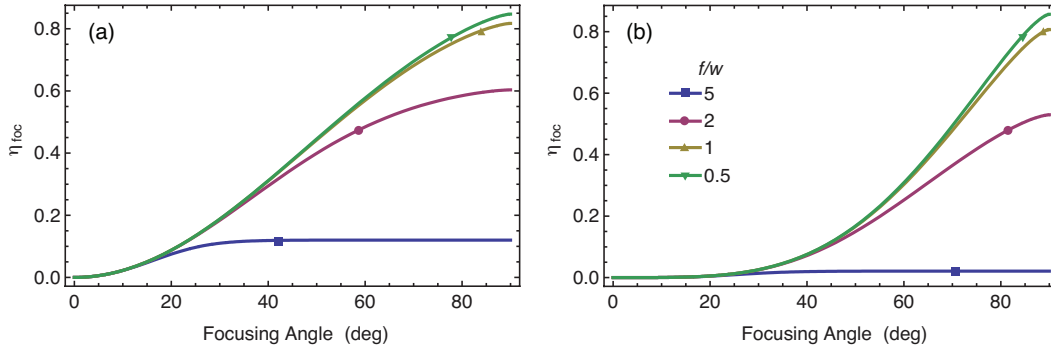


**Figure 4.24:** Focusing efficiency  $\eta_{\text{foc}}$  as a function of the focusing angle  $\alpha$  and the beam parameter  $d = f/w$  for a FGB (a) and a FRB (b).

Figures 4.24a and b show that  $\eta_{\text{foc}}$  increases with the focusing angle  $\alpha$  and decreases for larger values of the parameter  $d$ . The latter behavior can be explained by recalling that a strong focus requires that the incident beam overfills the entrance pupil. A large field amplitude at the lens edge is thus achieved for  $d$  comparable to or less than 1. In particular, when  $d$  tends to 0, the FGB becomes a focused plane wave (Richards and Wolf, 1959) and the FRB behaves as if the entrance pupil were an annular aperture (Quabis et al., 2001). For obtaining the same  $\eta_{\text{foc}}$  a FRB requires a larger focusing angle than a FGB. Note that a FRB resembles a directional dipole wave generated by reversing at the lens the field radiated by a dipole placed at the focus and oriented along the optical axis (Sheppard and Larkin, 1994; van Enk, 2004). Because most of the power propagates along the direction  $\alpha = 90^\circ$ , only a high-NA objective can effectively reverse such wave back to the focal spot. When  $d$  is close to 0 and  $\alpha = 90^\circ$ , the maximum value of  $\eta_{\text{foc}}$  is 0.853 for a FGB and 0.87 for a FRB. The latter is slightly closer to the theoretical maximum of 1 found for a directional dipole wave. However, these considerations have to be confronted with the fact that for  $d$  less than 2 a significant amount of incident power is lost at the entrance pupil.

### Total efficiency

When looking at the interaction of nanoscopic objects with single photons, both the focusing efficiency and the beam efficiency must be taken into consideration. We thus define total efficiency  $\eta_{\text{tot}} = \eta_{\text{inc}}\eta_{\text{foc}}$ . To investigate the competitive effects of  $\eta_{\text{inc}}$  and  $\eta_{\text{dp}}$ , we monitor  $\eta_{\text{tot}}$  as a function of  $d$  choosing two realistic values for the focusing angle,  $\alpha = 50^\circ$  and  $70^\circ$ , and the theoretical maximum  $\alpha = 90^\circ$ . The result for a FGB and a FRB is shown in Figure 4.25a and b, respectively. Depending on the focusing angle, the maximum efficiency is found for different values of  $d$ . Note that the total efficiency of a FRB is smaller than for a FGB.

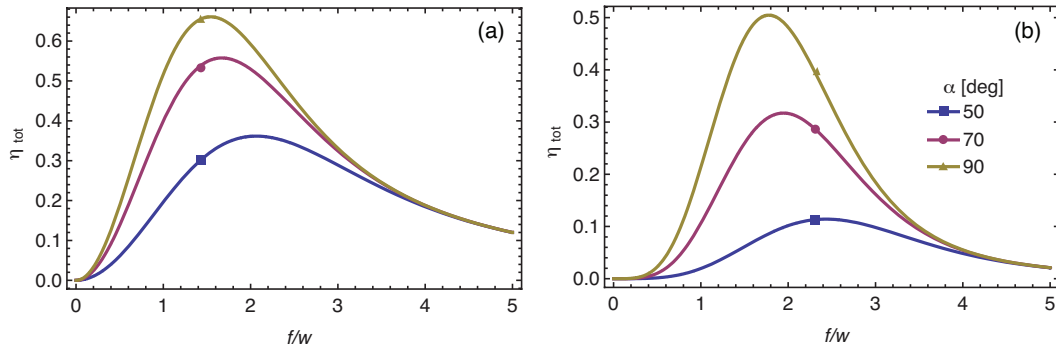


**Figure 4.25:** Total efficiency  $\eta_{\text{tot}}$  as a function of the focusing angle  $\alpha$  and the beam parameter  $d = f/w$  for a FGB (a) and a FRB (b).

### Application to optical antennas

We now investigate a silver nanoparticle using a polarizability  $\alpha$  derived from Mie theory (see Section 4.1.3). Figure 4.26a displays the cross sections for a 90 nm silver nanoparticle in oil (refractive index  $n_b = 1.47$ ). The resonance is located around the vacuum wavelength  $\lambda = 500$  nm. The fact that the scattering ( $C_{\text{sca}}$ ) and total ( $C_{\text{tot}}$ ) cross sections<sup>8</sup> are very close to each other confirms that most of the power is dissipated by radiation, like for an ideal classical oscillating dipole. However, because some of the power is absorbed, the nanoparticle cross section is smaller than  $\sigma = 3\lambda^2/2\pi$  (Jackson, 1999). To account for this effect, we define the nanoparticle efficiency  $\eta_{\text{NP}}$  as the ratio of the nanoparticle and the dipole cross sections,

$$\eta_{\text{NP}} = \frac{C_{\text{tot}}}{\sigma} = \frac{k^3 \text{Im}(\alpha)}{6\pi} \leq 1. \quad (4.22)$$

<sup>8</sup>The total cross section must be read as the sum of the scattering and absorption cross sections. The total power that has interacted with the nanoparticle corresponds to the interference term in the Poynting vector and it is often referred to as extinction (Bohren and Huffman, 1983). See Mojarad et al. (2009) for a detailed discussion.

The overall efficiency is thus  $\eta_{\text{tot}} = \eta_{\text{inc}}\eta_{\text{foc}}\eta_{\text{NP}}$ . If  $\eta_{\text{NP}}$  is close to 1, such as for silver nanoparticles, the curves given in Figures 4.25a and b can be assumed to be valid also for this situation.

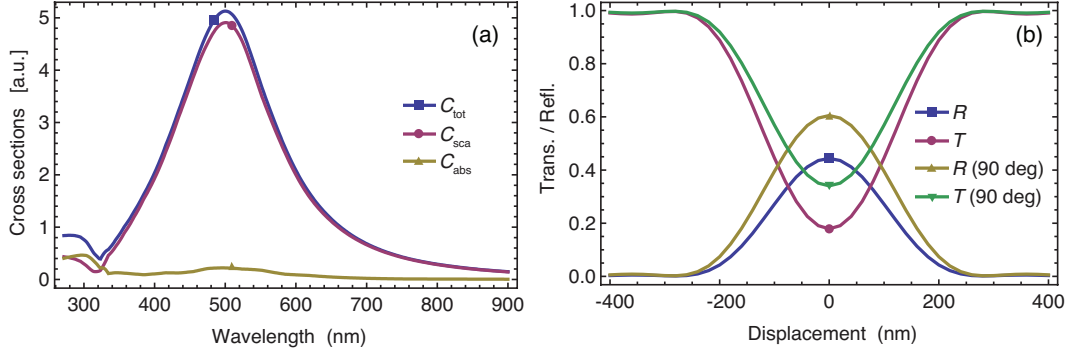


**Figure 4.26:** (a) Total  $C_{\text{tot}}$ , scattering  $C_{\text{sca}}$  and absorption  $C_{\text{abs}}$  cross sections for a 90 nm silver nanoparticle in oil (refractive index  $n_{\text{b}} = 1.47$ ). (b) transmission  $T$  and reflection  $R$  for a FGB ( $\alpha = \beta = 70^\circ$  and  $d = 1$ ) as a function of the nanoparticle displacement in the focal plane. The result for  $\beta = 90^\circ$  is also shown.

### Measuring the coupling efficiency

We have derived expressions for the transmission  $T$  and reflection  $R$  of focused light in the presence of an ideal dipole or a metal nanoparticle using the scattering and absorption ratios (Mojarad et al., 2009; Zumofen et al., 2008). However, because the incident and the transmitted light encounter the same optics in the way through the detector, we would like to formulate the coupling efficiency only as a function of  $T$ . While this is trivial for an ideal dipole (Zumofen et al., 2008), a metal nanoparticle requires some care due to absorption (Mojarad et al., 2009). The scattering efficiency  $\eta_{\text{sca}}$  accounts for the fraction of power that is scattered with respect to the total power that has interacted with the nanoparticle (Buchler et al., 2005),

$$\eta_{\text{sca}} = \frac{C_{\text{sca}}}{C_{\text{tot}}} = \frac{k^3 |\alpha|^2}{6\pi \text{Im}(\alpha)} \leq 1. \quad (4.23)$$

There is a second aspect that we need to consider. Assuming that the collection angle  $\beta$  is equal or larger than the focusing angle  $\alpha$ , the transmission will fully capture the power  $P_{\text{int}}$  associated with interference, because its angular spread equals that of the incident power in the forward direction. However, the power scattered by a dipolar radiator flows in both directions with the same strength with an angular spread of  $90^\circ$ . If  $X(\beta)$  is the fraction of the scattered power collected in the forward direction (see Section 3.4.2), the transmission formula of Eq. (3.40) becomes

$$T = 1 - \mathcal{K}_{\text{tot}} + \mathcal{K}_{\text{sca}} X(\beta), \quad (\beta \geq \alpha) \quad (4.24)$$



where  $\mathcal{K}_{\text{tot}}$  and  $\mathcal{K}_{\text{sca}}$  are respectively the power ratios for the metal nanoparticle. We now express these quantities as a function of  $\mathcal{K}_{\text{dp}}$ ,  $\eta_{\text{NP}}$  and  $\eta_{\text{sca}}$ , finding  $\mathcal{K}_{\text{tot}} = \mathcal{K}_{\text{dp}}\eta_{\text{NP}}$  and  $\mathcal{K}_{\text{sca}} = \mathcal{K}_{\text{dp}}\eta_{\text{NP}}\eta_{\text{sca}}$ . Substituting them in Eq. (4.24), a few algebraic steps lead to

$$\eta_{\text{foc}} = \frac{\mathcal{K}_{\text{dp}}}{2} = \frac{1 - T}{2\eta_{\text{NP}}}(1 - \eta_{\text{sca}}X(\beta))^{-1}. \quad (4.25)$$

As an example, we consider the silver nanosphere of Figure 4.26a in the focus of a FGB with  $\alpha = 70^\circ$ ,  $d = 1$  and  $\lambda = 500$  nm. The silver nanoparticle is displaced in the focal plane and the reflected and transmitted powers are collected using  $\beta = 70^\circ$ . The result is shown in Figure 4.26b, including the case for  $\beta = 90^\circ$ . When the collection angle increases from  $70^\circ$  to  $90^\circ$ ,  $T$  decreases and  $R$  increases, in accordance with Eq. (4.24) and the fact that  $R = \mathcal{K}_{\text{sca}}X(\beta)$ . A comparison of the reflection peak for  $\beta = 90^\circ$ , which amounts to  $\eta_{\text{foc}}\eta_{\text{NP}}\eta_{\text{sca}}$ , with the corresponding curve in Figure 4.24a confirms that the silver nanoparticle has both  $\eta_{\text{NP}}$  and  $\eta_{\text{sca}}$  close to unity. In other terms, a single SPP resonance could be coupled to a free-space single photon with an overall efficiency close to  $\eta_{\text{inc}}\eta_{\text{foc}}$ , as illustrated in Figure 4.25. Note that a stronger transmission deep or a larger reflection peak do not necessarily correspond to a better coupling efficiency  $\eta_{\text{tot}}$ , because these two quantities also depend on the collection angle  $\beta$ , as shown in Figure 4.26b.

These results have been derived within the classical electromagnetic theory and they require a deeper analysis from the quantum optical point of view. Nevertheless, they suggest that single photons could interact with single SPP resonance very effectively simply by focusing light and working at room temperature. The reason is that the cross section of silver nanospheres is close to that of an ideal dipole. In terms of quantum optics with SPPs these findings show that the coupling to single photons is smaller than for other configurations based on guided SPPs (Chang et al., 2006; Chen et al., 2009; Tame et al., 2008). However, this scheme presents some practical advantages for experiments when the coupling between the SPP and a quantum emitter is also considered (Akimov et al., 2007; Anger et al., 2006; Kühn et al., 2006; Rogobete, 2007).

### 4.3.2 Coupling to a nanofiber

Practical device proposals require a rapid and efficient conversion of SPPs into guided photons. In case of SPPs at planar interfaces, evanescent wave and grating couplers are very effective (Raether, 1988). Thus, researchers have extended these schemes to guided modes of dielectric nanofibers (NF) and metallic nanowires (NW) in a side by side arrangement (Chang et al., 2006; Lee et al., 2008), via tapers (Bouhelier et al., 2003; Ding et al., 2007; Janunts et al., 2005; Keilmann, 1999), or by etching a grating on a tapered NW (Ropers et al., 2007).

Here we investigate the most straightforward and practical way of interfacing guided SPPs and photons between a NW and a NF (Tong et al., 2003) in an axially-

symmetric butt-coupling scheme. We investigate the conversion process of photons to SPPs as a function of wavelength and material, identifying the moulding of SPPs at the coupling interface as the condition for reaching efficiencies above 95% in the visible and close to 100% in the near-infrared range.

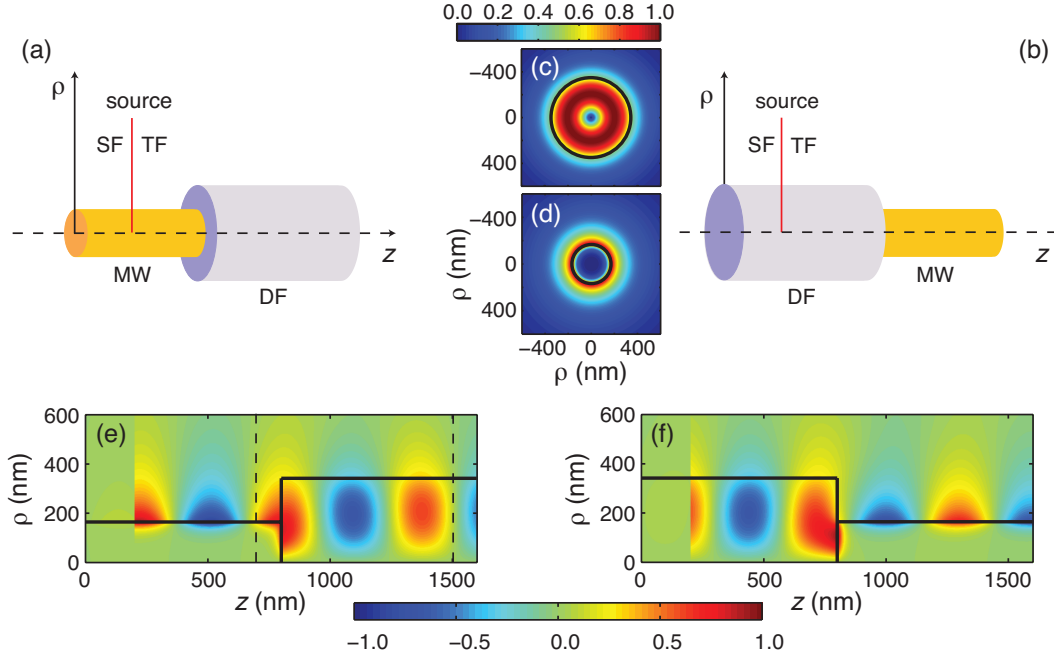


**Figure 4.27:** (a) and (b) Layout of the coupling geometry. The vertical red line indicates the separation between the total-field (TF) and the scattered-field (SF) region, and the position of the source. (c) and (d) are the magnetic field patterns of the modes in the NF and NW, respectively. (e) and (f) Snapshots of the magnetic field for the two propagating directions. The vertical dashed lines in (e) mark the area shown in Figure 4.28a. The radii of the silica NF and silver NW are 342 nm and 164 nm, respectively, and the wavelength was set to  $\lambda=633$  nm.

We performed BOR-FD-TD calculations to trace the propagation of the optical signal along the guides in a rigorous and computationally efficient manner, and to acquire an intuitive understanding of the mode conversion. Figure 4.27a and b sketch the geometrical arrangements for interfacing SPPs on a silver (Lide, 2006) NW to guided photons in a silica NF and vice versa for a vacuum surrounding. In each case, a steady-state SPP or a  $TM_{01}$  mode is launched from the left-hand side using the total-field/scatterer-field technique (Taflove and Hagness, 2005). Figure 4.27c and d depict the time-averaged transverse magnetic field profiles of the radially-polarized modes at the vacuum wavelength of  $\lambda = 633$  nm in the NF and NW with radii of 342 nm and 164 nm, respectively. The snapshots of the magnetic field in Figure 4.27e and f illustrate how SPPs travel on the surface of the NW and are converted to photons in the  $TM_{01}$  mode of the NF.

To determine the conversion efficiency  $\eta$ , we computed the ratio between the

transmitted power in the guided mode right after the NW-NF interface and the incident power at the position right before it. The latter was separately calculated for an infinitely long NW or NF using the same source. In the example of Figure 4.27e, the NW and NF yielded  $\eta \simeq 95\%$ . Likewise, we computed the reflectivity  $R$  into the incident guided mode and the fraction of power  $S$  scattered into free space. We find that the power dissipated at the NW-NF interface, given by  $1 - (\eta + R + S)$ , can be negligible. Figure 4.27f shows the reverse situation where light originates in the silica NF and is converted to SPPs of the silver NW with the same efficiency as in the previous case. The great advantage of the butt-coupling scheme is that the conversion between SPPs and guided photons takes place across an interface. This feature minimizes the impact of propagation losses, which significantly increase as wavelength and NW radius decrease (Novotny and Hafner, 1994). For instance, the NW at the wavelength considered in Figure 4.27 would yield losses as high as  $0.72 \text{ dB}/\mu\text{m}$ .

### Mode matching and tolerance

To explore the underlying coupling mechanism, in Figure 4.28a we plot the time-averaged magnetic field for the region between the dashed lines in Figure 4.27e. We find that the SPP moulds around the end of the NW in such a way that the magnetic field assumes a maximum value at a certain distance from the axis on the NW-NF interface. Here, we tuned the radii of the two guides to obtain an SPP field profile that optimizes its coupling to the  $\text{TM}_{01}$  mode of the NF. Our FD-TD analysis yielded  $\eta \simeq 95\%$ ,  $R \simeq 1.5\%$  and  $S \simeq 2.5\%$ .

Figure 4.28b displays another example of the field distribution for larger NW and NF radii of 600 nm and 800 nm, respectively. Here, the SPP magnetic field has three maxima, which clearly shows that the SPPs interfere and form a standing wave at the interface. In this case, 18.5% and 42.5% of the incident power are respectively converted into the  $\text{TM}_{01}$  and the higher-order  $\text{TM}_{0k}$  modes of the NF, while  $R \simeq 3\%$  and  $S \simeq 36\%$ . We have verified that  $R$  can also become large when the NW radius is not optimized for supporting an SPP standing wave at the NW-NF interface. Thus, a simple analysis based on mode-matching of the two guides (Snyder and Love, 1983) of Figure 4.27a only predicts  $\eta \simeq 87\%$  because it fails to account for the behavior of SPPs.

### Conversion efficiency

Next, we investigate the application of aluminum (Palik and Ghosh, 1998), silver and gold (Lide, 2006) NWs for operation at various wavelengths of interest in the ultraviolet, visible, and near infrared spectral regimes. We first found the radii by maximizing  $\eta$  for a given wavelength using a mode-matching approach (Snyder and Love, 1983) and then applied the FD-TD technique to optimize them in a

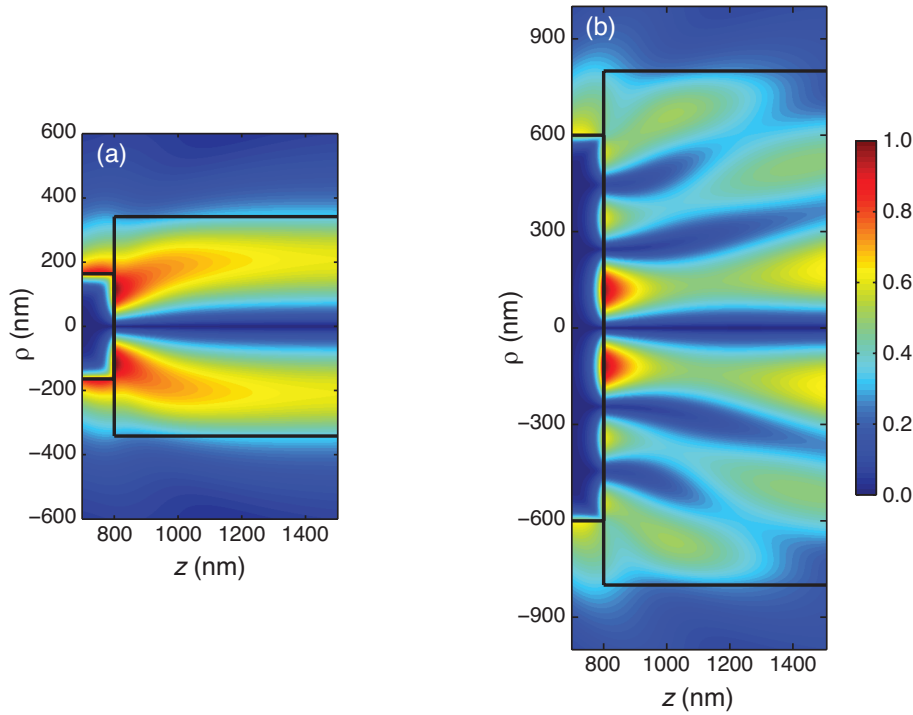


**Figure 4.28:** (a) and (b) Time-averaged magnetic field of a silver NW coupled to a silica NF for two different sets of radii (see text for details). The wavelength is set to  $\lambda=633$  nm.

rigorous manner, by scanning the radii around the previously estimated values.

Figure 4.29a summarizes the results for an aluminum NW with emphasis on the ultraviolet region, where a rapid conversion of SPPs and photons becomes more critical due to the very short SPP propagation length. The bottom panel plots the values of the NW and silica-NF radii corresponding to each optimized case. We find that even at a wavelength as short as  $\lambda = 266$  nm,  $\eta$  can reach 89% if the NF and NW radii are respectively chosen to be 158 nm and 68 nm, for which the SPP propagation loss in the NW amounts to 3.62 dB/ $\mu$ m. Figure 4.29b shows that for the case of silver NW,  $\eta$  increases from 91% to 98%, while reflection  $R$  decreases from 2.1% to 0.4% as the wavelength grows over a spectral range greater than 500 nm. If silver is replaced by gold,  $\eta$ ,  $R$  and the corresponding radii yield similar values and trends. We note that around the telecommunication wavelength of  $\lambda = 1550$  nm, a gold NW transmits nearly 100% of the power to the NF. The results for the opposite propagation direction are very similar (not shown).

### Scaling with the refractive index

Variation of the NF material can be used to engineer the coupling device for matching the confined SPP modes on thin NWs. As inferred from Figure 4.28 the optimal radius of the NW can be reduced by a high-refractive-index NF also because the SPP standing wave on the coupling interface gets compressed by the larger

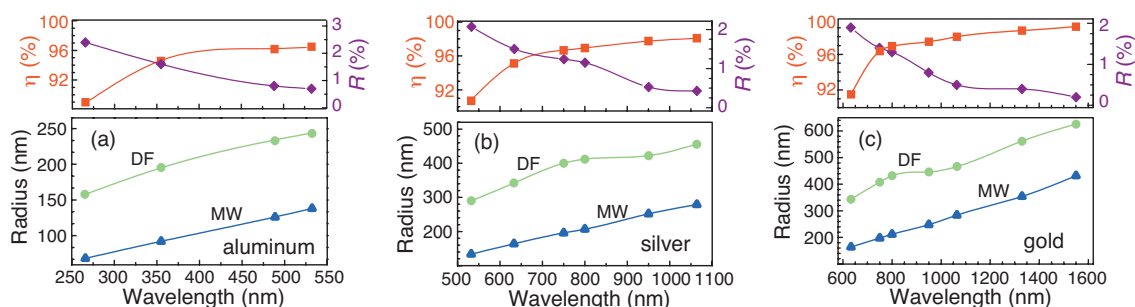


**Figure 4.29:** Conversion efficiency  $\eta$ , reflectivity  $R$  and optimal radii of the NW and NF as a function of wavelength. (a) aluminum, (b) silver, and (c) gold NW.

wavenumber. Figure 4.30a shows the mode conversion properties for a gold NW at  $\lambda=1550$  nm as a function of the refractive index of the NF. The optimal radii of the NW and NF decrease and converge to nearly the same value for larger NF refractive indices, while in each case  $\eta$  can be optimized beyond 99%.

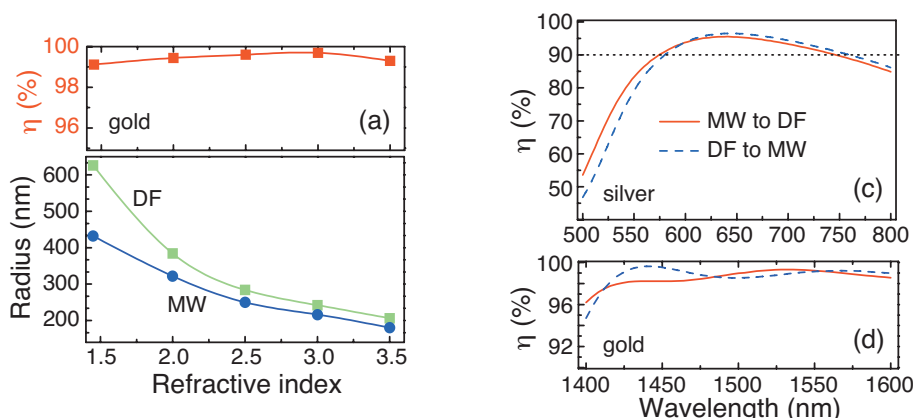


**Figure 4.30:** (a)  $\eta$  and optimal radii of a gold NW and NF as a function of the NF refractive index at  $\lambda=1550$  nm. (b)  $\eta$  for a silver NW of radius 164 nm, coupled to a silica NF of radius 342 nm. (c)  $\eta$  for a gold NW of radius 180 nm coupled to a silicon NF of radius 208 nm.

## Bandwidth

As a last important property of concern, we examined the bandwidth of  $\eta$  for a set of fixed NW and NF radii. Figure 4.30b and c display  $\eta$  for a silver and a gold NW coupled to a silica NF in the visible and in the near-infrared range, respectively. These results demonstrate that bandwidths greater than 150 nm are fully within reach for over 90% conversion of SPPs to photons and vice versa.

In summary we have shown that confined SPPs of a NW can be converted into guided photons of a dielectric nanofiber with a very high efficiency and large bandwidth using a simple butt-coupling scheme. For a given wavelength between

the visible and the near infrared spectral range, one can always obtain  $\eta$  larger than 95% by an appropriate choice of radius and material of the NW and NF. We have found that moulding of SPPs at the NW-NF interface plays a fundamental role in achieving these performances.

### 4.3.3 Coupling to a focused beam

Interfacing optical antennas with focused light is also very important. The main reason is that free-space beams are more suitable than optical fibers for propagating ultrashort pulses. Furthermore, the optical alignment is easier because it does not require physical contact with the antenna. Here we want to replace the dipole antenna discussed in Sec. 4.3.1 with a directional one.

#### Reflection and Directional Emission

We first consider the reflection and radiation of  $TM_0$  SPPs when they reach the end of a semi-infinite metal NW. In contrary to butt-coupling with a dielectric nanofiber and free-space coupling (Gordon, 2009; Li et al., 2009), here we placed a semi-infinite dielectric at the NW termination. Besides holding the NW, the substrate changes the reflection and radiation properties of SPPs. Figure 4.31a sketches the situation for a gold (Lide, 2006) NW on a glass substrate (refractive index  $n=1.5$ ) together with the simulation layout. Our calculations were carried out using the BOR-FD-TD method. We chose a wavelength of  $\lambda = 633$  nm, keeping in mind that these results are generally valid over a broad spectral range if the NW radius is properly scaled (Chen et al., 2009; Gordon, 2009).

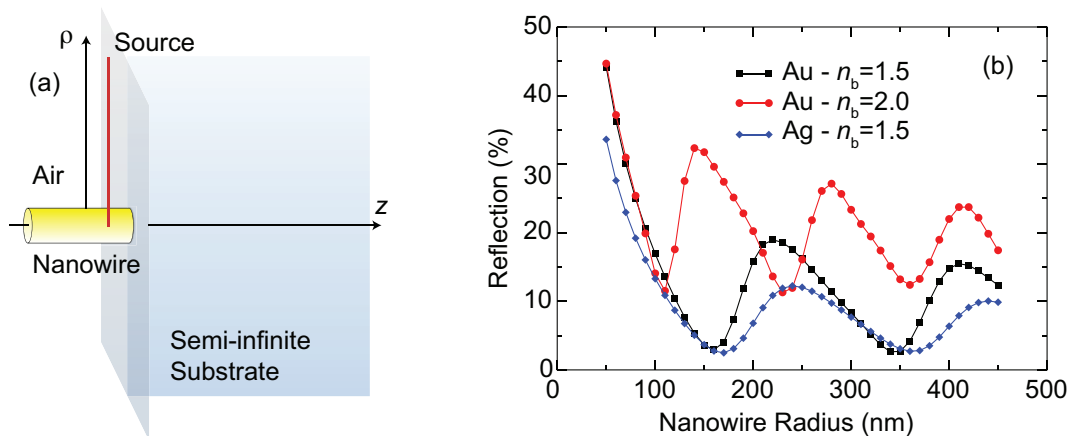


**Figure 4.31:** (a) Layout of a semi-infinite gold NW in air on a glass substrate. (b) Reflection as a function of the NW radius for different metals and substrates. In (b) the vacuum wavelength is 633 nm. In (a) the solid red line indicates the source position.

A SPP is launched on the gold NW and when it reaches the NW end it can be

reflected into the same SPP mode as well as scattered in the forward or backward directions. Figure 4.31b displays the amount of reflection for different metals and substrates, showing that it is minimized for certain values of the NW radius. Figures 4.32a and b plot the time-averaged magnetic field at two reflection minima corresponding to a gold NW on glass with radii of 160 nm and 340 nm, respectively. It turns out that the NW facet supports a standing wave (Chen et al., 2009), which leads to a directional radiation pattern with a profile determined by the field near the NW facet. There is no radiated power along the  $z$ -axis, a result that simply stems from the spatial symmetry and polarization of  $TM_0$  SPPs. Figure 4.31b also shows that when gold is replaced by silver (Lide, 2006) the NW reflection and emission are almost the same.

We then investigated the effect of changing the dielectric substrate. For example, when the refractive index is set to  $n_b = 2$ , reflections increase and the minima shift towards shorter NW radii. This is a further indication that the standing wave on the NW facet plays an important role in lowering reflection, as we found for the case of butt-coupling with a dielectric nanofiber. We have also considered the amount of reflection that is not channeled into SPPs and found that it can be negligible.

In summary, when SPPs reach the NW end they radiate in the forward direction with a very high efficiency if, for a given wavelength, the NW radius is appropriately chosen. Furthermore, the radius can be reduced by increasing the refractive index of the supporting substrate, but at the cost of increasing reflection.

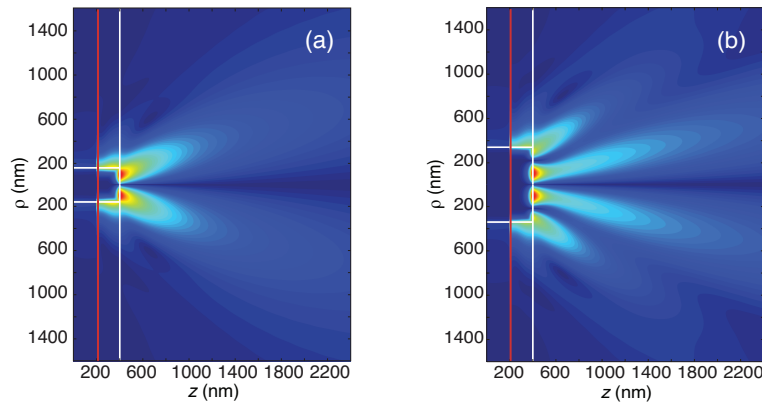


**Figure 4.32:** Time-averaged magnetic field for a gold NW on glass (refractive index  $n_b = 1.5$ ) with radii of (a) 160 nm and (b) 340 nm. The vacuum wavelength is 633 nm and the solid red lines indicate the source position.

### Optimizing the beam parameters

Here we are interested in the conversion of focused beams into SPPs of metal NWs. Reciprocity tells us that if the out-coupling efficiency is high, the same holds for the opposite direction. However, one has to clarify what beam profile should be used to perform this task. We thus considered the near field obtained from the



BOR-FD-TD calculations and transformed it to the far field. In the far region the field is a spherical transverse wave polarized along  $\theta$  since the  $\varphi$  component must be zero by symmetry considerations.

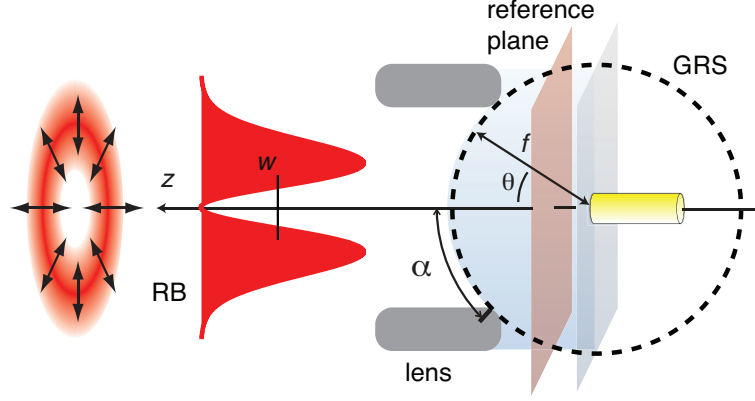


**Figure 4.33:** Matching the NW radiation pattern with a FRB. A radially-polarized beam RB is focused by an aplanatic lens onto the NW. The filled red curves sketch the intensity profile of a RB and the reference plane represents the integration domain used for the near-to-far-field transformation of the field radiated by the SPPs.

In the spherical coordinates  $(r, \theta, \varphi)$  we consider the Gaussian reference sphere GRS to interface the NW with the optical focusing system, as sketched in Figure 4.33. The polarization and spatial properties of the field on the GRS suggest that a good candidate for coupling optical energy in the NW would be a radially-polarized beam (Quabis et al., 2001). Its electric-field profile at the beam waist is given in Eq. (4.17). Figure 4.33 depicts how this enters the optical system to reach the GRS with a transformed field

$$\mathbf{E}(d, \theta) = E_0 \exp(-d^2 \sin^2 \theta / 2) d \sin \theta \sqrt{\cos \theta} \hat{\theta}, \quad (4.26)$$

where  $d = f/w$ ,  $\hat{\theta}$  is the unit vector, and  $\sqrt{\cos \theta}$  is the apodization function for an aplanatic system (Richards and Wolf, 1959).  $f$  is the lens focal length, which corresponds to the radius of the GRS, and  $w$  is the beam waist. The idea is to optimize the beam parameter  $d$  such that the FRB matches the SPPs radiation pattern, whose far field is given by Eq. (B.14) in Appendix B.1.5.

Figures 4.34a-d illustrate the calculated far field for different NWs and substrates at  $\lambda = 633$  nm. In Figure 4.34a the field of a gold NW on glass is maximum at about  $\theta = 18^\circ$  when the radius is 160 nm, showing that the FRB does not need to be tightly focused. Indeed, good overlap between the two fields is empirically obtained by setting  $d = 3.1$ , a value that leads to moderate focusing even with high-NA lenses (Quabis et al., 2001) and that exhibits a large  $\eta_{\text{inc}}$  (see Figure 4.23b). Interestingly, the radiation pattern does not depend very much on the refractive index of the substrate if one tunes the NW radius to minimize reflections, as seen by comparison of Figure 4.34a with b. An intuitive explanation is found if the NW



is considered as an aperture of radius  $r$ . A larger  $n_b$  increases the wavevector in the forward direction  $k_z = \sqrt{(2\pi/\lambda)^2 n_{br}^2 - k_\rho^2}$ , but a smaller aperture increases the span of the transverse wavevector  $k_\rho \in [0, 2\pi/r]$ . These effects compensate each others and lead to a small change in the radiation pattern.

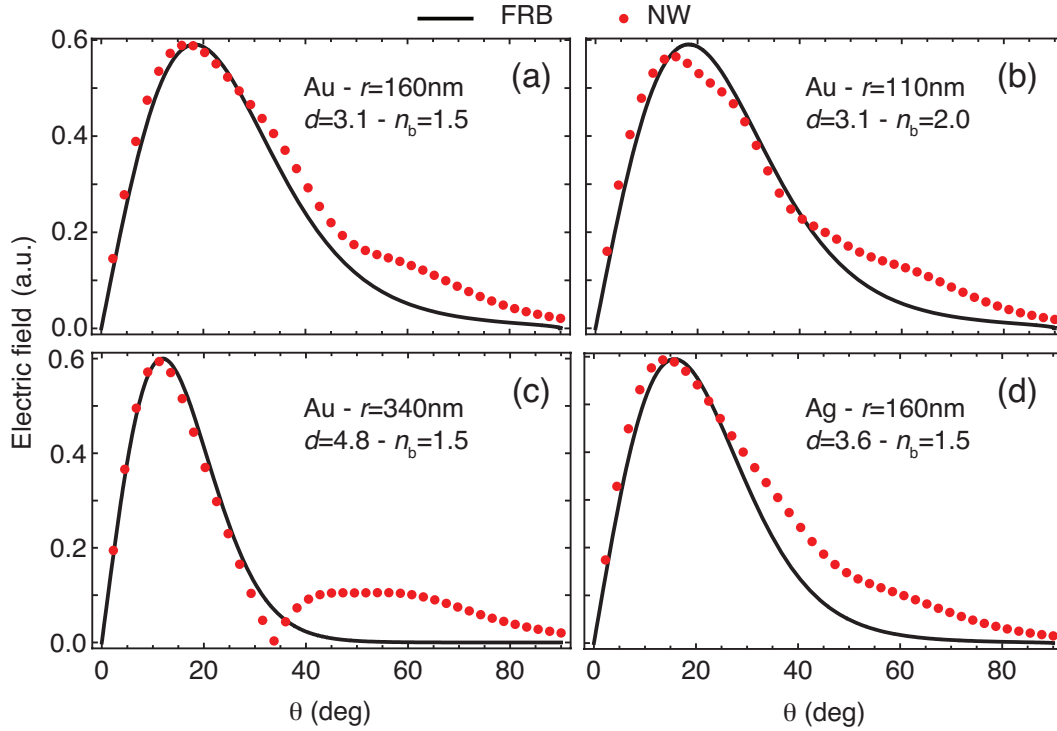


**Figure 4.34:** Matching the field radiated by a NW with FRBs on the Gaussian reference sphere. FRB (black solid curves) and the NW (red dots) on the GRS are displayed for different parameters. The vacuum wavelength is  $\lambda = 633 \text{ nm}$ ,  $f = 1.8 \text{ mm}$  and  $\alpha = 90^\circ$ .

As shown in Figure 4.34c, more directionality can be obtained by working with higher-order standing waves (see Figure 4.31d). The peak of the radiation pattern is now close to  $\theta = 12^\circ$  and its width is significantly narrower, but the radiation pattern exhibits a secondary lobe. As one last representative case, Figure 4.34d displays the SPPs radiation pattern for a silver NW on glass for a radius of 160 nm. The curve is very close to that of Figure 4.34a, as expected if one notes that the reflection minima in Figure 4.31b occur for nearly the same NW radii. While in Figure 4.34a the beam parameter  $d$  is set to overlap the NW and the FRB electric fields for both small and large angles, in Figure 4.34d the optimization targets only small angles. In the next section we will investigate how this affects the excitation of SPPs in the NW.

### Conversion efficiency and bandwidth

Having found that a FRB can match the radiation pattern of SPPs in semi-infinite metal NWs, we now assess the coupling efficiency in a more quantitative manner. To this end, we computed the electromagnetic field of a FRB in the focal region (Mojarad and Agio, 2009) and used it as a source for the BOR-FD-TD simulations.

Figure 4.35a shows the time-averaged magnetic field of a FRB in an infinite glass background for  $d = 3.1$  and  $\text{NA}=n_b$ . Next, we performed BOR-FD-TD simulations for gold and silver NWs on glass, varying  $d$  and the position of the focal spot with respect to the NW facet. The conversion efficiency was calculated by taking the ratio of the powers coupled in the SPP and in the incident FRB. To give more insight on the conversion process, Figure 4.35b displays the time-averaged magnetic field for the case of a FRB impinging on a gold NW on glass for a radius of 160 nm,  $d = 3.1$ , and the focal spot is 100 nm before the NW end facet. The beam is partially reflected, but the color scale shows that most of the energy is coupled into the SPP mode. Moreover, the field pattern confirms that the excitation of a standing wave on the NW facet plays a very important role in the conversion of photons into SPPs.

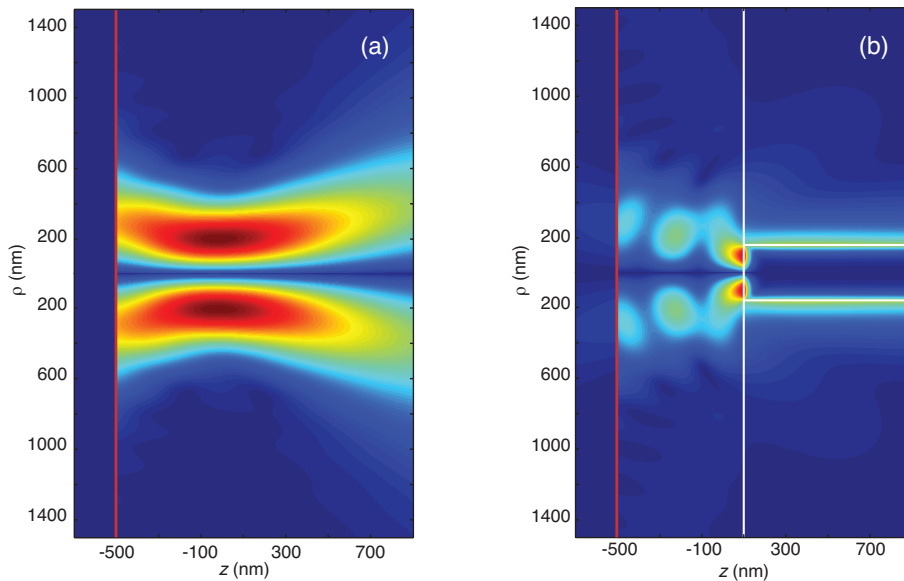


**Figure 4.35:** (a) Time-averaged magnetic field for a FRB in an infinite glass background ( $d = 3.1$ , refractive index  $n_b = 1.5$ ). (b) BOR-FD-TD simulation for a FRB incident on a gold NW on glass with  $r = 160$  nm. The beam parameter is  $d = 3.1$  and the focal spot is 100 nm before the NW facet. The white lines sketch the position of the substrate and the NW for the coupling problem. The  $z$  coordinate is with respect to the focal spot and the vertical red lines indicate the source position.

### Tolerance and bandwidth

Figure 4.36a shows that for both gold and silver NWs the efficiency is about 90% if the NW end is close to the focal spot and it remains larger than 60% even 400 nm away from the optimal position. The maximum does not occur exactly when the NW facet is in focus because the glass-air interface changes the properties of a focused beam (Ling and Lee, 1984). Choosing  $d = 3.6$  yields similar performances to the case for  $d = 3.1$ , suggesting that the FRB has to be optimized in the peak region. Therefore, lenses with a lower NA shall not affect these results. For example, in Figure 4.34c the field amplitude of the FRB at  $\theta = 45^\circ$  is about 10% of the maximum (1% for the intensity), meaning that an NA of 0.7 in air would be enough to couple most of the beam energy into the SPP. Figure 4.36b confirms that NW radius and operating wavelength are not independent from each others since the coupling efficiency drops when the radius departs from the value that minimizes reflections (see Figure 4.31b). Nonetheless, this analysis indicates a bandwidth of more than 50 nm if the coupling efficiency has to be larger than 80%.

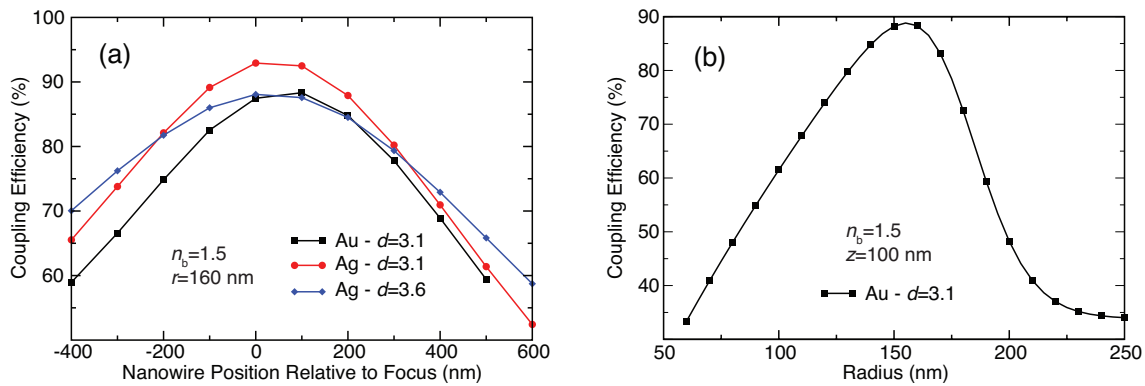


**Figure 4.36:** (a) Coupling efficiency as a function of the NW position with respect to the focal spot. (b) Coupling efficiency as a function of the NW radius, when the NW position is 100 nm.

### 4.3.4 High-throughput SNOM

We now discuss an immediate consequence of efficient and broad-band SPP-photon conversion between a NW and a NF from both directions. Over the last decade, several reports have pointed out that SPPs can be focused tightly to nanoscopic regions at metallic tips (Babadjanyan et al., 2000; Keilmann, 1999; Stockman, 2004). This phenomenon can indeed revolutionize high-resolution scanning near-field optical microscopy, which has suffered from a very low transmission through small apertures (Novotny et al., 1995). However, so far there has been no viable approach for feeding optical energy into the SPP mode of the NW with a high efficiency. The device concept sketched in Figure 4.37 provides an ideal solution for simultane-

ous intense and localized illumination as well as efficient collection. Furthermore, it is fully compatible with both state-of-the-art nanofabrication (De Angelis et al., 2008) and scanning implementations of fluorescence, Raman, or other nonlinear nanoscopies (Ichimura et al., 2004; Sánchez et al., 1999).

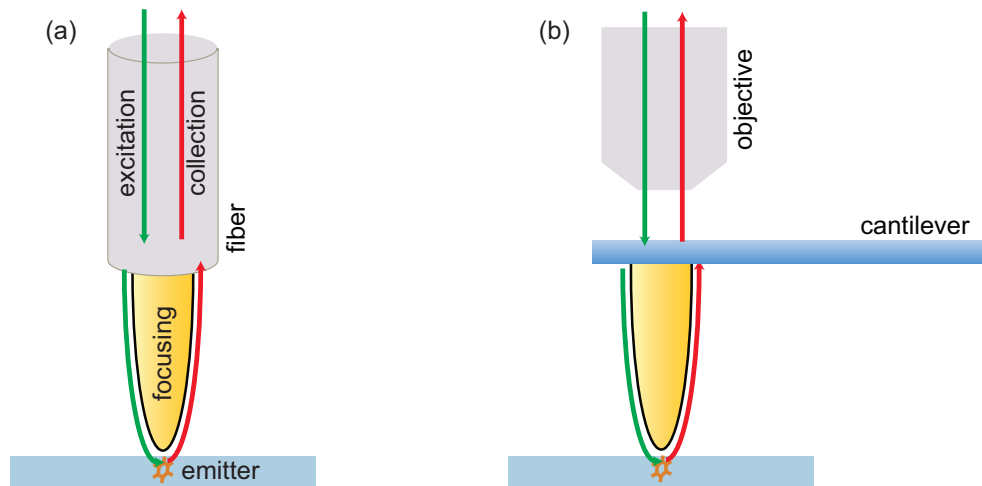


**Figure 4.37:** Schemes of a (a) fiber and (b) cantilever-based high-throughput SNOM.

The efficient excitation of SPPs in NWs by a focused radially polarized beam can also be immediately transferred to nanocones. Figure 4.37b sketches a possible implementation of a cantilever-based high-throughput SNOM. The radially polarized beam is focused by a lens onto the nanocone base. The dielectric interface between the lens and the cantilever has a small effect on the beam profile, which if necessary can be compensated by placing a solid-immersion lens. The energy is then converted into SPPs and nanofocused. Since the tip apex is out of focus, the direct light of the FRB is almost negligible in the scanning region. The device can also be operated in the collection mode, where SPPs generated by a local source near the nanocone tip propagate along the nanocone and radiate with a directional pattern towards the collection optics. The weak resonant character of the standing wave adds the important advantage of large operation bandwidths, which are sufficient for collecting and launching fs pulses in the device.

### Nanofocusing

Nanofocusing refers to the concentration of optical energy carried by a SPP wave while it propagates along a tapered metal NW (Babadjanyan et al., 2000; Goncharenko et al., 2007, 2006a,b; Issa and Guckenberger, 2007b; Keilmann, 1999; Stockman, 2004; Vogel and Gramotnev, 2007). Since the NW does not have a cutoff for the SPP wave, the latter can travel towards the tip even when the nanocone radius has become much smaller than the wavelength. Large field enhancements can be achieved if the cone apex is sufficiently sharp (Babadjanyan et al., 2000; Stockman,

2004), as shown in Figure 4.39. However, since nanocones suffer from propagation losses, a rapid and efficient conversion of SPPs into photons and vice versa is required. We thus exploit the previous findings to replace semi-infinite cones with truncated ones.

### Throughput and resolution

Here we focus the attention on the field enhancement and the spatial resolution of the SNOM device. To this purpose we consider the normalized energy density  $W/W_{\text{BL}}$ , where  $W_{\text{BL}} = P_{\text{inc}}k^2/(3\pi c)$  is the maximum achievable by far-field focusing for a given incident power  $P_{\text{inc}}$  and wavevector  $k$  (Bassett, 1986). Since in our model the FRB is propagating from a glass substrate, we set  $W_{\text{BL}}$  for a homogeneous medium with a refractive index equal to 1.5.

We then chose a gold nanocone with a base radius of 160 nm and a tapering angle of  $8^\circ$  illuminated by a FRB with  $d = 3.1$ . The tip apex was a paraboloid ( $z = \rho^2/(3.2 \text{ nm})$ ) and the cantilever was modeled as a semi-infinite glass substrate. Figure 4.38a plots  $W/W_{\text{BL}}$  at a distance  $z = 1115$  nm from the cantilever, which corresponds to a plane 5 nm away from the cone tip. A zoom of  $W/W_{\text{BL}}$  is shown in Figure 4.38b, where the contributions associated with the longitudinal  $E_z$  and transverse ( $E_\rho$ ) electric field components are also indicated. The FWHM for  $W/W_{\text{BL}}$  is of the order of 10 nm and it is primarily due to  $E_z$ . The maximum value of  $W/W_{\text{BL}}$  reveals that for the same  $P_{\text{inc}}$  the nanocone allows energy concentrations that are nearly 1000 times larger than what can be achieved by far-field focusing. Furthermore, the total energy at the observation plane is about 65% of that near the focus of the FRB, proving that a large fraction of optical energy can be transported to the nanoscale. Recent experiments on SPP excitation in NWs by adiabatic compressors have indeed found similar efficiencies in the near-infrared spectral range (Verhagen et al., 2009).

At last it is interesting to note how the features of a FRB can be exploited to minimize background illumination. To this aim, Figure 4.38b displays  $W/W_{\text{BL}}$  obtained without gold cone at different distances from the cantilever and for the same incident FRB. We found that near the cone tip ( $z = 1100$  nm)  $W/W_{\text{BL}}$  is more than two orders of magnitude smaller than in the focal region ( $z = 20$  nm). This corresponds to a strong background suppression compared to illuminations where the incident beam is focused on the cone tip.

### Collection efficiency

As a concrete example, we considered illumination at  $\lambda=730$  nm and fluorescence collection at  $\lambda=780$  nm from an emitter with a transition dipole moment oriented along the tip axis and embedded 5 nm below surface of a sample with a refractive index of 1.7. The excitation light was launched from a NF of 410 nm radius, coupled

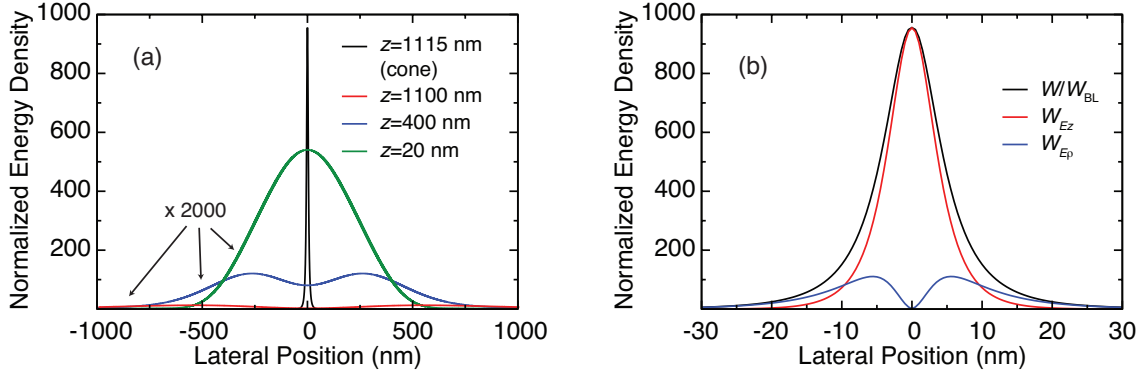


**Figure 4.38:** (a) Normalized energy density  $W/W_{BL}$  in a plane located at  $z = 1115$  nm from the cantilever when a gold cone is illuminated by a FRB under the same conditions of Figure 4.36b (see text for details). The plane is 5 nm from the cone tip. The graph shows also  $W/W_{BL}$  for various  $z$  when the cone is not present. (b) Zoom of (a) for the case where a gold cone is present. The contributions to  $W/W_{BL}$  due to the two electric field components  $E_z$  and  $E_\rho$  are indicated as  $W_{Ez}$  and  $W_{E\rho}$ , respectively.

to a gold nanocone with an initial radius of 200 nm, and an opening angle of  $14^\circ$ , which was terminated by a paraboloid. The tip was kept at a separation of 5 nm from the substrate. In Figure 4.39b we plot the electric field intensity normalized to that of the source in the NF on a logarithmic scale for a zoom of a small region around the tip. The intensity is enhanced by more than 5 orders of magnitude and exhibits strong localization. Figure 4.39c illustrates the emission process. We find that the radiated power is funneled in the SPP and is then converted into the  $TM_{01}$  mode of the NF with an overall collection efficiency of about 70%, which is only limited by propagation losses and radiation along the nanocone.

We demonstrated two highly efficient schemes for converting free-space photons into SPPs in NWs, and combined it with nanofocusing to concentrate optical energy below the diffraction limit with a high throughput. Our approach relies on the directional radiation and low reflection of SPPs at the NW end, which occur if the NW radius is chosen according to the operation wavelength and the supporting substrate. These properties are associated with the formation of a standing wave at the NW facet (Chen et al., 2009). Furthermore, by analyzing the radiation pattern and polarization in the far region we identified weakly-focused radially-polarized beams as the best way to excite SPPs from the NW facet (Chen et al., 2010a). We showed indeed that conversion efficiencies of 90% can be reached by optimizing the beam parameters and the position of the NW in the focal region.

In contrast to previous works on metal nanocones and radially-polarized light, which do not focus the beam on the nanocone base (Antosiewicz et al., 2009; Baida and Belkhir, 2009; Descrovi et al., 2005; Fleischer et al., 2008), our scheme yields a better conversion efficiency and lower background noise caused by direct illumination of the sample. These results were presented for  $\lambda = 633$  nm, but any

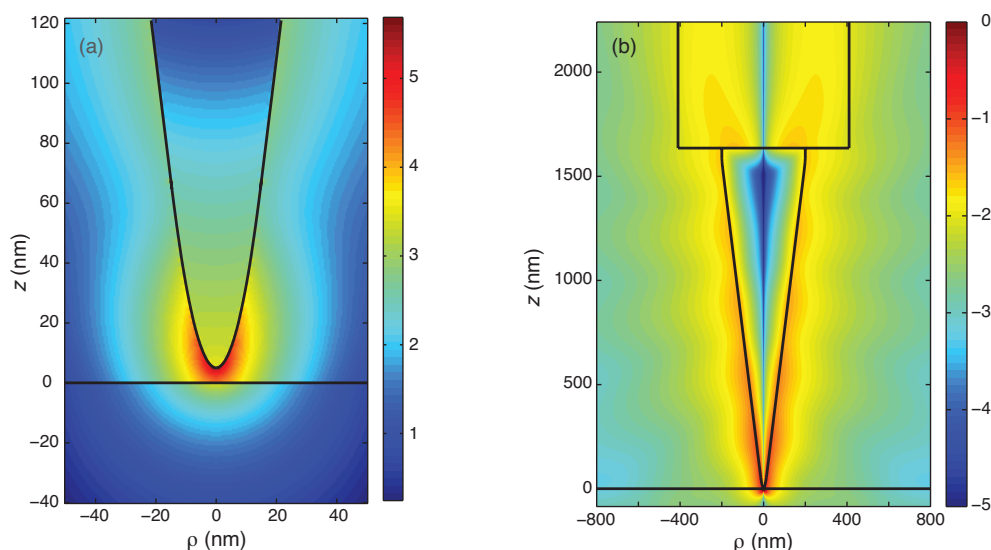


**Figure 4.39:** (a) Normalized distribution (logarithmic scale) of the electric field intensity near a substrate when photons are launched from the NF into the NW cone. (b) Time-averaged magnetic field radiated by a single emitter embedded in the substrate (see text for details).

wavelength from the ultraviolet to the near-infrared range would work by adjusting the NW radius and composition (Chen et al., 2009).

For the huge intensity that can be achieved at the nanocone tip and the large operation bandwidth, we envision not only better implementations of fluorescence, Raman and other nonlinear (time-resolved) nanoscopies (Hartschuh, 2008; Ichimura et al., 2004; Sánchez et al., 1999), but also applications in all areas that would benefit from high-throughput concentration of optical energy in nanoscale spots and fs time scales (Zavelani-Rossi et al., 2008). Efficient, broad-band and low-loss conversion of confined SPPs to guided photons is also key for a range of other applications such as high-resolution color imaging (Kawata et al., 2008), on-chip manipulation and processing of quantum optical signals (Chang et al., 2006, 2007b; Domokos et al., 2002), and actuation or sensing of physical, chemical, or biological processes at the molecular level (Zheng et al., 2009).

# Chapter 5

## Towards nanoscale cavities

In the previous chapters we have discussed the importance of light confinement for improving light-matter interactions and for enhancing quantum effects like the modification of the spontaneous emission rate (Purcell, 1946). For optical antennas we found that fluorescence can be increased by orders of magnitude and that the dipolar radiation pattern of a single molecule can be converted into a well-defined optical mode. In the past decades these phenomena have been extensively investigated and applied in the framework of optical resonators (Benisty et al., 1999; Vahala, 2003). In particular, in the late '90s progress in nanotechnology has enabled the fabrication of miniaturized cavities with mode volumes of the order of one cubic wavelength and very large quality factors (Akanane et al., 2003; Painter et al., 1999; Song et al., 2005).

Obtaining resonators with even smaller dimensions is however very difficult without degrading their performances. The problem is that dielectric mirrors require several Bragg layers to achieve a high reflectivity. On the other hand, metal mirrors exhibit large absorption losses at optical frequencies. Nonetheless, nanoscale metallic cavities are being explored for the realization of ultrasmall lasers (Hill et al., 2007; Kroekenstoel et al., 2009; Nezhad et al., 2010; Noginov et al., 2009; Oulton et al., 2009), and for controlling single-photon sources (Maksymov et al., 2010). These designs, however, insist on using metals as reflective mirrors to trap light, like in a standard Fabry-Pérot cavity. In parallel, theoretical works have discussed the enhancement of light-matter interaction by a metal nanocavity using the mode-volume picture and the Purcell factor (Koenderink, 2010; Kuttge et al., 2010; Maier, 2006; Oulton et al., 2008). They somewhat disagree on the definition of a mode volume because a dissipative environment does not have normalizable true modes (Dutra and Nienhuis, 2000), but they all point out that a nanoscale mode volume can compensate the low quality factor caused by absorption losses. These settings are indeed very attractive for the realization of nanoscale devices for light generation and signal amplification (Bergman and Stockman, 2003; Noginov et al., 2009; Protsenko et al., 2005; Stockman, 2010)

Motivated by these developments, in this chapter we make a connection be-



tween field-enhanced spectroscopy, antenna theory and cavity quantum electrodynamics. Our aim is to derive simplified antenna models to express figures of merit and scaling laws that can be compared with the common parameters of a resonator, i.e. quality factor, mode volume, device footprint, and Purcell factor. Furthermore, we pay attention to the antenna efficiency and study how it affects the other performances.

## 5.1 From antenna theory to nanoscale resonators

In this section we briefly review the formulation of cavity quantum electrodynamics in the perturbative regime. Next, we discuss the relationship between the Purcell factor and the modification of the spontaneous emission rate by optical antennas, with emphasis on the local density of photonic states. We then establish a connection between the field enhancement and the near-field zone of a radio-wave antenna.

### 5.1.1 Cavity quantum electrodynamics

The radiative properties of an atom are not intrinsic, but they also depend on the electromagnetic environment and on its coupling with the atom. These two parameters can be strongly modified by a high-finesse cavity, where the continuous of electromagnetic modes is redistributed in frequency and space. Under these circumstances a number of phenomena associated with the quantum nature of light can be observed. These include, for example, the enhancement or inhibition of spontaneous emission, vacuum Rabi splitting, and quantum collapse and revivals (see Haroche and Kleppner, 1989, for an introductory review).

Here we only consider the situation where light-matter interaction can be treated in the perturbative regime, which is the same level of theory used in the previous chapter for optical antennas. Furthermore, the cavity has well defined modes that lead to the canonical formulation of cavity QED. In what follows we will not discuss the technical issue of the field quantization in the presence of absorptive and dispersive media (Knöll et al., 2001; Wylie, 1986).

#### Modification of the spontaneous emission rate

Purcell (1946) was the first to recognize that the spontaneous emission rate of an excited TLS can be significantly enhanced when the transition is on resonance with the mode of an optical cavity. For a TLS the transition rate from the excited  $|2\rangle$  to the ground  $|1\rangle$  state is given by the Fermi golden rule (Loudon, 2000)

$$\Gamma_o = \frac{2\pi}{\hbar} \sum_{\mu} |\langle 1, \mu | \mathbf{d} \cdot \mathbf{E}(\mathbf{r}_o) | 2, 0 \rangle|^2 \delta(\hbar\omega - \hbar\omega_{\mu}), \quad (5.1)$$

where  $\mu$  represents a photon mode of energy  $\hbar\omega_\mu$ ,  $\mathbf{d}$  is the dipole moment,  $\mathbf{E}(\mathbf{r}_o)$  is the electric field at the TLS location and  $\hbar\omega$  is the transition energy of the TLS. In free space the quantized electromagnetic field is expressed by

$$\mathbf{E}(\mathbf{r}) = i \sum_{\mu} \sqrt{\frac{\hbar\omega_{\mu}}{2\epsilon_0 V}} \mathbf{e}_{\mu} \left( \hat{a}_{\mu} e^{i\mathbf{k}\cdot\mathbf{r}} - \text{h.c.} \right), \quad (5.2)$$

where h.c. means Hermitian conjugation of the preceding term.  $V$  is the quantization volume,  $\mathbf{e}_{\mu}$  is the polarization versor and  $\hat{a}_{\mu}$  is the destruction operator for one photon in the mode  $\mu$  (Loudon, 2000). Using Eq. (5.2) in Eq. (5.1) we obtain

$$\Gamma_o = \frac{2\pi}{\hbar} \sum_{\mu} \frac{\hbar\omega_{\mu}}{2\epsilon_0 V} |\mathbf{d} \cdot \mathbf{e}_{\mu}|^2 \delta(\hbar\omega - \hbar\omega_{\mu}) = \frac{2\pi}{3\epsilon_0} \omega d^2 g_o(\omega) = \frac{d^2 \omega^3}{3\pi\epsilon_0 \hbar c^3}. \quad (5.3)$$

$g_o(\omega)$  is the density of photonic states (DOS) in vacuo for one polarization and it is given by  $g_o(\omega) = \omega^2 / (2\pi^2 \hbar c^3)$ .

When the TLS is inside a resonator Eq. (5.2) needs to be replaced by (Haroche, 1992)

$$\mathbf{E}(\mathbf{r}) = i \sum_{\mu} \sqrt{\frac{\hbar\omega_{\mu}}{2\epsilon_0}} \left( \hat{a}_{\mu} \boldsymbol{\alpha}_{\mu}(\mathbf{r}) - \text{h.c.} \right), \quad (5.4)$$

where  $\boldsymbol{\alpha}_{\mu}(\mathbf{r})$  is the mode field profile. With Eq. (5.4) the spontaneous emission rate becomes

$$\Gamma = \frac{2\pi}{\hbar} \sum_{\mu} \frac{\hbar\omega_{\mu}}{2\epsilon_0} |\mathbf{d} \cdot \boldsymbol{\alpha}_{\mu}(\mathbf{r}_o)|^2 \delta(\hbar\omega - \hbar\omega_{\mu}). \quad (5.5)$$

This expression is the basis for the calculation of spontaneous emission rates in a microcavity.

### Purcell factor, mode volume and Q factor

We now assume that the transition frequency is resonant with only one mode  $\boldsymbol{\alpha}_{\mu}(\mathbf{r})$  and that the dipole moment is parallel to the electric field. Next, the atomic line is much narrower than the cavity mode and the latter has a Lorentzian profile with a FWHM  $\gamma_{\mu}$ . Under these circumstances the DOS reads

$$g_{\mu}(\omega_{\mu}) = \frac{2}{\pi \hbar \gamma_{\mu}} = \frac{2Q_{\mu}}{\pi \hbar \omega_{\mu}}, \quad (5.6)$$

where  $Q_{\mu} = \omega_{\mu} / \gamma_{\mu}$  is the quality factor. The mode volume for the position  $\mathbf{r}_o$  is defined as  $V_{\mu} = |\boldsymbol{\alpha}_{\mu}(\mathbf{r}_o)|^{-2}$  and Eq. (5.5) can be expressed in the form

$$\Gamma_{\mu} = \frac{2d^2 Q_{\mu}}{\epsilon_0 \hbar V_{\mu}} = F\Gamma_o, \quad (5.7)$$

where  $F$  is the Purcell factor

$$F = \frac{3}{4\pi^2} \lambda^3 \frac{Q_\mu}{V_\mu}. \quad (5.8)$$

The condition for having a large Purcell factor, hence a strong enhancement of the spontaneous emission rate, is that the cavity has a high  $Q$  factor and a small mode volume. In place of the Purcell factor one can define the local DOS (LDOS)  $\rho_\mu(\mathbf{r}_o, \omega) = g_\mu(\omega) |\boldsymbol{\alpha}_\mu(\mathbf{r}_o)|^2$  and express the modification of the spontaneous emission rate as

$$\Gamma_\mu = \frac{\pi d^2 \omega}{\epsilon_0} \rho_\mu(\mathbf{r}_o, \omega) = \frac{\rho_\mu(\mathbf{r}_o, \omega)}{\rho_o(\mathbf{r}_o, \omega)} \Gamma_o, \quad (5.9)$$

where  $\rho_o(\mathbf{r}_o, \omega)$  is the LDOS in vacuo. Note that the mode volume is often expressed in units of the cubic wavelength. We do so in the following sections and write  $V_m = (\lambda/n_b)^3 V_\mu$ , where the refractive index  $n_b$  is added to generalize the formula to dielectric media.

### 5.1.2 Field-enhanced spectroscopy

The theoretical models used for field-enhanced spectroscopy are often based on the semi-classical theory of light-matter interaction (Metiu, 1984; Moskovits, 1985). Moreover, optical resonators are replaced by interfaces and metal nanoparticles. These are systems that cannot be easily described with the standard toolbox of cavity QED, despite some recent attempts (Savasta et al., 2010; Trügler and Hohenester, 2008).

#### Modification of the spontaneous emission rate

First, we want to show the connection between the formalism of Fermi golden rule, the modification of the LDOS and the formulae used in Chapter 4. In Appendix B.2.2 we have discussed the calculation of the spontaneous emission rate using the expression

$$P_t = -\frac{1}{2} \int_V \text{Re} \{ \mathbf{j}^*(\mathbf{r}, \omega) \cdot \mathbf{E}(\mathbf{r}, \omega) \} dV, \quad (5.10)$$

where  $P_t$  is the total power dissipated by the current density  $\mathbf{j}(\mathbf{r}, \omega)$ . For an infinitesimal oscillating dipole  $\mathbf{p}$  located at  $\mathbf{r}_o$  one writes  $\mathbf{j}(\mathbf{r}, \omega) = -i\omega \mathbf{p} \delta(\mathbf{r} - \mathbf{r}_o)$  and the previous equation takes the form

$$P_t = \frac{\omega}{2} \text{Im} \{ \mathbf{p}^* \cdot \mathbf{E}(\mathbf{r}_o) \}. \quad (5.11)$$

To make the connection with the modification of the LDOS we recall that the electric field radiated by a dipole source at  $\mathbf{r}_o$  is related to the Green tensor  $\mathbf{G}$  by (Jackson, 1999)

$$\mathbf{E}(\mathbf{r}) = \frac{1}{\epsilon_0} \frac{\omega^2}{c^2} \mathbf{G}(\mathbf{r}, \mathbf{r}_o; \omega) \cdot \mathbf{p} \quad (5.12)$$

and that (Chance et al., 1978)

$$\rho(\mathbf{r}_o, \omega) = \frac{6\omega}{\pi c^2} [\mathbf{n}_p \cdot \text{Im} \{ \mathbf{G}(\mathbf{r}_o, \mathbf{r}_o; \omega) \} \cdot \mathbf{n}_p], \quad (5.13)$$

where  $\mathbf{n}_p$  represents the dipole orientation. By comparing Eqs. (5.11) and (5.13) we obtain

$$P_t = \frac{\pi\omega^2}{12\epsilon_0} |\mathbf{p}|^2 \rho(\mathbf{r}_o, \omega), \quad \text{and} \quad \frac{P_t}{P_r^o} = \frac{\rho(\mathbf{r}_o, \omega)}{\rho_o(\mathbf{r}_o, \omega)}, \quad (5.14)$$

where  $P_r^o$  and  $\rho_o(\mathbf{r}_o, \omega)$  are the radiated power and the LDOS without antenna, respectively. Note that the change in the LDOS affects the total decay rate. The radiative one is obtained by multiplying  $\Gamma_t$  by the antenna efficiency.

### Field enhancement

For an antenna that preserves the dipolar radiation pattern of the emitter the modification of the radiative decay rate can be related to the field intensity enhancement (Taminiau et al., 2008b). For an incident amplitude  $E_o$ , the electric field near the antenna tip reads (Wokaun et al., 1982)

$$E_{\text{tip}} = \zeta E_{\text{dip}} + E_o \simeq (1 - L)\chi E_o, \quad (5.15)$$

where  $\zeta$  represents the so-called lighting rod effect and  $E_{\text{dip}}$  is the near field caused by the electric dipole induced in the antenna Moskovits (1985). The expression can be reformulated using  $\chi$ , the antenna susceptibility, and  $L$ , a geometrical factor related to the lighting rod effect. Therefore, the change in the spontaneous emission rate can be written as

$$\frac{P_t}{P_r^o} = \left| \frac{E_{\text{tip}}}{E_o} \right|^2 \frac{1}{\eta_a}, \quad (5.16)$$

where  $\eta_a$  is the antenna efficiency (see Eq. (4.9)).

### 5.1.3 Antenna theory

Now that we have established a relationship between the perturbative regime of cavity QED and the modification of the spontaneous emission rate by optical antennas, we wish to investigate the connection between the field enhancement and conventional antenna theory.

#### Infinitesimal dipole antenna

Let us consider an infinitesimal dipole with length  $l \ll \lambda$  driven by a current  $I_o$ . In the spherical coordinates  $(r, \varphi, \theta)$  the electric field radiated by the antenna

reads (Balanis, 2005; Jackson, 1999)

$$E_r = Z \frac{I_0 l k^2 \cos \theta}{2\pi (kr)^2} \left(1 - \frac{1}{ikr}\right) e^{ikr} \quad (5.17)$$

$$E_\theta = -iZ \frac{I_0 l k^2 \sin \theta}{4\pi kr} \left(1 - \frac{1}{ikr} - \frac{1}{(kr)^2}\right) e^{ikr} \quad (5.18)$$

$$E_\varphi = 0, \quad (5.19)$$

where  $Z \simeq 376$  Ohms is the impedance of free space.

### Near-field and radiation zones

The electric field contains terms that are inversely proportional to  $kr$  and others that decay more rapidly. In antenna theory one defines the complex Poynting vector (Balanis, 2005)

$$\mathbf{S} = \frac{1}{2} \mathbf{E} \times \mathbf{H}^*. \quad (5.20)$$

Next we consider a spherical surface of radius  $r$  and compute the power flow

$$P = \frac{1}{2} \int_{4\pi} \mathbf{S} \cdot \mathbf{n} r^2 d\Omega = P_r + iP_i. \quad (5.21)$$

$P_r$  is the power radiated by the antenna, whereas  $iP_i$  is purely imaginary and there is no time-average power flow associated with it. It is in fact called reactive power and it stands for the electromagnetic energy stored near the antenna. From Poynting theorem one can write

$$P_i = 2\omega(W_e - W_m), \quad (5.22)$$

where  $W_e$  and  $W_m$  are the electric and magnetic energy densities in the radial direction, respectively. The relationship between  $P_i$  and the field enhancement near an optical antenna can be understood by considering the two quantities in Eq. (5.21) for an infinitesimal dipole antenna, which read (Balanis, 2005)

$$P_r = Z \frac{\pi}{3} \left| \frac{I_0 l}{\lambda} \right|^2, \quad P_i = Z \frac{\pi}{3} \left| \frac{I_0 l}{\lambda} \right|^2 \frac{1}{(kr)^3}. \quad (5.23)$$

$P_i$  decreases with  $(kr)^3$  and vanishes in the far field, whereas  $P_r$  is constant. The reactive part of the antenna radiation field can be associated with the field enhancements exhibited by metal nanoparticles. Since these have dimensions smaller than the wavelength, it turns out that near the metal surface  $P_i \gg P_r$ . By reciprocity, we can argue that the incoming radiation becomes reactive in the proximity of the nanoparticle and it gives rise to a concentration of electromagnetic energy.

## 5.2 Electrically small antennas

We now discuss some features of optical antennas starting from electrically small antennas. Their name stems from the fact that the characteristic dimensions are much smaller than the wavelength of the field they radiate. Since antennas are devices conceived to couple to free space waves, one expects limitations upon size reduction. These have been extensively studied since the end of World War II, when the miniaturization of radar systems emerged as a strategic warfare technology. In what follows we introduce these limits and discuss their role in determining the performances of optical antennas.

### 5.2.1 Fundamental limitations

The theory of electrically small antennas has been developed by several authors. Here we go after the works of Chu (1948), Hansen (1981) and McLean (1996) and focus on the relationship between the quality factor and the reactive energy as a function of the antenna dimensions.

#### Quality factor

Chu was the first to use the  $Q$  factor as a figure of merit to assess the performance limitations of electrically small antennas. For an antenna the  $Q$  factor is defined as

$$Q = 2\omega \frac{\max\{W_e, W_m\}}{P_r}, \quad (5.24)$$

where  $W_e$  and  $W_m$  are the time-averaged electric and magnetic energies associated with the non-propagating part of the electromagnetic field generated by the antenna. For electrically small antennas it turns out that  $W_e$  is much larger than  $W_m$ , as expected for an oscillating electric dipole (Jackson, 1999).

Chu considered an antenna enclosed in virtual sphere of radius  $kr$  and computed the minimum  $Q$  factor that it could have. The calculation can be conveniently carried out by a multipole expansion of the electromagnetic field, where the stored energy refers to the non-propagating power external to the sphere. For a linearly polarized antenna the theoretical minimum is given by (McLean, 1996)

$$Q \simeq \eta_a \left( \frac{1}{(kr)^3} + \frac{1}{kr} \right). \quad (5.25)$$

We have added the antenna efficiency  $\eta_a$  to facilitate the comparison with optical antennas. For radio-wave antennas  $\eta_a$  can be assumed close to unity. It is found that the  $Q$  factor goes to infinity when  $kr$  approaches the value of zero, meaning that an antenna cannot be made indefinitely small without compromising its radiation and bandwidth performances. Note that for an infinitesimal dipole antenna with

length  $2r$  much larger than its cross section  $2a$ , the  $Q$  factor,

$$Q \simeq \frac{6 \log(r/a) - 1}{(kr)^2 \tan(kr)}, \quad (5.26)$$

is larger than that of Eq. (5.25). In fact, the dipole antenna exhibits worse performances because it does not fully exploit the volume of the virtual sphere (Hansen, 1981). When an electrically small antenna approaches dimensions where  $kr \ll 1$ , the  $Q$  factor gets very large and the system behaves as a subwavelength resonator. It is worth pointing out that in a microcavity the electromagnetic energy is prevented from escaping into free space by high-reflectivity mirrors, while here it is stored because the antenna becomes a very inefficient radiator.

### Near-field zone

Interestingly, the increase in the  $Q$  factor corresponds to a decrease in the antenna volume. The latter is also associated with the field enhancement, as discussed in Section 5.1.3. We thus conclude that an electrically small antenna wins regarding another important feature of an optical resonator, namely its mode volume. This can indeed be related to the field enhancement, as pointed out by Maier (2006) and other authors. We therefore anticipate that the limitations of electrically small antennas become advantageous for enhancing the radiation properties of nearby quantum emitters.

## 5.2.2 Figures of merit for optical antennas

In Chapter 4 we have presented antenna designs that could significantly improve light-matter interaction. In place of rigorous electrodynamic calculations, it is useful to present an approximate but general model that can be used to gain insight on these concepts and to make the connection with antenna theory and quantum electrodynamics in the perturbative regime.

### The model

We consider a prolate spheroidal nanoparticle with long  $a$  and short  $b$  semi-axes, whose physical volume is given by  $V_{\text{ph}} = 4\pi ab^2/3$ . The antenna is made from a Drude metal with dielectric function

$$\epsilon(\omega) = \epsilon_b - \frac{\omega_p^2}{\omega(\omega + i\gamma)}, \quad (5.27)$$

where it is convenient to choose  $\epsilon_b$  equal to that of the surrounding medium.  $\omega_p$  and  $\gamma$  are the plasma and damping frequencies, respectively (Ashcroft and

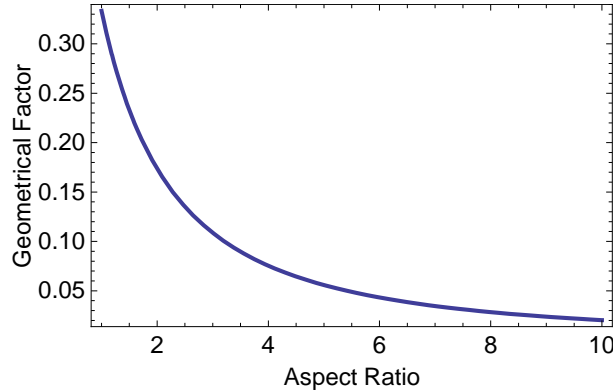
Mermin, 1976). The optical properties of the antenna can be worked out starting from a polarizability model with radiative corrections (Wokaun et al., 1982).

$$\alpha \simeq \frac{2\pi ab^2}{3L} \frac{\omega_o}{\omega_o - \omega - i \left( \frac{\gamma}{2} + k^3 \frac{ab^2}{9L} \omega_o \right)}, \quad (5.28)$$

where  $\omega_o = \omega_p \sqrt{L/\epsilon_b}$  and  $\gamma + 2k^3 ab^2 \omega_o / 9L = \Gamma_a$  are the antenna resonance frequency and linewidth, respectively. Note that  $\Gamma_a$  has two contributions. The first term represents absorption by the Drude metal and the second one radiation by the antenna. In Eq. (5.28) we have introduced the geometrical factor  $L$  (Bohren and Huffman, 1983), which for a prolate spheroid reads

$$L(e) = \frac{1 - e^2}{e^2} \left( -1 + \frac{1}{2e} \log \left( \frac{1 + e}{1 - e} \right) \right), \quad (5.29)$$

where the eccentricity  $e$  reads  $e^2 = 1 - (b/a)^2$  and  $AR = a/b$  is the aspect ratio. The geometrical factor and the aspect ratio will be present in several of the following expressions. Figure 5.1 plots  $L$  as a function of  $AR$ . For a sphere  $AR=1$  and  $L$  becomes equal to  $1/3$ . For a prolate spheroid  $AR > 1$  and the geometrical factor tends to 0 when  $AR \gg 1$ .



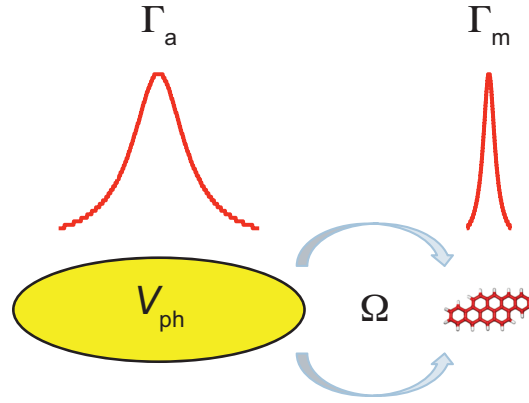
**Figure 5.1:** Geometrical factor  $L$  as a function of the aspect ratio  $AR$ . For a sphere  $AR=1$  and  $L$  takes the value of  $1/3$ .

Figure 5.2 illustrates our antenna model and the coupling to a single molecule. The latter has the resonance frequency equal to that of the antenna, but the emitter linewidth  $\Gamma_m$  is assumed to be much smaller than  $\Gamma_a$ . Furthermore, the interaction between the electromagnetic field associated with the optical antenna and the molecule is parametrized by the vacuum Rabi frequency  $\Omega$  (Cohen-Tannoudji et al., 2004).

### Antenna efficiency

We now derive the relevant antenna parameters starting from the efficiency  $\eta_a$ . As discussed in Chapter 4,  $\eta_a$  depends on the antenna as well as on the position





**Figure 5.2:** A single molecule coupled to an optical antenna in the cavity QED picture.  $V_{\text{ph}}$  is the physical volume and it reads  $4\pi ab^2/3$  for a prolate spheroid, where  $a$  and  $b$  are the long and short semi-axes, respectively.  $\Gamma_a$  and  $\Gamma_m$  are the antenna and the emitter linewidths, respectively. The interaction strength is represented by the Rabi frequency  $\Omega$ .

and orientation of the emitter. To avoid these details a good approximation for  $\eta_a$  is the ratio between the scattering  $C_{\text{sca}}$  and the extinction  $C_{\text{ext}}$  cross sections of the antenna. This definition should not be considered a crude approximation, but rather an upper bound that is very close to the realistic values obtained for high-performance antennas (Mohammadi et al., 2009a). By using Eq. (5.28) into Eqs. (2.24) we arrive at

$$\eta_a = \frac{1}{1 + \frac{\gamma}{\omega_p} \frac{9\sqrt{\epsilon_b} L A R^2}{2(ka)^3}}. \quad (5.30)$$

This formula shows that  $\eta_a$  decreases quite rapidly with the antenna volume, whereas the dependence on material losses enters through the quantity

$$\frac{\gamma}{\omega_p} \simeq \frac{1}{160} \sqrt{\frac{4\pi a_o^3}{3} n \rho}, \quad (5.31)$$

where  $a_o$  is the Bohr radius,  $n$  is the electron density, and  $\rho$  is the resistivity (Ashcroft and Mermin, 1976). Figure 5.3 displays this parameter for selected metals. Note, however, that these values are often given for a static electric field. At optical frequencies the resistivity  $\rho$  can be quite different and the onset of inter-band transitions may significantly affect the optical properties of the metal.

Figure 5.4 plots  $\eta_a$  as a function of the aspect ratio for different values of  $ka$ . For a resonance wavelength of 600 nm  $ka = 0.5$  corresponds to an optical antenna with linear dimensions of the order of 100 nm. Moreover, we choose  $\gamma/\omega_p = 0.005$  and  $\epsilon_b = 1$  to approximate the performances of the antennas presented in Chapter 4. As expected,  $\eta_a$  decreases with the aspect ratio and with  $ka$ . Nonetheless, for  $ka \simeq 0.5$  the antenna efficiency is very large for a broad range of aspect ratios.

Material	$T=273\text{ K}$	$T=77\text{ K}$
Au	0.0024	0.0006
Ag	0.0018	0.00036
Al	0.0051	0.00063
Cu	0.0022	0.00029

**Figure 5.3:** Tabulated values of  $\gamma/\omega_p$  for selected metals (Ashcroft and Mermin, 1976). Lowering the temperature reduces the absorption losses by an amount that is different for each metal.

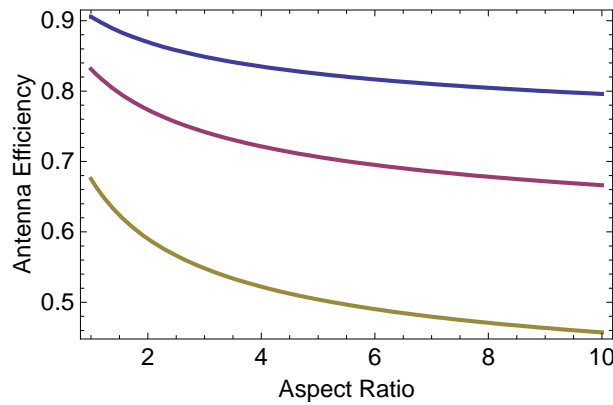


**Figure 5.4:** Antenna efficiency as a function of the aspect ratio plotted for three different values of  $ka$ : 0.5 (blue), 0.4 (amaranth), 0.3 (sepia).  $\gamma/\omega_p = 0.005$  for all curves.

### Quality factor

The  $Q$  factor can be easily obtained from the formula  $Q = \omega_o/\Gamma_a$  (Jackson, 1999). Introducing the antenna efficiency leads to

$$Q = \eta_a \frac{9L AR^2}{2(ka)^3}. \quad (5.32)$$

Figure 5.5 displays the  $Q$  factor as a function of the aspect ratio and  $ka$ . Note the competition between the decrease of  $\eta_a$  in Figure 5.4 and the increase of the  $Q$  factor with the aspect ratio. For  $ka \ll 1$  absorption losses dominate and the  $Q$  factor saturates to the value  $Q = (\omega_p/\gamma)\sqrt{L/\epsilon_b}$ .

### Field enhancement

For the calculation of the field enhancement we consider the position at one of the two spheroid sharp ends. We start from Eq. (5.15) and replace  $\xi$  and  $E_{\text{dip}}$  with the values obtained through Eq. (5.28). In particular, the lighting-rod effect reads  $\xi = 3AR^2(1-L)/2$  and  $E_{\text{dip}} = 2\alpha E_o/a^3$ . A few algebraic operations lead to the

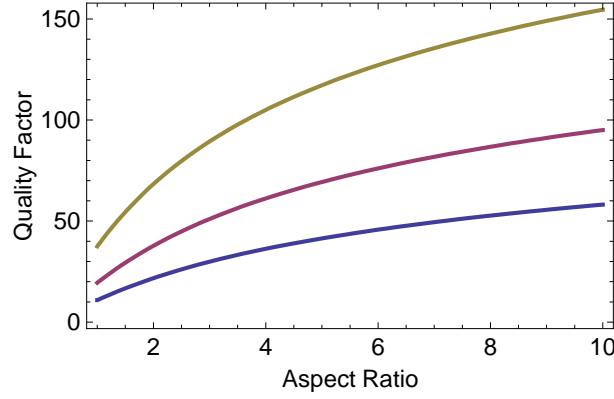


**Figure 5.5:** Quality factor as a function of the aspect ratio plotted for three different values of  $ka$ : 0.5 (blue), 0.4 (amaranth), 0.3 (sepia).  $\gamma/\omega_p = 0.005$  for all curves.

intensity enhancement

$$K = \left( \frac{9}{2} \eta_a \frac{AR^2}{(ka)^3} \right)^2 (1-L)^2. \quad (5.33)$$

Note that the  $(ka)^6$  dependence is compensated by the drop in the antenna efficiency  $\eta_a$ . In fact, when  $ka$  approaches zero,  $K$  saturates to the value

$$K_{ka \rightarrow 0} = \left( \frac{\omega_p}{\gamma} \right)^2 \frac{(1-L)^2}{\epsilon_b L}, \quad (5.34)$$

which only depends on the material losses and the geometrical factor. Indeed Figure 5.6 indicates that the intensity enhancement drops very rapidly when  $\gamma/\omega_p$  increases and it becomes less dependent on the aspect ratio.

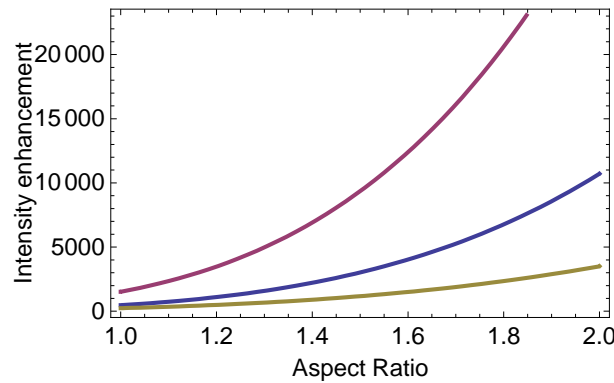


**Figure 5.6:** Intensity enhancement as a function of the aspect ratio plotted for different values of  $ka$  and  $\gamma/\omega_p$ :  $ka = 0.5$  (blue),  $ka = 0.4$  (amaranth),  $ka = 0.4$  and  $\gamma/\omega_p = 0.05$  (sepia).  $\gamma/\omega_p = 0.005$  for all curves if not otherwise stated.

### Optical antennas are electrically small

We now compare the performances of optical antennas with the fundamental limitations of electrically small antennas. The inset in Figure 5.7 depicts a nanospheroid and an infinitesimal dipole antenna enclosed in the virtual radiating sphere of radius  $r$ . We also consider a nanosphere and an ideal electrically small antenna that fulfills the Chu theory. The  $Q$  factor for these radiating systems is plotted in Figure 5.7 as a function of  $kr$ . As expected, the infinitesimal dipole exhibits worse performances, because it does not exploit all the available volume to radiate energy. According to the Chu theory a metal nanosphere should be a more efficient electrically small antenna, because it can fill the volume of the virtual sphere. Indeed the  $Q$  factor of a nanosphere agrees very well with the result of Eq. (5.25) when  $kr < 1$ . However, for  $kr \ll 1$  the curve saturates to  $\omega_p/(\sqrt{3}\gamma)$ .<sup>1</sup> When the nanosphere is replaced by a nanospheroid the  $Q$  factor increases. The reason is that the available radiating volume is not fully exploited.

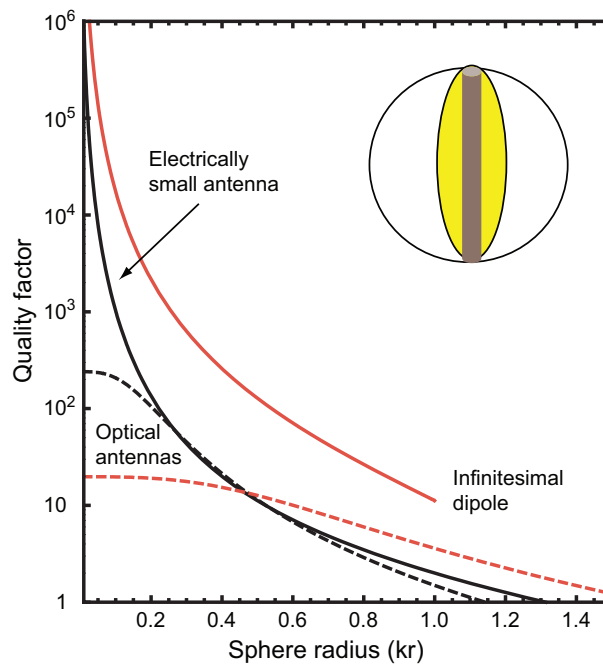


**Figure 5.7:** Quality factor as a function of the radius of the radiating sphere for an ideal electrically small antenna (black solid line), an infinitesimal dipole (red solid line), and optical antennas (dashed lines). The latter are a nanosphere (black) and a nanospheroid (red). We choose  $\gamma/\omega_p = 0.003$  for the nanosphere,  $AR=3$  and  $\gamma/\omega_p = 0.05$  for the nanospheroid, and  $r/a = 50$  for the infinitesimal dipole (see Eqs. (5.26) and (5.32)). The inset shows an infinitesimal dipole (brown) and a nanospheroid (yellow) enclosed in the radiating sphere.

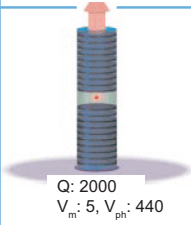
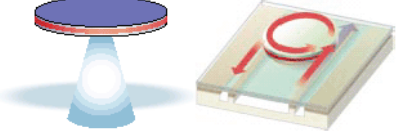
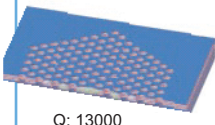
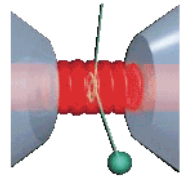
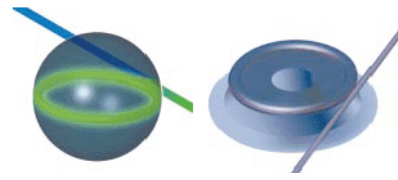
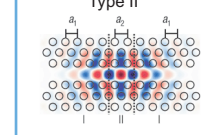
In summary, metal nanoparticles are electrically small optical antennas, agree

<sup>1</sup> $\omega_p/\sqrt{3}$  is known as the Fröhlich frequency and it represents the SPP resonance of a nanosphere in the electrostatic picture (Bohren and Huffman, 1983).

with the Chu theory and share the resulting limitations. These turn out to be very important for optical antennas, because the fact that the  $Q$  factor and the reactive energy increase when the antenna volume decreases may be exploited to enhance light-matter interactions.

### 5.3 Optical antennas as nanoscale cavities

We have combined the theory of electrically small antennas with a polarizability model of metal nanoparticles to derive figures of merit. Now we want to compare them with those of optical microcavities. For our purpose we choose the following cavity parameters: radiation efficiency,  $Q$  factor, mode volume  $V_m$  and footprint. The latter represents the actual device volume  $V_{ph}$ . Note that for a microresonator  $V_{ph}$  is typically much larger than the mode volume. Literature values for these quantities are indicated in Figure 5.8 for the corresponding resonator models (Song et al., 2005; Vahala, 2003). In what follows we consider the figures of merit for a micropillar, a microsphere, a microtoroid, and two photonic crystals nanocavities.

	Fabry-Perot	Whispering gallery	Photonic crystal
High Q	 <p>Q: 2000 <math>V_m: 5, V_{ph}: 440</math></p>		 <p>Q: 13000 <math>V_m: 1.2, V_{ph}: 200</math></p>
Ultrahigh Q		 <p>Q: <math>10^9</math> <math>V_m: 2000, V_{ph}: 30000</math></p>	 <p>Q: <math>10^7</math> <math>V_m: 2, V_{ph}: 200</math></p>

**Figure 5.8:** Figures of merit for optical resonators:  $Q$  factor, mode volume  $V_m$  and physical volume  $V_{ph}$ .  $V_m$  and  $V_{ph}$  are both in units of the cubic wavelength  $(\lambda/n_b)^3$ , where  $n_b$  is the refractive index in the dielectric medium (adapted from Song et al., 2005; Vahala, 2003).

#### Quantum efficiency

For a more direct comparison with optical resonators, we replace  $kr$  and the aspect ratio with the physical volume  $V_{ph}$  and obtain

$$\eta_a = \frac{1}{1 + \frac{\gamma}{\omega_p} \frac{3}{4\pi^2} \frac{\sqrt{\epsilon_b L}}{V_{ph}}}. \quad (5.35)$$

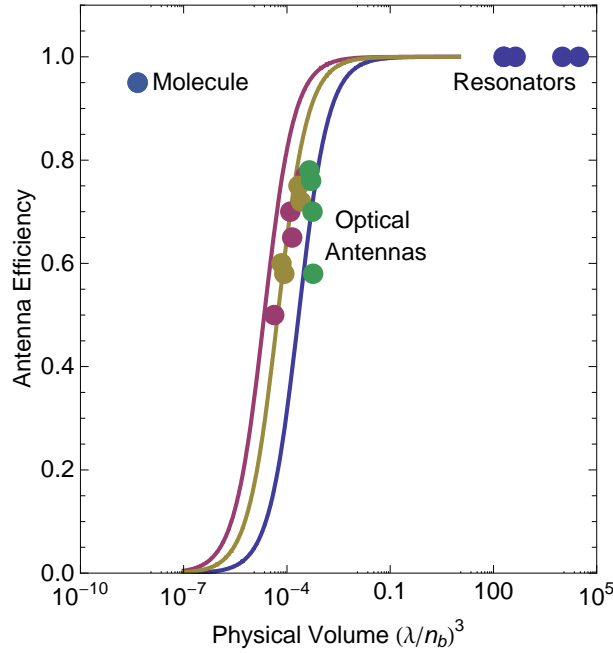


**Figure 5.9:** Antenna efficiency as a function of the device footprint (physical volume in units of the cubic wavelength). The curves refer to our antenna model for different parameters:  $AR=1$ ,  $\gamma/\omega_p = 0.005$  (blue),  $AR=10$ ,  $\gamma/\omega_p = 0.005$  (sepia),  $AR=1$ ,  $\gamma/\omega_p = 0.0005$  (amaranth). The filled circles refer to optical antennas, resonators and a molecule. The colors indicate different antenna designs: single nanospheroids (green), nanorods (amaranth), and nanorod pairs (sepia).

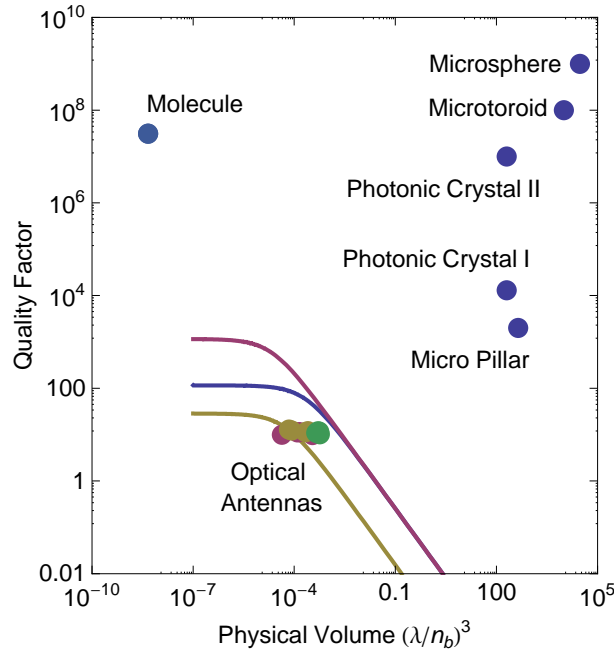
The curves plotted in Figure 5.9 correspond to different values of  $\gamma/\omega_p$  and of the aspect ratio (see the figure caption for details). It is shown that  $\eta_a$  drops when  $V_{ph}$  is smaller than about  $10^{-4}$  cubic wavelengths, a value that strongly depends on  $\gamma/\omega_p$ . On top of these curves the filled circles refer to the antenna designs discussed in Section 4.2.2, namely single nanospheroids (green), nanorods (amaranth) and nanorod pairs (sepia). Their  $\eta_a$  is obtained from FD-TD electrodynamic simulations that excite the antenna using a dipole source. The data agree very well with our model. The dependence of  $\eta_a$  on the antenna volume illustrates the competition between absorption and radiation losses and anticipates the conflict with the enhancement of light-matter interaction, which requires an optical antenna with a strong reactive behavior. For the sake of comparison we also indicate  $V_{ph}$  and  $\eta_a$  for optical resonators and a quantum emitter.

### Quality factor

The  $Q$  factor is inversely proportional to the physical volume, but it is also affected by the antenna efficiency, which takes into account the role of the absorption losses

through  $\gamma/\omega_p$ .

$$Q = \eta_a \frac{3}{4\pi^2} \frac{L}{V_{ph}} \quad (5.36)$$



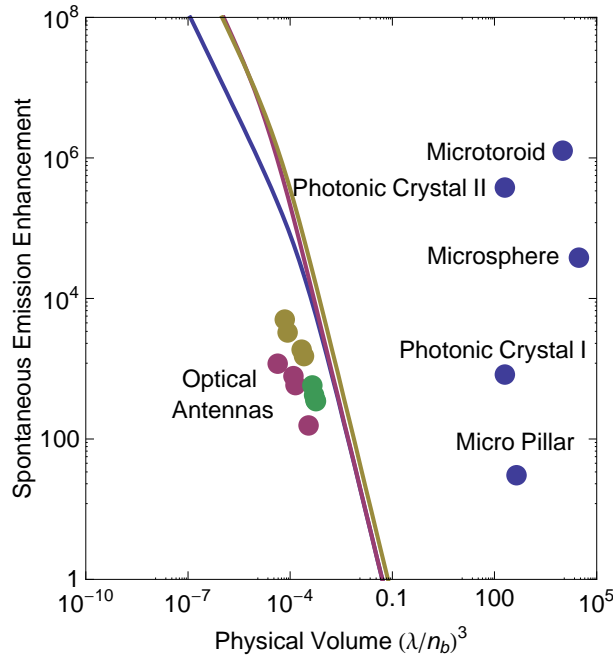
**Figure 5.10:** Quality factor as a function of the device footprint (physical volume in units of the cubic wavelength). The curves refer to our antenna model for different parameters:  $AR=1$ ,  $\gamma/\omega_p = 0.005$  (blue),  $AR=10$ ,  $\gamma/\omega_p = 0.005$  (sepia),  $AR=1$ ,  $\gamma/\omega_p = 0.0005$  (amaranth). The filled circles refer to optical antennas, resonators and one molecule. The colors indicate different antenna designs: single nanospheroids (green), nanorods (amaranth), and nanorod pairs (sepia).

Figure 5.10 compares the result of Eq. (5.36) with the antenna designs of Section 4.2.2, as well as with our selection of optical resonators and a single molecule. The  $Q$  factor of optical antennas is much smaller than the other systems and for very small values of  $V_{ph}$  it is determined by the absorption losses in the metal. Since the response time is proportional to the  $Q$  factor, optical antennas might represent a unique opportunity for enhancing light-matter interaction and, at the same time, meet the requirements of ultrafast optics. For example, a single molecule or a ultrahigh- $Q$  cavity like a microsphere have response times of the order of a few nanoseconds. Resonators with a very small mode volume like photonic crystal cavities can cope with picosecond pulses. Optical antennas offer the possibility of working with a few femtosecond pulses. In this respect the next important point of concern is whether antennas could increase light-matter interaction as much as optical resonators.

### Spontaneous emission enhancement

The enhancement of the spontaneous emission rate is obtained from Eq. (5.16) upon replacing the intensity enhancement with the expression given in Eq. (5.33). A few more algebraic steps lead to

$$\frac{\Gamma_t}{\Gamma_o} = \eta_a \frac{9}{16\pi^4} \frac{(1-L)^2}{V_{ph}^2}. \quad (5.37)$$



**Figure 5.11:** Enhancement of the spontaneous emission rate as a function of the device footprint (physical volume in units of the cubic wavelength). The curves refer to our antenna model for different parameters:  $AR=1$ ,  $\gamma/\omega_p = 0.005$  (blue),  $AR=10$ ,  $\gamma/\omega_p = 0.005$  (sepia),  $AR=1$ ,  $\gamma/\omega_p = 0.0005$  (amaranth). The filled circles refer to optical antennas and resonators. The colors indicate different antenna designs: single nanospheroids (green), nanorods (amaranth), and nanorod pairs (sepia).

Figure 5.11 demonstrates that the Purcell factor of optical resonators and the modification of the spontaneous emission rate by optical antennas can be of the same order of magnitude. Furthermore, it is shown that the designs discussed in Section 4.2.2 can compete with the performances of high- $Q$  photonic-crystal cavities

### Mode volume

The last topic to be discussed is the mode volume  $V_m$ . At the beginning of this chapter we pointed out that the mode volume is not a well defined quantity for optical antennas and that there is still disagreement on its definition (Koenderink,



2010; Kuttge et al., 2010; Maier, 2006; Oulton et al., 2008). Since we are more interested in presenting figures of merit and scaling laws, we are satisfied with a definition of the mode volume based on Eq. (5.8). We thus assume that the antenna supports only one SPP mode and write

$$V_m = \frac{3}{4\pi^2} Q \left( \frac{\Gamma_t}{\Gamma_o} \right)^{-1}. \quad (5.38)$$

We then replace the  $Q$  factor and the enhancement of the spontaneous emission rate using Eqs. (5.36) and (5.37), respectively, and arrive at

$$V_m = \frac{L}{(1-L)^2} V_{ph}. \quad (5.39)$$

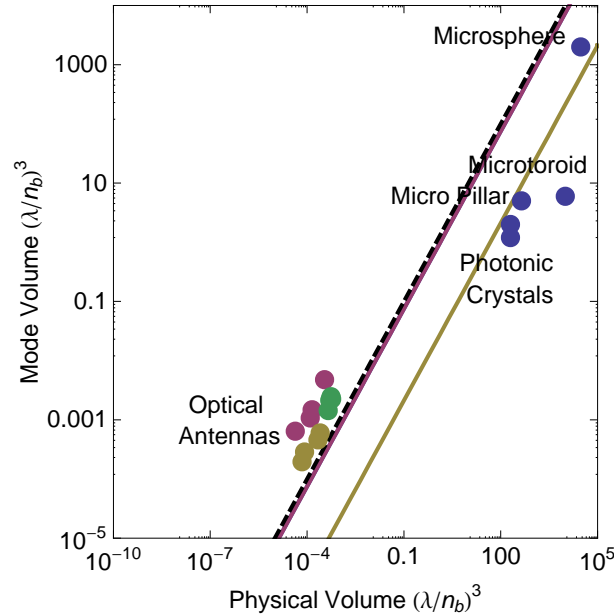


**Figure 5.12:** Mode volume as a function of the device footprint both in units of the cubic wavelength. The curves refer to our antenna model for different parameters:  $AR=1$ ,  $\gamma/\omega_p = 0.005$  (blue),  $AR=10$ ,  $\gamma/\omega_p = 0.005$  (sepia),  $AR=1$ ,  $\gamma/\omega_p = 0.0005$  (amaranth). The filled circles refer to optical antennas and resonators. The colors indicate different antenna designs: single nanospheroids (green), nanorods (amaranth), and nanorod pairs (sepia). The black dashed line represents the case where mode volume and physical volume are equal.

Figure 5.12 compares the result of Eq. (5.39) with the mode volume of optical resonators. Note the huge difference between these two systems. In fact, even the smallest photonic-crystal cavities exhibit a mode volume that is about three orders of magnitude larger than that of optical antennas. Furthermore, for optical antennas  $V_m$  is comparable to  $V_{ph}$  if the aspect ratio is small. On the other hand,

for achieving a high  $Q$  factor microcavities require a physical volume that is much larger than the mode volume.

An alternative way to derive the mode volume of an optical antenna utilizes the vacuum Rabi frequency  $\Omega$ . The latter can be obtained from a Green-function formulation of QED (Knöll et al., 2001; Wylie, 1986). If the antenna leads to a strong modification of the spontaneous emission rate ( $\Gamma_t/\Gamma_o \gg 1$ ), one can ignore the free-space radiation modes and approximate the imaginary part of the Green function with a Lorentzian of width  $\Gamma_a$ , which is the linewidth of the antenna resonance. It can be shown that the Rabi frequency is related to  $\Gamma_t$  and  $\Gamma_a$  through the formula

$$\Omega = \sqrt{\frac{\Gamma_t \Gamma_a}{4}}. \quad (5.40)$$

From Eqs. (5.28) and (5.37) we find

$$\Omega = \frac{1-L}{\sqrt{L}} \frac{1}{\sqrt{V_{\text{ph}}}}, \quad (5.41)$$

Note that the above expression is given in units of  $\omega^2 d / (4\sqrt{\epsilon_0 \hbar \pi^3 c^3})$ . Since  $\Omega = \sqrt{\omega_o d^2 / (2\epsilon_0 \hbar V_\mu)}$ , where  $V_\mu$  is the mode volume in dimensional units, one obtains the same result of Eq. (5.39).

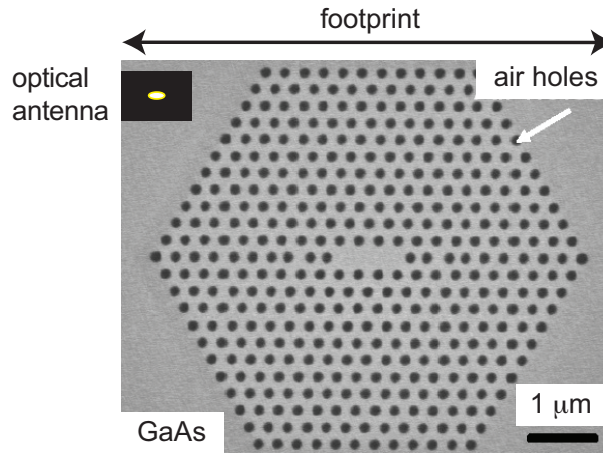


**Figure 5.13:** Comparison of the device footprint for a photonic-crystal nanocavity (adapted from Hennessy et al., 2007) and an optical antenna. Optical antennas offer similar performances, but they have a device size that is orders of magnitude smaller than state-of-the-art optical resonators.

### Final considerations

We conclude our analysis by discussing once more the competition between the antenna efficiency and the enhancement of light-matter interaction. Figure 5.14 plots these two quantities as a function of  $V_{\text{ph}}$ . The dashed lines refer to  $\eta_a$ , which

for a dielectric resonator is equal to one and it is therefore not indicated. While  $\eta_a$  drops very rapidly when the antenna dimensions become smaller than a certain value that depends on the parameter  $\gamma/\omega_p$ , the enhancement of the spontaneous emission rate increases and, despite the low  $Q$  factor, it reaches values that compete with those of state-of-the-art optical cavities. Within these opposite trends there is a parameter window where optical antennas could function as nanoscale resonators with a tiny device footprint (see Figure 5.13), manageable absorption losses and ultrafast operation.

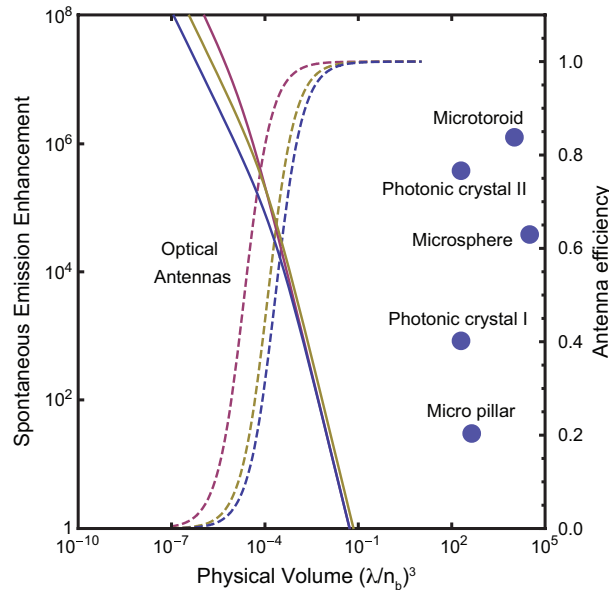


**Figure 5.14:** Enhancement (solid curves) and antenna efficiency (dashed curves) versus device footprint (physical volume in units of the cubic wavelength) for optical antennas and selected resonators (circles). The curves refer to our antenna model for different parameters:  $AR=1$ ,  $\gamma/\omega_p = 0.005$  (blue),  $AR=3$ ,  $\gamma/\omega_p = 0.005$  (sepia),  $AR=1$ ,  $\gamma/\omega_p = 0.0005$  (amaranth).

These settings make optical antennas very attractive for meeting the targeted performances of integrated photonic devices (Miller, 2009). In fact, the stringent requirements on photon management that we have explored for quantum optical applications might turn out to be extremely useful also for classical information processing. In both cases we have to fight the mismatch between light and matter to achieve strong and controllable interactions. We need to process very small optical signals, ideally down to single photons. Moreover, we have to look at nanotechnology and material science, which give us new opportunities and challenges. These considerations fuel research on the miniaturization of optical logic functions, which are based on nonlinearities (Gibbs, 1985). These have been extensively studied in photonic crystals, where much research is going on for all-optical switches and modulators (Leuthold et al., 2010; Matsuo et al., 2010). As to integrated light sources, the most aggressive designs are based on quantum dots in photonic-crystal

---

cavities (Gong et al., 2010; Hostein et al., 2010, and references therein). These functionalities (switching, lasing, etc...) could also be explored using active media coupled to nanoscale resonators/antennas. Studying the physics and engineering of these devices may thus pave the way to the next generation of nanophotonics systems.



# Chapter 6

## Conclusions and outlook

We investigated the optical response of a single dye molecule under strongly confined optical fields. For the sake of simplicity, but also to extend our results to a broader range of single quantum emitters (Brouri et al., 2000; Diedrich and Walther, 1987; Kimble et al., 1977; Kurtsiefer et al., 2000; Michler et al., 2000), we treated the molecule as a weakly-excited TLS. This is in fact a good approximation if we consider weak resonant excitation and systems that exhibit large Franck-Condon and Debye-Waller factors (Boiron et al., 1996; Jelezko et al., 1997; Lettow et al., 2007).

We used scattering theory to generalize the Beer-Lambert-Bouguer law to the situation of a point-like oscillating dipole under focused illumination. Until recently, it was commonly believed that an emitter had a small effect on a light beam. We demonstrated that, in fact, a TLS can strongly attenuate a tightly focused wave and that perfect reflection occurs if the incident field corresponds to a directional dipole wave (Zumofen et al., 2008). The latter is fully extinguished because it matches the radiation pattern of an oscillating dipole in the forward direction. Moreover, even for conditions that are more accessible in the laboratory, such as a focused plane wave, the transmission dip turns out to be only a few percents smaller. An alternative argument for explaining these findings considers the effective area  $A$  associated with the electric field intensity that can be obtained in the focal spot for a given incident power. When  $A$  is equal to one half the cross section, the incident beam is perfectly reflected. Interestingly, this value corresponds to the upper limit for the concentration of electromagnetic energy by passive optical systems (Bassett, 1986). The relationship between the strength of light-matter interaction and this limit stems from the dipole-wave content of a focused beam and from the fact that at the focus only the electric dipole wave contributes to the electric field intensity.

Our results have immediate implications for the detection and spectroscopy of single quantum emitters and non-fluorescent nano-objects at cryogenic (Alén et al., 2006; Bakr et al., 2009; Guest et al., 2002; Karrai and Warburton, 2003) and at ambient conditions (Arbouet et al., 2004; Boyer et al., 2002; Celebrano et al., 2011; Kukura et al., 2009, 2010; Lindfors et al., 2004). Moreover, extending these studies

to circularly polarized light may lead to improved single-spin measurements based on the Faraday rotation (Atatüre et al., 2007; Buckley et al., 2010). Note that these findings readily hold for the whole electromagnetic spectrum, and we expect interesting applications also in the detection and spectroscopy of subwavelength objects in the infrared, terahertz and radio-wave domains (Brehm et al., 2006; Huber et al., 2008).

We anticipate that an efficient coupling between a single photon and a single quantum system can be realized in a directional focal system without the need for high-finesse cavities. Such an arrangement would open new doors for quantum information processing using photons as information carriers. For example, a number of proposals of quantum information science that are based on cavity-assisted interactions (Boozer et al., 2007; Cirac et al., 1997; Duan and Kimble, 2004; Turchette et al., 1995; van Loock et al., 2006; Waks and Vuckovic, 2006; Wilk et al., 2007) could be explored using tightly focused beams. To this end we have also computed the phase shift that a TLS impresses on a beam incident on it. For a directional dipole wave the shift can be as large as 90 degrees and it reduces to a few tens of degrees for focusing conditions accessible to experiments. These values appear very promising for encoding and exchanging quantum information through dispersive interactions (Fushman et al., 2008; Savage et al., 1990; Turchette et al., 1995; van Loock et al., 2006, 2008).

Efficient coupling in free space is also relevant for the experimental investigation of quantum-optical links, where a quantum emitter is driven with the single photon emitted by another quantum system (Carmichael, 1993; Gardiner, 1993; Rist et al., 2008). Single-atom absorption using heralded single photons generated by spontaneous parametric down conversion has in fact been experimentally demonstrated with our arrangement (Piro et al., 2011). This “communication” regime poses a number of fundamental and practical questions on light-matter interaction and quantum optics as well. First, extending our analysis beyond the weak excitation limit would require a full quantum treatment of the interaction problem (Domokos et al., 2002; Dorner and Zoller, 2002; Kochan and Carmichael, 1994; Rist et al., 2008), because these strong coupling efficiencies make a TLS a single-photon turnstile device, where the response to an incident photon is dynamically regulated by the presence of another photon (Birnbaum et al., 2005; Chang et al., 2007a; Dayan et al., 2008; Faraon et al., 2008; Schuster et al., 2008). Furthermore, it would be interesting to investigate photon correlations, since photon bunching or antibunching is generally expected when there is respectively destructive or constructive interference (van Enk and Kimble, 2000, 2001), and to extend previous works dealing with optical resonators (Foster et al., 2000; Henrich et al., 2005).

Next, we investigated the enhancement of molecular fluorescence by optical antennas. These are metal nanoparticles that can boost the absorption and radiation of optical energy by an atom like conventional antennas do at radio frequencies for electronic circuits. However, previous work indicated that at optical wave-

lengths losses by real metals could quench light emission. We established that this is not a fundamental constraint and showed that the interaction could be enhanced by more than three orders of magnitude without substantial quenching (Rogobete et al., 2007). Furthermore, we took advantage of computational nano-optics to explore antenna structures that enhance emitters in the ultraviolet to the near-infrared spectral range (Mohammadi et al., 2010, 2008b). Because metals cannot be considered perfect conductors at optical frequencies, it is shown that the antenna's composition plays an important role in finding the optimal designs (Mohammadi et al., 2009b).

Moreover, we explored the possibility of controlling the emission pattern of a TLS by means of an optical antenna. In particular, we addressed the issue of interfacing antennas with optics and photonics to funnel light in a well-defined optical mode. That is desirable for increasing the signal-to-noise ratio in spectroscopy and sensing (Hartschuh, 2008; Hartschuh et al., 2004), and it becomes crucial for achieving controllable few-photon interactions for quantum information science (Englund et al., 2009; Faraon et al., 2008). We found that truncated metal cones behave as monolithic directional antennas that can efficiently convert strongly localized optical energy into a guided mode (Chen et al., 2009) or a weakly-focused beam (Chen et al., 2010a). In practice, the antenna acts as a  $4\pi$  focusing system that may function as a mode converter towards the perfect excitation of a TLS (Stobińska et al., 2009). Furthermore, these are fully compatible with scanning probe technology and state-of-the-art nanofabrication (De Angelis et al., 2010). We thus envision the immediate possibility of testing these ideas experimentally.

Since dephasing is often the mechanism that reduces the interaction cross section (Allen and Eberly, 1975), increasing the radiative decay rate by orders of magnitude could be a simple and effective strategy for improving the coupling strength. That would enable the efficiencies demonstrated for a TLS under focused illumination. Moreover, a faster single-photon emitter would allow us to generate, process and detect optical signals at much higher rates, with benefits for the signal-to-noise ratio and the throughput (Babinec et al., 2010; Schietinger et al., 2009). These settings could also enable the spectroscopy of new systems that suffer from weak optical transitions, such as rare-earth ions (Macfarlane and Shelby, 1987). Note also that quantum information protocols require sources of indistinguishable single photons with a high fidelity and rate (Knill et al., 2001). Since dephasing limits indistinguishability (Kiraz et al., 2004) and processes like stimulated Raman adiabatic passage are experimentally more challenging (Kuhn et al., 2002), optical antennas represent an interesting opportunity for improving the performances of single-photon sources also from this point of view.

An important theme of our research has been the exploration of novel methods to improve light-matter interaction towards levels comparable with those achievable with optical resonators. While focused light is relevant only for free-space arrangements, optical antennas are more versatile and may hold promise for dense



photonics integration (Kirchain and Kimerling, 2007; Miller, 2009). To this purpose we analyzed their figure of merits using antenna theory (Hansen, 1981) and compared them to common resonator designs (Vahala, 2003). Despite absorption losses we found that optical antennas exhibit performances compatible with optical resonators, but with a much smaller device footprint. Moreover, having a low quality factor, antennas do not suffer from the bandwidth and speed limitations that are common to high-finesse cavities.

Altogether, these settings hold great promise for interfacing photons to a quantum system beyond the framework of cavity QED (Haroche and Kleppner, 1989) and urge further thorough theoretical and experimental investigations. These include studying the quantum optical phenomena that take place when an optical antenna mediates the interaction between photons and single quantum emitters in the full quantum picture and beyond continuous wave weak excitation. Moreover, combining ultrafast spectroscopy, field-enhanced spectroscopy and quantum optics could push forward the possibility of the coherent optical access of a quantum emitter above cryogenic temperatures and achieve nonlinearities at the single-photon level with antennas and solid-state emitters.

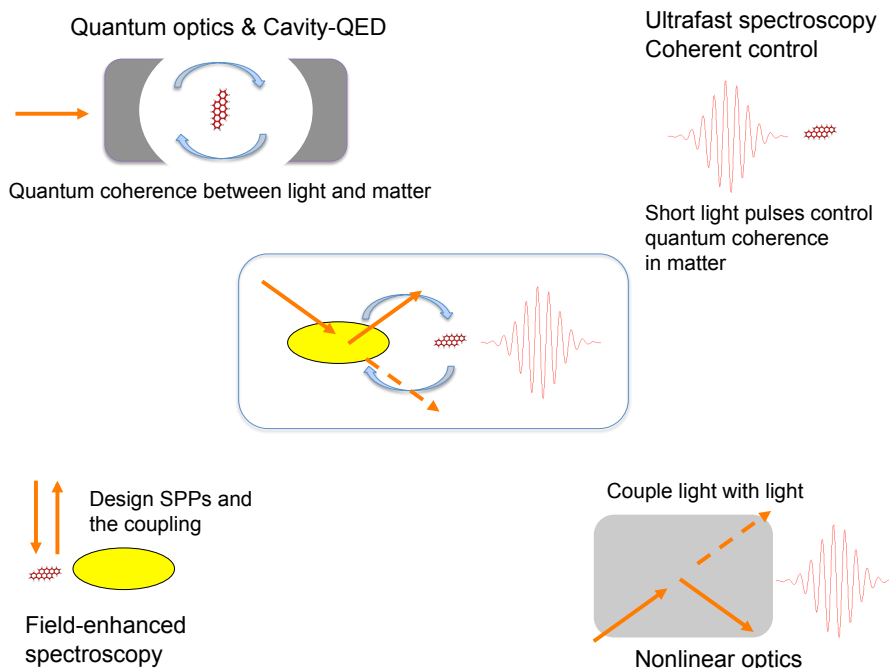


**Figure 6.1:** *Research areas that were previously disconnected can now find overlaps in optical antennas.*

The effect of optical antennas on light emitters has been treated in the weak-coupling perturbative regime, which leads to the calculation of spontaneous emission rates, antenna efficiencies and energy shifts (Klimov et al., 2002). A few groups

have started to go beyond this picture, but so far their treatments have been limited by various approximations. For instance, semi-classical descriptions that neglect photon correlations and quantum fluctuations, electrostatic approximations that ignore radiation and other dynamical effects, quantum treatments that assume scalar fields and disregard absorption losses (Chang et al., 2006; Lopata and Neuhauser, 2009; Ridolfo et al., 2010; Zhang et al., 2006). Indeed, a quantum-optical description of light with optical antennas imposes several challenges and the treatment of radiation quanta in complex electromagnetic environments with material losses and dispersion has received little attention so far. Nevertheless, an accurate study is important to gain a deeper understanding and to make possible a better use of these interactions. This line of research could give fundamental contributions not only to the development of novel light-matter quantum interfaces but also to the realization of, for instance, single-photon sources with completely engineered properties.

Single-photon nonlinearities play an important role in quantum photonics technologies (Faraon et al., 2008, and references therein). In this context, recent work indicates that optical antennas could be exploited to enhance quantum nonlinear processes. For instance, a single-photon transistor could be attained based on the efficient coupling between a quantum emitter and a SPP in tapered metal nanowires (Chang et al., 2007a). Various groups are indeed planning to couple metal nanowires with quantum emitters at low temperatures to demonstrate these proposals. However, the configuration looks challenging to achieve experimentally. First, SPPs need to be converted very rapidly into lossless photons in order to enable efficient and controlled interactions between single photons. Second, metal nanowires should be tapered down to 10 nm in diameter for achieving strong coherent coupling with the emitter and, at the same time, the emitter should be placed only a few nanometers away. One could perform experiments based on the recently proposed high-throughput SNOMs (Chen et al., 2009, 2010a). Our approach not only aims at solving these experimental issues, but it also represents a platform to pursue further investigations on nanoscale and ultrafast quantum-optical and nonlinear phenomena *per se*.

Under continuous weak excitation it is well established that fluorescence is proportional to the excitation field intensity and to the quantum yield. The latter accounts for the competition between the radiative and non-radiative decay rates, which are strongly modified by the presence of metals (Metiu, 1984). Time-resolved techniques, such as pump-probe spectroscopy (Zewail, 2001), quantum coherent control (Press et al., 2008) and triggered single-photon sources (Brunel et al., 1999), to mention a few, rely on (ultrafast) pulsed excitation. Here an important aspect, beside the coupling strength, is coherence. In quantum information science coherence enables the exchange of information between a photon and an atom (Monroe, 2002). In ultrafast spectroscopy and coherent control, it allows monitoring and manipulating the quantum dynamics of matter (Bandrauk et al., 2002; Rabitz et al.,

2000). Very recently, it has become possible to perform this kind of experiments on a single molecule at room temperature using focused femtosecond pulses (Brinks et al., 2010; Hildner et al., 2011). On the other hand, several groups are studying the behavior of optical pulses in metal nanostructures to control the localization of electromagnetic energy in space and time (Aeschlimann et al., 2007; Stockman, 2008). The immediate question that arises is thus how an optical antenna affects the response of an emitter under laser pulses of various widths, at room and cryogenic temperatures. Here the important points of concern are the competition between decay times, dephasing and pulse width, the increased interaction strength due to field enhancements, and the dispersion occurring when the pulse duration becomes comparable with the lifetime of the SPP resonance. These considerations lead us to combine atomic, molecular and optical physics (AMO) and ultrafast techniques with quantum optics to explore the possibilities of manipulating single quantum emitters and monitor coherent energy transfer under conditions where dephasing processes occur at very short time scales (Engel et al., 2007; Lee et al., 2007; Panitchayangkoon et al., 2010; Press et al., 2008, 2010; Reim et al., 2010).

In conclusion, we investigated schemes that improve light-matter interaction starting from concepts and techniques of spectroscopy and sensing. We found that the coupling strength can be made so large that even a single photon may have a large probability to interact with a single quantum emitter, a regime that so far belonged to the framework of cavity QED. Furthermore, these approaches do not exhibit the bandwidth limitations of high-finesse cavities. While these settings are very interesting for advancing spectroscopy and sensing, we believe that the major implications concern quantum and classical information science (Miller, 1989; Monroe, 2002). Let us think for instance that a solid-state quantum emitter be enhanced by an optical antenna to approach the response of an ideal TLS with an excited-state lifetime of the order of a picosecond (ps). The quantum nonlinearity of the TLS could switch an optical signal with energies near 1 aJ and times of 1 ps. These performances are more than two orders of magnitude more efficient and more than one order of magnitude faster than the current record obtained with semiconductor nonlinearities and photonic-crystal nanocavities (Nozaki et al., 2010). Note that lowering the switching energy by increasing the  $Q$  factor of the cavity would reduce the operation speed and vice versa. Our findings break this barrier and pave the way to signal processing at the energy scale of molecular electronics (Joachim and Ratner, 2005), but at rates that belong to the THz regime.

# Appendix A

## Strongly focused beams

We introduce the formalism to describe the electromagnetic field in the focal region of a tightly focused beam. We choose two equivalent approaches, namely Debye diffraction integrals and the multipole expansion. The latter offers more insight on the focusing process and on the choice of the focused beam, whereas Debye diffraction leads to analytical expressions that are more suitable for computing the scattering ratio.

### A.1 Debye diffraction integrals

An established approach for calculating the field in the focal area is provided by the Debye diffraction integrals. It was initiated by Debye using Greens theorem (Debye, 1909) and was extended by Wolf using the method of stationary phase (Wolf, 1959). For an incident plane wave the method was extensively applied by Richards and Wolf (Richards and Wolf, 1959). These integrals describe the evolution of the wavefront of an electromagnetic beam as it propagates in the focal region by a superposition of plane waves

$$\mathbf{E}(\mathbf{r}) = -\frac{ik}{2\pi} \int_{\Omega_a} \mathbf{A}(\theta, \varphi) e^{ik\hat{\mathbf{s}}\cdot\mathbf{r}} d\Omega, \quad \mathbf{E}(\mathbf{r}) = -\frac{ik}{2\pi} \int_{\Omega_a} \hat{\mathbf{s}} \times \mathbf{A}(\theta, \varphi) e^{ik\hat{\mathbf{s}}\cdot\mathbf{r}} d\Omega, \quad (\text{A.1})$$

where  $k$  is the vacuum wave number,  $c$  is the speed of light in vacuum,  $\Omega_a$  represents the solid angle associated with the aperture's boundaries,  $\hat{\mathbf{s}}$  is the unit vector along the propagation direction of each plane wave, and  $\mathbf{A}(\theta, \varphi)$  is the vectorial angular spectrum of the incident field, which is essentially the Fourier transform of the wavefront (Stamnes and Dhayalan, 1996). The physical interpretation of the Debye diffraction integrals is that the secondary waves of the wavefront right after the aperture can be taken as plane waves tangential to it with complex amplitudes. This is very similar to the Fresnel-Huygens principle where the secondary waves are spherical waves from point sources (Wolf, 1959). This formalism is only valid under the following conditions (Wolf and Li, 1981). The physical dimensions of

the aperture have to be much larger than the wavelength, i.e. large Fresnel number. The fields are calculated many wavelengths away from the aperture. No evanescent waves contribute to the beam.

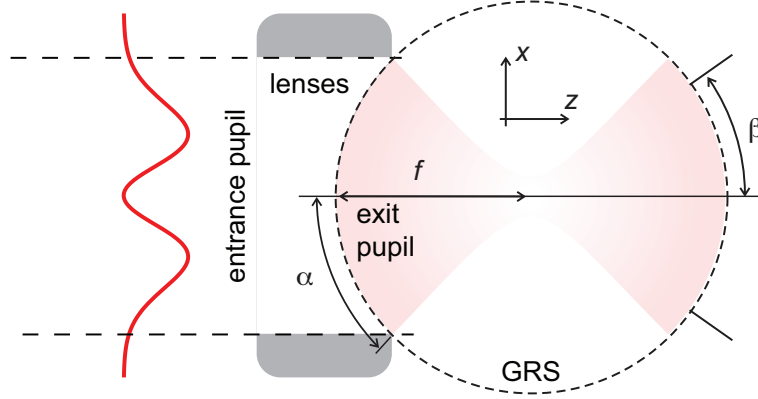


**Figure A.1:** A beam is focused by an aplanatic system. The field at the entrance pupil is transformed by the lens into a spherical wave front at the Gaussian reference sphere (GRS).  $f$  is the lens focal length, whereas  $\alpha$  and  $\beta$  are the focusing and collection semi-angles, respectively.

The procedure for obtaining the field in the focal region is made of two steps. First, the electric field right after the lens, i.e. at the Gaussian reference sphere (GRS), is obtained by a geometrical transformation of the incident wave. Second, the Debye diffraction integrals of the angular spectrum at the GRS yield the field in the image space (Richards and Wolf, 1959). The GRS is an imaginary sphere that includes the wavefront of the beam after passing through the lens, as illustrated in Figure A.1. The lens is assumed to be aplanatic (axially stigmatic), so that the wavefronts in the image space are spherical and converging to a geometrical focus at the origin of the coordinate system. Each ray of the plane wave is traced through the lens and its amplitude and polarization is obtained on the GRS. The conservation of energy in an aplanatic system implies the amplitude of each ray passing the lens to be weighted by a factor of  $a(\theta) = \sqrt{\cos \theta}$ , called the apodization function. The angle between the polarization of each ray and the meridional plane, which is the plane containing the ray and the optical axis, is left unchanged after refraction by the lens (Richards and Wolf, 1959). If one is only interested in knowing the field at the focus, the expression for the electric field simplifies to

$$\mathbf{E}(O) = -\frac{ik}{2\pi} \int_{\Omega_a} \mathbf{A}(\theta, \varphi) d\Omega. \quad (\text{A.2})$$

### A.1.1 Focused plane wave

In the case of a linearly polarized incident plane wave, the field  $\mathbf{E}(\mathbf{r})$  at the GRS is given by

$$\mathbf{E}(f, \theta, \varphi) = E_0 \sqrt{\cos \theta} (0, \cos \varphi, -\sin \varphi), \quad (\text{A.3})$$

in the spherical coordinates  $(r, \theta, \varphi)$ . Here we assume that the GRS has a radius equal to the lens focal length  $f$ . The vectorial angular spectrum  $\mathbf{A}(\theta, \varphi)$  is related to the electric field as

$$\mathbf{A}(\theta, \varphi) = f e^{ikf} E_0 \sqrt{\cos \theta} (0, \cos \varphi, -\sin \varphi). \quad (\text{A.4})$$

The term  $\exp(ikf)$  is responsible for a global phase shift of the field and it can be set equal to one. The diffraction integrals of Eq. (A.1) yield (Richards and Wolf, 1959)

$$E_x(\rho, \phi, z) = -iA_0(\mathcal{I}_0(\rho, z; \alpha) + \mathcal{I}_2(\rho, z; \alpha) \cos 2\phi), \quad (\text{A.5})$$

$$E_y(\rho, \phi, z) = -iA_0 \mathcal{I}_2(\rho, z; \alpha) \sin 2\phi, \quad (\text{A.6})$$

$$E_z(\rho, \phi, z) = -2\mathcal{I}_1(\rho, z; \alpha) \cos \phi, \quad (\text{A.7})$$

where  $(\rho, \phi, z)$  are cylindrical coordinates with respect to the focal spot and  $A_0 = E_0 f k / 2$ . Similar expressions hold for the magnetic field in the focal region. The diffraction integrals  $\mathcal{I}_0$ ,  $\mathcal{I}_1$  and  $\mathcal{I}_2$  depend on the focusing semi-angle  $\alpha$ , which is related to the numerical aperture  $\text{NA} = \sin \alpha$  in vacuo. Their expressions contain the Bessel functions  $J_n$  (Abramowitz and Stegun, 1972) and read

$$\mathcal{I}_0(\rho, z; \alpha) = \int_0^\alpha \sqrt{\cos \theta} \sin \theta (1 + \cos \theta) J_0(k\rho \sin \theta) e^{ikz \cos \theta} d\theta, \quad (\text{A.8})$$

$$\mathcal{I}_1(\rho, z; \alpha) = \int_0^\alpha \sqrt{\cos \theta} \sin^2 \theta J_1(k\rho \sin \theta) e^{ikz \cos \theta} d\theta, \quad (\text{A.9})$$

$$\mathcal{I}_2(\rho, z; \alpha) = \int_0^\alpha \sqrt{\cos \theta} \sin \theta (1 - \cos \theta) J_2(k\rho \sin \theta) e^{ikz \cos \theta} d\theta. \quad (\text{A.10})$$

### Focused Gaussian Beam

For an incident Gaussian beam polarized along the  $x$ -axis, see Eq. (4.16), the vectorial angular spectrum  $\mathbf{A}(\theta, \varphi)$  reads

$$\mathbf{A}(\theta, \varphi) = f E_0 \sqrt{\cos \theta} \exp\left(-\frac{d^2 \sin^2 \theta}{2}\right) \left\{ \left[ \cos \theta + \sin^2 \phi (1 - \cos \theta) \right] \hat{\mathbf{x}} + (\cos \theta - 1) \cos \phi \sin \phi \hat{\mathbf{y}} - \sin \theta \cos \phi \hat{\mathbf{z}} \right\}, \quad (\text{A.11})$$

where  $\hat{\mathbf{x}}$ ,  $\hat{\mathbf{y}}$  and  $\hat{\mathbf{z}}$  are the axes versors of the Cartesian coordinates. We remark that the angular spectrum is equal to that of a FPW (see Eq. (A.4)), except for the fact that the field amplitude has a Gaussian profile that depends on  $d$  (see Eq. (4.16)).

Using Eq. (A.11) in Eq. (A.2) yields  $\mathbf{E}(O) = -iA_0\mathcal{I}_0(\alpha, d)\hat{\mathbf{x}}$ , where  $A_0 = E_0fk/2$  and

$$\mathcal{I}_0(\alpha, d) = \int_0^\alpha \sin\theta\sqrt{\cos\theta}(1+\cos\theta)\exp\left(-\frac{d^2\sin^2\theta}{2}\right)d\theta. \quad (\text{A.12})$$

### A.1.2 Directional dipole wave $\mathbf{p}_x$

We follow the method of Stamnes and Dhayalan (1996) and define the field on the GRS as resulting from the radiation of a dipole oriented along the  $x$ -axis and placed at the focal spot. Moreover, we assume zero phase at the GRS, so that  $\mathbf{E}(\mathbf{r})$  reads

$$\mathbf{E}(f, \theta, \varphi) = E_0(0, \cos\theta\cos\varphi, -\sin\varphi). \quad (\text{A.13})$$

The electric field in the focal region is

$$E_x(\rho, \phi, z) = -iA_0(\mathcal{I}_0(\rho, z; \alpha) + \mathcal{I}_2(\rho, z; \alpha)\cos 2\phi), \quad (\text{A.14})$$

$$E_y(\rho, \phi, z) = -iA_0\mathcal{I}_2(\rho, z; \alpha)\sin 2\phi, \quad (\text{A.15})$$

$$E_z(\rho, \phi, z) = -2A_0\mathcal{I}_1(\rho, z; \alpha)\cos\phi, \quad (\text{A.16})$$

where the diffraction integrals are (Stamnes and Dhayalan, 1996)

$$\mathcal{I}_0(\rho, z; \alpha) = \int_0^\alpha \sin\theta(1+\cos^2\theta)J_0(k\rho\sin\theta)e^{ikz\cos\theta}d\theta, \quad (\text{A.17})$$

$$\mathcal{I}_1(\rho, z; \alpha) = \int_0^\alpha \sin^2\theta\cos\theta J_1(k\rho\sin\theta)e^{ikz\cos\theta}d\theta, \quad (\text{A.18})$$

$$\mathcal{I}_2(\rho, z; \alpha) = \int_0^\alpha \sin^3\theta J_2(k\rho\sin\theta)e^{ikz\cos\theta}d\theta. \quad (\text{A.19})$$

### A.1.3 Combined electric and magnetic dipole waves

As in the preceding Section, for combined electric and magnetic dipoles oriented along the  $x$ - and  $y$ -axis, respectively we write (Dhayalan and Stamnes, 1997; Sheppard and Larkin, 1994)

$$\mathbf{E}(f, \theta, \varphi) = E_0(1+\cos\theta)(0, \cos\varphi, -\sin\varphi). \quad (\text{A.20})$$

This equation turns out to be identical to Eq. (A.3), when the apodization function  $1+\cos\theta$  is replaced by  $\sqrt{\cos\theta}$ . Therefore we make use of the derivations in Section A.1.1. We find that the field in the focal region has the same form of

Eqs. (A.5)-(A.7), where the diffraction integrals are given by

$$\mathcal{I}_0(\rho, z; \alpha) = \int_0^\alpha \sin \theta (1 + \cos \theta)^2 J_0(k\rho \sin \theta) e^{ikz \cos \theta} d\theta, \quad (\text{A.21})$$

$$\mathcal{I}_1(\rho, z; \alpha) = \int_0^\alpha \sin^2 \theta (1 + \cos \theta) J_1(k\rho \sin \theta) e^{ikz \cos \theta} d\theta, \quad (\text{A.22})$$

$$\mathcal{I}_2(\rho, z; \alpha) = \int_0^\alpha \sqrt{\cos \theta} \sin \theta (1 - \cos^2 \theta) J_2(k\rho \sin \theta) e^{ikz \cos \theta} d\theta. \quad (\text{A.23})$$

#### A.1.4 Directional dipole wave $\mathbf{p}_z$

We determine the field at the GRS according to a dipole oriented along the  $z$ -axis (Sheppard and Larkin, 1994). In this case

$$\mathbf{E}(f, \theta, \varphi) = -E_0(0, \sin \theta, 0). \quad (\text{A.24})$$

Without details, the only diffraction integral of relevance for knowing the electric field at the focal spot is

$$\mathcal{I}_0(\rho, z; \alpha) = \int_0^\alpha \sin^3 \theta J_0(k\rho \sin \theta) e^{ikz \cos \theta} d\theta. \quad (\text{A.25})$$

#### Focused Radially-Polarized Beam

For an incident radially-polarized beam, see Eq. (4.17), the vectorial angular spectrum  $\mathbf{A}(\theta, \varphi)$  reads (Quabis et al., 2001)

$$\mathbf{A}(\theta, \varphi) = fE_0 \sqrt{\cos \theta} d \sin \theta \exp\left(-\frac{d^2 \sin^2 \theta}{2}\right) (\cos \theta \cos \varphi \hat{\mathbf{x}} + \cos \theta \sin \varphi \hat{\mathbf{y}} + \sin \theta \hat{\mathbf{z}}). \quad (\text{A.26})$$

Using Eq. (A.26) in Eq. (A.2) yields  $\mathbf{E}(O) = -iA_1 \mathcal{I}_1(\alpha, d) \hat{\mathbf{z}}$ , where  $A_1 = E_0 f k d$  and

$$\mathcal{I}_1(\alpha, d) = \int_0^\alpha \sin^3 \theta \sqrt{\cos \theta} \exp\left(-\frac{d^2 \sin^2 \theta}{2}\right) d\theta. \quad (\text{A.27})$$

#### A.1.5 Incident power

For an axially symmetric beam the incident power  $P_{\text{inc}}$  is more conveniently computed considering the field right before the entrance pupil, which is given by

$$P_{\text{inc}} = \frac{\pi}{Z} \int_0^{f \sin \alpha} d\rho |\mathbf{E}(\rho)|^2 \rho, \quad (\text{A.28})$$

where  $Z$  is the impedance of the medium in which the beam propagates and  $f \sin \alpha$  is the pupil radius. Using Eqs. (4.16) and (4.17) in Eq. (A.28),  $P_{\text{inc}}$  for a Gaussian



beam and a radially-polarized beam reads, respectively,

$$P_{\text{inc}} = \frac{\pi}{2Z} E_o^2 w^2 \left[ 1 - \exp\left(-d^2 \sin^2 \alpha\right) \right], \quad (\text{FGB}) \quad (\text{A.29})$$

$$P_{\text{inc}} = \frac{\pi}{2Z} E_o^2 w^2 \left[ 1 - \left(1 + d^2 \sin^2 \alpha\right) \exp\left(-d^2 \sin^2 \alpha\right) \right]. \quad (\text{FRB}) \quad (\text{A.30})$$

An alternative way of calculating  $P_{\text{inc}}$  is to consider the energy flow in the focal plane (Zumofen et al., 2008).

## A.2 Multipole expansion

Another convenient approach for the description of focused fields is the multipole expansion (Borghini, 2004; Mojarad et al., 2008; Sheppard and Török, 1997a; van Enk, 2004). Adopting the notation of (Bohren and Huffman, 1983) we write for the electric field in the most general form

$$\mathbf{E}(\mathbf{r}) = \sum_l \sum_{m=0}^l (B_{e,m,l} \mathbf{M}_{e,m,l}(\mathbf{r}) + A_{e,m,l} \mathbf{N}_{e,m,l}(\mathbf{r}) + B_{o,m,l} \mathbf{M}_{o,m,l}(\mathbf{r}) + A_{o,m,l} \mathbf{N}_{o,m,l}(\mathbf{r})), \quad (\text{A.31})$$

where  $\mathbf{M}_{o,m,l}(\mathbf{r})$  and  $\mathbf{N}_{o,m,l}(\mathbf{r})$  denote complete sets of magnetic and electric multipoles.  $B_{o,m,l}$  and  $A_{o,m,l}$  are the corresponding coefficients.

Assuming a linearly-polarized field in front of the lens and aligning the  $x$ -axis to the incident field polarization the expansion in Eq. (A.31) can be restricted to  $\mathbf{M}_{o,1,l}(\mathbf{r})$  and  $\mathbf{N}_{e,1,l}(\mathbf{r})$  multipoles for the electric field, and  $\mathbf{M}_{e,1,l}(\mathbf{r})$  and  $\mathbf{N}_{o,1,l}(\mathbf{r})$  for the magnetic field, respectively. Instead, for a radially or azimuthally polarized field the expansion in Eq. (A.31) contains only  $\mathbf{M}_{o,0,l}(\mathbf{r})$  and  $\mathbf{N}_{e,0,l}(\mathbf{r})$  multipoles for the electric field, and  $\mathbf{M}_{e,0,l}(\mathbf{r})$  and  $\mathbf{N}_{o,0,l}(\mathbf{r})$  for the magnetic field, respectively.

### A.2.1 Vector spherical harmonics

To understand more clearly the indices in the above equation we review the origins of  $\mathbf{M}_{o,m,l}$  and  $\mathbf{N}_{o,m,l}$ . The scalar fields  $\psi(r, \theta, \varphi)$  that satisfy Helmholtz equation and generate the multipoles are

$$\psi_{e,m,l}^{(p)}(r, \theta, \varphi) = \cos(m\varphi) P_l^m(\cos \theta) z_l^{(p)}(kr), \quad (\text{A.32})$$

$$\psi_{o,m,l}^{(p)}(r, \theta, \varphi) = \sin(m\varphi) P_l^m(\cos \theta) z_l^{(p)}(kr). \quad (\text{A.33})$$

The subscripts e and o represent the even and odd parity of the scalar potential.  $P_l^m(\cos \theta)$  is the associated Legendre functions with indices  $m$  and  $l$ .  $z_l^{(p)}(kr)$  denotes spherical Bessel or Hankel functions (Abramowitz and Stegun, 1972).

Hankel functions of the first type  $h_l^{(1)}(kr)$  represent outgoing waves, whereas Hankel functions of the second type  $h_l^{(2)}(kr)$  represent incoming waves. These are complex conjugates of  $h_l^{(1)}(kr)$ . The spherical Bessel functions of the first type are real functions given by  $j_l(kr) = (h_l^{(1)}(kr) + h_l^{(2)}(kr))/2$ . The second type of spherical Bessel functions corresponds to  $y_l(kr) = (h_l^{(1)}(kr) - h_l^{(2)}(kr))/2$ . The contribution of either of these functions is directly related to the boundary condition. For instance  $h_l^{(1)}(kr)$  cannot be used for expanding the incident field because they are singular at the origin.

The spherical vector harmonics are generated according to (Bohren and Huffman, 1983)

$$\mathbf{M}_{\mathbf{e},m,l}(\mathbf{r}) = \nabla \times (\mathbf{r} \psi_{\mathbf{e},m,l}(\mathbf{r})), \quad \mathbf{N}_{\mathbf{e},m,l}(\mathbf{r}) = \frac{\nabla \times \mathbf{M}_{\mathbf{e},m,l}(\mathbf{r})}{k}. \quad (\text{A.34})$$

The calculation of the coefficients  $B_{\mathbf{e},m,l}$  and  $A_{\mathbf{e},m,l}$  requires some attention (Nieminen et al., 2003). The source-free field mode may be considered as a sum of the converging incoming and diverging outgoing fields. Because the outgoing mode is purely a consequence of the incoming mode, only the latter is needed for a unique determination of the coefficients. This concept was applied for instance by Sheppard and Török, where the multipoles of the expansion were associated with spherical Hankel functions. The direct expansion in terms of multipoles for the source-free field is also possible. However, in this case the converging field at the entrance and the diverging field at the exit of the GRS have to be taken into account. For this purpose the field symmetry on the GRS has to be considered (Collett and Wolf, 1980; Wolf, 1980), which can be derived from the Debye scattering integrals in Eq. (A.1) when assuming positions diametral with respect to the origin

$$\mathbf{E}(-\mathbf{r}) = -\frac{ik}{2\pi} \int_{\Omega_a} \mathbf{A}(\theta, \varphi) e^{-ik\hat{\mathbf{s}} \cdot \mathbf{r}} d\Omega = \left( \frac{ik}{2\pi} \int_{\Omega_a} \mathbf{A}(\theta, \varphi) e^{ik\hat{\mathbf{s}} \cdot \mathbf{r}} d\Omega \right)^* = -\mathbf{E}^*(\mathbf{r}), \quad (\text{A.35})$$

which means that the field is anti-Hermitian for diametral positions on the GRS. The corresponding relationship of the fields phase  $\phi$  reads

$$\phi(x, y, z) = -\phi(-x, -y, -z) - \pi, \quad \text{mod } 2\pi. \quad (\text{A.36})$$

The phase shift of  $-\pi$  demonstrates the phase anomaly in the neighborhood of the focal spot and it is equal to the Gouy phase acquired when the beam traverses the focus (Born and Wolf, 1999; Gouy, 1890a,b; Linfoot and Wolf, 1956).

Here we will follow the approach of Sheppard and Török (1997a). The converging focused beam is expanded by incoming waves matched over the GRS at the exit pupil side and the multipole coefficients are determined accordingly. Then outgoing multipoles are added with the same weight of the incoming ones to remove the singularity at the origin.

## A.2.2 Focused plane wave

Consider an  $x$ -polarized plane wave  $\mathbf{E}(z) = E_0 \exp(-ikz)\hat{\mathbf{x}}$  focused by an aplanatic system. In such case the multipole expansion of Eq. (A.31) reads

$$\mathbf{E}(\mathbf{r}) = \sum_l (A_{e,1,l} \mathbf{N}_{e,1,l}(\mathbf{r}) + B_{o,1,l} \mathbf{M}_{o,1,l}(\mathbf{r})). \quad (\text{A.37})$$

The expansion coefficients are obtained by enforcing the boundary condition set by Eq. (A.3) on the GRS for outgoing multipoles. Using the asymptotic expression  $h_l^{(2)}(kr) \simeq \exp(-i(kr - l\pi/2))/\rho$  we find the conditions  $B_{o,1,l} = -iA_{e,1,l}$  and

$$\sum_l i^l A_{e,1,l} \left[ \frac{P_l^1(\cos \theta)}{\sin \theta} + \frac{dP_l^1(\cos \theta)}{d\theta} \right] = kfE_0 \sqrt{\cos \theta}. \quad (\text{A.38})$$

Exploiting the orthogonality of the angular dependent functions  $\tau_l(\theta) = dP_l^1(\cos \theta)/d\theta$  and  $\pi_l(\theta) = P_l^1(\cos \theta)/\sin \theta$  (Bohren and Huffman, 1983) we arrive to

$$A_{e,1,l} = E_0 kf \frac{(-i)^l (2l+1)}{2l^2(l+1)^2} \int_0^\alpha \sqrt{\cos \theta} [\pi_l(\theta) + \tau_l(\theta)] \sin \theta d\theta. \quad (\text{A.39})$$

The regularity of the electromagnetic field at the focus requires that Eq. (A.37) also contains outgoing multipoles represented by the spherical Hankel function of the first kind with the same amplitude of the incoming ones, i.e., no sources at the origin. That implies  $h_l^{(1)} + h_l^{(2)} = 2j_l$  and we use the notations  $\mathbf{N}_{e,1,l}^{(1)}$  and  $\mathbf{M}_{o,1,l}^{(1)}$  for multipoles with  $j_l$  and include the factor 2 into  $A_{e,1,l}$  to eliminate it from Eq. (A.37).

An important advantage of using this formalism is that the field is decomposed into modes that have known electromagnetic properties, such as directivity, confinement, etc. The multipole strength, defined as  $|A_{e,1,l}/A_{e,1,1}|$  provides us with a good measure of the relative contribution of different modes. Figure A.2 shows this figure of merit for three different focusing angles. For plane-wave illumination ( $\alpha = 0^\circ$ ), modes up to  $l = 10$  have a significant contribution in the field. As the beam gets focused more tightly higher order modes become less important. In the case of  $\alpha = 60^\circ$ , effectively only the first three multipole orders contribute to the beam forming. In conclusion, the tighter the focusing the less is the contribution of higher order modes (Mojarad et al., 2008; van Enk, 2004).

## A.2.3 Directional dipole wave $\mathbf{p}_x$

We have mentioned that a directional dipole wave  $\mathbf{p}_x$  or  $\mathbf{p}_z$  is respectively generated by reversing the field created by a dipole placed at the focal spot and oriented along  $\hat{\mathbf{x}}$  or  $\hat{\mathbf{z}}$ . Here we focus our attention on a  $\mathbf{p}_x$  wave and represent it using a multipole expansion (Zumofen et al., 2009). Once more, instead of considering the angular spectrum (Borghini, 2004; Borghini et al., 2005), we use the electric field on the GRS (see Eq. (A.13)) as a boundary condition for the multipole coefficients. With

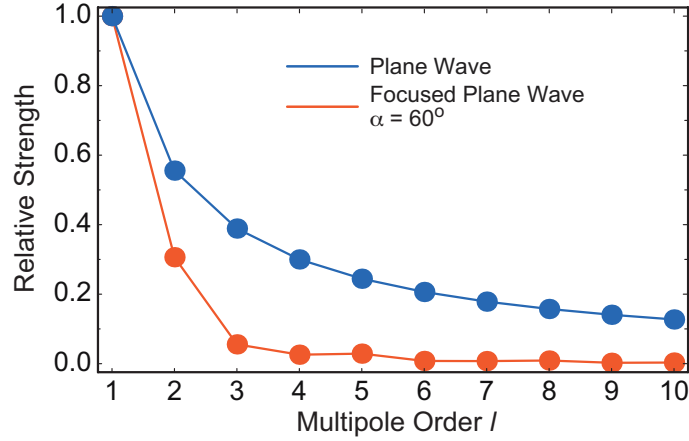


**Figure A.2:** Relative strength of the multipole coefficients for the expansion of a plane wave and of a focused plane wave with  $\alpha = 60^\circ$ .

respect to diffraction integrals, this approach offers more insight on the scattering problem and gives guidelines for engineering the radiation pattern to maximize light-matter interaction. Following Sheppard and Török (1997a), and Stamnes and Dhayalan (1996) the electric field  $\mathbf{E}(\mathbf{r})$  for a  $p_x$  wave reads

$$\mathbf{E}(\mathbf{r}) = \sum_l \left( A_{e,1,l} \mathbf{N}_{e,1,l}^{(1)} - i B_{o,1,l} \mathbf{M}_{o,1,l}^{(1)} \right), \quad (\text{A.40})$$

where the multipole coefficients are

$$A_{e,1,l} = 2(-i)^l E_0 k f \frac{2l+1}{2l^2(l+1)^2} \int_0^\alpha [\pi_l(\theta) \cos \theta + \tau_l(\theta)] \sin \theta d\theta, \quad (\text{A.41})$$

$$B_{o,1,l} = 2(-i)^l E_0 k f \frac{2l+1}{2l^2(l+1)^2} \int_0^\alpha [\pi_l(\theta) + \tau_l(\theta) \cos \theta] \sin \theta d\theta. \quad (\text{A.42})$$

In Figure A.3 we depict the coefficients  $A_{e,1,l}$  and  $B_{o,1,l}$  of a  $p_x$  wave for  $\alpha = 60^\circ$ . The fact that coefficients with  $l > 1$  do not vanish for a directional dipole wave is somewhat surprising. However, these are required to maintain the propagation characteristics of a directional wave and to guarantee power conservation throughout the space on the basis of a source-free focused field. We remark that even for  $\alpha = 90^\circ$   $A_{e,1,l}$  differs from zero for even  $l$  except for  $l = 1$ , while the  $B_{o,1,l}$  coefficients differ from zero exclusively for odd  $l$ . Obviously the expansion for a FPW and  $p_x$  wave must be truncated. It is found that quite a few terms are required for a decent reproduction of the fields for  $\alpha = 90^\circ$  and even more terms must be included for  $\alpha < 90^\circ$  (Zumofen et al., 2009).

#### A.2.4 Focused radially polarized beam

Radially-polarized doughnut beams are constructed by superposing the Gauss-Hermite modes with normal polarizations (Oron et al., 2000). The effect of the

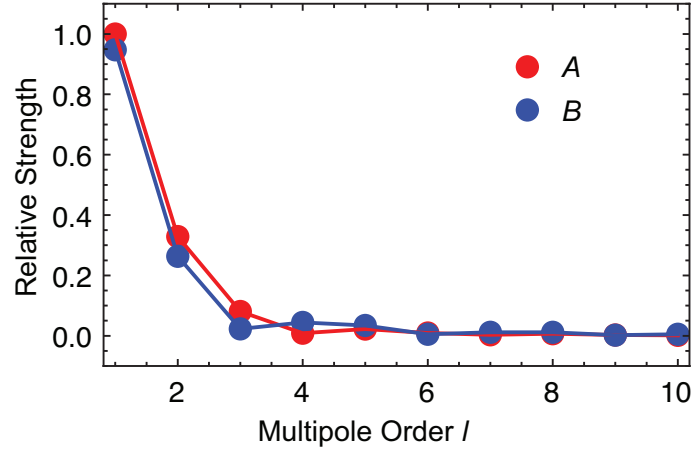


**Figure A.3:** Relative strength of the multipole coefficients (A)  $|A_{e,1,l}/A_{e,1,1}|$  and (B)  $|B_{o,1,l}/B_{o,1,1}|$  for the expansion of a  $p_x$  wave with  $\alpha = 60^\circ$ .

lens is identified by two parameters, the focusing semi-angle  $\alpha$  and the  $d$  factor defined as  $f/w$  (van Enk, 2004), where  $f$  is the focal length of the lens and  $w$  is the beam waist (see Figure 4.33). Using the Richards and Wolf (1959) formalism for an aplanatic system and adapting it to radially-polarized illumination, the field  $\mathbf{E}(d, \theta)$  right after passing the lens is given by Eq. (4.26) (Quabis et al., 2001; Youngworth and Brown, 2000). Note that it depends only on  $d$  and  $\theta$ .

The electric field in the image space can now be found by the multipole expansion, where the weight coefficient of each multipole is determined by matching the field at the lens boundary. Since the electric field has only the  $\theta$  component in the far field, the azimuthal number is  $m = 0$ , and the symmetry around the  $z$  axis implies that transverse electric multipoles have no contribution. The multipole expansion of the focused beam is

$$\mathbf{E}(\mathbf{r}) = \sum_l B_{e,0,l} \mathbf{N}_{e,0,l}, \quad (\text{A.43})$$

and its coefficients read

$$B_{e,0,l} = 2kf(-i)^l \frac{2l+1}{2l(l+1)} \int_0^\alpha |\mathbf{E}(d, \theta)| \frac{dP_l(\cos \theta)}{d\theta} \sin \theta d\theta, \quad (\text{A.44})$$

where  $P_l(\cos \theta)$  are Legendre polynomials (Abramowitz and Stegun, 1972). This expansion is a special case of tightly focused spirally-polarized beams (Borghini et al., 2005).

The relative strength  $|B_{e,0,l}/B_{e,0,1}|$  in Figure A.4 shows how many multipoles contribute to the field in comparison to the dipole wave ( $l = 1$ ). A tightly focused beam ( $\alpha = 90^\circ$  and  $d = 2$ ) mainly consists of a dipole and a quadrupole. Changing the focusing strength  $\alpha$  and the beam parameter  $d$  can give rise to a situation where the dipole wave has a smaller weight. In summary, the general trend is as follows: by increasing  $\alpha$ , i.e. focusing more tightly, higher-order modes are suppressed

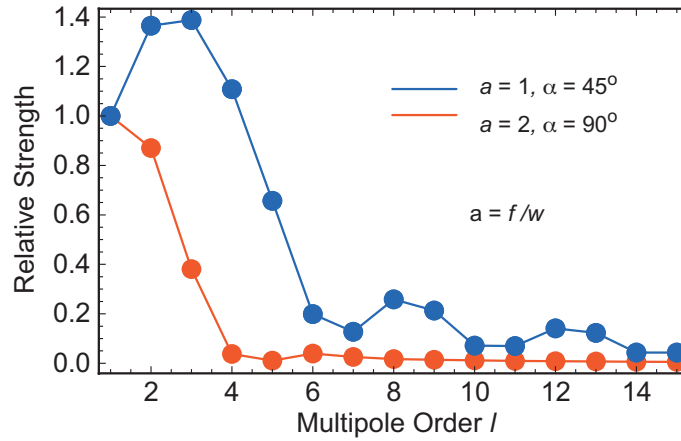


**Figure A.4:** Relative strength  $|B_{e,0,l}/B_{e,0,1}|$  of the multipoles that form a focused radially polarized beam for two different values of  $\alpha$  and  $d$ .

and by increasing the value of  $d$ , i.e. longer focal length or smaller beam waist, higher-order modes get stronger. This additional degree of freedom can be used to farther control light-matter interactions (Mojarad and Agio, 2009). Note indeed that for a focused plane wave or a Gaussian beam higher-order modes can only be suppressed with respect to a plane wave (Lock et al., 1995; Mojarad et al., 2008).



# Appendix B

## Modeling light-matter interactions near metal nanostructures

Many of the results presented in Chapters 3 and 4 require a numerical solution of Maxwell's equations. For example, the modification of the radiative decay rates by optical antennas and the response of a single molecule illuminated by a SNOM probe. These problems cannot be solved using commercial Maxwell solvers, which are typically designed for dealing with engineering problems. Therefore, we developed a customized software based on the FD-TD algorithm that allowed us to tackle the various computational tasks. In what follows we discuss the main features of the FD-TD algorithm, with emphasis on our implementation tuned for studying nano-optical problems. Next, we explain in detail the model for the calculation of molecular scattering near a SNOM tip and the settings for the computation of the decay rates near optical antennas. In the last section we test the FD-TD algorithm and pay special attention on the effects that may compromise the use of this method in nano-optics. These are the mesh discretization in the near field, the excitation of SPPs and the staircasing approximation.

### B.1 The FD-TD algorithm

The FD-TD method has been extensively applied for solving electromagnetic problems in electrical engineering, such as antennas, radar systems and high-speed electronic circuits (Taflov and Hagness, 2005). The use of FD-TD algorithms for studying the behaviour of light in complex electromagnetic environments became very popular with the advent of photonic crystals (John, 1987; Yablonovitch, 1987). However, its application to near-field problems took more time (Girard and Dereux, 1996) due to the need for very fine discretizations and high-performance absorbing boundary conditions for the near field. The latter were proposed only recently (Roden and Gedney, 2000), while the continuous improvement of computers made possible working with finer computational meshes. After a brief introduction of



the basic algorithm we discuss the main aspects that one needs to consider in nano-optics. In particular, we present some advanced FD-TD schemes that we developed for improving the accuracy of the method.

### B.1.1 Governing equations

The FD-TD method, also known as the Yee algorithm (Yee, 1966) from the name of its inventor, is based on the space and time discretization of the Maxwell curl equations

$$\frac{\partial \mathbf{H}}{\partial t} = -\frac{1}{\mu} \nabla \times \mathbf{E}, \quad (\text{B.1})$$

$$\frac{\partial \mathbf{E}}{\partial t} = \frac{1}{\epsilon} \nabla \times \mathbf{H} - \frac{1}{\epsilon} \mathbf{J}_{\text{src}}, \quad (\text{B.2})$$

where we consider isotropic, linear, and non-magnetic media. The structure of Equations (B.1) and (B.2) suggests that the substitution of the space and time derivatives with finite central differences can be implemented using a staggered mesh where electric and magnetic field components are located at different positions as depicted in Figure B.1. The same holds for the time derivative, where electric and magnetic fields are arranged in the so-called *leapfrog* scheme. In this way, the space derivatives on the right of Equations (B.1) and (B.2) are computed at the same time and position as the time derivatives on the left side. If the FD-TD mesh has steps  $\Delta x$ ,  $\Delta y$  and  $\Delta z$  (all equal to  $\Delta$ ), and  $\Delta t$  for the time, rearranging the discretized forms of Equations (B.1) and (B.2) leads to update equations that march the electromagnetic field in space and time. As an example, we write here the FD-TD update equation for the  $x$  component of the electric field (Taflove and Hagness, 2005)

$$E_x|_{i+1/2,j,k}^{n+1} = E_x|_{i+1/2,j,k}^n + \frac{\Delta t}{\epsilon_{i+1/2,j,k}} \cdot \left\{ \begin{aligned} & \frac{H_z|_{i+1/2,j+1/2,k}^{n+1/2} - H_z|_{i+1/2,j-1/2,k}^{n+1/2}}{\Delta y} - \\ & \frac{H_y|_{i+1/2,j,k+1/2}^{n+1/2} - H_y|_{i+1/2,j,k-1/2}^{n+1/2}}{\Delta z} - \\ & J_{x,\text{src}}|_{i+1/2,j,k}^{n+1/2} \end{aligned} \right\}, \quad (\text{B.3})$$

where  $i, j, k, n$  are integers running on the space-time mesh and the terms  $\pm 1/2$  represent the fact that the field components are staggered. Note the simplicity of the algorithm and its flexibility in handling arbitrary structures as that information

enters only via the space discretization of the dielectric function  $\epsilon$ . Moreover, a source for the electromagnetic field can be implemented by defining the desired orientation, space and time profile of the current  $\mathbf{J}_{\text{src}}$ . Another advantage of FD-TD is the time-resolved nature of the algorithm, which allows the computation of a broad range of frequencies in a single run as well as the analysis of transient regimes.

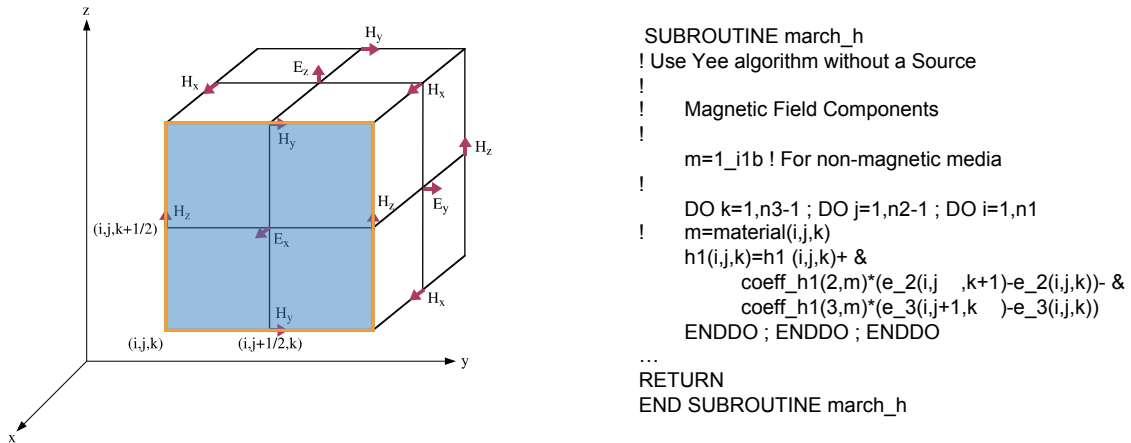


**Figure B.1:** (left panel) The Yee cell. (right panel) The FD-TD time-marching algorithm for the  $H_x$  magnetic field component.

## B.1.2 Boundary conditions

The FD-TD mesh has to be limited to a finite region of space to store the field variables and the auxiliary quantities in the computer memory. On the other hand, an artificial boundary creates non-physical reflections and will therefore lead to a wrong result. To reduce this problem an absorbing medium is positioned as a buffer between the simulation domain and the mesh boundary. In an ideal case it is designed to absorb any field that is incident on it without reflection. Because the modeling of nanostructures requires fine meshes to resolve the geometrical features, to save memory and CPU time it is convenient to reduce the simulation domain as much as possible. An efficient absorber that fulfills these requirements is the so-called Convolutional Perfectly Matched Layer (CPML) (Roden and Gedney, 2000), which we have chosen for our FD-TD implementation. We employ at least 20 CPML layers in our simulations with the conductivity increasing as the power of three towards the mesh boundary (Taflove and Hagness, 2005). In our tests we did not find a noticeable change for thicker layers. Figure B.2 illustrates two situations where CPML are crucial for the FD-TD simulation of nano-optical systems.

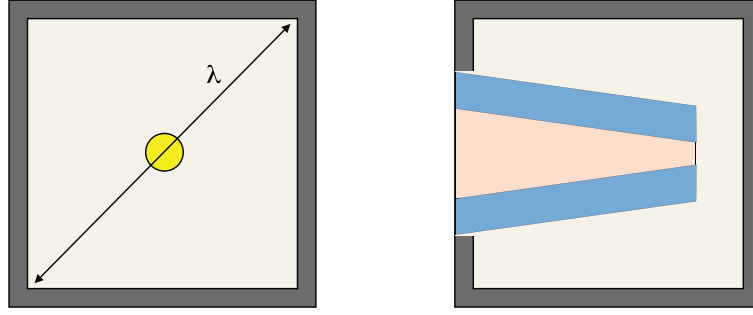


**Figure B.2:** Two examples where CMPL boundary conditions are necessary in the FD-TD simulation of nano-optical systems. The gray frame represents the region where the absorbing boundary conditions are implemented. (left panel) Modeling an object much smaller than the wavelength may require a much larger mesh to ensure that the near field has decayed at the boundaries. (right panel) Semi-infinite metallic object must be terminated in the boundary conditions to avoid spurious resonances due to truncation.

### B.1.3 Metals at optical frequencies

Since we study metal nanostructures at optical wavelengths, where the perfect conductor approximation is not valid, we have to account for a dispersive negative dielectric function. Unfortunately, in the time domain the constitutive relation  $\mathbf{D}(\omega) = \epsilon(\omega)\mathbf{E}(\omega)$  becomes a convolution

$$\mathbf{D}(t) = \epsilon_{\infty}\mathbf{E}(t) + \int_0^t \chi(t-t')\mathbf{E}(t') dt', \quad (\text{B.4})$$

where  $\epsilon_{\infty}$  is the high frequency limit and  $\chi(t)$  is the susceptibility. There are several ways to include Equation (B.4) in the FD-TD method (Taflove and Hagness, 2005). All of them though are limited by the fact that an analytical expression for  $\chi(t)$  is required. Consequently, the modeling of real metals is performed by fitting the optical constants with dispersion models that can be handled by FD-TD. As discussed by Vial et al. (2005), the dielectric function of noble metals can be well fitted in the optical and near-infrared domain using the combination of Drude and Lorentz dispersion.

$$\epsilon(\omega) = \epsilon_{\infty} - \frac{\omega_p^2}{\omega(\omega + i\gamma)} + \frac{\Delta\epsilon \Omega^2}{\Omega^2 - \omega^2 - 2i\delta\omega'} \quad (\text{B.5})$$

where the free parameters are  $\omega_p$ ,  $\gamma$ ,  $\Delta\epsilon$ ,  $\Omega$  and  $\delta$ . Figure B.3 shows a comparison between the optical constants of gold (Lide, 2006) and the fit using Equation (B.5). The agreement is excellent for the real part and quite good for the imaginary part. The fit has been performed over a wavelength range from 500 nm to 1100 nm.

When the Drude-Lorentz model of Equation (B.5) is expressed in the time domain, the convolution in Equation (B.4) must be solved for the Drude  $\chi_D$  and

Lorentz  $\chi_L$  susceptibilities

$$\chi_D(t) = \frac{\omega_p^2}{\gamma}(1 - e^{-\gamma t})\Theta(t), \quad (\text{B.6})$$

$$\chi_L(t) = \frac{\Delta\epsilon\Omega^2}{\sqrt{\Omega^2 - \delta^2}}e^{-\delta t} \sin(\sqrt{\Omega^2 - \delta^2})\Theta(t), \quad (\text{B.7})$$

where  $\Theta(t)$  is the step function. Our FD-TD implementation of Equation (B.4) is based on a recursive convolution method (Sakoda et al., 2001). Referring to Equation (B.3) the Yee algorithm is modified as follows

$$E_x|_{i+1/2,j,k}^{n+1} = E_x|_{i+1/2,j,k}^n + \frac{\Delta t}{\epsilon_{i+1/2,j,k}} \cdot \left\{ \dots \right\} - \frac{\Delta t}{\epsilon_{i+1/2,j,k}} \left( \omega_p^2 F_x|_{i+1/2,j,k}^{n+1/2} - \frac{\Delta\epsilon\Omega^2}{\sqrt{\Omega^2 - \delta^2}} \text{Im} \left[ G_x|_{i+1/2,j,k}^{n+1/2} \right] \right), \quad (\text{B.8})$$

where the term  $\{\dots\}$  represents the braced quantity in Equation (B.3) and  $\epsilon$  stands for  $\epsilon_\infty$  in Equation (B.5). The recursion accumulators  $F_x$  and  $G_x$  obey the following update equations

$$F_x|_{i+1/2,j,k}^{n+1/2} = \Delta t e^{-\gamma\Delta t/2} E_x|_{i+1/2,j,k}^n + e^{-\gamma\Delta t} F_x|_{i+1/2,j,k}^{n-1/2} \quad (\text{B.9})$$

$$G_x|_{i+1/2,j,k}^{n+1/2} = \Delta t (-\delta + i\sqrt{\Omega^2 - \delta^2}) e^{(-\delta + i\sqrt{\Omega^2 - \delta^2})\Delta t/2} E_x|_{i+1/2,j,k}^n + e^{(-\delta + i\sqrt{\Omega^2 - \delta^2})\Delta t} G_x|_{i+1/2,j,k}^{n-1/2}. \quad (\text{B.10})$$

Similar equations hold for the other field components. Notice that  $G_x$  is a complex quantity, which is necessary for having a recursive convolution, and that also the quantities  $\omega_p$ ,  $\gamma$ ,  $\Delta\epsilon$ ,  $\Omega$  and  $\delta$  are functions of  $i$ ,  $j$  and  $k$  like  $\epsilon$  to account for position-dependent material properties.

### B.1.4 Advanced FD-TD approaches

Staircasing, as illustrated in the inset of Fig. B.4a, refers to the approximate representation of actual body shapes in a Cartesian FD-TD mesh. Since optical antennas and metallic waveguides feature geometries with very small radii of curvatures and dimensions compared to the working wavelength, great attention must be paid to spurious effects and slow convergence issues associated with staircasing.

For instance, a FD-TD calculation of the scattering cross section of a 10 nm gold sphere exhibits two peaks in the spectrum. If the calculation is repeated with another mesh discretization, it is found that one peak changes position, as shown in Figure B.4a. In fact, while the SPP resonance is almost equal for the two

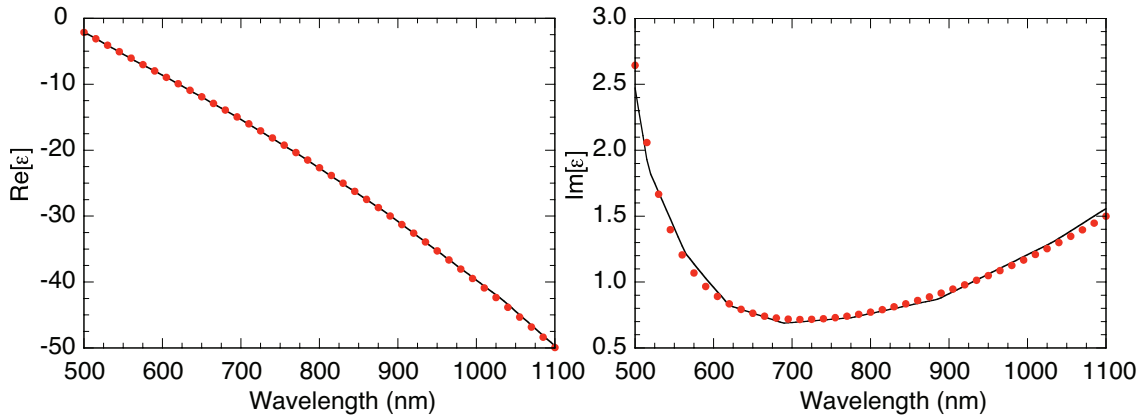


**Figure B.3:** *Fit of the dielectric function  $\epsilon$  of gold for wavelengths between 500 and 1100 nm (Lide, 2006). The experimental data are represented by a continuous line.*

meshes and agrees well with Mie theory (Mie, 1908), the one that changes position represents a spurious peak originating from the sharp edges caused by staircasing. These can be made very small by reducing the mesh pitch, but at the expense of a significantly higher computational cost. Spurious peaks are a typical issue in the FD-TD modeling of metals and it has already been reported twenty years ago for perfect conductors (Cangellaris and Wright, 1991). Our tests show that this phenomenon exists also for real metals and that it is particularly problematic for structures with a small radius of curvature.

### Effective permittivities

A possible solution to staircasing is to depart from the simple Cartesian mesh picture and use non-orthogonal grids or curvilinear coordinates that follow exactly the shape of the objects (Fusco, 1990; Harms et al., 1992; Holland, 1983; Madsen and Ziolkowski, 1990; Mei et al., 1984; Shankar et al., 1990). However, while improving the accuracy, the approach not only considerably increases the complexity of the algorithm, but it may also cause numerical artifacts due to a highly irregular grid, like time instability, velocity dispersion and spurious wave reflection (Railton et al., 1995). Better is to exploit a Cartesian mesh as much as possible and introduce distorted cells only when necessary. For the special cells, a Contour Path (CP) FD-TD algorithm can be obtained directly from Maxwell's equations in integral form (Jurgens and Taflove, 1993; Jurgens et al., 1992). The CP-FD-TD method can still contain cells that potentially generate instability because of non-reciprocal nearest neighbor borrowing steps (Railton et al., 1995). Moreover, the introduction of auxiliary field components and update equations slightly increases memory and CPU time. There have been improvements to CP-FD-TD that solve the instability issue (Hao and Railton, 1998; Kosmanis and Tsiboukis, 2003; Railton et al., 1995). Another possible way for reducing the staircasing error is refining the Cartesian

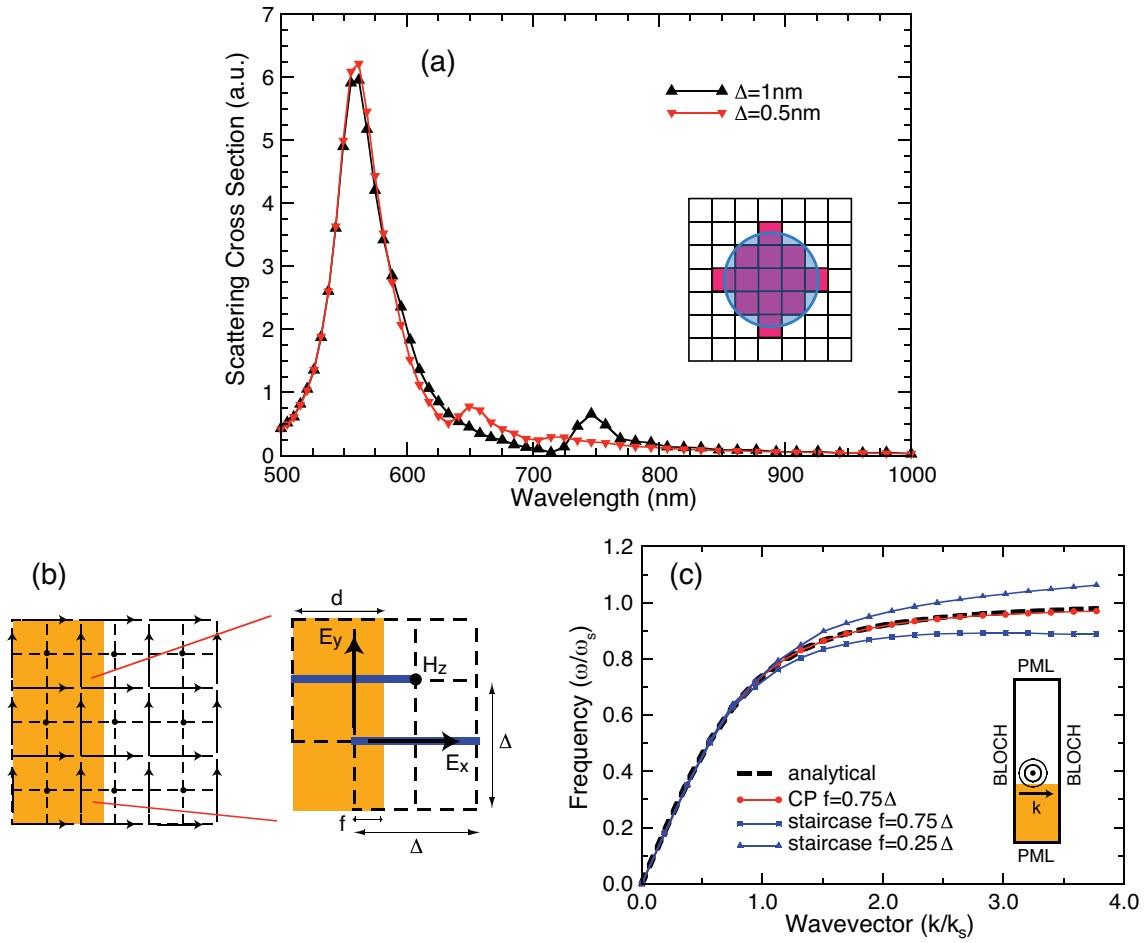


**Figure B.4:** (a) Scattering cross section for a gold nanosphere of radius 5 nm computed for two different discretizations (1 nm and 0.5 nm). The spurious peak is identified by its strong dependence on the FD-TD mesh pitch. The inset illustrates how a nanosphere is approximated by staircasing. (b) Layout of the FD-TD mesh on the metal-dielectric interface (metal at the left). The integration paths for  $E_y$  and  $E_x$  are marked by thick lines. (c) Dispersion relation for a SPP at a glass/copper interface. Frequencies and wavevectors are expressed in units of  $\omega_s = \omega_p / \sqrt{\epsilon_d + \epsilon_\infty}$  and  $k_s = \omega_s \sqrt{\epsilon_d} / c$  ( $\lambda_s = 2\pi/k_s \simeq 450$  nm). The discretization corresponds to  $\Delta = 5$  nm. Inset: simulation scheme (see Mohammadi and Agio, 2006, for details).

mesh in proximity of the interfaces, the so-called subgridding method (Kim and Hofer, 1990; Zivanovic et al., 1991). However, this scheme implies modifications at the fields-marching level, making the algorithm more complicated to implement, besides other numerical issues like spurious wave reflection.

A different approach specific to dielectrics relies on effective permittivities (EPs) for the partially filled cells, without any distortion of the Cartesian grid. The question is, what value for the permittivity has to be chosen in order to get the best approximation of the dielectric interface? An early attempt in this direction has been made for modeling thin material sheets (Maloney and Smith, 1992), even

though there is still usage of auxiliary terms for field components normal to the interface and the procedure is limited to rectangular objects aligned with the mesh. A few years later, Kaneda et al. (1997) proposed a phenomenological formula for the EP applicable to any kind of interface geometry, including curved surfaces. Their expression matches the rigorous result that can be obtained when the field component is perpendicular or parallel to the interface (Hirono et al., 2000; Hwang and Cangellaris, 2001). These EPs improve the accuracy of the FD-TD method, while keeping the same stability and simple structure of the original algorithm. However, there is no guarantee that the formula fulfills the proper boundary conditions at a curved interface or simply at a flat interface tilted with respect to the mesh axes. There are several works presenting other kinds of EPs: a volume average (Dey and Mittra, 1999), a first-neighbor average (Yang et al., 2004; Yu et al., 2000), Maxwell-Garnett, inverted Maxwell-Garnett and Bruggeman formulae (Yang et al., 2000), and other phenomenological derivations (Yu and Mittra, 2001). Some of them have been tested together for the purpose of comparison (Sun and Fu, 2000). These proposals are not fundamentally more accurate than Kaneda's approach.

The main problem with the formulation of EPs resides in the vectorial nature of the electromagnetic field. In fact, the same discontinuity can lead to quite different EP values depending on the orientation of the electric field with respect to the interface (Hirono et al., 2000; Hwang and Cangellaris, 2001). Therefore, it is crucial that in the derivation of the EP, not only the geometry, but also the proper boundary conditions are taken into account. Along this line a non-diagonal EP-tensor can be obtained via the homogenization of a partially filled cell (Lee and Myung, 1999; Nadobny et al., 2003). However, its implementation requires the usage of both  $\mathbf{E}$  and  $\mathbf{D}$ , implying more storage and CPU time. Moreover, because in the FD-TD method the field components are not defined in the same position, a nearest-neighbor average is required for linking  $\mathbf{E}$  with  $\mathbf{D}$ . Such average, can wash out the fulfillment of the boundary conditions at the interface. Recently, there have been other original ideas that improve the accuracy of the FD-TD method under a rigorous treatment of the electromagnetic field at the dielectric interface, even though they considerably increase the complexity of the algorithm (Ditkowski et al., 2001; Dridi et al., 2001; Farjadpour et al., 2006; Fujii et al., 2003; Xiao and Liu, 2004).

We have developed a novel contour path approach to obtain EPs starting from Maxwell's equations in integral form. These permittivities account for the boundary conditions for the electromagnetic field at a dielectric interface and, at the same time, they do not require any modification of the FD-TD algorithm (Mohammadi et al., 2005). Moreover, our method has been generalized to handle metal-dielectric interfaces of arbitrary shape. We named this approach dispersive contour-path (DCP) FD-TD (Mohammadi et al., 2008a). By carrying out the implementation of dispersion using the Z-transform (Sullivan, 1996) we have also shown that for flat interfaces the method reduces to that of Mohammadi and Agio (2006).

To give an example of the DCP-FD-TD method in Figure B.4 we consider SPP propagating along the interface between two semi-infinite isotropic and non-magnetic media, with dielectric functions  $\epsilon_d$  and  $\epsilon_m(\omega) = \epsilon_\infty - \omega_p^2/(\omega(\omega + i\gamma))$ , respectively. The constitutive relations for the electromagnetic field must be expressed in time domain to be compatible with the FD-TD paradigm. Here we used the Z-transform as a suitable transformation to replace discrete convolutions with multiplications. To properly account for the electromagnetic boundary conditions, we derive the FD-TD algorithm starting from the Maxwell's equations in integral form. As depicted in Figure B.4b, because we are dealing with a flat interface we refer to a 2D mesh with TM polarized light (non-zero field components  $E_x, E_y, H_z$ ). The details of the derivation can be found in Mohammadi and Agio (2006).

In order to compare the accuracy of the CP method with respect to staircasing and investigate how well FD-TD can model SPPs, we use the 2D-FD-TD method to compute the dispersion relation  $\omega(k)$  of SPPs propagating along the metal-dielectric interface. For a metal-dielectric interface, the dispersion relation of SPPs is given by (Raether, 1988)

$$k = \frac{\omega}{c} \sqrt{\frac{\epsilon_d \epsilon_m(\omega)}{\epsilon_d + \epsilon_m(\omega)}}. \quad (\text{B.11})$$

The calculation scheme is shown in the inset to Figure B.4c. The FD-TD mesh has Bloch boundary conditions (Chan et al., 1995) at the terminations perpendicular to the interface and PML (Ramadan and Oztoprak, 2003) boundary conditions at the remaining sides. A dipole placed in the proximity of the interface excites the SPP. Because of the Bloch boundary conditions, only the energies corresponding to the imposed wavevector survive as time evolves. By Fourier transforming the recorded time series, one obtains frequency peaks, which yield the SPP dispersion relation when considering all wavevectors. We choose glass ( $\epsilon_d=2.25$ ) and copper ( $\epsilon_\infty=1.0$ ,  $\omega_p = 5.0 \times 10^{15}$  rad/s and  $\gamma = 0.01\omega_p$ ) (Ashcroft and Mermin, 1976). The dispersion relation computed using staircasing, the CP method and the analytical solutions is plotted in Figure B.4c. While in the region where the SPP has a high group velocity both methods agree very well with the analytical curve, as the group velocity decreases staircasing exhibits a much larger error. Indeed, this is the case where the SPP is tightly localized at the interface and thus a proper treatment of the electromagnetic boundary conditions becomes important.

### B.1.5 Body of revolution

Since the onset of large electric fields at the nanoparticle surface and the nanoscale geometry require fine meshes for getting accurate results (Kaminski et al., 2007; Oubre and Nordlander, 2004), even if the overall size of the system is small the computational burden becomes considerable. When the optical antenna and the source exhibit rotational symmetry we can exploit the body of revolution (BOR) technique



in the FD-TD method (Taflove and Hagness, 2005) to reduce the original three-dimensional (3D) problem to a two-dimensional (2D) one (see Figure B.5). When we deal with very fine mesh, the BOR-FD-TD method can significantly decrease the required memory and computation time. This approach has been used in various applications such as modeling wave propagation through optical lenses (Davidson and Ziolkowski, 1994), resonant cavities (Chen et al., 1996), and the calculation of spontaneous emission lifetime in a microcavity (Xu et al., 1999).

For a rotationally symmetric problem, the electric and magnetic fields in cylindrical coordinates can be expressed as an infinite Fourier-series expansion of the form

$$\mathbf{E}(\rho, \phi, z) = \sum_{m=0}^{\infty} (\mathbf{E}_{e,m}(\rho, z) \cos m\phi + \mathbf{E}_{o,m}(\rho, z) \sin m\phi), \quad (\text{B.12})$$

$$\mathbf{H}(\rho, \phi, z) = \sum_{m=0}^{\infty} (\mathbf{H}_{e,m}(\rho, z) \cos m\phi + \mathbf{H}_{o,m}(\rho, z) \sin m\phi), \quad (\text{B.13})$$

where  $m$  is the mode number. For isotropic materials, these modes are uncoupled from each other, and their number depends on the excitation symmetry. In our case, where a dipole is located at and directed along the  $z$ -axis, only the zeroth-order mode is necessary ( $m = 0$ ). Furthermore, only three electromagnetic-field components are required ( $E_{\rho,e,0}$ ,  $E_{z,e,0}$  and  $H_{\phi,e,0}$ ), corresponding to a transverse magnetic mode. As shown in Figure B.5, we employ PML absorbing boundary conditions to truncate the computational domain without introducing spurious reflections (Prather and Shi, 1999). Although the model is limited to emitters located and oriented such that the system preserves cylindrical symmetry, BOR-FD-TD allows the study of several cases with the computational burden and speed of a 2D FD-TD calculation.

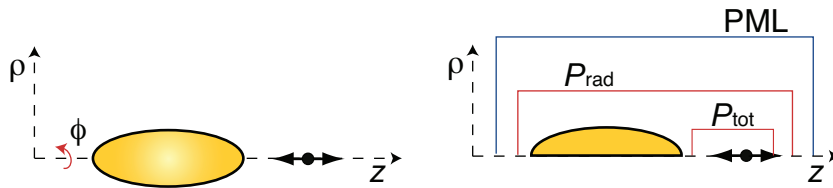


**Figure B.5:** A single emitter coupled to an optical antenna. (left panel) The antenna and the emitter are such that the system forms a body of revolution. (right panel) In the BOR-FD-TD approach the 3D problem can be reduced to a 2D one by considering only a plane containing the  $z$ -axis. The total and radiated powers are computed using Poynting theorem (red lines). The mesh is truncated using PML absorbing boundary conditions (blue line).

### Near-to-Far-Field Transformation

A near-to-far field transformation can be performed starting from the electromagnetic field obtained by BOR-FD-TD calculations. For instance, on the reference plane shown in Figure 4.33, one defines equivalent electric and magnetic surface current densities, which respectively are  $\mathbf{J}_s = -\mathbf{n} \times \mathbf{E}$  and  $\mathbf{M}_s = \mathbf{n} \times \mathbf{H}$ , where  $\mathbf{n}$  is the unit vector normal to the surface. Each current element radiates to the far field as a dipolar source. By integrating the contribution of these elements over that plane, one obtains the electromagnetic field in the far region (Taflove and Hagness, 2005). Symmetry considerations imply that on the GRS the electric field has only the  $\theta$  component in spherical coordinates  $(r, \theta, \varphi)$ , which reads

$$\mathbf{E}(r, \theta) = -\frac{ke^{-ikr}}{2r} e^{ikz_o \cos \theta} \int_0^{\rho_{\max}} d\rho \rho J_1(k\rho \sin \theta) (E_\rho(\rho, z_o) + ZH_\phi(\rho, z_o) \cos \theta) \hat{\theta}. \quad (\text{B.14})$$

$J_1$  is the Bessel function of the first kind (Abramowitz and Stegun, 1972),  $z_o$  is where the reference plane intercepts the  $z$ -axis,  $Z$  is the medium impedance and  $k$  is the wavevector.  $\rho_{\max}$  should be large enough to make the contribution of the excluded field negligible.

## B.2 Modeling interactions

We used the FD-TD method to model two phenomena associated with light-matter interaction at the single-molecule level. First, we developed a model to investigate the extinction signal due to a single molecule excited by a subwavelength aperture created in a SNOM probe (see Section 3.3). Second, we computed the modification of the spontaneous emission rate when a molecule is in the near-field of an optical antenna (see Sections 4.2 and 4.3). Here we provide technical details on how we tackled these problems.

### B.2.1 Molecular scattering

The molecule is modeled as an anisotropic Lorentz medium that occupies only one FD-TD cell. In practice, the dielectric function  $\epsilon$  is dispersive only along  $x$  and it is equal to that of the background medium along  $y$  and  $z$ . We now derive an expression that relates the induced molecular dipole moment  $\mathbf{p}$  to the incident field  $\mathbf{E}_{\text{tip}}$  via the polarizability  $\alpha$ . The dispersive part of  $\epsilon$  reads

$$\epsilon_x(\omega) = \epsilon_\infty + \frac{\Delta\epsilon\omega_0^2}{\omega_0^2 - \omega^2 - 2i\gamma\omega}, \quad (\text{B.15})$$

where  $\epsilon_\infty$  corresponds to the dielectric function of the background medium,  $\Delta\epsilon$  parametrizes the oscillator strength,  $\omega_0$  is the resonance frequency, and  $2\gamma$  is the

radiative linewidth. The associated polarizability  $\alpha$  can be derived starting from a Clausius-Mossotti relation

$$\alpha_x \propto \frac{\epsilon_x(\omega) - \epsilon_\infty}{\epsilon_x(\omega) + 2\epsilon_\infty} = \frac{\Delta\epsilon\omega_0^2}{3\epsilon_\infty \left[ \omega_0^2 \left( 1 + \frac{\Delta\epsilon}{3\epsilon_\infty} \right) - \omega^2 - 2i\gamma\omega \right]}. \quad (\text{B.16})$$

Writing  $\omega'_0 = \omega_0[1 + \Delta\epsilon/(3\epsilon_\infty)]$  and assuming  $\gamma \ll \omega'_0$  lead to

$$\alpha_x = -\frac{1}{2} \frac{\Delta\epsilon\omega'_0}{3\epsilon_\infty + \Delta\epsilon} \frac{\omega - \omega'_0 - i\gamma}{(\omega - \omega'_0)^2 + \gamma^2}. \quad (\text{B.17})$$

This corresponds to the expression in Eq. (3.24), where

$$A = \frac{\pi}{\gamma} \left( \frac{\Delta\epsilon\omega'_0}{3\epsilon_\infty + \Delta\epsilon} \right). \quad (\text{B.18})$$

## B.2.2 Decay rates

In Section 4.1.1 we stated that the decay rates can be obtained by computing the power radiated by a classical dipole placed near a metal nanostructure. The dipole source is implemented in the FD-TD method by letting  $\mathbf{J}_{\text{src}}$  be zero everywhere except at the FD-TD cell corresponding to the position of the emitter. The dipole orientation is determined by the components of  $\mathbf{J}_{\text{src}}$ . According to Poynting theorem (Jackson, 1999)

$$P_t = -\frac{1}{2} \int_V \text{Re}[\mathbf{j}^*(\mathbf{r}, \omega) \cdot \mathbf{E}(\mathbf{r}, \omega)] dV \quad (\text{B.19})$$

is the total power dissipated by the dipole, which goes into radiation and absorption due to the Ohmic losses in the metal nanostructure. Note that  $P_t$  is computed using a volume integral because in FD-TD the dipole source has a finite extension determined by the cell volume  $V = \Delta^3$ . The radiated power is instead given by

$$P_r = \int_\Sigma \mathbf{S} \cdot \mathbf{n} r^2 ds, \quad (\text{B.20})$$

where  $\mathbf{S}$  is the Poynting vector and  $\mathbf{n}$  is the normal to a closed spherical surface  $\Sigma$  of radius  $r$  that encloses both dipole and nanostructure.

To compute  $P_t$  and  $P_r$  with FD-TD two detectors are needed, as shown in Figure B.6. The large one, used for  $P_r$ , is a closed surface on which the flux of the Poynting vector  $\mathbf{S}$  is calculated. The small one takes only the FD-TD cell of the dipole source and it implements the calculation of  $P_t$ . The detectors perform an *on-the-fly* discrete Fourier transform to obtain the fields in frequency domain. This allows the calculation of decay rates over the desired spectral range. It is worth to mention a couple of technical issues related to the calculation of  $P_r$  and  $P_t$ . For a lossless system, energy conservation implies that  $P_r = P_t$ . This equality is valid

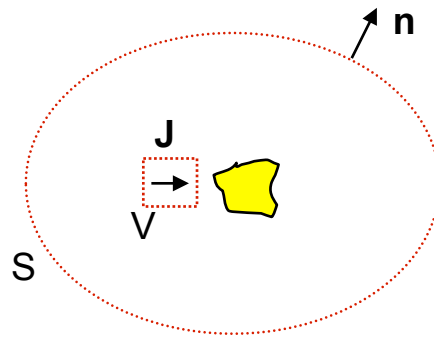


**Figure B.6:** Schematics of the calculation for the decay rates with the FD-TD method.

also in FD-TD only if the Poynting theorem is properly reformulated by taking into account the mesh discretization and the staggered position of the field components (De Moerloose and De Zutter, 1995). Moreover, the expression for  $P_t$  contains  $\text{Re}[\mathbf{J}^* \cdot \mathbf{E}]$ , which represents a small difference of two large numbers. As a result, any numerical noise present in the simulation will be amplified in  $P_t$ . Such noise is primarily due to the Fourier transform and to the absorbing boundary conditions.

### B.3 Numerical tests

The FD-TD method has been extensively tested and applied to the calculation of decay rates in a dielectric environment (Hermann and Hess, 2002; Xu et al., 2000). However, when one considers metal nanostructures two new effects have to be taken into account with respect to dielectrics: SPPs and Ohmic losses. Because SPPs strongly depend on the shape of the object and the FD-TD method approximates a curved surface with a segmented profile, the so-called *staircasing* approximation (see Appendix B.1.4), it is important to understand what are the consequences on the accuracy of the calculation. Secondly, because a certain portion of the radiated power will be absorbed by the metal, one has to compute both radiative and non-radiative decays to completely assess the performance of a nanostructure. Moreover, since the strongest effects are obtained when the emitter is very close to the metal surface, it is also important to evaluate how the near-field coupling is modeled. For these reasons, we test the FD-TD method on systems for which an analytical solution exists, so that a direct comparison is possible. Furthermore, we choose examples that allow us to understand the different sources of error that occur in a simulation.

We consider a perfect mirror to study only the error on the near field of a dipole source. Because we are interested in the near-field coupling of emitters to nanostructures, it is important to understand if the commonly used discretization  $\Delta = \lambda/20$  (Taflove and Hagness, 2005) is also valid in the near field, where high

wavevector components are not negligible. Furthermore, because the system is lossless, we use it to check that  $P_t$  and  $P_r$  give the same result in FD-TD (De Moerloose and De Zutter, 1995). We then move to the case of a real metal mirror, defined by a simple Drude dispersion model. In this case we focus on the evaluation of the non radiative decay rate, which is known to increase very rapidly as the dipole approaches the interface (Chance et al., 1978). In this situation we want to understand how well the penetration of the field in the metal and the coupling to non-radiative SPPs are modeled. At last, we study the staircasing effect by considering a gold sphere. The stepwise discretization of the curved boundary introduces an error on the optical properties of the nanoparticle (Oubre and Nordlander, 2004), and, consequently, an error on the decay rates. We present two situations, one where the cell size is much smaller than the radius of the sphere, and one where the cell size is comparable to it. In both cases the discretization is fine enough for modeling the near field and the skin depth so that we expect that the error be primarily caused by staircasing.

### B.3.1 Perfect mirror

A dipole, with two possible orientations, is positioned at a certain distance  $z$  from a perfect mirror, as shown in the inset to Figure B.7. The perfect conductor is implemented by simply imposing that the field must be zero inside the metal. Because the system does not have a length scale nor dispersion, it is equivalent to scan the distance from the mirror or scan the dipole wavelength  $\lambda$  and express the decay rates as a function of the dimensionless quantity  $kz$ , where  $k = 2\pi/\lambda$ . In FD-TD calculations we find convenient to define a characteristic length  $a$  that allows to write the wavelength and the structure parameters as dimensionless quantities that are close to unity. This is advantageous both for the floating point operations and for the handling of data. Therefore, we use dimensionless wavelengths  $\lambda_o = \lambda/a$ , lengths  $d_o = d/a$  and frequencies  $\nu_o = a/\lambda$ . The decay rates are calculated by scanning  $\nu_o$  for a fixed distance  $z_o$ , which is equivalent to changing  $kz = 2\pi\nu_o z_o$ . This is computationally more efficient than running several simulations at different distances and has the additional benefit that the wavelength sampling, for a given discretization  $\Delta = a/N$ , where  $N$  is an integer number, is inversely proportional to  $kz$ , thus making the calculation of the near-field coupling more accurate.

A Gaussian pulse centered at the frequency  $\nu_o$  and bandwidth  $\sigma_o$  is launched at the dipole position using a current  $\mathbf{J}_{\text{src}}$  perpendicular or orthogonal to the interface. Note that a smaller frequency corresponds to a smaller  $kz$ , since  $z$  is constant. The normalized decay rates are compared to the analytical solutions (Chance et al.,

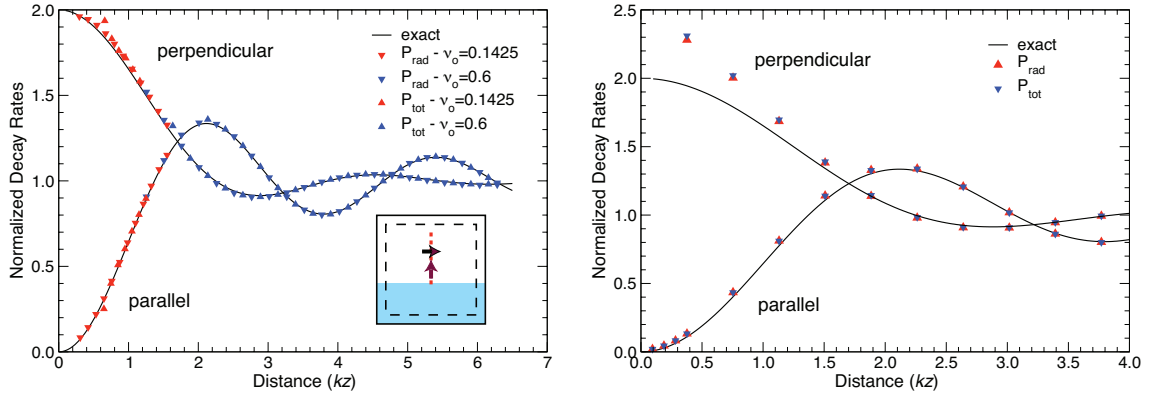


**Figure B.7:** Normalized radiative and total decay rates for a dipole in front of a perfectly conducting flat metal surface as a function of  $kz$  obtained by scanning the wavelength (left panel) or the distance (right panel). Inset: layout of the FD-TD simulation with the two possible dipole orientations. The distance is changed along the red dotted line, while the black dashed line indicates the radiation detector.

1978)

$$\frac{\Gamma_{\perp}}{\Gamma_{\text{r}}^0} = 1 - 3\text{Im} \left[ \left( \frac{1}{(2kz)^3} - \frac{i}{(2kz)^2} \right) e^{i2kz} \right], \quad (\text{B.21})$$

$$\frac{\Gamma_{\parallel}}{\Gamma_{\text{r}}^0} = 1 + \frac{3}{2}\text{Im} \left[ \left( \frac{1}{(2kz)^3} - \frac{i}{(2kz)^2} + \frac{1}{(2kz)} \right) e^{i2kz} \right], \quad (\text{B.22})$$

where  $\perp$  and  $\parallel$  refer to dipole orientations perpendicular and parallel to the interface, respectively. The left panel of Figure B.7 displays the FD-TD result and the analytical solution for both dipole orientations. The  $kz$  scan is achieved by concatenating two FD-TD simulations, one with  $\nu_o = 0.1425$ ,  $\sigma_o = 0.02$  and the other one with  $\nu_o = 0.6$ ,  $\sigma_o = 0.1$ . The dipole is at a distance  $z_o = 1.0$  and the number of cells per characteristic length  $a$  is  $N = 40$ . The agreement with the exact result is quite good over the whole range of  $kz$  thanks to the fact that we used a fine discretization and that the wavelength sampling increases as  $kz$  decreases. If we keep the wavelength fixed at  $\nu_o = 0.6$  and perform a distance scan, shown in the right panel of Figure B.7, we find an increasing error as  $kz$  approaches to zero, especially for the dipole perpendicular to the interface, for which the near-field coupling is stronger. This confirms that the  $\lambda/20$  criterion does not apply in the near field and that as the dipole approaches the nanostructure one needs to use finer discretizations.

The data presented in Figure B.7 confirm that for a lossless system total and radiative decays are equal, to within a small numerical error. To investigate the different accuracy in the calculation of  $P_{\text{t}}$  and  $P_{\text{r}}$  we have computed them up to several  $\sigma_o$  from the central frequency. We found that  $P_{\text{r}}$  is correct over a larger bandwidth than  $P_{\text{t}}$  (Kaminski et al., 2007). This confirms that the quantity  $\text{Re}[\mathbf{J}^* \mathbf{E}]$  is more sensitive to numerical noise than the flux of the Poynting vector. For this

reasons, great care must be taken when analyzing the FD-TD data. In general, we have found that the usable bandwidth for  $P_t$  decreases with  $\nu_o$  and that it is always narrower than that for  $P_r$ .

### B.3.2 Metal mirror

For the case of a real metal mirror we replace the perfect conductor with a Drude metal. The parameters of Drude dispersion are chosen to be  $\omega_p = 1.0$ ,  $\gamma = 0.05$  and  $\epsilon_\infty = 1.0$ , where  $\omega_p$  and  $\gamma$  are expressed in dimensionless units like  $\nu_o$  for  $a=100$  nm. Because of Ohmic losses the radiative and total decay rates are no longer equal. As sketched in the inset to Figure B.8 the dipole excites also a SPP wave at the metal-vacuum interface that propagates outside the simulation domain. The energy stored in the SPP is collected by the detector for  $P_r$  before being completely dissipated in the metal. Therefore,  $P_r$  is always overestimated and only the total decay rate is correctly computed. Nevertheless, since the non-radiative decay is predominant in the near field, the total decay is sufficient for testing how FD-TD accounts for the Ohmic losses. The total decay rates, computed for dipole orientations parallel and perpendicular to the interface are compared to the analytical solution (Chance et al., 1978)

$$\frac{\Gamma_\perp}{\Gamma_r^o} = 1 - \frac{3}{2} \text{Im} \left[ \int_0^\infty R^\parallel e^{-2lkz} \frac{u^3}{l} du \right], \quad (\text{B.23})$$

$$\frac{\Gamma_\parallel}{\Gamma_r^o} = 1 + \frac{3}{4} \text{Im} \left[ \int_0^\infty [(1 - u^2)R^\parallel + R^\perp] e^{-2lkz} \frac{u}{l} du \right], \quad (\text{B.24})$$

where  $u$  is the normalized wavevector along the interface  $u = k_x/k$  and  $l = -i(1 - u^2)^{1/2}$ , with  $k = 2\pi/\lambda$ .  $R^\perp$  and  $R^\parallel$  are the Fresnel reflection coefficients of the interface.

Due to the dispersive dielectric function, the decay rate is not only a function of  $kz$ , but also of the wavelength itself. For this reason, distance and wavelength scans are not equivalent any more. Choosing a dipole wavelength  $\lambda=600$  nm and a characteristic length  $a=100$  nm give  $\nu_o \simeq 0.167$  and  $a$  is divided into  $N = 40$  cells (mesh's pitch  $\Delta=2.5$  nm). Alternatively, a characteristic length  $a=300$  nm implies  $\nu_o = 0.5$  and, for the same  $N$ , a coarser mesh ( $\Delta=7.5$  nm). In other terms, one can improve the accuracy either by increasing  $N$  or by decreasing  $a$  for the same wavelength. As mentioned in the previous section, the fact that the available bandwidth depends on  $\nu_o$ , the two approaches are not equivalent. The distance of the dipole from the metal surface is only up to 300 nm because we are interested only in the near-field effects. Figure B.8 compares the FD-TD result with the exact ones for different discretizations. Above 150 nm the agreement is very good for all meshes, while for smaller distances it is necessary to use the finer one, which yields a reasonable result up to a distance of about 20 nm. Both dipole orientations show the

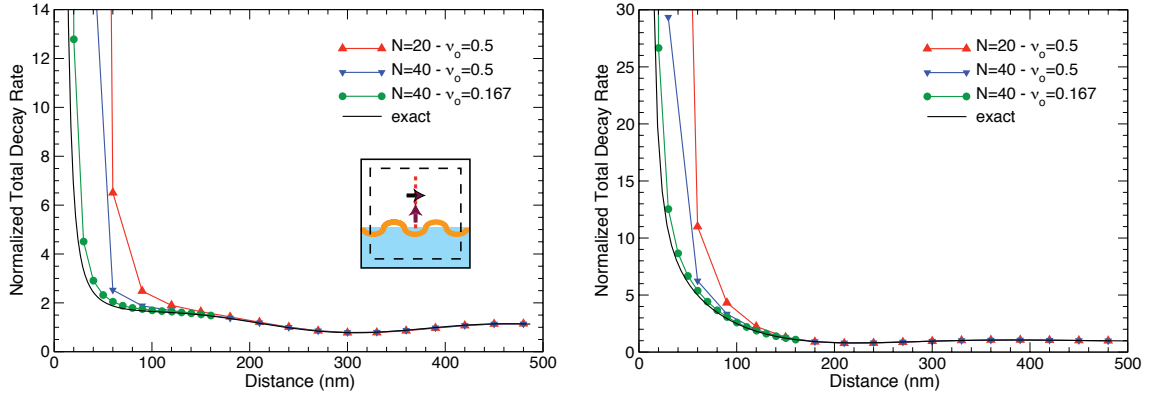


**Figure B.8:** Normalized total decay rate for a dipole in front of a flat real metal surface as a function of distance. The dipole is oriented parallel (left panel) and perpendicular (right panel) to the interface. The curves are obtained using different discretizations. Inset: sketch of an excited SPP passing through the radiation detector, which leads to an incorrect estimate of the radiative decay rate.

correct  $(kz)^{-3}$  behavior due to the non-radiative contribution (Chance et al., 1978) only for the finest mesh, suggesting that the discretization strongly affects the energy dissipation into the metal. Indeed, for the given Drude parameters, at  $\lambda=600$  nm the attenuation length for a plane wave in the metal corresponds to 16 nm. The mesh must be chosen accordingly to ensure that the field is approximately constant over an FD-TD cell.

### B.3.3 Gold nanosphere

Having understood how the FD-TD method models the near-field coupling and the Ohmic losses, we consider the case of a dipole in the vicinity of a gold sphere as shown in the inset to Figure B.9. The staircasing issue can be negligible for relatively large spheres, but it is important when the sphere radius is comparable to the cell size. Moreover, since the aim is to enhance decay rates using SPPs, the artificial surface roughness induced by staircasing could lead to inaccurate results (Oubre and Nordlander, 2004).

For a finite structure we can compute both total and radiative decays for dipole orientations perpendicular and parallel to the surface of the sphere. These are



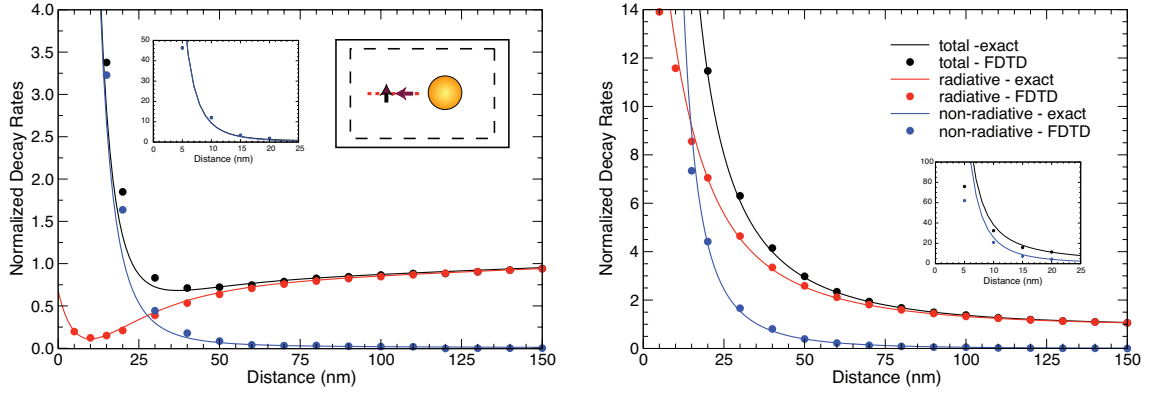


**Figure B.9:** Normalized decay rates for a dipole oriented parallel (left panel) and perpendicular (right panel) to a gold sphere of radius 50 nm as a function of the distance from the sphere surface. Insets: layout of the simulation and zoom to close distances for total and non-radiative decays.

compared to the analytical formulae (Ruppin, 1982)

$$\frac{\Gamma_{r,\perp}}{\Gamma_r^o} = \frac{3}{2} \sum_{n=1}^{\infty} (2n+1)n(n+1) \frac{|j_n(kr) + b_n^m h_n(kr)|^2}{(kr)^2}, \quad (\text{B.25})$$

$$\begin{aligned} \frac{\Gamma_{r,\parallel}}{\Gamma_r^o} = & \frac{3}{4} \sum_{n=1}^{\infty} (2n+1) \left\{ |j_n(kr) + h_n(kr)a_n^m|^2 \right. \\ & \left. + \left| \frac{[krj_n(kr)]' + b_n^m [krh_n(kr)]'}{kr} \right|^2 \right\}, \quad (\text{B.26}) \end{aligned}$$

where  $j_n$  and  $h_n$  are the spherical Bessel and Hankel functions, respectively (Abramowitz and Stegun, 1972).  $r$  is the distance of the dipole from the center of the sphere and  $a_n^m$ ,  $b_n^m$  are the Mie coefficients (Bohren and Huffman, 1983; Ruppin, 1982). The analytical expression for the total decay rate reads instead (Klimov et al., 1996)

$$\begin{aligned} \frac{\Gamma_t}{\Gamma_r^o} = & 1 - \frac{3}{2} \text{Re} \left[ \cos^2 \psi \sum_{n=1}^{\infty} n(n+1)(2n+1)q_n \left[ \frac{h_n^{(1)}(r)}{r} \right]^2 + \right. \\ & \left. \sin^2 \psi \sum_{n=1}^{\infty} (n+1/2) \left\{ p_n [h_n^{(1)}(r)]^2 + q_n \left[ \frac{d[rh_n^{(1)}(r)]}{rdr} \right]^2 \right\} \right]. \quad (\text{B.27}) \end{aligned}$$

The coefficients  $p_n$  and  $q_n$  can be written as functions of the spherical Bessel and Hankel functions (see Klimov et al., 1996).  $\psi$  is the angle of the dipole relative to the sphere, with  $\psi = 0^\circ$  corresponding to the perpendicular case and  $\psi = 90^\circ$  to the parallel case.

First we consider a dipole at the fixed wavelength  $\lambda=580$  nm, corresponding to the emission wavelength of a terrylene molecule in para-terphenyl (Kühn et al., 2006) at different distances from a gold sphere of radius 50 nm embedded in a homogeneous background with index  $n = 1.7$ , typical of immersion oils and transparent oxides. The mesh cell size is chosen to be  $\Delta=2$  nm. Figure B.9 compares the FD-TD results with the analytical theory for a dipole parallel or perpendicular to the sphere. The agreement for the radiative decay rate is very good for all distances, even down to 5 nm. However, the total decay rate is correct up to a distance of about 40 nm. The accuracy for the non-radiative decay is analogous since it is evaluated by taking the difference of the total and radiative rates. For the perpendicular dipole orientation the results match the analytical values up to 20 nm. Therefore, for  $\Delta=2$  nm the staircasing effect does not affect the accuracy of the calculation. The deviation from the exact solution for very small distances is rather attributed to the difficulty in modeling the near field of the dipole, as discussed in the section on the perfect mirror.

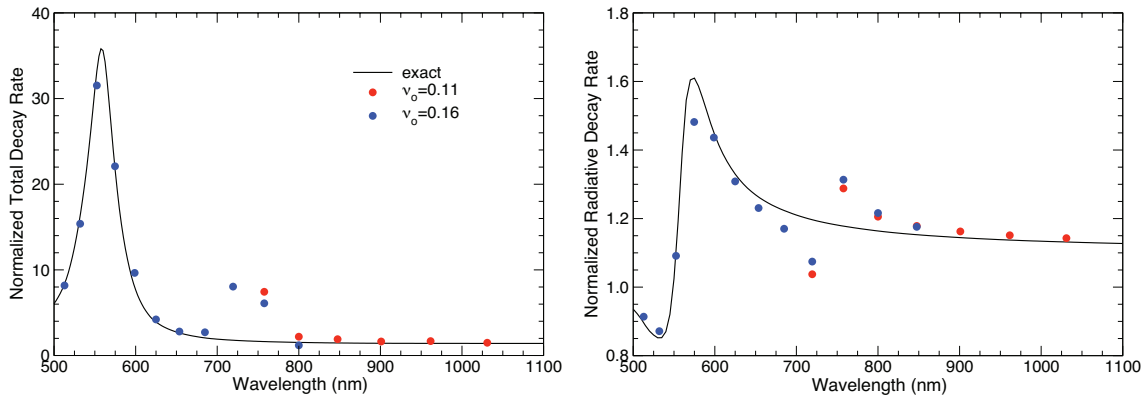


**Figure B.10:** Normalized total (left panel) and radiative (right panel) decay rates for a dipole with perpendicular orientation placed 12 nm away from a gold sphere with radius 5 nm. A spurious peak appears at about  $\lambda=750$  nm for both decay rates.

In a second test a dipole with perpendicular orientation is fixed at a distance of 12 nm away from a gold sphere with radius 5 nm, again embedded in a background medium with  $n = 1.7$ . The decay rates are calculated as a function of the excitation wavelength, which covers the range from 500 nm to 1100 nm. Because of the very small dimensions of the scatterer and the close distance, the FD-TD mesh was refined to  $\Delta=1$  nm. The purpose of scanning the wavelength is to investigate the accuracy across the SPP resonance, where the enhancement of the decay rates is expected to be stronger. The FD-TD results are compared to the analytical solution in Figure B.10. The data shown in the graphs are obtained by concatenating two FD-TD simulations ( $\nu_0 = 0.11$  and  $\nu_0 = 0.16$ ) to overcome the problem of the bandwidth for  $P_t$ . Good agreement with theory is found for the total rate (left panel), in spite of an unidentified peak at approximately  $\lambda=750$  nm. The curve for

the radiative rate (right panel) shows the same peak which does not have a correspondence with the exact result. Nevertheless, the peak due to the SPP resonance around  $\lambda=550$  nm is well reproduced even though the radiative decay rate looks slightly less accurate. A comparison with Figure B.4 indicates that the spurious peak is essentially due to staircasing and not to near-field interactions with the dipole source.

# Bibliography

- Abramowitz, M. and I. A. Stegun, (Eds.) , 1972: *Handbook of mathematical functions*. tenth ed., Dover, New York.
- Aeschlimann, M., et al., 2007: Adaptive subwavelength control of nano-optical fields. *Nature*, **446 (7133)**, 301–304.
- Agio, M., G. Zumofen, N. M. Mojarad, and V. Sandoghdar, 2009: Coupling light to a localized surface plasmon-polariton. *Plasmonics: Nanoimaging, Nanofabrication, and their Applications V*, S. Kawata, V. M. Shalaev, and D. P. Tsai, Eds., Proc. SPIE, Vol. 7395, 739512.
- Agio, M., et al., 2007: Engineering gold nano-antennae to enhance the emission of quantum emitters. *Optomechatronic Micro/Nano Devices and Components III*, L. Dong, Y. Katagiri, E. Higurashi, H. Toshiyoshi, and Y.-A. Peter, Eds., Proc. SPIE, Vol. 6717, 67170R.
- Airy, G. B., 1835: On the diffraction of an object-glass with circular aperture. *Trans. Cambridge Phil. Soc.*, **5**, 283291.
- Aizpurua, J., G. W. Bryant, L. J. Richter, F. J. García de Abajo, B. K. Kelley, and T. Mallouk, 2005: Optical properties of coupled metallic nanorods for field-enhanced spectroscopy. *Phys. Rev. B*, **71 (23)**, 235420.
- Akahane, Y., T. Asano, B.-S. Song, and S. Noda, 2003: High-Q photonic nanocavity in a two-dimensional photonic crystal. *Nature*, **425 (6961)**, 944–947.
- Akimov, A. V., A. Mukherjee, C. L. Yu, D. E. Chang, A. S. Zibrov, P. R. Hemmer, H. Park, and M. D. Lukin, 2007: Generation of single optical plasmons in metallic nanowires coupled to quantum dots. *Nature*, **450 (7168)**, 402–406.
- Albrecht, M. G. and J. A. Creighton, 1977: Anomalously intense raman spectra of pyridine at a silver electrode. *J. Am. Chem. Soc.*, **99 (15)**, 5215–5217.
- Alén, B., et al., 2006: Absorptive and dispersive optical responses of excitons in a single quantum dot. *Appl. Phys. Lett.*, **89 (12)**, 123124.

- Aljunid, S. A., M. K. Tey, B. Chng, T. Liew, G. Maslennikov, V. Scarani, and C. Kurt-siefer, 2009: Phase shift of a weak coherent beam induced by a single atom. *Phys. Rev. Lett.*, **103** (15), 153 601.
- Allen, L. and J. Eberly, 1975: *Optical resonance and two-level atoms*. Dover, New York.
- Alù, A. and N. Engheta, 2008: Input impedance, nanocircuit loading, and radiation tuning of optical nanoantennas. *Phys. Rev. Lett.*, **101** (4), 043901.
- Ambrose, W. P., P. M. Goodwin, R. A. Keller, and J. C. Martin, 1994: Alterations of single molecule fluorescence lifetimes in near-field optical microscopy. *Science*, **265** (5170), 364–367.
- Amos, R. M. and W. L. Barnes, 1997: Modification of the spontaneous emission rate of  $\text{Eu}^{3+}$  ions close to a thin metal mirror. *Phys. Rev. B*, **55** (11), 7249–7254.
- Anger, P., P. Bharadwaj, and L. Novotny, 2006: Enhancement and quenching of single-molecule fluorescence. *Phys. Rev. Lett.*, **96** (11), 113002.
- Anker, J. N., W. P. Hall, O. Lyandres, N. C. Shah, J. Zhao, and R. P. V. Duyne, 2008: Biosensing with plasmonic nanosensors. *Nat. Mater.*, **7** (6), 442–453.
- Antosiewicz, T. J., P. Wróbel, and T. Szoplik, 2009: Nanofocusing of radially polarized light with dielectric-metal-dielectric probe. *Opt. Express*, **17** (11), 9191–9196.
- Aravind, P., A. Nitzan, and H. Metiu, 1981: The interaction between electromagnetic resonances and its role in spectroscopic studies of molecules adsorbed on colloidal particles or metal spheres. *Surf. Sci.*, **110** (1), 189–204.
- Arbouet, A., D. Christofilos, N. Del Fatti, F. Vallée, J. R. Huntzinger, L. Arnaud, P. Billaud, and M. Broyer, 2004: Direct measurement of the single-metal-cluster optical absorption. *Phys. Rev. Lett.*, **93** (12), 127 401.
- Ashcroft, N. W. and N. D. Mermin, 1976: *Solid state physics*. Saunders College Publishing, Fort Worth.
- Ashkin, A., 1970: Acceleration and trapping of particles by radiation pressure. *Phys. Rev. Lett.*, **24** (4), 156–159.
- Atatüre, M., J. Dreiser, A. Badolato, and A. Imamoğlu, 2007: Observation of faraday rotation from a single confined spin. *Nat. Phys.*, **3** (2), 101–106.
- Atkins, P. W. and R. Friedman, 2005: *Molecular Quantum Mechanics*. 4th ed., Oxford University Press, Oxford, UK.
- Aubry, A., D. Y. Lei, A. I. Fernandez-Domnguez, Y. Sonnefraud, S. A. Maier, and J. B. Pendry, 2010: Plasmonic light-harvesting devices over the whole visible spectrum. *Nano Lett.*, **10** (7), 2574–2579.

- Babadjanyan, A. J., N. L. Margaryan, and K. V. Nerkararyan, 2000: Superfocusing of surface polaritons in the conical structure. *J. Appl. Phys.*, **87** (8), 3785–3788.
- Babinec, T. M., B. J. M. Hausmann, M. Khan, Y. Zhang, J. R. Maze, P. R. Hemmer, and M. Lončar, 2010: A diamond nanowire single-photon source. *Nat. Nano.*, **5** (3), 195–199.
- Baida, F. I. and A. Belkhir, 2009: Superfocusing and light confinement by surface plasmon excitation through radially polarized beam. *Plasmonics*, **4** (1), 51–59.
- Bakker, R. M., et al., 2008: Enhanced localized fluorescence in plasmonic nanoantennae. *Appl. Phys. Lett.*, **92** (4), 043101.
- Bakr, W. S., J. I. Gillen, A. Peng, S. Foelling, and M. Greiner, 2009: A quantum gas microscope for detecting single atoms in a hubbard-regime optical lattice. *Nature*, **462** (7269), 74–77.
- Balanis, C. A., 2005: *Antenna Theory*. 3d ed., John Wiley & Sons, Hoboken, NJ.
- Bandrauk, A. D., Y. Fujimura, and G. R.J., 2002: *Laser control and manipulation of molecules*. Oxford University Press, Oxford, UK.
- Barnes, W., 1998: Fluorescence near interfaces: the role of photonic mode density. *J. Mod. Opt.*, **45** (4), 661–699.
- Barnes, W., G. Björk, J. Gérard, P. Jonsson, J. Wasey, P. Worthing, and V. Zwiller, 2002: Solid-state single photon sources: light collection strategies. *Eur. Phys. J. D*, **18** (2), 197–210.
- Barnes, W. L., A. Dereux, and T. W. Ebbesen, 2003: Surface plasmon subwavelength optics. *Nature*, **424** (6950), 824–830.
- Barton, J. P. and D. R. Alexander, 1989: Fifth-order corrected electromagnetic field components for a fundamental gaussian beam. *J. Appl. Phys.*, **66** (7), 2800–2802.
- Basché, T., S. Kummer, and C. Bräuchle, 1995: Direct spectroscopic observation of quantum jumps of a single molecule. *Nature*, **373** (6510), 132–134.
- Bassett, I. M., 1984: Limits to concentration in resonant cavities. *Optica Acta*, **31** (11), 1211–1232.
- Bassett, I. M., 1986: Limit to concentration by focusing. *Optica Acta*, **33** (3), 279–286.
- Bassett, I. M. and R. Winston, 1984: Limits to concentration in physical optics and wave mechanics. *Optica Acta*, **31** (5), 499–505.
- Beer, A., 1852: Bestimmung der Absorption des rothen Lichts in farbigen Flüssigkeiten. *Ann. Phys. (Leipzig)*, **86** (1), 7888.

- Benisty, H., J.-M. Gérard, R. Houdré, J. Rarity, and C. Weisbuch, (Eds.) , 1999: *Confined photon systems: Fundamentals and Applications*. Springer Verlag, Berlin, New York.
- Bergman, D. J. and M. I. Stockman, 2003: Surface plasmon amplification by stimulated emission of radiation: Quantum generation of coherent surface plasmons in nanosystems. *Phys. Rev. Lett.*, **90** (2), 027 402.
- Berman, P. R., R. W. Boyd, and P. W. Milonni, 2006: Polarizability and the optical theorem for a two-level atom with radiative broadening. *Phys. Rev. A*, **74** (5), 053 816.
- Berntsen, S., E. Bozhevolnaya, and S. Bozhevolnyi, 1993: Macroscopic self-consistent model for external-reflection near-field microscopy. *J. Opt. Soc. Am. A*, **10** (5), 878–885.
- Bethe, H. A., 1944: Theory of diffraction by small holes. *Phys. Rev.*, **66** (7-8), 163–182.
- Betzig, E. and R. J. Chichester, 1993: Single molecules observed by near-field scanning optical microscopy. *Science*, **262** (5138), 1422–1425.
- Betzig, E. and J. K. Trautman, 1992: Near-field optics: Microscopy, spectroscopy, and surface modification beyond the diffraction limit. *Science*, **257** (5067), 189–195.
- Betzig, E., J. K. Trautman, T. D. Harris, J. S. Weiner, and R. L. Kostelak, 1991: Breaking the diffraction barrier: Optical microscopy on a nanometric scale. *Science*, **251** (5000), 1468–1470.
- Bharadwaj, P., B. Deutsch, and L. Novotny, 2009: Optical antennas. *Adv. Opt. Photon.*, **1** (3), 438–483.
- Bian, R. X., R. C. Dunn, X. S. Xie, and P. T. Leung, 1995: Single molecule emission characteristics in near-field microscopy. *Phys. Rev. Lett.*, **75** (26), 4772–4775.
- Birnbaum, K. M., A. Boca, R. Miller, A. D. Boozer, T. E. Northup, and H. J. Kimble, 2005: Photon blockade in an optical cavity with one trapped atom. *Nature*, **436** (7047), 87–90.
- Biteen, J. S., D. Pacifici, N. S. Lewis, and H. A. Atwater, 2005: Enhanced radiative emission rate and quantum efficiency in coupled silicon nanocrystal-nanostructured gold emitters. *Nano Lett.*, **5** (9), 1768–1773.
- Black, E. D., 2001: An introduction to Pound-Drever-Hall laser frequency stabilization. *Am. J. Phys.*, **69** (1), 79–87.

- Blanco, L. A. and F. J. García de Abajo, 2004: Spontaneous light emission in complex nanostructures. *Phys. Rev. B*, **69** (20), 205 414.
- Bloess, A., Y. Durand, M. Matsushita, R. Verberk, E. J. J. Groenen, and J. Schmidt, 2001: Microscopic structure in a shpol'skii system: a single-molecule study of dibenzanthanthrene in n-tetradecane. *J. Phys. Chem. A*, **105** (13), 3016–3021.
- Bohren, C. F., 1983: How can a particle absorb more than the light incident on it? *Am. J. Phys.*, **51** (4), 323–327.
- Bohren, C. F. and D. R. Huffman, 1983: *Absorption and Scattering of Light by Small Particles*. John Wiley & Sons, New York.
- Boiron, A.-M., B. Lounis, and M. Orrit, 1996: Single molecules of dibenzanthanthrene in n-hexadecane. *J. Chem. Phys.*, **105** (10), 3969–3974.
- Boivin, A., J. Dow, and E. Wolf, 1967: Energy flow in the neighborhood of the focus of a coherent beam. *J. Opt. Soc. Am.*, **57** (10), 1171–1175.
- Bonod, N., A. Devilez, B. Rolly, S. Bidault, and B. Stout, 2010: Ultracompact and unidirectional metallic antennas. *Phys. Rev. B*, **82** (11), 115 429.
- Boozer, A. D., A. Boca, R. Miller, T. E. Northup, and H. J. Kimble, 2007: Reversible state transfer between light and a single trapped atom. *Phys. Rev. Lett.*, **98** (19), 193 601.
- Borghi, R., 2004: On the angular-spectrum representation of multipole wave fields. *J. Opt. Soc. Am. A*, **21** (9), 1805–1810.
- Borghi, R., M. Santarsiero, and M. A. Alonso, 2005: Highly focused spirally polarized beams. *J. Opt. Soc. Am. A*, **22** (7), 1420–1431.
- Borgström, M. T., V. Zwiller, E. Müller, and A. Imamoğlu, 2005: Optically bright quantum dots in single nanowires. *Nano Lett.*, **5** (7), 1439–1443.
- Born, M. and E. Wolf, 1999: *Principles of Optics*. seventh (expanded) ed., Cambridge U. Press, Cambridge, UK.
- Bouguer, P., 1729: *Essai d'optique, Sur la gradation de la lumière*. Claude Jombert, Paris.
- Bouhelier, A., J. Renger, M. R. Beversluis, and L. Novotny, 2003: Plasmon-coupled tip-enhanced near-field optical microscopy. *J. Microsc.*, **210** (3), 220–224.
- Bouwkamp, C. J., 1950: On Bethe's theory of diffraction by small holes. *Philips Res. Rep.*, **5** (5), 321–332.
- Bouwkamp, C. J., 1954: Diffraction theory. *Rep. Prog. Phys.*, **17** (1), 35.



- Boyer, D., P. Tamarat, A. Maali, B. Lounis, and M. Orrit, 2002: Photothermal imaging of nanometer-sized metal particles among scatterers. *Science*, **297** (5584), 1160–1163.
- Brehm, M., T. Taubner, R. Hillenbrand, and F. Keilmann, 2006: Infrared spectroscopic mapping of single nanoparticles and viruses at nanoscale resolution. *Nano Lett.*, **6** (7), 1307–1310.
- Brinks, D., F. D. Stefani, F. Kulzer, R. Hildner, T. H. Taminiau, Y. Avlasevich, K. Mullen, and N. F. van Hulst, 2010: Visualizing and controlling vibrational wave packets of single molecules. *Nature*, **465** (7300), 905–908.
- Brouri, R., A. Beveratos, J.-P. Poizat, and P. Grangier, 2000: Photon antibunching in the fluorescence of individual color centers in diamond. *Opt. Lett.*, **25** (17), 1294–1296.
- Brouwer, A. C. J., J. Köhler, E. J. J. Groenen, and J. Schmidt, 1996:  $^{13}\text{C}$  isotope effects for pentacene in p-terphenyl: High-resolution spectroscopy and single-spin detection. *J. Chem. Phys.*, **105** (6), 2212–2222.
- Brunel, C., B. Lounis, P. Tamarat, and M. Orrit, 1998: Rabi resonances of a single molecule driven by rf and laser fields. *Phys. Rev. Lett.*, **81** (13), 2679–2682.
- Brunel, C., B. Lounis, P. Tamarat, and M. Orrit, 1999: Triggered source of single photons based on controlled single molecule fluorescence. *Phys. Rev. Lett.*, **83** (14), 2722–2725.
- Buchler, B. C., T. Kalkbrenner, C. Hettich, and V. Sandoghdar, 2005: Measuring the quantum efficiency of the optical emission of single radiating dipoles using a scanning mirror. *Phys. Rev. Lett.*, **95** (6), 063003.
- Buckley, B. B., G. D. Fuchs, L. C. Bassett, and D. D. Awschalom, 2010: Spin-light coherence for single-spin measurement and control in diamond. *Science*, **330** (6008), 1212–1215.
- Calander, N. and M. Willander, 2002: Theory of surface-plasmon resonance optical-field enhancement at prolate spheroids. *J. Appl. Phys.*, **92** (9), 4878–4884.
- Cangellaris, A. and D. Wright, 1991: Analysis of the numerical error caused by the stair-stepped approximation of a conducting boundary in fdtd simulations of electromagnetic phenomena. *Antennas Propag., IEEE Trans.*, **39** (10), 1518–1525.
- Carmichael, H. J., 1993: Quantum trajectory theory for cascaded open systems. *Phys. Rev. Lett.*, **70** (15), 2273–2276.

- Carminati, R., J.-J. Greffet, C. Henkel, and J. Vigoureux, 2006: Radiative and non-radiative decay of a single molecule close to a metallic nanoparticle. *Opt. Commun.*, **261** (2), 368–375.
- Carney, P. S., 1999: The optical cross-section theorem with incident fields containing evanescent components. *J. Mod. Opt.*, **46** (5), 891–899.
- Carter, T. P., M. Manavi, and W. E. Moerner, 1988: Statistical fine structure in the inhomogeneously broadened electronic origin of pentacene in p-terphenyl. *J. Chem. Phys.*, **89** (4), 1768–1779.
- Celebrano, M., P. Kukura, A. Renn, and V. Sandoghdar, 2011: Single-molecule imaging by optical absorption. *Nat. Photon.*, **5** (2), 95–98.
- Celebrano, M., R. Lettow, P. Kukura, M. Agio, A. Renn, S. Götzinger, and V. Sandoghdar, 2010: Efficient coupling of single photons to single plasmons. *Opt. Express*, **18** (13), 13 829–13 835.
- Chan, C. T., Q. L. Yu, and K. M. Ho, 1995: Order-n spectral method for electromagnetic waves. *Phys. Rev. B*, **51** (23), 16 635–16 642.
- Chan, G. H., J. Zhao, G. C. Schatz, and R. P. V. Duyne, 2008: Localized surface plasmon resonance spectroscopy of triangular aluminum nanoparticles. *J. Phys. Chem. C*, **112** (36), 13 958–13 963.
- Chance, R., A. Prock, and R. Silbey, 1978: Molecular fluorescence and energy transfer near interfaces. *Adv. Chem. Phys.*, **37**, 1–65.
- Chance, R. R., A. Prock, and R. Silbey, 1974: Lifetime of an excited molecule near a metal mirror: Energy transfer in the  $\text{Eu}^{3+}$  /silver system. *J. Chem. Phys.*, **60** (5), 2184–2185.
- Chang, D. E., A. S. Sørensen, E. A. Demler, and M. D. Lukin, 2007a: A single-photon transistor using nanoscale surface plasmons. *Nat. Phys.*, **3** (11), 807–812.
- Chang, D. E., A. S. Sørensen, P. R. Hemmer, and M. D. Lukin, 2006: Quantum optics with surface plasmons. *Phys. Rev. Lett.*, **97** (5), 053002.
- Chang, D. E., A. S. Sørensen, P. R. Hemmer, and M. D. Lukin, 2007b: Strong coupling of single emitters to surface plasmons. *Phys. Rev. B*, **76** (3), 035 420.
- Chari, M. and S. Salon, 2000: *Numerical methods in electromagnetism*. Academic Press, San Diego, CA.
- Chen, X.-W., V. Sandoghdar, and M. Agio, 2009: Highly efficient interfacing of guided plasmons and photons in nanowires. *Nano Lett.*, **9** (11), 3756–3761.

- Chen, X.-W., V. Sandoghdar, and M. Agio, 2010a: Nanofocusing radially-polarized beams for high-throughput funneling of optical energy to the near field. *Opt. Express*, **18** (10), 10 878–10 887.
- Chen, Y., R. Mittra, and P. Harms, 1996: Finite-difference time-domain algorithm for solving Maxwell's equations in rotationally symmetric geometries. *Microwave Theory Tech., IEEE Trans.*, **44** (6), 832–839.
- Chen, Y., T. R. Nielsen, N. Gregersen, P. Lodahl, and J. Mørk, 2010b: Finite-element modeling of spontaneous emission of a quantum emitter at nanoscale proximity to plasmonic waveguides. *Phys. Rev. B*, **81** (12), 125 431.
- Chong, S., W. Min, and X. S. Xie, 2010: Ground-state depletion microscopy: Detection sensitivity of single-molecule optical absorption at room temperature. *J. Phys. Chem. Lett.*, **1** (23), 3316–3322.
- Chowdhury, M. H., K. Ray, S. K. Gray, J. Pond, and J. R. Lakowicz, 2009: Aluminum nanoparticles as substrates for metal-enhanced fluorescence in the ultraviolet for the label-free detection of biomolecules. *Analytical Chem.*, **81** (4), 1397–1403.
- Chu, L. J., 1948: Physical limitations of omni-directional antennas. *J. Appl. Phys.*, **19** (12), 1163–1175.
- Cirac, J. I., P. Zoller, H. J. Kimble, and H. Mabuchi, 1997: Quantum state transfer and entanglement distribution among distant nodes in a quantum network. *Phys. Rev. Lett.*, **78** (16), 3221–3224.
- Claudon, J., et al., 2010: A highly efficient single-photon source based on a quantum dot in a photonic nanowire. *Nat. Photon.*, **4** (3), 174–177.
- Cline, M. P., P. W. Barber, and R. K. Chang, 1986: Surface-enhanced electric intensities on transition- and noble-metal spheroids. *J. Opt. Soc. Am. B*, **3** (1), 15–21.
- Cohen-Tannoudji, C., J. Dupont-Roc, and G. Grynberg, 2004: *Atom-Photon Interactions*. Wiley-VCH, Weinheim, Germany.
- Collett, E. and E. Wolf, 1980: Symmetry properties of focused fields. *Opt. Lett.*, **5** (6), 264–266.
- Cremer, C. and T. Cremer, 1978: Considerations on a laser-scanning microscope with high resolution and depth of field. *Microsc. Acta*, **81** (1), 31–44.
- Crozier, K. B., A. Sundaramurthy, G. S. Kino, and C. F. Quate, 2003: Optical antennas: Resonators for local field enhancement. *J. Appl. Phys.*, **94** (7), 4632–4642.
- Curto, A. G., G. Volpe, T. H. Taminiau, M. P. Kreuzer, R. Quidant, and N. F. van Hulst, 2010: Unidirectional emission of a quantum dot coupled to a nanoantenna. *Science*, **329** (5994), 930–933.

- Dantus, M. and V. V. Lozovoy, 2004: Experimental coherent laser control of physicochemical processes. *Chem. Rev.*, **104** (4), 1813–1860.
- Davidson, D. B. and R. W. Ziolkowski, 1994: Body-of-revolution finite-difference time-domain modeling of space-time focusing by a three-dimensional lens. *J. Opt. Soc. Am. A*, **11** (4), 1471–1490.
- Dayan, B., A. S. Parkins, T. Aoki, E. P. Ostby, K. J. Vahala, and H. J. Kimble, 2008: A photon turnstile dynamically regulated by one atom. *Science*, **319** (5866), 1062–1065.
- De Angelis, F., M. Patrini, G. Das, I. Maksymov, M. Galli, L. Businaro, L. C. Andreani, and E. Di Fabrizio, 2008: A hybrid plasmonic-photonic nanodevice for label-free detection of a few molecules. *Nano Lett.*, **8** (8), 2321–2327.
- De Angelis, F., et al., 2010: Nanoscale chemical mapping using three-dimensional adiabatic compression of surface plasmon polaritons. *Nat. Nano.*, **5** (1), 67–72.
- De Moerloose, J. and D. De Zutter, 1995: Poynting's theorem for the finite-differencetime-domain method. *Microwave Opt. Techn. Lett.*, **8** (5), 257–260.
- Debye, P., 1909: Das Verhalten von Lichtwellen in der Nähe eines Brennpunktes oder einer Brennlinie. *Ann. Phys.*, **335** (14), 755–776.
- Descrovi, E., L. Vaccaro, L. Aeschimann, W. Nakagawa, U. Staufer, and H.-P. Herzig, 2005: Optical properties of microfabricated fully-metal-coated near-field probes in collection mode. *J. Opt. Soc. Am. A*, **22** (7), 1432–1441.
- Devilez, A., B. Stout, and N. Bonod, 2010: Compact metallo-dielectric optical antenna for ultra directional and enhanced radiative emission. *ACS Nano*, **4** (6), 3390–3396.
- Dey, S. and R. Mittra, 1999: A conformal finite-difference time-domain technique for modeling cylindrical dielectric resonators. *Microwave Theory Tech., IEEE Trans.*, **47** (9), 1737–1739.
- Dhayalan, V. and J. J. Stamnes, 1997: Focusing of mixed-dipole waves. *Pure and Appl. Opt. A*, **6** (3), 317–345.
- Diedrich, F. and H. Walther, 1987: Nonclassical radiation of a single stored ion. *Phys. Rev. Lett.*, **58** (3), 203–206.
- Ding, W., S. R. Andrews, and S. A. Maier, 2007: Internal excitation and superfocusing of surface plasmon polaritons on a silver-coated optical fiber tip. *Phys. Rev. A*, **75** (6), 063822.

- Ditkowski, A., K. Dridi, and J. S. Hesthaven, 2001: Convergent cartesian grid methods for Maxwell's equations in complex geometries. *J. Comput. Phys.*, **170** (1), 39–80.
- Domokos, P., P. Horak, and H. Ritsch, 2002: Quantum description of light-pulse scattering on a single atom in waveguides. *Phys. Rev. A*, **65** (3), 033 832.
- Dorner, U. and P. Zoller, 2002: Laser-driven atoms in half-cavities. *Phys. Rev. A*, **66** (2), 023 816.
- Drexhage, K., 1974: Interaction of light with monomolecular dye layers. North-Holland, Amsterdam, *Progr. Opt.*, Vol. 12, 164–232.
- Drexhage, K. H., 1966: Optische Untersuchungen an neuartigen monomolekularen Farbstoffschichten. Habilitationsschrift, University of Marburg, Germany.
- Drexhage, K. H., M. Fleck, , F. P. Schäfer, and W. Sperling, 1966: *Ber. Bunsenges. Phys. Chem.*, **20**, 1179.
- Drexhage, K. H., H. Kuhn, and F. P. Schäfer, 1968: Variation of the fluorescence decay time of a molecule in front of a mirror. *Ber. Bunsenges. Phys. Chem.*, **72** (2), 329.
- Dridi, K., J. Hesthaven, and A. Ditkowski, 2001: Staircase-free finite-difference time-domain formulation for general materials in complex geometries. *Antennas Propag., IEEE Trans.*, **49** (5), 749–756.
- Duan, L.-M. and H. J. Kimble, 2004: Scalable photonic quantum computation through cavity-assisted interactions. *Phys. Rev. Lett.*, **92** (12), 127 902.
- Dulkeith, E., et al., 2002: Fluorescence quenching of dye molecules near gold nanoparticles: Radiative and nonradiative effects. *Phys. Rev. Lett.*, **89** (20), 203 002.
- Dürig, U., D. W. Pohl, and F. Rohner, 1986: Near-field optical-scanning microscopy. *J. Appl. Phys.*, **59** (10), 3318–3327.
- Dutra, S. M. and G. Nienhuis, 2000: Quantized mode of a leaky cavity. *Phys. Rev. A*, **62** (6), 063 805.
- Ekinci, Y., H. H. Solak, and J. F. Löffler, 2008: Plasmon resonances of aluminum nanoparticles and nanorods. *J. Appl. Phys.*, **104** (8), 083107.
- Engel, G. S., T. R. Calhoun, E. L. Read, T.-K. Ahn, T. Mancal, Y.-C. Cheng, R. E. Blankenship, and G. R. Fleming, 2007: Evidence for wavelike energy transfer through quantum coherence in photosynthetic systems. *Nature*, **446** (7137), 782–786.

- Englund, D., I. Fushman, A. Faraon, and J. Vučković, 2009: Quantum dots in photonic crystals: From quantum information processing to single photon nonlinear optics. *Photon. Nanostruct.*, **7** (1), 56–62.
- Esteban, R., T. V. Teperik, and J. J. Greffet, 2010: Optical patch antennas for single photon emission using surface plasmon resonances. *Phys. Rev. Lett.*, **104** (2), 026 802.
- Ewers, H., V. Jacobsen, E. Klotzsch, A. E. Smith, A. Helenius, and V. Sandoghdar, 2007: Label-free optical detection and tracking of single virions bound to their receptors in supported membrane bilayers. *Nano Lett.*, **7** (8), 2263–2266.
- Farahani, J. N., D. W. Pohl, H.-J. Eisler, and B. Hecht, 2005: Single quantum dot coupled to a scanning optical antenna: A tunable superemitter. *Phys. Rev. Lett.*, **95** (1), 017402.
- Faraon, A., I. Fushman, D. Englund, N. Stoltz, P. Petroff, and J. Vučković, 2008: Coherent generation of non-classical light on a chip via photon-induced tunnelling and blockade. *Nat. Phys.*, **4** (11), 859–863.
- Farjadpour, A., D. Roundy, A. Rodriguez, M. Ibanescu, P. Bermel, J. D. Joannopoulos, S. G. Johnson, and G. W. Burr, 2006: Improving accuracy by subpixel smoothing in the finite-difference time domain. *Opt. Lett.*, **31** (20), 2972–2974.
- Feenberg, E., 1932: The scattering of slow electrons by neutral atoms. *Phys. Rev.*, **40** (1), 40–54.
- Feng, J., T. Okamoto, and S. Kawata, 2005: Enhancement of electroluminescence through a two-dimensional corrugated metal film by grating-induced surface-plasmon cross coupling. *Opt. Lett.*, **30** (17), 2302–2304.
- Fleischer, M., et al., 2008: Three-dimensional optical antennas: Nanocones in an apertureless scanning near-field microscope. *Appl. Phys. Lett.*, **93** (11), 111114.
- Fleischer, M., et al., 2009: Nanocones on transparent substrates for investigations in scanning probe microscopes. *Microelectr. Eng.*, **86** (4-6), 1219–1221.
- Fleury, L., J.-M. Segura, G. Zumofen, B. Hecht, and U. P. Wild, 2000: Nonclassical photon statistics in single-molecule fluorescence at room temperature. *Phys. Rev. Lett.*, **84** (6), 1148–1151.
- Ford, G. W. and W. H. Weber, 1984: Electromagnetic interactions of molecules with metal surfaces. *Phys. Rep.*, **113** (4), 195–287.
- Foster, G. T., L. A. Orozco, H. M. Castro-Beltran, and H. J. Carmichael, 2000: Quantum state reduction and conditional time evolution of wave-particle correlations in cavity qed. *Phys. Rev. Lett.*, **85** (15), 3149–3152.

- Fredriksson, H., Y. Alaverdyan, A. Dmitriev, C. Langhammer, D. Sutherland, M. Zäch, and B. Kasemo, 2007: Hole-mask colloidal lithography. *Adv. Mater.*, **19** (23), 4297–4302.
- Frey, H. G., S. Witt, K. Felderer, and R. Guckenberger, 2004: High-resolution imaging of single fluorescent molecules with the optical near-field of a metal tip. *Phys. Rev. Lett.*, **93** (20), 200801.
- Friedler, I., P. Lalanne, J. P. Hugonin, J. Claudon, J. M. Gérard, A. Beveratos, and I. Robert-Philip, 2008: Efficient photonic mirrors for semiconductor nanowires. *Opt. Lett.*, **33** (22), 2635–2637.
- Friedler, I., C. Sauvan, J. P. Hugonin, P. Lalanne, J. Claudon, and J. M. Gérard, 2009: Solid-state single photon sources: the nanowire antenna. *Opt. Express*, **17** (4), 2095–2110.
- Friedrich, J. and D. Haarer, 1984: Photochemical hole burning: A spectroscopic study of relaxation processes in polymers and glasses. *Angew. Chem. Int. Ed.*, **23** (2), 113–140.
- Fujii, M., D. Lukashevich, I. Sakagami, and P. Russer, 2003: Convergence of FDTD and wavelet-collocation modeling of curved dielectric interface with the effective dielectric constant technique. *Microwave Wireless Comp. Lett., IEEE*, **13** (11), 469–471.
- Fusco, M., 1990: FDTD algorithm in curvilinear coordinates [EM scattering]. *Antennas Propag., IEEE Trans.*, **38** (1), 76–89.
- Fushman, I., D. Englund, A. Faraon, N. Stoltz, P. Petroff, and J. Vučković, 2008: Controlled phase shifts with a single quantum dot. *Science*, **320** (5877), 769–772.
- García de Abajo, F. J., 2007: Colloquium: Light scattering by particle and hole arrays. *Rev. Mod. Phys.*, **79** (4), 1267–1290.
- Gardiner, C. W., 1993: Driving a quantum system with the output field from another driven quantum system. *Phys. Rev. Lett.*, **70** (15), 2269–2272.
- Genet, C. and T. W. Ebbesen, 2007: Light in tiny holes. *Nature*, **445** (7123), 39–46.
- Gerardot, B. D., S. Seidl, P. A. Dalgarno, R. J. Warburton, M. Kroner, K. Karrai, A. Badolato, and P. M. Petroff, 2007: Contrast in transmission spectroscopy of a single quantum dot. *Appl. Phys. Lett.*, **90** (22), 221106.
- Gerhardt, I., 2006: Scattering & absorption of light by a single molecule under a subwavelength aperture. Ph.D. thesis, ETH Zurich, Zurich, Switzerland, Diss. ETH No. 16812.

- Gerhardt, I., G. Wrigge, M. Agio, P. Bushev, G. Zumofen, and V. Sandoghdar, 2007a: Scanning near-field optical coherent spectroscopy of single molecules at 1.4 $\mu$ m. *Opt. Lett.*, **32** (11), 1420–1422.
- Gerhardt, I., G. Wrigge, P. Bushev, G. Zumofen, M. Agio, R. Pfab, and V. Sandoghdar, 2007b: Strong extinction of a laser beam by a single molecule. *Phys. Rev. Lett.*, **98** (3), 033601.
- Gersten, J. and A. Nitzan, 1980: Electromagnetic theory of enhanced raman scattering by molecules adsorbed on rough surfaces. *J. Chem. Phys.*, **73** (7), 3023–3037.
- Gersten, J. and A. Nitzan, 1981: Spectroscopic properties of molecules interacting with small dielectric particles. *J. Chem. Phys.*, **75** (3), 1139–1152.
- Gibbs, H. M., 1985: *Optical bistability: controlling light with light*. Academic, New York.
- Girard, C., 2005: Near fields in nanostructures. *Rep. Prog. Phys.*, **68** (8), 1883.
- Girard, C., X. Bouju, and A. Dereux, 1993: Optical near-field detection and local spectroscopy of a surface: a self-consistent theoretical study near-field optics. Kluwer, Dordrecht, NATO ASI Series E, Vol. 242, 199–208.
- Girard, C. and A. Dereux, 1996: Near-field optics theories. *Rep. Prog. Phys.*, **59** (5), 657–699.
- Girard, C., A. Dereux, O. J. F. Martin, and M. Devel, 1994: Importance of confined fields in near-field optical imaging of subwavelength objects. *Phys. Rev. B*, **50** (19), 14 467–14 473.
- Goncharenko, A., H.-C. Chang, and J.-K. Wang, 2007: Electric near-field enhancing properties of a finite-size metal conical nano-tip. *Ultramicroscopy*, **107** (2-3), 151–157.
- Goncharenko, A. V., M. M. Dvoynenko, H.-C. Chang, and J.-K. Wang, 2006a: Electric field enhancement by a nanometer-scaled conical metal tip in the context of scattering-type near-field optical microscopy. *Appl. Phys. Lett.*, **88** (10), 104101.
- Goncharenko, A. V., J.-K. Wang, and Y.-C. Chang, 2006b: Electric near-field enhancement of a sharp semi-infinite conical probe: Material and cone angle dependence. *Phys. Rev. B*, **74** (23), 235442.
- Gong, Y., B. Ellis, G. Shambat, T. Sarmiento, J. S. Harris, and J. Vučković, 2010: Nanobeam photonic crystal cavity quantum dot laser. *Opt. Express*, **18** (9), 8781–8789.



- Gordon, R., 2009: Reflection of cylindrical surface waves. *Opt. Express*, **17 (21)**, 18 621–18 629.
- Gouesbet, G. and G. Grehan, 1982: On the scattering of light by a mie scatter center located on the axis of an axisymmetric light profile. *J. Opt. (Paris)*, **13 (2)**, 97.
- Gouy, L. G., 1890a: Sur la propagation anormale des ondes. *Comptes Rendus Acad. Sci. (Paris)*, 33–35.
- Gouy, L. G., 1890b: Sur une propriété nouvelle des ondes lumineuses. *Comptes Rendus Acad. Sci. (Paris)*, **110**, 1251–1253.
- Greffet, J.-J., 2005: Nanoantennas for light emission. *Science*, **308 (5728)**, 1561–1563.
- Greffet, J.-J., M. Laroche, and F. m. c. Marquier, 2010: Impedance of a nanoantenna and a single quantum emitter. *Phys. Rev. Lett.*, **105 (11)**, 117701.
- Gregersen, N., T. R. Nielsen, J. Claudon, J.-M. Gérard, and J. Mørk, 2008: Controlling the emission profile of a nanowire with a conical taper. *Opt. Lett.*, **33 (15)**, 1693–1695.
- Grober, R. D., R. J. Schoelkopf, and D. E. Prober, 1997: Optical antenna: Towards a unity efficiency near-field optical probe. *Appl. Phys. Lett.*, **70 (11)**, 1354–1356.
- Guest, J. R., et al., 2002: Measurement of optical absorption by a single quantum dot exciton. *Phys. Rev. B*, **65 (24)**, 241 310.
- Guzatov, D. V. and V. V. Klimov, 2007: Spontaneous emission of an atom placed near a nanobelt of elliptical cross section. *Phys. Rev. A*, **75 (5)**, 052 901.
- Hafner, C., J. Smajic, and M. Agio, 2010: Numerical methods for the electrodynamic analysis of nanostructures. *Nanoclusters and Nanostructured Surfaces*, A. K. Ray, Ed., American Scientific Publishers, CA, USA.
- Hansen, R. C., 1981: Fundamental limitations in antennas. *IEEE, Proc.*, **69 (2)**, 170–182.
- Hao, E. and G. C. Schatz, 2004: Electromagnetic fields around silver nanoparticles and dimers. *J. Chem. Phys.*, **120 (1)**, 357–366.
- Hao, Y. and C. Railton, 1998: Analyzing electromagnetic structures with curved boundaries on Cartesian FDTD meshes. *Microwave Theory Tech., IEEE Trans.*, **46 (1)**, 82–88.
- Harms, G., T. Irngartinger, D. Reiss, A. Renn, and U. Wild, 1999: Fluorescence lifetimes of terrylene in solid matrices. *Chem. Phys. Lett.*, **313**, 533–538.

- Harms, P., J.-F. Lee, and R. Mittra, 1992: A study of the nonorthogonal FDTD method versus the conventional FDTD technique for computing resonant frequencies of cylindrical cavities. *Microwave Theory Tech., IEEE Trans.*, **40 (4)**, 741–746.
- Haroche, S., 1992: Cavity quantum electrodynamics. *Fundamental systems in quantum optics*, J. Dalibard, J. M. Raimond, and J. Zinn-Justin, Eds., Elsevier, Amsterdam, 769.
- Haroche, S. and D. Kleppner, 1989: Cavity Quantum Electrodynamics. *Phys. Today*, **42 (1)**, 24–30.
- Hartschuh, A., 2008: Tip-enhanced near-field optical microscopy. *Angew. Chem. Int. Ed.*, **47 (43)**, 8178–8191.
- Hartschuh, A., H. N. Pedrosa, L. Novotny, and T. D. Krauss, 2003a: Simultaneous fluorescence and raman scattering from single carbon nanotubes. *Science*, **301 (5638)**, 1354–1356.
- Hartschuh, A., E. J. Sánchez, X. S. Xie, and L. Novotny, 2003b: High-resolution near-field raman microscopy of single-walled carbon nanotubes. *Phys. Rev. Lett.*, **90 (9)**, 095 503.
- Hartschuh, A. M., A. B. Beversluis, and L. Novotny, 2004: Tip-enhanced optical spectroscopy. *Phil. Trans. Royal Soc. London A*, **362**, 807.
- Hennessy, K., et al., 2007: Quantum nature of a strongly coupled single quantum dot-cavity system. *Nature*, **445 (7130)**, 896–899.
- Hennrich, M., A. Kuhn, and G. Rempe, 2005: Transition from antibunching to bunching in cavity QED. *Phys. Rev. Lett.*, **94 (5)**, 053 604.
- Hermann, C. and O. Hess, 2002: Modified spontaneous-emission rate in an inverted-opal structure with complete photonic bandgap. *J. Opt. Soc. Am. B*, **19 (12)**, 3013–3018.
- Hess, H. F., E. Betzig, T. D. Harris, L. N. Pfeiffer, and K. W. West, 1994: Near-field spectroscopy of the quantum constituents of a luminescent system. *Science*, **264 (5166)**, 1740–1745.
- Heugel, S., A. Villar, M. Sondermann, U. Peschel, and G. Leuchs, 2010: On the analogy between a single atom and an optical resonator. *Laser Phys.*, **20**, 100–106.
- Hildner, R., D. Brinks, and N. F. van Hulst, 2011: Femtosecond coherence and quantum control of single molecules at room temperature. *Nat. Phys.*, **7 (2)**, 172–177.

- Hill, M. T., et al., 2007: Lasing in metallic-coated nanocavities. *Nat. Photon.*, **1** (10), 589–594.
- Hirono, T., Y. Shibata, W. Lui, S. Seki, and Y. Yoshikuni, 2000: The second-order condition for the dielectric interface orthogonal to the Yee-lattice axis in the FDTD scheme. *Microwave Guided Wave Lett., IEEE*, **10** (9), 359–361.
- Hirschfeld, T., 1976: Optical microscopic observation of single small molecules. *Appl. Opt.*, **15** (12), 2965–2966.
- Hofmann, C., A. Nicolet, M. A. Kol'chenko, and M. Orrit, 2005: Towards nanoprobe for conduction in molecular crystals: Dibenzoterrylene in anthracene crystals. *Chem. Phys.*, **318** (1-2), 1–6.
- Hofmann, H. F., T. Kosako, and Y. Kadoya, 2007: Design parameters for a nano-optical yagi-uda antenna. *New J. Phys.*, **9** (7), 217.
- Holland, R., 1983: Finite-difference solution of Maxwell's equations in generalized nonorthogonal coordinates. *Nuclear Sci., IEEE Trans.*, **30** (6), 4589–4591.
- Hollas, J. M., 1998: *High resolution spectroscopy*. 2d ed., John Wiley & Sons, Chichester, UK.
- Hollas, J. M., 2004: *Modern spectroscopy*. 4th ed., John Wiley & Sons, Chichester, UK.
- Hostein, R., R. Braive, L. L. Gratiet, A. Talneau, G. Beaudoin, I. Robert-Philip, I. Sagnes, and A. Beveratos, 2010: Demonstration of coherent emission from high- $\beta$  photonic crystal nanolasers at room temperature. *Opt. Lett.*, **35** (8), 1154–1156.
- Huber, A. J., F. Keilmann, J. Wittborn, J. Aizpurua, and R. Hillenbrand, 2008: Terahertz near-field nanoscopy of mobile carriers in single semiconductor nanodevices. *Nano Lett.*, **8** (11), 3766–3770.
- Hwang, J., M. M. Fejer, and W. E. Moerner, 2006: Scanning interferometric microscopy for the detection of ultrasmall phase shifts in condensed matter. *Phys. Rev. A*, **73** (2), 021 802.
- Hwang, J., M. Pototschnig, R. Lettow, G. Zumofen, A. Renn, S. Götzinger, and V. Sandoghdar, 2009: A single-molecule optical transistor. *Nature*, **460** (7251), 76–80.
- Hwang, K.-P. and A. Cangellaris, 2001: Effective permittivities for second-order accurate FDTD equations at dielectric interfaces. *Microwave Wireless Comp. Lett., IEEE*, **11** (4), 158–160.

- Ichimura, T., N. Hayazawa, M. Hashimoto, Y. Inouye, and S. Kawata, 2004: Tip-enhanced coherent anti-stokes raman scattering for vibrational nanoimaging. *Phys. Rev. Lett.*, **92**, 220 801.
- Issa, N. A. and R. Guckenberger, 2007a: Fluorescence near metal tips: The roles of energy transfer and surface plasmon polaritons. *Opt. Express*, **15 (19)**, 12 131–12 144.
- Issa, N. A. and R. Guckenberger, 2007b: Optical nanofocusing on tapered metallic waveguides. *Plasmonics*, **2 (1)**, 31–37.
- ITRS, 2009: International technology roadmap for semiconductors. ITRS.
- Jackson, J. D., 1999: *Classical Electrodynamics*. 3d ed., John Wiley & Sons, New York.
- Janunts, N., K. Baghdasaryan, K. Nerkararyan, and B. Hecht, 2005: Excitation and superfocusing of surface plasmon polaritons on a silver-coated optical fiber tip. *Opt. Commun.*, **253 (1-3)**, 118–124.
- Jeanmaire, D. L. and R. P. V. Duyne, 1977: Surface raman spectroelectrochemistry: Part I. Heterocyclic, aromatic, and aliphatic amines adsorbed on the anodized silver electrode. *J. Electroanal. Chem.*, **84 (1)**, 1–20.
- Jelezko, F., B. Lounis, and M. Orrit, 1997: Pump-probe spectroscopy and photophysical properties of single di-benzanthanthrene molecules in a naphthalene crystal. *J. Chem. Phys.*, **107 (6)**, 1692–1702.
- Jelezko, F., P. Tamarat, B. Lounis, and M. Orrit, 1996: Dibenzoterrylene in naphthalene: A new crystalline system for single molecule spectroscopy in the near infrared. *J. Phys. Chem.*, **100 (33)**, 13 892–13 894.
- Jin, J., 2002: *The Finite Element Method in Electromagnetics*. 2d ed., Wiley-IEEE Press, New York.
- Joachim, C. and M. A. Ratner, 2005: Molecular electronics: Some views on transport junctions and beyond. *Proc. Natl. Acad. Sci.*, **102 (25)**, 8801–8808.
- John, S., 1987: Strong localization of photons in certain disordered dielectric superlattices. *Phys. Rev. Lett.*, **58 (23)**, 2486–2489.
- Johnson, P. B. and R. W. Christy, 1972: Optical constants of the noble metals. *Phys. Rev. B*, **6 (12)**, 4370–4379.
- Jun, Y. C., R. M. Briggs, H. A. Atwater, and M. L. Brongersma, 2009: Broadband enhancement of light emission insilicon slot waveguides. *Opt. Express*, **17 (9)**, 7479–7490.

- Jurgens, T. and A. Taflove, 1993: Three-dimensional contour FDTD modeling of scattering from single and multiple bodies. *Antennas Propag., IEEE Trans.*, **41 (12)**, 1703–1708.
- Jurgens, T., A. Taflove, K. Umashankar, and T. Moore, 1992: Finite-difference time-domain modeling of curved surfaces [EM scattering]. *Antennas Propag., IEEE Trans.*, **40 (4)**, 357–366.
- Kador, L., D. E. Horne, and W. E. Moerner, 1990: Optical detection and probing of single dopant molecules of pentacene in a p-terphenyl host crystal by means of absorption spectroscopy. *J. Phys. Chem.*, **94 (4)**, 1237–1248.
- Kador, L., T. Latychevskaia, A. Renn, and U. P. Wild, 1999: Absorption spectroscopy on single molecules in solids. *J. Chem. Phys.*, **111 (19)**, 8755–8758.
- Kalkbrenner, T., U. Håkanson, and V. Sandoghdar, 2004: Tomographic plasmon spectroscopy of a single gold nanoparticle. *Nano Lett.*, **4 (12)**, 2309–2314.
- Kaminski, F., V. Sandoghdar, and M. Agio, 2007: Finite-difference time-domain modeling of decay rates in the near field of metal nanostructures. *J. Comput. Theor. Nanosci.*, **4 (3)**, 635–643.
- Kaneda, N., B. Houshmand, and T. Itoh, 1997: FDTD analysis of dielectric resonators with curved surfaces. *Microwave Theory Tech., IEEE Trans.*, **45 (9)**, 1645–1649.
- Kann, J. L., T. D. Milster, F. F. Froehlich, R. W. Ziolkowski, and J. B. Judkins, 1995a: Linear behavior of a near-field optical scanning system. *J. Opt. Soc. Am. A*, **12 (8)**, 1677–1682.
- Kann, J. L., T. D. Milster, F. F. Froehlich, R. W. Ziolkowski, and J. B. Judkins, 1995b: Near-field optical detection of asperities in dielectric surfaces. *J. Opt. Soc. Am. A*, **12 (3)**, 501–512.
- Kao, K. C. and G. A. Hockham, 1966: Dielectric-fibre surface waveguides for optical frequencies. *Proc. IEE (London)*, **113 (7)**, 1151–1158.
- Karrai, K. and R. J. Warburton, 2003: Optical transmission and reflection spectroscopy of single quantum dots. *Superlattices and Microstructures*, **33 (5-6)**, 311–337.
- Kasha, M., 1950: Characterization of electronic transitions in complex molecules. *Discuss. Faraday Soc.*, **9**, 14–19.
- Kawata, S., A. Ono, and P. Verma, 2008: Subwavelength colour imaging with a metallic nanolens. *Nat. Photon.*, **2**, 438–442.

- Keilmann, F., 1999: Surface-polariton propagation for scanning near-field optical microscopy application. *J. Microsc.*, **194** (2-3), 567–570.
- Kharlamov, B. M., R. I. Personov, and L. A. Bykovskaya, 1974: Stable ‘gap’ in absorption spectra of solid solutions of organic molecules by laser irradiation. *Opt. Commun.*, **12** (2), 191–193.
- Kim, I. and W. Hoefer, 1990: A local mesh refinement algorithm for the time domain-finite difference method using Maxwell’s curl equations. *Microwave Theory Tech., IEEE Trans.*, **38** (6), 812–815.
- Kim, T.-I., J.-H. Kim, S. J. Son, and S.-M. Seo, 2008: Gold nanocones fabricated by nanotransfer printing and their application for field emission. *Nanotechnology*, **19** (29), 295 302.
- Kimble, H. J., 2008: The quantum internet. *Nature*, **453** (7198), 1023–1030.
- Kimble, H. J., M. Dagenais, and L. Mandel, 1977: Photon antibunching in resonance fluorescence. *Phys. Rev. Lett.*, **39** (11), 691–695.
- Kimble, H. J. and L. Mandel, 1976: Theory of resonance fluorescence. *Phys. Rev. A*, **13** (6), 2123–2144.
- Kiraz, A., M. Atatüre, and A. Imamoglu, 2004: Quantum-dot single-photon sources: Prospects for applications in linear optics quantum-information processing. *Phys. Rev. A*, **69** (3), 032 305.
- Kirchain, R. and L. Kimerling, 2007: A roadmap for nanophotonics. *Nat. Photon.*, **1** (6), 303–305.
- Kitson, S. C., W. L. Barnes, and J. R. Sambles, 1996: Photoluminescence from dye molecules on silver gratings. *Opt. Commun.*, **122** (4-6), 147–154.
- Klimov, V., M. Ducloy, and V. Letokhov, 1996: Radiative frequency shift and linewidth of an atom dipole in the vicinity of a dielectric microsphere. *J. Mod. Opt.*, **43** (11), 2251–2267.
- Klimov, V., M. Ducloy, and V. Letokhov, 2002: Spontaneous emission of an atom placed near a prolate nanospheroid. *Eur. Phys. J. D*, **20**, 133–148.
- Klimov, V. V. and M. Ducloy, 2004: Spontaneous emission rate of an excited atom placed near a nanofiber. *Phys. Rev. A*, **69** (1), 013 812.
- Kneipp, K., Y. Wang, H. Kneipp, L. T. Perelman, I. Itzkan, R. R. Dasari, and M. S. Feld, 1997: Single molecule detection using surface-enhanced Raman scattering (SERS). *Phys. Rev. Lett.*, **78** (9), 1667–1670.

- Knill, E., R. Laflamme, and G. J. Milburn, 2001: A scheme for efficient quantum computation with linear optics. *Nature*, **409 (6816)**, 46–52.
- Knöll, L., S. Scheel, and D.-G. Welsch, 2001: QED in dispersing and absorbing dielectric media. *Coherence and Statistics of Photons and Atoms*, J. Perina, Ed., Wiley, New York, 1–60.
- Knoll, W., M. R. Philpott, J. D. Swalen, and A. Girlando, 1981: Emission of light from Ag metal gratings coated with dye monolayer assemblies. *J. Chem. Phys.*, **75 (10)**, 4795–4799.
- Kochan, P. and H. J. Carmichael, 1994: Photon-statistics dependence of single-atom absorption. *Phys. Rev. A*, **50 (2)**, 1700–1709.
- Koenderink, A. F., 2009: Plasmon nanoparticle array waveguides for single photon and single plasmon sources. *Nano Lett.*, **9 (12)**, 4228–4233.
- Koenderink, A. F., 2010: On the use of Purcell factors for plasmon antennas. *Opt. Lett.*, **35 (24)**, 4208–4210.
- Kosako, T., Y. Kadoya, and H. F. Hofmann, 2010: Directional control of light by a nano-optical yagi-uda antenna. *Nat. Photon.*, **4 (5)**, 312–315.
- Kosmanis, T. and T. Tsiboukis, 2003: A systematic and topologically stable conformal finite-difference time-domain algorithm for modeling curved dielectric interfaces in three dimensions. *Microwave Theory Tech., IEEE Trans.*, **51 (3)**, 839–847.
- Kottmann, J. P., O. J. F. Martin, D. R. Smith, and S. Schultz, 2001: Plasmon resonances of silver nanowires with a nonregular cross section. *Phys. Rev. B*, **64 (23)**, 235402.
- Koyama, K., M. Yoshita, M. Baba, T. Suemoto, and H. Akiyama, 1999: High collection efficiency in fluorescence microscopy with a solid immersion lens. *Appl. Phys. Lett.*, **75 (12)**, 1667–1669.
- Kramer, A., W. Tragesinger, B. Hecht, and U. P. Wild, 2002: Optical near-field enhancement at a metal tip probed by a single fluorophore. *Appl. Phys. Lett.*, **80 (9)**, 1652–1654.
- Kreibig, U., 2008: Interface-induced dephasing of Mie plasmon polaritons. *Appl. Phys. B*, **93 (1)**, 79–89.
- Kroekenstoel, E. J. A., E. Verhagen, R. J. Walters, L. Kuipers, and A. Polman, 2009: Enhanced spontaneous emission rate in annular plasmonic nanocavities. *Appl. Phys. Lett.*, **95 (26)**, 263106.

- Krug II, J. T., E. J. Sánchez, and X. S. Xie, 2002: Design of near-field optical probes with optimal field enhancement by finite difference time domain electromagnetic simulation. *J. Chem. Phys.*, **116** (24), 10 895–10 901.
- Kuhn, A., M. Hennrich, and G. Rempe, 2002: Deterministic single-photon source for distributed quantum networking. *Phys. Rev. Lett.*, **89** (6), 067 901.
- Kühn, S., 2006: Modifikation der Emission eines Moleküls im optischen Nahfeld eines Nanoteilchens. Ph.D. thesis, ETH Zurich, Zurich, Switzerland, Diss. ETH No. 16935.
- Kühn, S., U. Håkanson, L. Rogobete, and V. Sandoghdar, 2006: Enhancement of single-molecule fluorescence using a gold nanoparticle as an optical nanoantenna. *Phys. Rev. Lett.*, **97** (1), 017402.
- Kühn, S., G. Mori, M. Agio, and V. Sandoghdar, 2008: Modification of single molecule fluorescence close to a nanostructure: radiation pattern, spontaneous emission and quenching. *Mol. Phys.*, **106** (7), 893–908.
- Kukura, P., M. Celebrano, A. Renn, and V. Sandoghdar, 2009: Imaging a single quantum dot when it is dark. *Nano Lett.*, **9** (3), 926–929.
- Kukura, P., M. Celebrano, A. Renn, and V. Sandoghdar, 2010: Single-molecule sensitivity in optical absorption at room temperature. *J. Phys. Chem. Lett.*, **1** (23), 3323–3327.
- Kulakovich, O., N. Strekal, A. Yaroshevich, S. Maskevich, S. Gaponenko, I. Nabiev, U. Woggon, and M. Artemyev, 2002: Enhanced luminescence of CdSe quantum dots on gold colloids. *Nano Lett.*, **2** (12), 1449–1452.
- Kulzer, F. and M. Orrit, 2004: Single-molecule optics. *Annu. Rev. Phys. Chem.*, **55** (1), 585–611.
- Kümmerlen, J., A. Leitner, H. Brunner, F. R. Aussenegg, and A. Wokaun, 1993: Enhanced dye fluorescence over silver island films: analysis of the distance dependence. *Mol. Phys.*, **80** (5), 1031–1046.
- Kurtsiefer, C., S. Mayer, P. Zarda, and H. Weinfurter, 2000: Stable solid-state source of single photons. *Phys. Rev. Lett.*, **85** (2), 290–293.
- Kuttge, M., F. J. García de Abajo, and A. Polman, 2010: Ultrasmall mode volume plasmonic nanodisk resonators. *Nano Lett.*, **10** (5), 1537–1541.
- Labeke, D. V. and D. Barchiesi, 1992: Scanning-tunneling optical microscopy: a theoretical macroscopic approach. *J. Opt. Soc. Am. A*, **9** (5), 732–739.



- Labeke, D. V. and D. Barchiesi, 1993: Probes for scanning tunneling optical microscopy: a theoretical comparison. *J. Opt. Soc. Am. A*, **10** (10), 2193–2201.
- Ladd, T. D., F. Jelezko, R. Laflamme, Y. Nakamura, C. Monroe, and J. L. O’Brien, 2010: Quantum computers. *Nature*, **464** (7285), 45–53.
- Lakowicz, J. R., 2005: Radiative decay engineering 5: metal-enhanced fluorescence and plasmon emission. *Analytical Biochem.*, **337** (2), 171–194.
- Lambert, J. H., 1760: *Photometria, sive de mensura et gradibus luminis, colorum et umbrae*. sumptibus Vidae Eberhardi Klett, typis Christophori Petri Detleffsen.
- Langhammer, C., M. Schwind, B. Kasemo, and I. Zorić, 2008: Localized surface plasmon resonances in aluminum nanodisks. *Nano Lett.*, **8** (5), 1461–1471.
- Lecamp, G., P. Lalanne, and J. P. Hugonin, 2007: Very large spontaneous-emission  $\beta$  factors in photonic-crystal waveguides. *Phys. Rev. Lett.*, **99** (2), 023 902.
- Lee, H., Y.-C. Cheng, and G. R. Fleming, 2007: Coherence dynamics in photosynthesis: Protein protection of excitonic coherence. *Science*, **316** (5830), 1462–1465.
- Lee, H. W., M. A. Schmidt, H. K. Tyagi, L. P. Sempere, and P. S. J. Russell, 2008: Polarization-dependent coupling to plasmon modes on submicron gold wire in photonic crystal fiber. *Appl. Phys. Lett.*, **93** (11), 111102.
- Lee, J.-Y. and N.-H. Myung, 1999: Locally tensor conformal FDTD method for modeling arbitrary dielectric surfaces. *Microwave Opt. Tech. Lett.*, **23** (4), 245–249.
- Lee, K., X.-W. Chen, H. Eghlidi, P. Kukura, R. Lettow, A. Renn, V. Sandoghdar, and S. Götzinger, 2011: A planar dielectric antenna for directional single-photon emission and near-unity collection efficiency. *Nat. Photon.*, **5** (3), 166–169.
- Lee, P. C. and D. Meisel, 1982: Adsorption and surface-enhanced raman of dyes on silver and gold sols. *J. Phys. Chem.*, **86** (17), 3391–3395.
- Leitner, A., M. E. Lippitsch, S. Draxler, M. Riegler, and F. R. Aussenegg, 1985: Fluorescence properties of dyes adsorbed to silver islands, investigated by picosecond techniques. *Appl. Phys. B*, **36** (2), 105–109.
- Lettow, R., V. Ahtee, R. Pfab, A. Renn, E. Ikonen, S. Götzinger, and V. Sandoghdar, 2007: Realization of two fourier-limited solid-state single-photon sources. *Opt. Express*, **15** (24), 15 842–15 847.
- Leung, P. T., 1990: Decay of molecules at spherical surfaces: Nonlocal effects. *Phys. Rev. B*, **42** (12), 7622–7625.
- Leuthold, J., C. Koos, and W. Freude, 2010: Nonlinear silicon photonics. *Nat. Photon.*, **4** (8), 535–544.

- Leviatan, Y., 1986: Study of near-zone fields of a small aperture. *J. Appl. Phys.*, **60** (5), 1577–1583.
- Lewis, A., M. Isaacson, A. Harootunian, and A. Muray, 1984: Development of a 500 Å spatial resolution light microscope: I. light is efficiently transmitted through  $[\lambda]/16$  diameter apertures. *Ultramicroscopy*, **13** (3), 227–231.
- Li, J., A. Salandrino, and N. Engheta, 2007: Shaping light beams in the nanometer scale: A yagi-uda nanoantenna in the optical domain. *Phys. Rev. B*, **76** (24), 245403.
- Li, Z., F. Hao, Y. Huang, Y. Fang, P. Nordlander, and H. Xu, 2009: Directional light emission from propagating surface plasmons of silver nanowires. *Nano Lett.*, **9** (12), 4383–4386.
- Lide, D. R., (Ed.) , 2006: *CRC Handbook of Chemistry and Physics*. 87th ed., CRC Press, Boca Raton, FL.
- Lindfors, K., T. Kalkbrenner, P. Stoller, and V. Sandoghdar, 2004: Detection and spectroscopy of gold nanoparticles using supercontinuum white light confocal microscopy. *Phys. Rev. Lett.*, **93** (3), 037401.
- Linfoot, E. H. and E. Wolf, 1956: Phase distribution near focus in an aberration-free diffraction image. *Proc. Phys. Soc. B*, **69** (8), 823–832.
- Ling, H. and S.-W. Lee, 1984: Focusing of electromagnetic waves through a dielectric interface. *J. Opt. Soc. Am. A*, **1** (9), 965–973.
- Liu, M., P. Guyot-Sionnest, T.-W. Lee, and S. K. Gray, 2007: Optical properties of rodlike and bipyramidal gold nanoparticles from three-dimensional computations. *Phys. Rev. B*, **76** (23), 235428.
- Lock, J. A., 1995: Interpretation of extinction in gaussian-beam scattering. *J. Opt. Soc. Am. A*, **12** (5), 929–938.
- Lock, J. A., J. T. Hodges, and G. Gouesbet, 1995: Failure of the optical theorem for gaussian-beam scattering by a spherical particle. *J. Opt. Soc. Am. A*, **12** (12), 2708–2715.
- Lopata, K. and D. Neuhauser, 2009: Multiscale maxwell-schrödinger modeling: A split field finite-difference time-domain approach to molecular nanopolaritonics. *J. Chem. Phys.*, **130** (10), 104707.
- Loudon, R., 2000: *The Quantum Theory of Light*. 3d ed., Oxford University Press, Oxford, UK.

- Loudon, R. and S. M. Barnett, 2006: Theory of the linear polarizability of a two-level atom. *J. Phys. B*, **39** (15), S555–S563.
- Lukosz, W. and R. E. Kunz, 1977: Light emission by magnetic and electric dipoles close to a plane dielectric interface. II. Radiation patterns of perpendicular oriented dipoles. *J. Opt. Soc. Am.*, **67** (12), 1615–1619.
- Lund-Hansen, T., S. Stobbe, B. Julsgaard, H. Thyrrestrup, T. Sünner, M. Kamp, A. Forchel, and P. Lodahl, 2008: Experimental realization of highly efficient broadband coupling of single quantum dots to a photonic crystal waveguide. *Phys. Rev. Lett.*, **101** (11), 113 903.
- Lupton, J. M., 2010: Single-molecule spectroscopy for plastic electronics: Materials analysis from the bottom-up. *Adv. Mater.*, **22** (15), 1689–1721.
- Macfarlane, R. and R. Shelby, 1987: Spectroscopy of solids containing rare earth ions. *Modern problems in condensed matter sciences*, North Holland, Vol. 21, chap. 3, 51–184.
- Mackowski, S., et al., 2008: Metal-enhanced fluorescence of chlorophylls in single light-harvesting complexes. *Nano Lett.*, **8** (2), 558–564.
- Madsen, N. K. and R. W. Ziolkowski, 1990: A three-dimensional modified finite volume technique for Maxwell's equations. *Electromagnetics*, **10** (1), 147–161.
- Maier, S. A., 2006: Plasmonic field enhancement and SERS in the effective mode volume picture. *Opt. Express*, **14** (5), 1957–1964.
- Maiman, T. H., 1960: Stimulated optical radiation in ruby. *Nature*, **187** (4736), 493–494.
- Maksymov, I. S., M. Besbes, J. P. Hugonin, J. Yang, A. Beveratos, I. Sagnes, I. Robert-Philip, and P. Lalanne, 2010: Metal-coated nanocylinder cavity for broadband nonclassical light emission. *Phys. Rev. Lett.*, **105** (18), 180 502.
- Maloney, J. and G. Smith, 1992: The efficient modeling of thin material sheets in the finite-difference time-domain (FDTD) method. *Antennas Propag., IEEE Trans.*, **40** (3), 323–330.
- Mandel, L., 1961: Photon degeneracy in light from optical maser and other sources. *J. Opt. Soc. Am.*, **51** (7), 797–798.
- Marconi, G., 1967: Wireless telegraphic communication. *Noble lectures. Physics 1901-1921*, Elsevier, Amsterdam, Vol. 196-222, 206, 11 December 1909.
- Markham, J. J., 1959: Interaction of normal modes with electron traps. *Rev. Mod. Phys.*, **31** (4), 956–989.

- Martin, O. J. F., C. Girard, and A. Dereux, 1995: Generalized field propagator for electromagnetic scattering and light confinement. *Phys. Rev. Lett.*, **74** (4), 526–529.
- Martin, Y. C., H. F. Hamann, and H. K. Wickramasinghe, 2001: Strength of the electric field in apertureless near-field optical microscopy. *J. Appl. Phys.*, **89** (10), 5774–5778.
- Matsuda, K., T. Saiki, S. Nomura, M. Mihara, Y. Aoyagi, S. Nair, and T. Takagahara, 2003: Near-field optical mapping of exciton wave functions in a GaAs quantum dot. *Phys. Rev. Lett.*, **91** (17), 177401.
- Matsuo, S., A. Shinya, T. Kakitsuka, K. Nozaki, T. Segawa, T. Sato, Y. Kawaguchi, and M. Notomi, 2010: High-speed ultracompact buried heterostructure photonic-crystal laser with 13 fJ of energy consumed per bit transmitted. *Nat. Photon.*, **4** (9), 648–654.
- Maxwell, J. C., 1865: A dynamical theory of the electromagnetic field. *Phil. Trans. Royal Soc. London*, **155**, 459–512.
- McLean, J. S., 1996: A re-examination of the fundamental limits on the radiation Q of electrically small antennas. *Antennas Propag., IEEE Trans.*, **44** (5), 672–676.
- Mei, K., A. Cangellaris, and D. Angelakos, 1984: Conformal time domain finite-difference method. *Radio Sci.*, **19** (5), 1145–1147.
- Meier, M. and A. Wokaun, 1983: Enhanced fields on large metal particles: dynamic depolarization. *Opt. Lett.*, **8** (11), 581–583.
- Meixner, J. and W. Andrejewski, 1950: Strenge Theorie der Beugung ebener elektromagnetischer Wellen an der vollkommen leitenden Kreisscheibe und an der kreisförmigen Öffnung im vollkommen leitenden ebenen Schirm. *Ann. Phys.*, **7**, 157–168.
- Mertens, H., A. F. Koenderink, and A. Polman, 2007: Plasmon-enhanced luminescence near noble-metal nanospheres: Comparison of exact theory and an improved Gersten and Nitzan model. *Phys. Rev. B*, **76** (11), 115123.
- Mertens, H. and A. Polman, 2009: Strong luminescence quantum-efficiency enhancement near prolate metal nanoparticles: Dipolar versus higher-order modes. *J. Appl. Phys.*, **105** (4), 044302.
- Messinger, B. J., K. U. von Raben, R. K. Chang, and P. W. Barber, 1981: Local fields at the surface of noble-metal microspheres. *Phys. Rev. B*, **24** (2), 649–657.
- Metiu, H., 1984: Surface enhanced spectroscopy. *Progr. Surf. Sci.*, **17** (3-4), 153–320.

- Michaelis, J. and C. Bräuchle, 2010: Reporters in the nanoworld: diffusion of single molecules in mesoporous materials. *Chem. Soc. Rev.*, **39**, 4731–4740.
- Michler, P., A. Kiraz, C. Becher, W. V. Schoenfeld, P. M. Petroff, L. Zhang, E. Hu, and A. Imamoglu, 2000: A quantum dot single-photon turnstile device. *Science*, **290** (5500), 2282–2285.
- Mie, G., 1908: Beiträge zur Optik trüber Medien, speziell kolloidaler Metallösungen. *Ann. Phys.*, **25** (3), 377452.
- Miller, D. A. B., 1989: Optics for low-energy communication inside digital processors: quantum detectors, sources, and modulators as efficient impedance converters. *Opt. Lett.*, **14** (2), 146–148.
- Miller, D. A. B., 2009: Device requirements for optical interconnects to silicon chips. *IEEE, Proc.*, **97** (7), 1166–1185.
- Moerner, W. E., 1994: Examining nanoenvironments in solids on the scale of a single, isolated impurity molecule. *Science*, **265** (5168), 46–53.
- Moerner, W. E., 2002: A dozen years of single-molecule spectroscopy in physics, chemistry, and biophysics. *J. Phys. Chem. B*, **106** (5), 910927.
- Moerner, W. E. and L. Kador, 1989: Optical detection and spectroscopy of single molecules in a solid. *Phys. Rev. Lett.*, **62** (21), 2535–2538.
- Moerner, W. E., T. Plakhotnik, T. Irngartinger, U. P. Wild, D. W. Pohl, and B. Hecht, 1994: Near-field optical spectroscopy of individual molecules in solids. *Phys. Rev. Lett.*, **73** (20), 2764–2767.
- Mohammadi, A. and M. Agio, 2006: Dispersive contour-path finite-difference time-domain algorithm for modelling surface plasmon polaritons at flat interfaces. *Opt. Express*, **14** (23), 11 330–11 338.
- Mohammadi, A., T. Jalali, and M. Agio, 2008a: Dispersive contour-path algorithm for the two-dimensional finite-difference time-domain method. *Opt. Express*, **16** (10), 7397–7406.
- Mohammadi, A., F. Kaminski, V. Sandoghdar, and M. Agio, 2009a: Spheroidal nanoparticles as nanoantennas for fluorescence enhancement. *Intl. J. Nanotechnology*, **6** (10-11), 902–914.
- Mohammadi, A., F. Kaminski, V. Sandoghdar, and M. Agio, 2010: Fluorescence enhancement with the optical (bi-) conical antenna. *J. Phys. Chem. C*, **114** (16), 7372–7377.

- Mohammadi, A., H. Nadgaran, and M. Agio, 2005: Contour-path effective permittivities for the two-dimensional finite-difference time-domain method. *Opt. Express*, **13** (25), 10 367–10 381.
- Mohammadi, A., V. Sandoghdar, and M. Agio, 2008b: Gold nanorods and nanospheroids for enhancing spontaneous emission. *New J. Phys.*, **10** (10), 105 015 (14pp).
- Mohammadi, A., V. Sandoghdar, and M. Agio, 2009b: Gold, copper, silver and aluminum nanoantennas to enhance spontaneous emission. *J. Comput. Theor. Nanosci.*, **6** (9), 2024–2030.
- Mojarad, N. M. and M. Agio, 2009: Tailoring the excitation of localized surface plasmon-polariton resonances by focusing radially-polarized beams. *Opt. Express*, **17** (1), 117–122.
- Mojarad, N. M., V. Sandoghdar, and M. Agio, 2008: Plasmon spectra of nanospheres under a tightly focused beam. *J. Opt. Soc. Am. B*, **25** (4), 651–658.
- Mojarad, N. M., G. Zumofen, V. Sandoghdar, and M. Agio, 2009: Metal nanoparticles in strongly confined beams: transmission, reflection and absorption. *J. Eur. Opt. Soc.: RP*, **4**, 09 014.
- Monroe, C., 2002: Quantum information processing with atoms and photons. *Nature*, **416** (6877), 238–246.
- Morawitz, H. and M. R. Philpott, 1974: Coupling of an excited molecule to surface plasmons. *Phys. Rev. B*, **10** (12), 4863–4868.
- Morita, N., T. Tanaka, T. Yamasaki, and Y. Nakanishi, 1968: Scattering of a beam wave by a spherical object. *Antennas Propag., IEEE Trans.*, **16** (6), 724–727.
- Moskovits, M., 1985: Surface-enhanced spectroscopy. *Rev. Mod. Phys.*, **57** (3), 783–826.
- Mühlschlegel, P., H.-J. Eisler, O. J. F. Martin, B. Hecht, and D. W. Pohl, 2005: Resonant optical antennas. *Science*, **308** (5728), 1607–1609.
- Nadobny, J., D. Sullivan, W. Wlodarczyk, P. Deuffhard, and P. Wust, 2003: A 3-D tensor FDTD-formulation for treatment of sloped interfaces in electrically inhomogeneous media. *Antennas Propag., IEEE Trans.*, **51** (8), 1760–1770.
- Newton, R. G., 1976: Optical theorem and beyond. *Am. J. Phys.*, **44** (7), 639–642.
- Nezhad, M. P., A. Simic, O. Bondarenko, B. Slutsky, A. Mizrahi, L. Feng, V. Lomakin, and Y. Fainman, 2010: Room-temperature subwavelength metallo-dielectric lasers. *Nat. Photon.*, **4** (6), 395–399.

- Nie, S. and S. R. Emory, 1997: Probing single molecules and single nanoparticles by surface-enhanced raman scattering. *Science*, **275 (5303)**, 1102–1106.
- Nielsen, M. A. and I. L. Chuang, 2000: *Quantum Computation and Quantum Information*. Cambridge University Press, Cambridge, UK.
- Nieminen, T. A., H. Rubinsztein-Dunlop, and N. R. Heckenberg, 2003: Multipole expansion of strongly focussed laser beams. *J. Quant. Spectr. Rad. Trans.*, **79-80**, 1005–1017.
- Noginov, M. A., et al., 2009: Demonstration of a spaser-based nanolaser. *Nature*, **460 (7259)**, 1110–1112.
- Nomura, Y. and S. Katsura, 1955: Diffraction of electromagnetic waves by circular plate and circular hole. *J. Phys. Soc. Jpn.*, **10 (4)**, 285–304.
- Novotny, L., 1996: Single molecule fluorescence in inhomogeneous environments. *Appl. Phys. Lett.*, **69 (25)**, 3806–3808.
- Novotny, L., 2007: Effective wavelength scaling for optical antennas. *Phys. Rev. Lett.*, **98 (26)**, 266802.
- Novotny, L. and C. Hafner, 1994: Light propagation in a cylindrical waveguide with a complex, metallic, dielectric function. *Phys. Rev. E*, **50 (5)**, 4094–4106.
- Novotny, L. and D. Pohl, 1995: Light propagation in scanning near-field optical microscopy. *Photons and Local Probes*, O. Marti and R. Möller, Eds., Kluwer, Dordrecht, NATO ASI Series E.
- Novotny, L., D. W. Pohl, and B. Hecht, 1995: Scanning near-field optical probe with ultrasmall spot size. *Opt. Lett.*, **20 (9)**, 970–972.
- Novotny, L. and N. van Hulst, 2011: Antennas for light. *Nat. Photon.*, **5 (2)**, 83–90.
- Nozaki, K., T. Tanabe, A. Shinya, S. Matsuo, T. Sato, H. Taniyama, and M. Notomi, 2010: Sub-femtojoule all-optical switching using a photonic-crystal nanocavity. *Nat. Photon.*, **4 (7)**, 477–483.
- O'Brien, J. L., 2007: Optical quantum computing. *Science*, **318 (5856)**, 1567–1570.
- O'Connell, M. J., et al., 2002: Band gap fluorescence from individual single-walled carbon nanotubes. *Science*, **297 (5581)**, 593–596.
- Oron, R., S. Blit, N. Davidson, A. A. Friesem, Z. Bomzon, and E. Hasman, 2000: The formation of laser beams with pure azimuthal or radial polarization. *Appl. Phys. Lett.*, **77 (21)**, 3322–3324.

- Orrit, M. and J. Bernard, 1990: Single pentacene molecules detected by fluorescence excitation in a p-terphenyl crystal. *Phys. Rev. Lett.*, **65 (21)**, 2716–2719.
- Oubre, C. and P. Nordlander, 2004: Optical properties of metallodielectric nanostructures calculated using the finite difference time domain method. *J. Phys. Chem. B*, **108 (46)**, 17740–17747.
- Oulton, R. F., G. Bartal, D. F. P. Pile, and X. Zhang, 2008: Confinement and propagation characteristics of subwavelength plasmonic modes. *New J. Phys.*, **10 (10)**, 105018.
- Oulton, R. F., V. J. Sorger, T. Zentgraf, R.-M. Ma, C. Gladden, L. Dai, G. Bartal, and X. Zhang, 2009: Plasmon lasers at deep subwavelength scale. *Nature*, **461 (7264)**, 629–632.
- Painter, O., R. K. Lee, A. Scherer, A. Yariv, J. D. O'Brien, P. D. Dapkus, and I. Kim, 1999: Two-dimensional photonic band-gap defect mode laser. *Science*, **284 (5421)**, 1819–1821.
- Pakizeh, T. and M. Käll, 2009: Unidirectional ultracompact optical nanoantennas. *Nano Letters*, **9 (6)**, 2343–2349.
- Pakizeh, T., C. Langhammer, I. Zorić, P. Apell, and M. Käll, 2009: Intrinsic fano interference of localized plasmons in pd nanoparticles. *Nano Lett.*, **9 (2)**, 882–886.
- Palik, E. D. and G. Ghosh, (Eds.) , 1998: *Handbook of Optical Constants of Solids*. Academic Press.
- Panitchayangkoon, G., D. Hayes, K. A. Fransted, J. R. Caram, E. Harel, J. Wen, R. E. Blankenship, and G. S. Engel, 2010: Long-lived quantum coherence in photosynthetic complexes at physiological temperature. *Proc. Natl. Acad. Sci.*, **107 (29)**, 12766–12770.
- Patterson, G., M. Davidson, S. Manley, and J. Lippincott-Schwartz, 2010: Superresolution imaging using single-molecule localization. *Annu. Rev. Phys. Chem.*, **61 (1)**, 345–367.
- Paul, H. and R. Fischer, 1983: Light absorption by a dipole. *Sov. Phys. Usp.*, **26 (10)**, 923–926.
- Pellegrini, G., G. Mattei, and P. Mazzoldi, 2009: Light extraction with dielectric nanoantenna arrays. *ACS Nano*, **3 (9)**, 2715–2721.
- Pelton, M., C. Santori, J. Vučković, B. Zhang, G. S. Solomon, J. Plant, and Y. Yamamoto, 2002: Efficient source of single photons: A single quantum dot in a micropost microcavity. *Phys. Rev. Lett.*, **89 (23)**, 233602.



- Persson, B. N. J., 1978: Theory of the damping of excited molecules located above a metal surface. *J. Phys. C*, **11 (20)**, 4251–4269.
- Pfab, R. J., J. Zimmermann, C. Hettich, I. Gerhardt, A. Renn, and V. Sandoghdar, 2004: Aligned terrylene molecules in a spin-coated ultrathin crystalline film of p-terphenyl. *Chem. Phys. Lett.*, **387 (4-6)**, 490–495.
- Piro, N., et al., 2011: Heralded single-photon absorption by a single atom. *Nat. Phys.*, **7 (1)**, 17–20.
- Plakhotnik, T., 1995: Detection of single molecules with a scanning near-field optical microscope: absorption and luminescence. *Opt. Spectrosc.*, **79 (5)**, 747–755.
- Plakhotnik, T. and V. Palm, 2001: Interferometric signatures of single molecules. *Phys. Rev. Lett.*, **87 (18)**, 183 602.
- Pohl, D., 2000: Near-field optics seen as an antenna problem. *Near-field Optics: Principles and Applications*, M. Ohtsu and X. Zhu, Eds., World Scientific Publ., Singapore, 9–21.
- Pohl, D. W., W. Denk, and M. Lanz, 1984: Optical stethoscopy: Image recording with resolution  $\lambda/20$ . *Appl. Phys. Lett.*, **44 (7)**, 651–653.
- Pototschnig, M., Y. Chassagneux, J. Hwang, G. Zumofen, A. Renn, and V. Sandoghdar, 2011: Controlling the phase of a light beam with a single molecule. *ArXiv e-prints*, 1103.6048.
- Prather, D. W. and S. Shi, 1999: Formulation and application of the finite-difference time-domain method for the analysis of axially symmetric diffractive optical elements. *J. Opt. Soc. Am. A*, **16 (5)**, 1131–1142.
- Press, D., T. D. Ladd, B. Zhang, and Y. Yamamoto, 2008: Complete quantum control of a single quantum dot spin using ultrafast optical pulses. *Nature*, **456 (7219)**, 218–221.
- Press, D., et al., 2010: Ultrafast optical spin echo in a single quantum dot. *Nat. Photon.*, **4 (6)**, 367–370.
- Protsenko, I. E., A. V. Uskov, O. A. Zaimidoroga, V. N. Samoilo, and E. P. O'Reilly, 2005: Dipole nanolaser. *Phys. Rev. A*, **71 (6)**, 063 812.
- Purcell, E., 1946: Spontaneous emission probabilities at radio frequencies. *Phys. Rev.*, **69**, 681.
- Quabis, S., R. Dorn, M. Eberler, O. Glöckl, and G. Leuchs, 2000: Focusing light to a tighter spot. *Opt. Commun.*, **179 (1-6)**, 1–7.

- Quabis, S., R. Dorn, M. Eberler, O. Glöckl, and G. Leuchs, 2001: The focus of light theoretical calculation and experimental tomographic reconstruction. *Appl. Phys. B*, **72** (1), 109–113.
- Quan, Q., I. Bulu, and M. Lončar, 2009: Broadband waveguide QED system on a chip. *Phys. Rev. A*, **80** (1), 011810.
- Quinten, M., A. Pack, and R. Wannemacher, 1999: Scattering and extinction of evanescent waves by small particles. *Appl. Phys. B*, **68**, 87–92.
- Rabitz, H., R. de Vivie-Riedle, M. Motzkus, and K. Kompa, 2000: Whither the future of controlling quantum phenomena? *Science*, **288** (5467), 824–828.
- Raether, H., 1988: *Surface Plasmons on Smooth and Rough Surfaces and on Gratings*. Springer-Verlag.
- Railton, C., I. Craddock, and J. Schneider, 1995: Improved locally distorted CPFDTD algorithm with provable stability. *Electronics Lett.*, **31** (18), 1585–1586.
- Ramadan, O. and A. Oztoprak, 2003: Z-transform implementation of the perfectly matched layer for truncating fdtd domains. *Microwave and Wireless Components Lett., IEEE*, **13** (9), 402–404.
- Raman, C. V. and K. S. Krishnan, 1928: A new type of secondary radiation. *Nature*, **121** (3048), 501–502.
- Rattier, M., et al., 2002: High extraction efficiency, laterally injected, light emitting diodes combining microcavities and photonic crystals. *Opt. Quantum Electron.*, **34**, 79–89.
- Ray, K., M. H. Chowdhury, and J. R. Lakowicz, 2007: Aluminum nanostructured films as substrates for enhanced fluorescence in the ultraviolet-blue spectral region. *Anal. Chem.*, **79** (17), 6480–6487.
- Rebane, K. K., 1970: *Impurity spectra of solids*. Plenum Press, New York.
- Rechberger, W., A. Hohenau, A. Leitner, J. R. Krenn, B. Lamprecht, and F. R. Aussenegg, 2003: Optical properties of two interacting gold nanoparticles. *Opt. Commun.*, **220** (1-3), 137–141.
- Reim, K. F., J. Nunn, V. O. Lorenz, B. J. Sussman, K. C. Lee, N. K. Langford, D. Jaksch, and I. A. Walmsley, 2010: Towards high-speed optical quantum memories. *Nat. Photon.*, **4** (4), 218–221.
- Richards, B. and E. Wolf, 1959: Electromagnetic diffraction in optical systems. ii. structure of the image field in an aplanatic system. *Proc. Royal Soc. London A*, **253** (1274), 358–379.

- Ridolfo, A., O. Di Stefano, N. Fina, R. Saija, and S. Savasta, 2010: Quantum plasmonics with quantum dot-metal nanoparticle molecules: Influence of the fano effect on photon statistics. *Phys. Rev. Lett.*, **105** (26), 263 601.
- Rigneault, H., F. Lemarchand, A. Sentenac, and H. Giovannini, 1999: Extraction of light from sources located inside waveguide grating structures. *Opt. Lett.*, **24** (3), 148–150.
- Ringler, M., A. Schwemer, M. Wunderlich, A. Nichtl, K. Kürzinger, T. A. Klar, and J. Feldmann, 2008: Shaping emission spectra of fluorescent molecules with single plasmonic nanoresonators. *Phys. Rev. Lett.*, **100** (20), 203 002.
- Rist, S., J. Eschner, M. Hennrich, and G. Morigi, 2008: Photon-mediated interaction between two distant atoms. *Phys. Rev. A*, **78** (1), 013 808.
- Roberts, A., 1987: Electromagnetic theory of diffraction by a circular aperture in a thick, perfectly conducting screen. *J. Opt. Soc. Am. A*, **4** (10), 1970–1983.
- Roberts, A., 1989: Near-zone fields behind circular apertures in thick, perfectly conducting screens. *J. Appl. Phys.*, **65** (8), 2896–2899.
- Roberts, A., 1991: Small-hole coupling of radiation into a near-field probe. *J. Appl. Phys.*, **70** (8), 4045–4049.
- Roden, J. A. and S. D. Gedney, 2000: Convolution PML (CPML): An efficient FDTD implementation of the CFS-PML for arbitrary media. *Microwave Opt. Technol. Lett.*, **27** (5), 334–339.
- Rogobete, L., 2007: The influence of the nano-environment on the optical properties of a dipole emitter a theoretical study. Ph.D. thesis, ETH Zurich, Zurich, Switzerland, Diss. ETH No. 16813.
- Rogobete, L., F. Kaminski, M. Agio, and V. Sandoghdar, 2007: Design of plasmonic nanoantennae for enhancing spontaneous emission. *Opt. Lett.*, **32** (12), 1623–1625.
- Ropers, C., C. C. Neacsu, T. Elsaesser, M. Albrecht, M. B. Raschke, and C. Lienau, 2007: Grating-coupling of surface plasmons onto metallic tips; a nanoconfined light source. *Nano Lett.*, **7** (9), 2784–2788.
- Ruppin, R., 1982: Decay of an excited molecule near a small metal sphere. *J. Chem. Phys.*, **76** (4), 1681–1684.
- Ryu, H. Y., Y. H. Lee, R. L. Sellin, and D. Bimberg, 2001: Over 30-fold enhancement of light extraction from free-standing photonic crystal slabs with ingaas quantum dots at low temperature. *Appl. Phys. Lett.*, **79** (22), 3573–3575.

- Sakoda, K., N. Kawai, T. Ito, A. Chutinan, S. Noda, T. Mitsuyu, and K. Hirao, 2001: Photonic bands of metallic systems. i. principle of calculation and accuracy. *Phys. Rev. B*, **64** (4), 045116.
- Sánchez, E. J., L. Novotny, and X. S. Xie, 1999: Near-field fluorescence microscopy based on two-photon excitation with metal tips. *Phys. Rev. Lett.*, **82** (20), 4014–4017.
- Savage, C. M., S. L. Braunstein, and D. F. Walls, 1990: Macroscopic quantum superpositions by means of single-atom dispersion. *Opt. Lett.*, **15** (11), 628.
- Savasta, S., R. Saija, A. Ridolfo, O. Di Stefano, P. Denti, and F. Borghese, 2010: Nanopolaritons: Vacuum rabi splitting with a single quantum dot in the center of a dimer nanoantenna. *ACS Nano*, **4** (11), 6369–6376.
- Schietinger, S., M. Barth, T. Aichele, and O. Benson, 2009: Plasmon-enhanced single photon emission from a nanoassembled metal-diamond hybrid structure at room temperature. *Nano Lett.*, **9** (4), 1694–1698.
- Schuck, P. J., D. P. Fromm, A. Sundaramurthy, G. S. Kino, and W. E. Moerner, 2005: Improving the mismatch between light and nanoscale objects with gold bowtie nanoantennas. *Phys. Rev. Lett.*, **94** (1), 017402.
- Schuller, J. A., E. S. Barnard, W. Cai, Y. C. Jun, J. S. White, and M. L. Brongersma, 2010: Plasmonics for extreme light concentration and manipulation. *Nat. Mater.*, **9** (3), 193–204.
- Schuster, I., A. Kubanek, A. Fuhrmanek, T. Puppe, P. W. H. Pinkse, K. Murr, and G. Rempe, 2008: Nonlinear spectroscopy of photons bound to one atom. *Nat. Phys.*, **4** (5), 382–385.
- Shankar, V., A. H. Mohammadian, and W. F. Hall, 1990: A time-domain, finite-volume treatment for the Maxwell equations. *Electromagnetics*, **10**, 127–145.
- Sheng, P., 1995: *Introduction to Wave Scattering, Localization and Mesoscopic Phenomena*. Academic, New York.
- Sheppard, C. J. R., 1978: Electromagnetic field in the focal region of wide-angular annular lens and mirror systems. *IEE J. Microw. Opt. Acoust.*, **2** (5), 163–166.
- Sheppard, C. J. R., 2007: The optics of microscopy. *J. Opt. A*, **9** (6), S1.
- Sheppard, C. J. R. and K. G. Larkin, 1994: Optimal concentration of electromagnetic radiation. *J. Mod. Opt.*, **41** (7), 1495–1505.
- Sheppard, C. J. R. and S. Saghafi, 1999: Electromagnetic gaussian beams beyond the paraxial approximation. *J. Opt. Soc. Am. A*, **16** (6), 1381–1386.

- Sheppard, C. J. R. and P. Török, 1997a: Efficient calculation of electromagnetic diffraction in optical systems using a multipole expansion. *J. Mod. Opt.*, **44** (4), 803–818.
- Sheppard, C. J. R. and P. Török, 1997b: Electromagnetic field in the focal region of an electric dipole wave. *Optik (Jena)*, **104** (4), 175–177.
- Shimizu, K. T., W. K. Woo, B. R. Fisher, H. J. Eisler, and M. G. Bawendi, 2002: Surface-enhanced emission from single semiconductor nanocrystals. *Phys. Rev. Lett.*, **89** (11), 117 401.
- Snyder, A. W. and J. Love, 1983: *Optical Waveguide Theory*. Springer.
- Sommerfeld, A., 1909: über die Ausbreitung der Wellen in der drahtlosen Telegraphie. *Ann. Phys. (Leipzig)*, **28** (4), 665–736.
- Sondermann, M., R. Maiwald, H. Konermann, N. Lindlein, U. Peschel, and G. Leuchs, 2007: Design of a mode converter for efficient light-atom coupling in free space. *Appl. Phys. B*, **89**, 489–492.
- Song, B.-S., S. Noda, T. Asano, and Y. Akahane, 2005: Ultra-high-Q photonic double-heterostructure nanocavity. *Nat. Mater.*, **4** (3), 207–210.
- Sönnichsen, C., T. Franzl, T. Wilk, G. von Plessen, J. Feldmann, O. Wilson, and P. Mulvaney, 2002: Drastic reduction of plasmon damping in gold nanorods. *Phys. Rev. Lett.*, **88** (7), 077 402.
- Stade, F., A. Heeren, M. Fleischer, and D. Kern, 2007: Fabrication of metallic nanostructures for investigating plasmon-induced field enhancement. *Microelectr. Eng.*, **84** (5-8), 1589–1592.
- Stamnes, J., 1986: *Waves in focal regions*. Hilger, Bristol, UK.
- Stamnes, J. J. and V. Dhayalan, 1996: Focusing of electric-dipole waves. *Pure Appl. Opt. A*, **5** (2), 195–225.
- Stobińska, M., G. Alber, and G. Leuchs, 2009: Perfect excitation of a matter qubit by a single photon in free space. *Eur. Phys. Lett.*, **86** (1), 14 007.
- Stockman, M. I., 2004: Nanofocusing of optical energy in tapered plasmonic waveguides. *Phys. Rev. Lett.*, **93** (13), 137 404.
- Stockman, M. I., 2008: Ultrafast nanoplasmonics under coherent control. *New J. Phys.*, **10** (2), 025 031 (20pp).
- Stockman, M. I., 2010: The spaser as a nanoscale quantum generator and ultrafast amplifier. *J. Opt.*, **12** (2), 024 004.

- Strauf, S., N. G. Stoltz, M. T. Rakher, L. A. Coldren, P. M. Petroff, and D. Bouwmeester, 2007: High-frequency single-photon source with polarization control. *Nat. Photon.*, **1** (12), 704–708.
- Sullivan, D., 1996: Z-transform theory and the FDTD method. *Antennas Propag., IEEE Trans.*, **44** (1), 28–34.
- Sun, W. and Q. Fu, 2000: Finite-difference time-domain solution of light scattering by dielectric particles with large complex refractive indices. *Appl. Opt.*, **39** (30), 5569–5578.
- Sundaramurthy, A., K. B. Crozier, G. S. Kino, D. P. Fromm, P. J. Schuck, and W. E. Moerner, 2005: Field enhancement and gap-dependent resonance in a system of two opposing tip-to-tip au nanotriangles. *Phys. Rev. B*, **72** (16), 165 409.
- Taflove, A. and S. C. Hagness, 2005: *Computational Electrodynamics: The Finite-Difference Time-Domain Method*. 3d ed., Artech House, Norwood, MA.
- Tamarat, P., B. Lounis, J. Bernard, M. Orrit, S. Kummer, R. Kettner, S. Mais, and T. Basché, 1995: Pump-probe experiments with a single molecule: ac-stark effect and nonlinear optical response. *Phys. Rev. Lett.*, **75** (8), 1514–1517.
- Tamarat, P., A. Maali, B. Lounis, and M. Orrit, 2000: Ten years of single-molecule spectroscopy. *J. Phys. Chem. A*, **104** (1), 1–16.
- Tame, M. S., C. Lee, J. Lee, D. Ballester, M. Paternostro, A. V. Zayats, and M. S. Kim, 2008: Single-photon excitation of surface plasmon polaritons. *Phys. Rev. Lett.*, **101** (19), 190504.
- Taminiau, T. H., F. D. Stefani, F. B. Segerink, and N. F. van Hulst, 2008a: Optical antennas direct single-molecule emission. *Nat. Photon.*, **2** (4), 234–237.
- Taminiau, T. H., F. D. Stefani, and N. F. van Hulst, 2008b: Enhanced directional excitation and emission of single emitters by a nano-optical yagi-uda antenna. *Opt. Express*, **16** (14), 10 858–10 866.
- Tey, M. K., Z. Chen, S. A. Aljunid, B. Chng, F. Huber, G. Maslennikov, and C. Kurtziefer, 2008: Strong interaction between light and a single trapped atom without the need for a cavity. *Nat. Phys.*, **4** (12), 924–927.
- Thomas, M., J.-J. Greffet, R. Carminati, and J. R. Arias-Gonzalez, 2004: Single-molecule spontaneous emission close to absorbing nanostructures. *Appl. Phys. Lett.*, **85** (17), 3863–3865.
- Tilaki, R., A. Irajizad, and S. Mahdavi, 2007: Size, composition and optical properties of copper nanoparticles prepared by laser ablation in liquids. *Appl. Phys. A*, **88**, 415–419.

- Tong, L., R. R. Gattass, J. B. Ashcom, S. He, J. Lou, M. Shen, I. Maxwell, and E. Mazur, 2003: Subwavelength-diameter silica wires for low-loss optical wave guiding. *Nature*, **426 (6968)**, 816–819.
- Toninelli, C., K. Early, J. Breimi, A. Renn, S. Götzinger, and V. Sandoghdar, 2010: Near-infrared single-photons from aligned molecules in ultrathin crystalline films at room temperature. *Opt. Express*, **18 (7)**, 6577–6582.
- Trautman, J. K., J. J. Macklin, L. E. Brus, and E. Betzig, 1994: Near-field spectroscopy of single molecules at room temperature. *Nature*, **369 (6475)**, 40–42.
- Trügler, A. and U. Hohenester, 2008: Strong coupling between a metallic nanoparticle and a single molecule. *Phys. Rev. B*, **77 (11)**, 115 403.
- Tsai, W.-C. and R. J. Pogorzelski, 1975: Eigenfunction solution of the scattering of beam radiation fields by spherical objects. *J. Opt. Soc. Am.*, **65 (12)**, 1457–1463.
- Turchette, Q. A., C. J. Hood, W. Lange, H. Mabuchi, and H. J. Kimble, 1995: Measurement of conditional phase shifts for quantum logic. *Phys. Rev. Lett.*, **75 (25)**, 4710–4713.
- Turukhin, A. V., C.-H. Liu, A. A. Gorokhovskiy, R. R. Alfano, and W. Phillips, 1996: Picosecond photoluminescence decay of Si-doped chemical-vapor-deposited diamond films. *Phys. Rev. B*, **54 (23)**, 16 448–16 451.
- Uda, S., 1927: High angle radiation of short electric waves. *Proc. Inst. Radio Engineers*, **15 (5)**, 377–385.
- Vahala, K. J., 2003: Optical microcavities. *Nature*, **424 (6950)**, 839–846.
- Vamivakas, A. N., et al., 2007: Strong extinction of a far-field laser beam by a single quantum dot. *Nano Lett.*, **7 (9)**, 2892–2896.
- van de Hulst, H. C., 1949a: *Light scattering by small particles*. Dover, New York.
- van de Hulst, H. C., 1949b: On the attenuation of plane waves by obstacles of arbitrary size and form. *Physica*, **15 (8-9)**, 740–746.
- van Enk, S. J., 2004: Atoms, dipole waves, and strongly focused light beams. *Phys. Rev. A*, **69 (4)**, 043 813.
- van Enk, S. J. and H. J. Kimble, 2000: Single atom in free space as a quantum aperture. *Phys. Rev. A*, **61 (5)**, 051 802.
- van Enk, S. J. and H. J. Kimble, 2001: Strongly focused light beams interacting with single atoms in free space. *Phys. Rev. A*, **63 (2)**, 023 809.

- van Loock, P., 2011: Optical hybrid approaches to quantum information. *Laser & Photonics Rev.*, **5** (2), 167–200.
- van Loock, P., T. D. Ladd, K. Sanaka, F. Yamaguchi, K. Nemoto, W. J. Munro, and Y. Yamamoto, 2006: Hybrid quantum repeater using bright coherent light. *Phys. Rev. Lett.*, **96** (24), 240501.
- van Loock, P., N. Lütkenhaus, W. J. Munro, and K. Nemoto, 2008: Quantum repeaters using coherent-state communication. *Phys. Rev. A*, **78** (6), 062319.
- Vaubel, G., H. Baessler, and D. Möbius, 1971: Reaction of singlet excitons at an anthracene/metal interface: Energy transfer. *Chem. Phys. Lett.*, **10** (3), 334–336.
- Verhagen, E., M. Spasenović, A. Polman, and L. Kuipers, 2009: Nanowire plasmon excitation by adiabatic mode transformation. *Phys. Rev. Lett.*, **102** (20), 203904.
- Vial, A., A.-S. Grimault, D. Macías, D. Barchiesi, and M. L. de la Chapelle, 2005: Improved analytical fit of gold dispersion: Application to the modeling of extinction spectra with a finite-difference time-domain method. *Phys. Rev. B*, **71** (8), 085416.
- Vigoureux, J. M. and D. Courjon, 1992: Detection of nonradiative fields in light of the Heisenberg uncertainty principle and the Rayleigh criterion. *Appl. Opt.*, **31** (16), 3170–3177.
- Vogel, M. W. and D. K. Gramotnev, 2007: Adiabatic nano-focusing of plasmons by metallic tapered rods in the presence of dissipation. *Phys. Lett. A*, **363** (5-6), 507–511.
- Waks, E. and J. Vuckovic, 2006: Dipole induced transparency in drop-filter cavity-waveguide systems. *Phys. Rev. Lett.*, **96** (15), 153601.
- Weiss, S., 1999: Fluorescence spectroscopy of single biomolecules. *Science*, **283** (5408), 1676–1683.
- Weiss, S., 2000: Measuring conformational dynamics of biomolecules by single molecule fluorescence spectroscopy. *Nat. Struct. Mol. Biol.*, **7** (9), 724–729.
- Welford, W. T. and R. Winston, 1978: *The Optics of Nonimaging Concentrators*. Academic, New York.
- Wilk, T., S. C. Webster, A. Kuhn, and G. Rempe, 2007: Single-atom single-photon quantum interface. *Science*, **317** (5837), 488–490.
- Wineland, D. J., W. M. Itano, and J. C. Bergquist, 1987: Absorption spectroscopy at the limit: detection of a single atom. *Opt. Lett.*, **12** (6), 389–391.



- Wokaun, A., J. P. Gordon, and P. F. Liao, 1982: Radiation damping in surface-enhanced raman scattering. *Phys. Rev. Lett.*, **48 (14)**, 957–960.
- Wokaun, A., H.-P. Lutz, A. P. King, U. P. Wild, and R. R. Ernst, 1983: Energy transfer in surface enhanced luminescence. *J. Chem. Phys.*, **79 (1)**, 509–514.
- Wolf, E., 1959: Electromagnetic diffraction in optical systems. I. An integral representation of the image field. *Proc. Royal Soc. London A*, **253 (1274)**, 349–357.
- Wolf, E., 1980: Phase conjugacy and symmetries in spatially bandlimited wavefields containing no evanescent components. *J. Opt. Soc. Am.*, **70 (11)**, 1311–1319.
- Wolf, E. and Y. Li, 1981: Conditions for the validity of the debye integral representation of focused fields. *Opt. Commun.*, **39 (4)**, 205–210.
- Wrigge, G., 2008: Coherent and incoherent light scattering in the resonance fluorescence of a single molecule. Ph.D. thesis, ETH Zurich, Zurich, Switzerland, Diss. ETH No. 17684.
- Wrigge, G., I. Gerhardt, J. Hwang, G. Zumofen, and V. Sandoghdar, 2008a: Efficient coupling of photons to a single molecule and the observation of its resonance fluorescence. *Nat. Phys.*, **4 (1)**, 60–66.
- Wrigge, G., J. Hwang, I. Gerhardt, G. Zumofen, and V. Sandoghdar, 2008b: Exploring the limits of single emitter detection in fluorescence and extinction. *Opt. Express*, **16 (22)**, 17358–17365.
- Wylie, J., 1986: Quantum electrodynamics near an interface. Ph.D. thesis, University of Toronto, Canada.
- Wylie, J. M. and J. E. Sipe, 1984: Quantum electrodynamics near an interface. *Phys. Rev. A*, **30 (3)**, 1185–1193.
- Xiao, T. and Q. H. Liu, 2004: A staggered upwind embedded boundary (SUEB) method to eliminate the FDTD staircasing error. *Antennas Propag., IEEE Trans.*, **52 (3)**, 730–741.
- Xie, X. S. and J. K. Trautman, 1998: Optical studies of single molecules at room temperature. *Annu. Rev. Phys. Chem.*, **49 (1)**, 441–480.
- Xu, H., X.-H. Wang, M. P. Persson, H. Q. Xu, M. Käll, and P. Johansson, 2004: Unified treatment of fluorescence and raman scattering processes near metal surfaces. *Phys. Rev. Lett.*, **93 (24)**, 243002.
- Xu, Y., R. K. Lee, and A. Yariv, 2000: Quantum analysis and the classical analysis of spontaneous emission in a microcavity. *Phys. Rev. A*, **61 (3)**, 033807.

- Xu, Y., J. S. Vučković, R. K. Lee, O. J. Painter, A. Scherer, and A. Yariv, 1999: Finite-difference time-domain calculation of spontaneous emission lifetime in a microcavity. *J. Opt. Soc. Am. B*, **16** (3), 465–474.
- Yablonovitch, E., 1982: Statistical ray optics. *J. Opt. Soc. Am.*, **72** (7), 899–907.
- Yablonovitch, E., 1987: Inhibited spontaneous emission in solid-state physics and electronics. *Phys. Rev. Lett.*, **58** (20), 2059–2062.
- Yagi, H., 1928: Beam transmission of ultra short waves. *Proc. Inst. Radio Engineers*, **16** (6), 715–740.
- Yang, P., G. W. Kattawar, K.-N. Liou, and J. Q. Lu, 2004: Comparison of cartesian grid configurations for application of the finite-difference time-domain method to electromagnetic scattering by dielectric particles. *Appl. Opt.*, **43** (23), 4611–4624.
- Yang, P., K. N. Liou, M. I. Mishchenko, and B.-C. Gao, 2000: Efficient finite-difference time-domain scheme for light scattering by dielectric particles: Application to aerosols. *Appl. Opt.*, **39** (21), 3727–3737.
- Yee, K., 1966: Numerical solution of initial boundary value problems involving Maxwell's equations in isotropic media. *Antennas Propag., IEEE Trans.*, **14** (3), 302–307.
- Youngworth, K. and T. Brown, 2000: Focusing of high numerical aperture cylindrical-vector beams. *Opt. Express*, **7** (2), 77–87.
- Yu, W., S. Dey, and R. Mittra, 2000: On the modeling of periodic structures using the finite-difference time-domain algorithm. *Microwave Opt. Tech. Lett.*, **24** (3), 151–155.
- Yu, W. and R. Mittra, 2001: A conformal finite difference time domain technique for modeling curved dielectric surfaces. *Microwave Wireless Comp. Lett., IEEE*, **11** (1), 25–27.
- Zavelani-Rossi, M., et al., 2008: Near-field second-harmonic generation in single gold nanoparticles. *Appl. Phys. Lett.*, **92** (9), 093119.
- Zelmann, M., et al., 2003: Seventy-fold enhancement of light extraction from a defectless photonic crystal made on silicon-on-insulator. *Appl. Phys. Lett.*, **83** (13), 2542–2544.
- Zeman, E. J. and G. C. Schatz, 1987: An accurate electromagnetic theory study of surface enhancement factors for silver, gold, copper, lithium, sodium, aluminum, gallium, indium, zinc, and cadmium. *J. Phys. Chem.*, **91** (3), 634–643.

- Zewail, A. H., 2001: Femtochemistry: Atomic-scale dynamics of the chemical bond using ultrafast lasers (nobel lecture). *Femtochemistry*, Wiley-VCH Verlag GmbH, 1–85.
- Zhang, J., Y. Fu, M. H. Chowdhury, and J. R. Lakowicz, 2007: Metal-enhanced single-molecule fluorescence on silver particle monomer and dimer: coupling effect between metal particles. *Nano Lett.*, **7** (7), 2101–2107.
- Zhang, W., A. O. Govorov, and G. W. Bryant, 2006: Semiconductor-metal nanoparticle molecules: Hybrid excitons and the nonlinear fano effect. *Phys. Rev. Lett.*, **97** (14), 146 804.
- Zheng, Y. B., et al., 2009: Active molecular plasmonics: Controlling plasmon resonances with molecular switches. *Nano Lett.*, **9** (2), 819–825.
- Zivanovic, S., K. Yee, and K. Mei, 1991: A subgridding method for the time-domain finite-difference method to solve Maxwell's equations. *Microwave Theory Tech., IEEE Trans.*, **39** (3), 471–479.
- Zou, Y., P. Steinvurzel, T. Yang, and K. B. Crozier, 2009: Surface plasmon resonances of optical antenna atomic force microscope tips. *Appl. Phys. Lett.*, **94** (17), 171107.
- Zumofen, G., N. M. Mojarad, and M. Agio, 2009: Light scattering by an oscillating dipole in a focused beam. *N. Cimento C*, **31** (4), 475–485.
- Zumofen, G., N. M. Mojarad, V. Sandoghdar, and M. Agio, 2008: Perfect reflection of light by an oscillating dipole. *Phys. Rev. Lett.*, **101** (18), 180404.

# Acknowledgments

These findings have been to a great extent the results of one another. First and foremost, I am indebted to my mentor prof. Vahid Sandoghdar, and I thank him for his continuous support and advice. I would like to express my appreciation for Franziska Kaminski, Amir Baradaran Ghasemi, Florian Haupt, Ahmad Mohammadi Eslami, Nassiredin M. Mojarad, Xue-Wen Chen and Gert Zumofen. They worked in close collaboration with me and contributed to many of the results presented here. I am also thankful to Pavel Bushev, Ilja Gerhardt, and Gert Wrigge (the Absorption Team), as well as to Lavinia Rogobete, Ulf Håkanson, Sergei Kühn and Giorgio Mori (the Antenna Team).

I furthermore acknowledge stimulating discussions with Michele Celebrano, Hadi Eghlidi, Stephan J. Götzinger, Jaesuk Hwang, Volker Jacobsen, Madhavi Krishnan, Philipp Kukura, Kwang-Geol Lee, Robert Lettow, Alois Renn, Yves Rezus, Costanza Toninelli, as well as with Stefano Buzzi, Yasin Ekinci, Francesco De Angelis, Prof. Enzo Di Fabrizio, Prof. John Sipe, and many others. I am particularly grateful to Prof. Lucio Claudio Andreani, Prof. Costas M. Soukoulis, Prof. Christian Hafner, Prof. Atac Imamoğlu, Prof. Frédéric Merkt and Prof. Martin Quack for the many helpful conversations and the time they dedicated to me. Let me also warmly thank all current and past members of the Nano-Optics Group and of the Laboratory of Physical Chemistry for providing a stimulating and pleasant scientific environment. Last but not least, many thanks go to Xue-Wen Chen, Alois Renn and Gert Zumofen for a critical reading of this manuscript and to Juliane Bremi for her help and patience throughout these years.

This work was financed by the ETH Zurich initiative on Composite Doped Metamaterials (CDM) and by the ETH Zurich grant TH-49/06-1 “Theoretical investigation of the coupling between an emitter and strongly confined optical fields”.

I dedicate the *Habilitationsschrift* to my two little daughters Sofia and Anna and to my wife Marta, who shared with me the joys and difficulties of these intense years.